Werkstoffanwendungen im Maschinenbau

Band 33

Valérian Rémi Iss

Tooth Flank Fracture Risk Evaluation in Carburized Spur Gears with Simulation-Based Prediction of Residual Stresses

Institut für Werkstoffanwendungen im Maschinenbau

RWTH AACHEN UNIVERSITY

Institut für Anwendungstechnik Pulvermetallurgie und Keramik an der RWTH Aachen e.V.

Herausgeber: Prof. Dr.-Ing. C. Broeckmann

Tooth Flank Fracture Risk Evaluation in Carburized Spur Gears with Simulation-Based Prediction of Residual Stresses

Bewertung des Zahnflankenbruchsrisikos in einsatzgehärteten Stirnrädern mittels numerischer Simulation der Eigenspannungen

Von der Fakultät für Maschinenwesen der Rheinisch-Westfälischen Technischen Hochschule Aachen zur Erlangung des akademischen Grades eines Doktors der Ingenieurwissenschaften genehmigte Dissertation

vorgelegt von

Valérian Rémi Iss

Berichter: Univ.-Prof. Dr.-Ing. Christoph Broeckmann
Univ.-Prof. Dr.-Ing. habil. Volker Schulze

Tag der mündlichen Prüfung: 7. Januar 2025

Diese Dissertation ist auf den Internetseiten der Universitätsbibliothek online verfügbar.

Werkstoffanwendungen im Maschinenbau
hrsg. von Prof. Dr.-Ing. Christoph Broeckmann

Band 33

Valérian Rémi Iss

Tooth Flank Fracture Risk Evaluation in Carburized Spur Gears with Simulation-Based Prediction of Residual Stresses

Shaker Verlag
Düren 2025

Bibliographic information published by the Deutsche Nationalbibliothek
The Deutsche Nationalbibliothek lists this publication in the Deutsche Nationalbibliografie; detailed bibliographic data are available in the Internet at http://dnb.d-nb.de.

Zugl.: D 82 (Diss. RWTH Aachen University, 2025)

Copyright Shaker Verlag 2025
All rights reserved. No part of this publication may be reproduced, stored in a retrieval system, or transmitted, in any form or by any means, electronic, mechanical, photocopying, recording or otherwise, without the prior permission of the publishers.

Printed in Germany.

Print-ISBN 978-3-8440-9941-6
PDF-ISBN 978-3-8191-0021-5
ISSN 2195-2981
eISSN 2944-8573
https://doi.org/10.2370/9783819100215

Shaker Verlag GmbH • Am Langen Graben 15a • 52353 Düren
Phone: 0049/2421/99011-0 • Telefax: 0049/2421/99011-9
Internet: www.shaker.de • e-mail: info@shaker.de

Zusammenfassung

Der komplexe Spannungszustand in einsatzgehärteten Zahnrädern wird durch eine Vielfalt von Parametern beeinflusst, darunter die Makro- und Mikrogeometrie der Zahnnflanke, die tribologischen Eigenschaften und Schmierbedingungen, der verwendete Werkstoff und die wärmebehandlungsbedingten Härte- und Eigenspannungsgradiente. Dementsprechend können verschiedene Versagensarten mit verschiedenen zugrunde liegenden Mechanismen im Betrieb auftreten. Der Zahnflankenbruch (TFF) ist ein Ermüdungsversagen, das durch einen Primärriss im Bereich der aktiven Kontaktfläche gekennzeichnet ist, der unterhalb der Oberfläche entsteht und hauptsächlich bei einsatzgehärteten Zahnrädern beobachtet wird. Während die Wärmebehandlung der aktiven Flanke positive Druckeigenspannungen und eine erhöhte Oberflächenhärte verleiht, können Zugeigenspannungen, die sich zwischen der Randschicht und dem Kernbereich bilden, das Risiko eines TFF erheblich erhöhen. Es liegen bereits zahlreiche Methoden vor, welche das Risiko eines Zahnflankenbruchs bei einsatzgehärteten Stirnrädern beurteilen. Da diese Methoden in der Regel starke Vereinfachungen bei der Bewertung von Eigenspannungen zu Grunde legen, ist die Genauigkeit oder der Anwendungsbereich dieser jedoch begrenzt. Faktoren wie Einsatzhärtungstiefe, Kohlenstofftiefenprofil, Werkstoffqualität und Zahnradgröße sowie deren Wechselwirkungen werden nur teilweise berücksichtigt. Mit besonderem Fokus auf die Vorhersage und Bewertung von Eigenspannungen, die durch die aufkohlende Wärmebehandlung hervorgerufen werden, wird in dieser Arbeit eine neuartige Methode zur Bewertung des Risikos eines Zahnflankenbruchs bei Stirnrädern vorgestellt. Auf der Grundlage umfangreicher dilatometrischer Untersuchungen an 18CrNiMo7-6-Stahlproben wird ein gekoppeltes Finite-Elemente Modell erstellt. Das numerische Modell integriert die wesentlichen Mechanismen, welche für die Entwicklung von Dehnungen und Spannungen während der Wärmebehandlung verantwortlich sind, in eine thermisch-mechanisch-metallurgische Berechnung. Durch eine umfassende simulative Parameterstudie an zylindrischen Proben werden Aspekte der Eigenspannungsentstehung in einsatzgehärteten Bauteilen untersucht und die wichtigsten Einflussfaktoren und Korrelationen identifiziert. Die Anwendbarkeit des Simulationsmodells wird anhand verfügbarer Eigenspannungsmessungen für ein breites Spektrum von Zahnradgrößen und Wärmebehandlungsparametern validiert. Schließlich werden verschiedene Methoden und Annahmen untersucht und in den verfügbaren numerischen Berechnungsverfahren aufgenommen, um die Risiken von TFF in einsatzgehärteten Stirnrädern vorherzusagen. Es konnte gezeigt werden, dass die Berechnung der Eigenspannungs- und Härteprofile durch die entwickelte Simulationsmethode ein erhebliches Potenzial zur Verbesserung der Genauigkeit der TFF-Bewertung bietet, wodurch weitere Verbesserungen der Zuverlässigkeit und Leistungsdichte von Getrieben ermöglicht werden können.

Abstract

The complex stress states in carburized gear teeth depend on a wide range of factors, including gear design, operating circumstances, lubricant and tribological characteristics, gear material and hardness or case depth resulted from the heat treatment procedure. As a result, several failure types with various underlying mechanisms can arise. Tooth flank fracture (TFF) is a fatigue failure characterized by a primary crack in the region of the active contact area, which is initiated below the surface and most often observed on carburized gears. While the carburizing heat treatment provides the active flank with favorable compressive residual stresses and increased surface hardness, tensile residual stresses that may form between the case and core area can significantly raise the chances of TFF. There are a number of methods available to address the risks of tooth flank fracture in carburized spur gears. However, primarily because of oversimplifications in the assessment of residual stresses, the accuracy or applicability range of these methods is typically limited. Factors such as carburized depth, carbon depth profile, material quality and gear size, along with their interactions, are only partially accounted for. With a particular focus on the estimation and assessment of residual stresses brought on by the carburizing heat treatment, a novel method for evaluating the risks of tooth flank fracture in spur gears is presented in this work. A coupled finite-element (FE) model is built using extensive dilatometric investigations on 18CrNiMo7-6 steel samples. The model integrates key mechanisms responsible for strain and stress development during heat treatment in a thermal-mechanical-metallurgical calculation. Through a comprehensive numerical parameter study on cylindrical samples, fundamental aspects of residual stress evaluation in carburized components are explored, identifying main influencing factors and correlations. The simulation model's applicability is validated across a wide range of gear sizes and heat treatment procedures using available residual stress measurements. Finally, different methods and sets of assumptions are investigated and included in the simulation framework to predict the risks of TFF in carburized gears. Among these methods, incorporating residual stresses and hardness calculations through FE simulation shows significant potential for enhancing the accuracy of TFF assessment, thereby enabling further improvements in gearbox reliability and power density.

Acknowledgement

The writing of a dissertation is marked by many difficult tasks. These few words of preface are one of them, because I can hardly summarize in so few sentences the years that have passed, the moments of laughter, of doubt, of exciting and tedious work, the proportions of which may have varied considerably from one phase to another. On the other hand, it's easy to find people to thank, to whom I feel indebted and without whom this work would not have been possible.

The first of these is Prof. Dr.-Ing. Christoph Broeckmann, who placed his trust in me during the 5 years I spent at his institute. I was given unreserved support and a high degree of autonomy to carry out this and many other projects in the way that is best suited to my needs. I would also like to thank Univ.-Prof. Dr.-Ing. habil. Volker Schulze for accepting the role of co-examiner and for his invaluable advice.

In Aachen, I have had the opportunity to learn continuously from Ali Rajaei, with whom I have had an extremely pleasant and productive exchange, and who has contributed greatly to my work through his enthusiasm, technical expertise and high standards.

I would like to thank Jean-André Meis for his expert advice on my research work, but above all for the many fruitful collaborations and discussions, as well as for his inspiring ideas. As an academic, it has been especially enriching to have privileged interlocutors from the industry, always interested in productive discussions and new projects. In this context, I would like to extend my special thanks to Markus Schneider and the participants in the AVIF A325 project.

I would also like to thank Oliver Schenk and Bengt Hallstedt for their availability and pertinent advice concerning my work. All in all, I have developed close and friendly relationships with many colleagues at IWM. Although I cannot mention them all by name, I hope they recognise themselves in these few lines, as their presence has made my professional and private life so much easier over the years.

I'm also grateful to Adrien Vinel for his help with the proof-reading of my manuscript.

I'd like to thank my partner Sophia for her constant support, and for the happiness and stability she's brought to my life. I'd also like to thank her for her patience and tolerance when my schedule didn't allow me to give her the space she deserved.

I would like to thank my friends from all horizons, on whom I can count and whose company is essential to me, even those I rarely see.

Finally, I'd like to thank my parents, my brother, my sister and the rest of my family. Even though they are not directly involved in my work, they have been my role models day after day and have always ensured that I have the material and psychological conditions that are needed to carry out my projects.

Contents

1. Introduction **1**

2. Theory and state of the art **3**

2.1. Fatigue properties of carburized steels and influencing factors 3

2.1.a. Static strength 5

2.1.b. Defects and non-metallic inclusions 7

2.1.c. Mean stresses and residual stresses 11

2.1.d. Multi-axiality and time evolution of load 17

2.1.e. Size effect and further aspects 21

2.2. Tooth flank fracture of carburized gears 28

2.2.a. Experimental findings 28

2.2.b. Assessment methods for tooth flank fracture 32

2.3. Residual stress development in carburized components 44

2.4. Summary and objectives of this work 53

3. Material model for carburizing heat treatment **57**

3.1. Material investigation 57

3.1.a. Yield stress and flow properties 57

3.1.b. Transformation behavior, thermal expansion and transformation strains 60

3.1.c. Transformation-induced plasticity 65

3.1.d. Tempering behavior 66

3.2. Material modeling 70

3.2.a. Modeling of flow properties 70

3.2.b. Modeling of transformation behavior 71

3.2.c. Modeling of thermal expansion and transformation strains 74

3.2.d. Hardness model 77

3.2.e. Modeling of tempering effects 77

4. Finite-element prediction of residual stress in carburized gears **81**

4.1. Methods 82

4.1.a. Geometry 83

4.1.b. Model set up 86

4.1.c. Evaluation of the simulation results 87

4.1.d. Correction of calculated residual stresses for comparison with measurement results 88

4.2. Results . . . 91
4.2.a. Analysis of calculated residual stresses on hollow cylindrical samples . 91
4.2.b. Correlation analysis . . . 96
4.2.c. Detailed analysis of selected gear simulations . . . 99
4.2.d. Validation of the heat treatment simulation model . . . 103
4.2.e. Analysis of the residual stress equilibrium . . . 112
4.2.f. Investigated influencing parameters on the residual stresses in carburized gears . . . 113

5. Calculation of tooth flank fracture risks 117
5.1. Prediction model for load stresses . . . 117
5.2. Prediction model for tooth flank fracture . . . 119
5.2.a. Model based on Witzig's approach . . . 120
5.2.b. Model based on Böhme's approach . . . 125
5.2.c. Model based on Meis' approach . . . 129
5.2.d. Summary of the tested TFF prediction approaches . . . 134

6. Conclusion 137

A. Appendix 153
A1. Chemical composition of alloys used in this work . . . 153
A2. Austenite flow properties . . . 153
A3. Bainite flow properties . . . 155
A4. Martensite flow properties . . . 157
A5. Characterization tests for isothermal bainite phase transformation kinetics . 159
A6. Transformation kinetics model parameters . . . 160
A7. Strain model parameters . . . 164
A8. Heat transfer coefficients for quench simulation . . . 165
A9. Residual stress simulation results for cylindrical samples . . . 167

List of symbols and acronyms

Acronyms

AISI	American Iron and Steel Institute
CASH	Computer aided simulation of heat treatment research project
CHD	Case hardness depth
CP	Contact point
CT	Computer tomography
CCT	Continuous cooling transformation curves
DIN	German Institute for Standardization
DOE	Design of Experiments
FE	Finite element
FKM	Forschungskuratorium Maschinenbau e.V.
FVA	Research Association for Drive Technology
FZG	Gear Research Center at the Technical University of Munich
HCF	High cycle fatigue
HSV	Highly stressed volume
HTC	Heat treatment coefficient
ISO	International Organization for Standardization
IWM	Insitute for Material Applications in Mechanical Engineering at RWTH Aachen University
IWT	Leibniz Institute for Materials Engineering in Bremen
KEV	Critical plane hypothesis for determination of equivalent stress
LZ	Liu-Zenner fatigue multi-axial criterion
ML/ME	Material quality classes according to ISO 6336-5
MAE	Mean absolute error

ME	Moore & Evans correction method for residual stress measurements
ODA	Optical dark area
OES	Optical emission spectroscopy
PIN	Papuga Integral Criterion for mutli-axial fatigue
SEP	Steel Iron Test Sheets (technical standards) from Steel Institute VDEh
SIH	Shear stress intensity hypothesis
S-N	Curve describing the relation between cyclic stress amplitude and number of cycles to failure
TFF	Tooth flank fracture
TIFF	Tooth interior flank fracture
TRIP	Phase transformation induced plasticity
VHCF	Very high cycle fatigue
XRD	X-Ray diffraction

Gear and contact parameters

$b_{h,CP}$	Half of Hertzian contact width at contact point CP
E_r	Reduced modulus of elasticity
F_N	Normal contact force
H	Thickness of model plate geometry for correction of residual stress measurement
L	Contact width
m_n	Gear module
M_1	Input torque at driving pinion
$p_{h,CP}$	Hertzian pressure at contact point CP
$R_{b,2}$	Base circle radius of driven gear
X_{CP}	Load sharing factor at contact point CP
z	Number of teeth
ν	Poisson coefficient

$\rho_{red,CP}$	Equivalent radius of curvature at contact point CP

Heat treatment and phase transformations

A	Austenite
B	Bainite
FP	Ferrite/pearlite
M	Martensite
RA	Residual austenite
T	Temperature
b_k	Transformation strain of phase k with regards of a defined reference state
b_{KM}	Material coefficient for Koistinen Marburger equation
C_0	Nominal carbon concentration for calculation of phase transformation kinetics
C_a	Carbon potential corrected for alloying elements
C_c	Carbon concentration
C_{eff}	Effective carbon content for calculation of phase transformation kinetics
C_p	Carbon potential
D_c	Diffusion coefficient for carbon atoms
f_k	Correction scalar function for non-isothermal diffusive phase transformation of austenite in phase k
h	Heat transfer coefficient
k_a	Correction factor of carbon potential for alloyed steels
k_k	Empirical coefficient for correction of carbon content in kinetics of phase transformation of austenite into phase k
K_k^{tp}	Transformation plastiticity coefficient for transition of austenite in phase k
M_S	Martensite start temperature
n	Avrami exponent for phase transformation kinetics
Q	Heat flow from workpiece to quenchant

t	Time
$t_{8/5}$	Characteristic cooling time between $800\,°C$ and $500\,°C$
T_L	Melting temperature
T_q	Quenchant temperature
T_s	Surface temperature
X	Variable describing the evolution of tempering process
α_k	Thermal expansion coefficient of phase k
β	Transition number for carbon atoms during gas carburizing
τ	Avrami time constant for phase transformation kinetics
ξ_k	Volume fraction of phase k
$\overline{\xi}_k$	Maximal reachable volume fraction for phase k
$\vec{j_c}$	Diffusion flux in direction perpendicular to plane suface with normal unit vector $\vec{n}$
$\overline{\overline{\epsilon^{cr}}}$	Creep strain tensor
$\overline{\overline{\epsilon^{el}}}$	Elastic strain tensor
$\overline{\overline{\epsilon^{pl}}}$	Plastic strain tensor
$\overline{\overline{\epsilon^{th}}}$	Thermal strain tensor
$\overline{\overline{\epsilon^{total}}}$	Total strain tensor
$\overline{\overline{\epsilon^{tr}}}$	Transformation strain tensor
$\overline{\overline{\epsilon^{tp}}}$	Transformation plasticity strain tensor

Material strength properties

f_{-1}	Alternate fatigue strength under axial load
f_0	Fatigue strength under axial load with stress ratio $R = 0$
H_V	Vickers hardness
K_{Pos}	Coefficient for local fatigue strength reduction as a function of defect position
k_w	Ductility ratio for fatigue strength

M_m	Mean stress sensitivity
M'_m	Reduced mean stress sensitivity for stress ratios $0 < R < 0.5$
M_{RS}	Residual stress sensitivity
R	Stress ratio
R_m	Tensile strength
t_{-1}	Fatigue strength under torsional load with stress ratio $R = -1$
t_0	Fatigue strength under torsional load with stress ratio $R = 0$
σ_a	Cyclic stress amplitude
σ_D	Fatigue strength limit without specifying the type of load
σ_m	Cyclic mean stress
$\sigma_{p,cyc}$	Cyclic yield stress
σ_{RS}	Scalar residual stress

Stresses, equivalent stress and failure models

A	Material exposure
a_{Bo}	Auxiliary parameter for damage calculation in Böhme's model
A_{crit}	Threshold value for material exposure
b_{Bo}	Auxiliary parameter for damage calculation in Böhme's model
a_{DV}	Dang Van model parameter for influence of hydrostatic stress
b_{DV}	Dang Van model parameter for damage threshold value
C	Auxiliary parameter for damage calculation in Böhme's model
c_{Bo}	Auxiliary parameter for damage calculation in Böhme's model
C_d	Volume concentration of material defects
d_{Bo}	Auxiliary parameter for damage calculation in Böhme's model
D_{Bo}	Damage parameter for Böhme's calculation model
K_{defect}	Factor for consideration of reduced local shear strength due to defects in material exposure calculation

K_{mat}	Material factor for calculation of local material exposure
$K_{\tau,perm}$	Hardness conversion factor for calculation of local material exposure
n_V	Number of elementary volumes V_i in volume V
$P_S^{(V)}$	Survival probability of volume V
$P_S^{(V_i)}$	Survival probability of elementary volume V_i
R_{corr}	Pearson correlation coefficient
p	Probability of null hypothesis for correlation analysis
V_0	Reference volume
(x, y, z)	Material point coordinates in global system
(x', y', z')	Material point coordinates in local system
α_k	Geometry form factor
ζ_{dist}	Shape parameter for generalized extreme values distribution function
θ	Pole coordinate
κ	Weibull module
λ	Auxiliary parameter for damage calculation in Böhme's model
μ_{dist}	Mean defect size for generalized extreme values or lognormal distribution function
χ	Dimensionless scalar stress gradient
σ^*	Normalized stress in notch region
$\sigma_{\theta\phi,a}$	Amplitude of stresses normal to plane (θ, ϕ)
$\sigma_{\theta\phi,m}$	Mean value of stresses normal to plane (θ, ϕ)
σ_{dist}	Scale parameter for generalized extreme values or lognormal distribution function
$\bar{\sigma}_{dist}$	Defect size standard deviation for lognormal distribution function
σ_h	Hydrostatic stress
σ_{max}	Notch root stress

σ_{ax}	Axial stress component axial with regards to the selected direction
σ_n	Normal stress component with regards to the selected direction
σ_{tan}	Tangential stress component tangential with regards to the selected direction
$\sigma^{RS,I}$	Scalar residual stress of first kind
$\sigma^{RS,II}$	Scalar residual stress of second kind
$\sigma^{RS,III}$	Scalar residual stress of third kind
σ_y^{RS}	Scalar residual stress as a function of the material depth
$\sigma_{\theta\phi,va}$	Equivalent stress amplitude for plane (θ, ϕ)
$\sigma_{\theta\phi,vm}$	Equivalent mean stress for plane (θ, ϕ)
τ_{12}	Principal shear stress
τ_{eff}	Effective shear stress according to SIH
$\tau_{eff,EL,RS}$	Equivalent shear stress with superposed residual and load stresses
$\tau_{eff,RS}$	Equivalent shear stress of residual stress state
τ_n	Scalar shear stress
τ_{perm}	Permissible equivalent shear stress
$\tau_{\theta\phi,a}$	Amplitude of shear stresses in plane (θ, ϕ)
$\tau_{\theta\phi,m}$	Mean value of shear stresses in plane (θ, ϕ)
ϕ	Azimuth coordinate
$\vec{n}$	Normal unit vector to a selected plane
$\vec{P_n}$	Stress vector
$\vec{u}$	First unit vector defining local coordinate system in plane (θ, ϕ)
$\vec{v}$	Second unit vector defining local coordinate system in plane (θ, ϕ)
$\vec{w}$	Third unit vector defining local coordinate system in plane (θ, ϕ)
$\overline{\overline{\sigma}}$	Stress tensor
$\overline{\overline{S}}$	Deviatoric stress tensor

List of Figures

2.1. Correlation plots between steel hardness and fatigue strength. 7
2.2. Effects of a non-metallic inclusion on the fatigue strength. 8
2.3. Schematic Haigh diagram. 12
2.4. Classification of residual stresses depending on the scale of observation. . 13
2.5. Mean stress and residual stress sensitivity. 15
2.6. Coordinate transformation of stresses. 18
2.7. Definition of normal and shear stresses and their time evolution. 20
2.8. Residual stresses of samples with varying CHD and diameters. 24
2.9. Effect of CHD on the rotating bending fatigue strength. 26
2.10. Schematic characteristics of TFF. 29
2.11. Main interactions in FE-simulation of a carburizing heat treatment. . . . 51

3.1. Flow properties of austenitic 18CrNiMo7-6. 59
3.2. Time-temperature-transformation diagrams of 18CrNiMo7-6 steel. 61
3.3. Phase transformation determination by dilatometry. 62
3.4. Thermal expansion coefficients and transformation strains. 63
3.5. Dilatometer curves of 18CrNiMo7-6 samples. 63
3.6. Carbon dependent microstructure after rapid cooling. 64
3.7. TRIP-strains during quenching. 66
3.8. Tempering-induced strains. 67
3.9. Post-processed tempering-induced strains. 67
3.10. Hardness of quenched and tempered samples. 68
3.11. Tempering-induced strains under axial load. 68
3.12. Segregated microstructure in dilatometer samples. 69
3.13. Segregated microstructure in heat treated dilatometer samples. 69
3.14. Martensite start temperature as a function of carbon content. 71
3.15. Schematic sequence of the calculation of phase transformations. 72
3.16. Validation of the phase transformation kinetics model. 74
3.17. Comparison between simulated and experimental dilatometer curves. . . 75
3.18. Comparison between model and selected experiments on TRIP-strains during martensite transformation. 76
3.19. Carbon-dependent TRIP-factors for bainite and martensite. 76
3.20. Schematic description of the tempering process. 78
3.21. Validation of strain model for tempering. 79

4.1. Definition of the mechanical boundary conditions for the heat treatment simulation of gears. . . . 86
4.2. Definition of paths and local coordinate systems. . . . 89
4.3. Schematic representation of the correction of residual stress measurements. 91
4.4. Residual stresses in reference cylinder simulation. . . . 92
4.5. Residual stresses in cylinders with varying CHD. . . . 93
4.6. Residual stresses in cylinders with varying geometry and CHD. . . . 94
4.7. Residual stresses in cylinders with varying wall thickness. . . . 95
4.8. Correlation analysis of residual stresses in cylinders for path 1. . . . 97
4.9. Correlation analysis of residual stresses in cylinders for path 2. . . . 98
4.10. Calculated spatial distribution of carbon in tooth region prior to quenching for gear simulation 1 with module 3 mm and CHD 0.5 mm. . . . 99
4.11. Comparison of the simulated and measured temperature curves during oil quenching of the gear with module 3 mm. . . . 100
4.12. Predicted phase fractions in gear module 3 mm with CHD = 0.5 mm and oil quenching. . . . 101
4.13. Predicted stress distribution in gear module 3 mm with CHD = 0.5 mm and oil quenching. . . . 101
4.14. Residual stress tensor components of gear module 3 mm with CHD = 0.5 mm and oil quenching. . . . 102
4.15. Residual stress profile of gear module 3 mm with CHD = 0.5 mm and oil quenching. . . . 103
4.16. Validation of residual stress predictions for gear module 3 mm with oil quenching. . . . 104
4.17. Validation of residual stress predictions for gear module 3 mm with gas quenching. . . . 105
4.18. Validation of residual stress predictions for gear module 3 mm with salt bath or polymer bath quenching. . . . 106
4.19. Validation of residual stress predictions for gear module 3 mm with varying carbon depth profiles. . . . 107
4.20. Validation of residual stress predictions for gear module 18 mm with oil quenching. . . . 108
4.21. Validation of residual stress predictions for gear module 18 mm with salt bath or polymer bath quenching. . . . 109
4.22. Evaluation of the accuracy of residual stress prediction model. . . . 110
4.23. Evaluation of the accuracy of alternative residual stress prediction models. 111
4.24. Evaluation of the accuracy of hardness prediction model. . . . 111
4.25. Residual stress equilibrium in carburized gears. . . . 113
4.26. Impact of CHD variations on predicted residual stresses in gears. . . . 114

4.27. Impact of gear geometry variations on predicted residual stresses. 115

5.1. Computed contact stresses using two different approaches. 119
5.2. Material exposure of gear module with 3 mm. 121
5.3. Material exposure of gear with module 3 mm with varying CHD and load. 122
5.4. Material exposure of gears with module 5 mm. 123
5.5. Failure probability of gear with module 3 mm based on material exposure calculation. 124
5.6. Failure probability of gear with module 5 mm based on material exposure calculation. 124
5.7. Damage parameter of gear with module 3 mm. 126
5.8. Damage parameter of gear with module 3 mm with varying CHD. 126
5.9. Damage parameter of gears with module 5 mm. 127
5.10. Failure probability of gear with module 3 mm based on damage calculation. 128
5.11. Failure probability of gear with module 5 mm based on damage calculation. 129
5.12. Size distribution functions for non-metallic inclusions. 131
5.13. Failure probability of gear with module 3 mm based on statistical model. 131
5.14. Characteristics of critical defects for gear with module 3 mm. 132
5.15. Position of critical defects for gear with module 3 mm. 133
5.16. Failure probability of gear with module 5 mm based on statistical model. 134

A5.1. Time-length change diagram of isothermal bainite phase transformation as a function of carbon concentration. 159
A5.2. Post-processed kinetics parameters τ_B and n_B for equation 3.1 from isothermal bainite phase transformation trials in figure A5.1. 159
A8.3. Applied heat transfer coefficient and quenched surfaces in heat treatment simulation: oil bath quenching Marquench 875 at 90 $°C$ [132]. 165
A8.4. Applied heat transfer coefficient and quenched surfaces in heat treatment simulation: polymer bath quenching Aquacool AC (15%) at 40 $°C$, inverse fit with initial parameters from [132]. 165
A8.5. Applied heat transfer coefficient and quenched surfaces in heat treatment simulation: salt bath AS135 with temperature 170 $°C$, inverse fit with initial parameters from [167]. 166
A8.6. Applied heat transfer coefficient and quenched surfaces in heat treatment simulation: high pressure gas with 18 bar N_2, values derived from [158]. . 166
A9.7. Results for heat treatment simulation 1 on cylindrical samples along *path 1* (left) and *path 2* (right). 167
A9.8. Results for heat treatment simulation 2 on cylindrical samples along *path 1* (left) and *path 2* (right). 167

A9.9. Results for heat treatment simulation 3 on cylindrical samples along *path 1* (left) and *path 2* (right). . . . 168
A9.10. Results for heat treatment simulation 4 on cylindrical samples along *path 1* (left) and *path 2* (right). . . . 168
A9.11. Results for heat treatment simulation 5 on cylindrical samples along *path 1* (left) and *path 2* (right). . . . 168
A9.12. Results for heat treatment simulation 6 on cylindrical samples along *path 1* (left) and *path 2* (right). . . . 169
A9.13. Results for heat treatment simulation 7 on cylindrical samples along *path 1* (left) and *path 2* (right). . . . 169
A9.14. Results for heat treatment simulation 8 on cylindrical samples along *path 1* (left) and *path 2* (right). . . . 169
A9.15. Results for heat treatment simulation 9 on cylindrical samples along *path 1* (left) and *path 2* (right). . . . 170
A9.16. Results for heat treatment simulation 10 on cylindrical samples along *path 1* (left) and *path 2* (right). . . . 170
A9.17. Results for heat treatment simulation 11 on cylindrical samples along *path 1* (left) and *path 2* (right). . . . 170
A9.18. Results for heat treatment simulation 12 on cylindrical samples along *path 1* (left) and *path 2* (right). . . . 171
A9.19. Results for heat treatment simulation 13 on cylindrical samples along *path 1* (left) and *path 2* (right). . . . 171
A9.20. Results for heat treatment simulation 14 on cylindrical samples along *path 1* (left) and *path 2* (right). . . . 171
A9.21. Results for heat treatment simulation 15 on cylindrical samples along *path 1* (left) and *path 2* (right). . . . 172
A9.22. Results for heat treatment simulation 16 on cylindrical samples along *path 1* (left) and *path 2* (right). . . . 172
A9.23. Results for heat treatment simulation 17 on cylindrical samples along *path 1* (left) and *path 2* (right). . . . 172
A9.24. Results for heat treatment simulation 18 on cylindrical samples along *path 1* (left) and *path 2* (right). . . . 173
A9.25. Results for heat treatment simulation 19 on cylindrical samples along *path 1* (left) and *path 2* (right). . . . 173
A9.26. Results for heat treatment simulation 20 on cylindrical samples along *path 1* (left) and *path 2* (right). . . . 173
A9.27. Results for heat treatment simulation 21 on cylindrical samples along *path 1* (left) and *path 2* (right). . . . 174

A9.28. Results for heat treatment simulation 22 on cylindrical samples along *path 1* (left) and *path 2* (right). 174
A9.29. Results for heat treatment simulation 23 on cylindrical samples along *path 1* (left) and *path 2* (right). 174
A9.30. Results for heat treatment simulation 24 on cylindrical samples along *path 1* (left) and *path 2* (right). 175
A9.31. Results for heat treatment simulation 25 on cylindrical samples along *path 1* (left) and *path 2* (right). 175
A9.32. Results for heat treatment simulation 26 on cylindrical samples along *path 1* (left) and *path 2* (right). 175
A9.33. Results for heat treatment simulation 27 on cylindrical samples along *path 1* (left) and *path 2* (right). 176
A9.34. Results for heat treatment simulation 28 on cylindrical samples along *path 1* (left) and *path 2* (right). 176
A9.35. Results for heat treatment simulation 29 on cylindrical samples along *path 1* (left) and *path 2* (right). 176
A9.36. Results for heat treatment simulation 30 on cylindrical samples along *path 1* (left) and *path 2* (right). 177
A9.37. Results for heat treatment simulation 31 on cylindrical samples along *path 1* (left) and *path 2* (right). 177
A9.38. Results for heat treatment simulation 32 on cylindrical samples along *path 1* (left) and *path 2* (right). 177
A9.39. Results for heat treatment simulation 33 on cylindrical samples along *path 1* (left) and *path 2* (right). 178
A9.40. Results for heat treatment simulation 34 on cylindrical samples along *path 1* (left) and *path 2* (right). 178
A9.41. Results for heat treatment simulation 35 on cylindrical samples along *path 1* (left) and *path 2* (right). 178
A9.42. Results for heat treatment simulation 36 on cylindrical samples along *path 1* (left) and *path 2* (right). 179
A9.43. Results for heat treatment simulation 37 on cylindrical samples along *path 1* (left) and *path 2* (right). 179

List of Tables

3.1. Test plan for flow curve determination. 58
3.2. Hardness values of bainite and ferrite-pearlite used in the simulation model. 77

4.1. Experimental heat treatment tests on gears. 82
4.2. Design of Experiments (DoE) for hollow cylindrical samples. 84
4.3. DoE for gear heat treatment. 85

5.1. Gear pairs for numerical investigation of TFF. 120
5.2. Weibull module values for calculation of failure probability. 121

A.1. Comparison of the chemical composition of steel 18CrNiMo7-6 used for dilatometer samples and carburized gears [47]. 153
A.2. Temperature-dependent flow properties of 18CrNiMo7-6 with austenite microstructure 153
A.3. Temperature-dependent flow properties of 50CrNiMo7-6 with austenite microstructure 154
A.4. Temperature-dependent flow properties of 82CrNiMo7-6 with austenite microstructure 154
A.5. Temperature-dependent flow properties of 18CrNiMo7-6 with bainitic microstructure (isothermally transformed at 450 °C). 155
A.6. Temperature-dependent flow properties of 32CrNiMo7-6 with bainitic microstructure (isothermally transformed at 400 °C). 155
A.7. Temperature-dependent flow properties of 50CrNiMo7-6 with bainitic microstructure (isothermally transformed at 300 °C). 156
A.8. Temperature-dependent flow properties of 66CrNiMo7-6 with bainitic microstructure (isothermally transformed at 300 °C). 156
A.9. Temperature-dependent flow properties of 18CrNiMo7-6 with martensitic microstructure. 157
A.10. Temperature-dependent flow properties of 32CrNiMo7-6 with martensitic microstructure. 157
A.11. Temperature-dependent flow properties of 50CrNiMo7-6 with martensitic microstructure. 158
A.12. Temperature-dependent flow properties of 66CrNiMo7-6 samples with martensitic (+ residual austenite) microstructure. 158
A.13. Temperature-dependent flow properties of 82CrNiMo7-6 samples with martensitic (+ residual austenite) microstructure. 158

A.14.Transformation kinetics of ferrite/pearlite - τ_{FP}. 160
A.15.Transformation kinetics of ferrite/pearlite - $\overline{\xi}_{FP}$. 161
A.16.Transformation kinetics of ferrite/pearlite - $f_{FP}(\dot{T})$. 162
A.17.Transformation kinetics of bainite - $f_B(\dot{T})$. 163

Chapter 1

Introduction

The development of wind turbines in terms of global quantity and power density is critical to achieving net-zero scenarios for the reduction of carbon greenhouse gas emissions in the energy sector. According to the International Energy Agency, in order to meet the climate targets by 2050, a total installed power of around 2.75 TW would be required by 2030 [1]. Conventional high-speed or medium-speed gearboxes accounted for about 70 % of the market share in 2022 among the drivetrain technologies used in wind turbines to convert mechanical energy into electrical power, followed by direct drive systems that don't require gearboxes [2]. In the majority of wind turbines, gearboxes are among the most expensive components. Additionally, since gearbox failures result in noticeably long turbine downtime, gearbox design is crucial to the continuous deployment and economic viability of wind turbines. Favorable compressive residual stresses and hardness gradients, optimized tooth flank geometry, surface condition and lubrication as well as increased material quality enable to delay or prevent the onset of failure initiation at the loaded surface of carburized gears in gearboxes. Under these conditions, the stress and material state of the layers located beneath the surface gain importance and may lead to tooth flank fracture (TFF). Residual stresses from the carburizing heat treatment play a critical role in this fatigue failure as tensile stresses that may form between the case and core area can significantly raise the chances of TFF. While there are a number of methods available to address the risks of TFF in carburized spur gears, the accuracy or applicability of these methods is typically limited due to the oversimplification of residual stress assessment. Factors such as carburized depth, carbon depth profile, material quality and gear size, along with their interactions, are only partially accounted for. Residual stresses pose a challenge both in terms of determination and integration into design concepts.

With a particular focus on the estimation and assessment of residual stresses brought on by carburizing heat treatment, a novel method for evaluating the risks of tooth flank fracture in spur gears is presented in this work. A coupled FE model is built using extensive dilatometric investigations on 18CrNiMo7-6 steel samples. The model integrates key mechanisms responsible for strain and stress development during carburizing heat treatment in a thermal-mechanical-metallurgical calculation. Through a comprehensive numerical parameter study on cylindrical samples, fundamental aspects of residual stress evolution in carburized components are explored, identifying main influencing factors and correlations. The simulation model's applicability is validated across a wide range of gear sizes and heat

treatment procedures using available residual stress measurements. Finally, different methods and sets of assumptions are investigated and included in the simulation framework to predict the risks of TFF in carburized gears. The impact of integrated simulation models for residual stress prediction in evaluation methods for TFF is assessed. Incorporating residual stresses and hardness calculations through FE simulation shows significant potential for enhancing the accuracy of TFF assessment, thereby enabling the overall ambition of further performance and reliability improvements in gears.

Chapter 2

Theory and state of the art

2.1. Fatigue properties of carburized steels and influencing factors

ISO/TS 6336-4 defines tooth flank fracture (TFF) as a fatigue failure characterized by a primary crack in the region of the active contact area, which is initiated below the surface and most often observed on carburized gears [3]. Fatigue failure design is crucial in mechanical engineering. Failure through fatigue can happen at levels that seem harmless under low cycle numbers, even without macroscopic plastic deformation. Due to the wide range of influencing factors and the significant statistical variability of fatigue failure in steel components, prediction and safe design are difficult and time-consuming tasks. The fatigue properties of carburised steels have been the subject of many investigations and a considerable amount of research has been carried out – studies which are obviously too numerous to be discussed here. To estimate and evaluate the risks of TFF in carburized gears, it is however necessary to first comprehend some of the key findings on this topic.

This work considers the fatigue problem from the point of view of classical high cycle fatigue (HCF), which assumes for steels to reach a strength limit with constant stress amplitude at cycle numbers between $2 \cdot 10^6$ and $1 \cdot 10^7$. Recent studies, which consider investigations in the very high cycle fatigue range (VHCF) and describe a further decrease in fatigue strength with increasing number of cycles, are not considered here. It is quite conceivable that this assumption severely limits the practical applicability of the results of this work, as it is a very non-conservative approach, especially for components with a high number of load cycles, such as in electromobility. However, the VHCF fatigue properties of case-hardened steels are still the subject of on-going research [4], the modeling of which requires further experimental investigation and is beyond the scope of this thesis.

In general, the fatigue failure of steel components can be described as the succession of three steps: crack initiation, crack propagation and failure.

Crack initiation is caused by the accumulation of dislocation motion and plastic deformation at persistent slip bands in the material. Microstructures like grain boundaries, non-metallic inclusions or surface roughness can increase the stress concentration and cause local plastic deformation even when the loads are far below the material's macroscopic yield stress.

Cracks with a length of about the grain size to about 1 mm are typically referred to be physically short cracks. There is debate on the precise definition and the threshold value of 1 mm, which can differ substantially depending on the steel under consideration. Nevertheless, growth of physically short cracks is reported to be the most decisive factor for the fatigue limit of steel components [5, 6]. While the crack initiation substantially influences the fatigue strength in the finite life domain, many authors only attribute a very moderate impact on the cracking behavior at the HCF limit [5, 6]. Several experimental studies show that the crack initiation phase in HCF typically accounts for less than 10 % of a component's lifetime until a crack length of about 1 mm is reached, with the remaining 90 % corresponding to the propagation of short cracks [7]. During the initiation stage, a significant number of cracks can form, each characterized by a strong interaction with the local microstructure and some discontinuities in the crack growth rate. Only a small percentage of cracks, however, usually overcomes the microstructural barriers and reaches the stage of so-called mechanically/physically short cracks, where the influence of the local microstructure is averaged out along the crack front [6, 8]. As present non-destructive testing methods can only reliably discover defect sizes larger than about 0.5 mm, short crack behavior is basically of little importance in terms of practical safety considerations based on detected cracks. On the other hand, it is critical to estimate the service life of components under cyclic stress.

Cracks tend to propagate along a slip plane until they reach obstacles such as grain boundaries. During the first phase, the crack propagation in ductile materials is controlled by shear stresses. Stage II cracks then grow in a direction normal to the the first principal stress [7, 9]. Depending on the stress level, however, small cracks with a length of about the size of a grain or smaller can exhibit a non-propagating behavior and thus not participate to the fatigue failure of components [5].

Regardless of why small cracks can stop to propagate – because of plasticity-induced crack closure or of some other interactions with microstructural features –, the existence of a fatigue limit for steel samples in the HCF regime appears to be based on a threshold stress value for small cracks to propagate or not [5]. In the presence of sharp notches or residual stresses, however, crack arrest can occur not only due to microscopic barriers such as grain boundaries, but also due to steep gradients in the local stress field, resulting in a decrease in the driving force for further crack propagation [9]. Crack arrest is dependent on both stress level and size of the cracks and defects and can be represented by the horizontal limit curve in the Kitagawa-Takahashi diagram [6, 10].

When short cracks approach microstructural barriers like grain boundaries or inclusions, further growth can be suppressed. On the other hand, long cracks accelerate proportionally to their length with no noticeable effect of the obstacles [8]. Macro-cracks subjected to stresses above the threshold stress can propagate with each load cycle until the remaining cross-section can no longer withstand the load and the component breaks [7]. Intergranu-

lar cracking at the prior-austenite grain boundaries is typical in carburized and quenched sample fatigue failure. This implies that the grain boundary strength is lower than the grain strength, yet this cracking tendency can be reduced with a proper tempering treatment [11, 12]. Aside from integranular cracking, various experimental fatigue studies on carburized steel samples report transgranular fatigue propagation mechanisms. These failures, which indicate enhanced grain boundary strength, are typically linked with bending fatigue endurance limits larger than 1400 MPa, good surface quality, and compressive superficial residual stresses [13]. Crack initiation can occur at non-metallic inclusions, at hardening defects such as non-martensitic transformation products, at disproportionately large grains, or even in a rather homogeneous martensite matrix [9, 13, 14, 15, 5, 4].

The fatigue properties of steels behave stochastically. Fatigue tests always exhibit a statistical scatter, which may be due to variations in the chemical composition, in the surface and residual stress states or in the position and size of the material defects between otherwise identical specimens [8].

There has been an extensive amount of research done on the subject of fatigue properties of carburized parts and the literature mentions a wide range of influencing factors. Instead of providing a detailed explanation of all the mechanisms involved, this section focuses on a few key elements that are considered to be especially significant when it comes to tooth flank fracture in carburized gears. Even though this chapter is structured with distinct influencing parameters, it is important to recall that there are numerous coupling interactions between them.

2.1.a. Static strength

While the strength of steels under static loading correlates with the fatigue properties, prediction models for the fatigue of steel components based on the results of tensile or hardness tests typically only have very limited reliability or validity domain.

Although the crack initiation is related to the plastic deformation within grains, fatigue limit prediction based on the yield stress of the material usually delivers unsatisfactory results. Higher correlations can be reached using the ultimate tensile strength R_m or the hardness $\mathrm{H_V}$. The latter has the advantage of enabling local and quasi non-destructive measurements [5, 16, 17]. Applications of previously derived empirical equations include $f_{-1} = 0.4 \cdot R_m$ [18, 19], $f_{-1} = 0.385 \cdot R_m + 30$ [20] and $f_{-1} = (1.6 \pm 0.1) \cdot \mathrm{H_V}$ [5, 21], where f_{-1} is the alternate fatigue strength limit under axial load. Since the hardness of steels is usually linearly related to the tensile strength, the two types of equations are practically equivalent [8].

For hardness levels below 400 $\mathrm{H_V}$, the roughly linear correlation between hardness and fatigue strength is confirmed for a wide range of alloys and microstructures [8, 5]. Likewise, Velten finds that the ultimate tensile strength can predict the rotational bending fatigue

strength with a linear relationship for steel samples made of 20MoCrS4 and 30CrNiMo8 that have undergone a hardening, carburizing, or nitriding process. The proportionality coefficient is equal to 1.27 and the intercept depends on the material and heat treatment, while this linear equation is only valid up to a maximum hardness value of 500 H_V. Winderlich compiles a series of empirical correlations between hardness and rotating bending strength of steels and finds that these differ only insignificantly for hardness values below approximately 400 H_V [22]. Above 400 H_V, other studies however report that it is no longer possible to predict the fatigue properties of steels solely based on hardness, as other factors come to dominate mechanical strength. The hardness *vs* fatigue strength diagram deviates from its linear trend and has a significant statistical scatter [21, 22]. Consequently, some studies document a flattening of the fatigue strength with increased hardness, some extend the increase further, and other investigations report a reduction of the fatigue properties, as in figure 2.1 left.

This material behavior is attributed to microstructural flaws. Hard steels are particularly susceptible to the effects of internal notches such as non-metallic inclusions. In [5], Murakami analyzed the circumstances for the non-propagation of small cracks, which determines fatigue strength, based on publications by other Japanese researchers as well as his own investigations featuring synthetic defects and non-metallic inclusions. The tendency of a steel to show non-propagating cracks in a wide range of stress amplitudes or crack lengths decreases with its hardness [5]. Accordingly, a hard steel's microstructure has a more negative impact on its fatigue properties than a softer material does when small defects or cracks are present. As long as the fatigue fracture is not caused by defects, it is expected that the nearly linear relationship between fatigue strength and Vickers hardness also applies to the high-strength condition and thus gives the upper limit for the fatigue strength of an inclusion-free high-strength steel [22, 5]. Investigations on vacuum-cleaned steels also indicate that the linear domain can extend up to values of over 400 H_V, whereas typical production processes show the saturation or even decrease of the fatigue limit with increasing hardness due to the presence of inclusions and cracks with sizes not satisfying the criteria for non-propagation of short cracks in the microstructure [5]. The limit range for the linear domain varies depending on the material and a variety of factors, including the cleanliness of the steel, the prior-austenite grain size, and the surface condition [8, 11].

Figure 2.1 right exemplarily shows the relationship beween hardness and fatigue strength for a vacuum remelted steel that exhibits small amounts of non metallic inclusions. Here, the linear dependency is applicable despite the level of hardness and irrespective of the loading direction [5, 23]. On the other hand, the fatigue limit vs. hardness curve for open melted steel flattens already starting from about 200 H_V when the specimen axis is transverse to the rolling direction, for which the size of inclusions in the loaded cross-section appears higher. The next section 2.1.b provides a complete explanation of these effects.

Overall, there are many examples of identified relationships between the steel's static

mechanical characteristics and its fatigue strength. These may however only be regarded as adequate for low hardness levels since other microstructural variables have a significant impact on the fatigue behavior of hard steels. Aside from the fact that different states of a material, such as heat treatment, cleanliness, rolling direction, *etc.* cannot be captured on the basis of hardness or tensile strength alone, the aspect of significant scatter in the fatigue properties of hard steels, which is of the utmost importance in practical applications, cannot be taken into account without additional parameters [16].

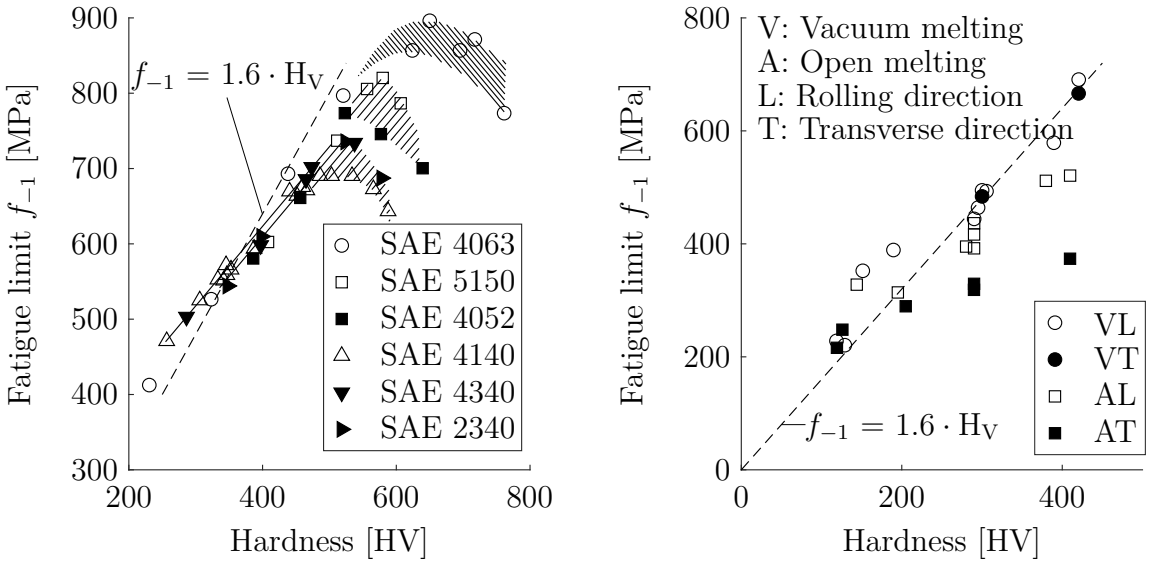


Figure 2.1: Left: Correlation between hardness and fatigue limit for different steels, adapted from [5, 21]. Right: Effects of loading direction and melting method on the fatigue limit *vs* hardness curve, adapted from [5, 23].

2.1.b. Defects and non-metallic inclusions

Steels harder than $400\,\mathrm{H_V}$ show increased susceptibility to strain concentration effects on small microscopic features like cracks or non-metallic inclusions, thus limiting the benefits of hard materials when just considering the lower bound of fatigue strength [24]. For components made of materials having a high fatigue limit, such as bearings, springs, crankshafts and gears, non-metallic inclusions are common possible root causes for failure [6].

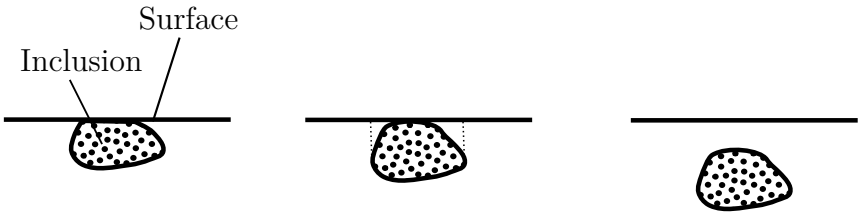
Both surface roughness and internal defects can serve as the origin of persistent slip bands and cracks, with the latter occurring more frequently in weakly notched or surface-hardened components [25]. Non-metallic inclusions are compounds between metallic and non-metallic atoms and include oxides, sulphides, nitrides or oxisulphides. These can result from reactions between the molten metal and deoxidizing particles like silicon, manganese or aluminum, as well as from external contamination during the subsequent processing of the metal [6]. Although their size and frequency can be reduced and their shape altered

through adequate metallurgical operations like vacuum degazing or desulfurization, non-metallic inclusions cannot be completely excluded in semi-finished steel products [26, 11].

A strain concentration occurs close to the interface as a result of mismatches between the inclusions and the metallic matrix, which can be caused by variations in stiffness, ductility, strength or thermal expansion [6]. The bonding between a non-metallic inclusion and the matrix can break during the initial loading cycles already and might even happen during the heat treatment or forming operations. According to Murakami, a non-metallic inclusion has effects on fatigue strength that are similar to cracks of the same size. One of the most important aspects affecting the fatigue strength limit σ_D is inclusion size. In his research, he finds out that an accurate parameter for describing this impact is the square root value of the defect's area $\sqrt{area}$ on a plane section perpendicular to the first principal stress [5]. Investigations of the conditions that lead to non-propagating cracks starting from non-metallic inclusions or artificial defects result in the following equation 2.1 determined from rotating bending fatigue experiments:

$$\sigma_D = K_{Pos} \cdot \frac{\mathrm{H_V} + 120}{\sqrt{area}^{\frac{1}{6}}}, \tag{2.1}$$

where H_V is the Vickers hardness and K_{Pos} is a coefficient depending on the position of the defect relative to the surface of the component, as displayed in figure 2.2.



a) $K_{Pos} = 1.43$ b) $K_{Pos} = 1.41$ c) $K_{Pos} = 1.56$

Figure 2.2: Effects of a non-metallic inclusion on the fatigue strength depending on its location [5]. a) Surface inclusion, b) Inclusion in contact with surface, c) Internal inclusion.

The role of inclusions in the fatigue properties of the material is minimal as long as their size does not exceed a certain threshold. Either the micro-cracks formed at inclusions are not propagating or some other microstructural features act as crack initiation sites. However, for hard steels, the maximal defect size for non-propagating cracks can be less than a few micrometers [5].

Practically all steel components contain some non-metallic inclusions. Large defects may exist with a low frequency even in modern steels with high cleanliness specifications and have a significant negative impact on a component's fatigue strength [26]. Knowledge of the frequency of occurrence, size, and location of non-metallic inclusions is thus extremely

useful, especially because key mechanical components are often designed for extremely low failure probability [25]. This problem is even more acute, as such inclusions can hardly be detectable in the range of failure probabilities usually accessible through fatigue testing [17]. Non-metallic inclusions can be characterized using a variety of techniques, as presented in [25, 26] and [16]:

- First, light microscopy analysis of micrographs of a specific size can be used as a representation of the entire material. Unetched surface contrasts offer information about the statistical distribution, type and size of defects in the material. This method, which is fairly simple and hence very widespread, can be automated and standardized, as for example in DIN EN 10247 [27] or SEP 1571 [28]. Several biases and issues, however, have an impact on the results and interpretation. Even when a large number of sections are evaluated, the observed surface can be many orders of magnitude lower than the volume in large components such as wind turbine gears. Low frequency defects cannot be assessed directly and reliably and must be estimated using extrapolation and extreme value analysis [5]. Even the shapes and sizes of the observed inclusions can be misleading. The largest dimension of the defects is rarely in the plane of the micrograph, which may result in a significant underestimation of the size distribution. Conversion techniques can at least partially address these deficiencies. Nevertheless, it is not straightforward to accurately determine the distribution of sizes and positions of non-metallic inclusions in a component; this task calls for sophisticated statistical techniques and relies on additional assumptions.

- It is possible to dissolve the matrix chemically and look for any leftover non-metallic impurities. In addition to the information about the position of inclusions being lost during the process, this technology has some restrictions on the volume of material that can be processed as well as drawbacks in terms of cost and environmental harm.

- Significant volumes can be evaluated using ultrasonic technology, but only large defects above $\sim 0.1\,\mathrm{mm}$ can be detected, making it possible to characterize only this side of the size distribution. On the other hand, computer tomography (CT) essentially makes it possible to identify the location and size of defects in a sample. However, because the resolution of this method is highly dependent on the observed volume, the range of 10-100 μm defects can only be accessed for very small samples, which may not be representative of the whole component.

- Information regarding a material's non-metallic inclusions can also be obtained via fatigue testing of samples that fail at internal inclusions. A scanning electron microscope can be used for inspection of the fracture surface in order to locate the crack initiation point and assess the size and chemical composition of the relevant defect. This method is usually paired with a shot blasting procedure since it is only effective

when the fracture initiation at the sample's surface is prevented. Since only one defect is characterized for each sample, which is the most critical for the particular stress distribution and sample volume examined, relatively little information is collected. Therefore, this method is not sufficient to statistically describe the size and shape distributions of defects in a material and is rather employed as a supplement to other methods, such as microsection analysis.

Fracture surface of cracks initiated at subsurface typically exhibits a so-called *Fish-Eye* with the inclusion at its center. The inclusion is surrounded by a circular region which can be designated as *Optical Dark Area* (ODA), *Fine Granular Area* or *Granular Bright Facet* and characterizes the slow crack growth under vacuum, as opposed to surface cracks exposed to atmosphere [29, 30]. There is still some debate regarding the impact of the defect's shape. Even though it is clear that the geometry of an inclusion can affect the stress concentration factor directly at the interface, current knowledge indicates that a defect's shape has a considerably smaller impact on a material's fatigue strength than its size. In [5], non-metallic inclusions are treated in a manner comparable to cracks with the same dimensions, which is consistent with experimental reports of early matrix debonding during the first load cycles [31]. Other investigations, on the other hand, insist on the effects of different bonding properties between matrix and inclusions on the initiation of fatigue cracks [32]. The type of inclusion affects the cohesion characteristics with the matrix as well as shape and ductility. Oxides are typically thought of as hard defects that have a propensity to break away from the matrix. Due to the forming processes used to create semi-finished steel products, ductile sulfide inclusions like MnS typically exhibit elongated geometry and tend to deform together with the matrix [32]. The fracture initiation phase can account for a significant portion of finite-life fatigue, in contrast to the HCF limit, which is primarily influenced by the propensity of cracks to exhibit non-propagation behavior. Hence, it is appropriate to attribute a stronger influence of the shape and bonding of non-metallic inclusions on the fatigue properties when considering load levels corresponding to the finite life of components than for HCF limit [5, 16].

Another important aspect of defects is how they interact with each other. Experimental investigations report fatigue crack initiation at clusters formed from multiple, small sized, inclusions [33, 34, 31]. Meis' work includes a discussion of the consequences of inclusion clusters in both calculating methods and the determination of model functions for the sizes of defects that are present in the material [16].

Even though experimental validation is a complex task, it is anticipated that non-metallic inclusions may induce a residual stress field in the neighboring regions during heat treatment operations due to differences in the thermal expansion coefficients of the matrix and the inclusion. Depending on various factors such as the relative values of the thermal expansion coefficients, the yield stress, the shape of the inclusion and the bonding strength, multiple

scenarios can be taken into consideration [35, 5]. Although the quantitative analysis of these effects is rather hypothetical, working principles on fatigue strength can be formed from the effects described in section 2.1.c.

The consequences previously described make it clear that the non-metallic inclusions' presence and characteristics – and consequently the cleanliness of steel – have a significant impact on the material's fatigue properties. According to [11], a substantial percentage of the recent advances in case-hardened gears over the past few decades can be credited to the increased quality of steels. As an illustration, the specifications ISO 6336-5 forecast an enhanced nominal stress number from 1300 to 1650 MPa for contact by raising the material quality standards from ML to ME and an improved nominal stress number for bending of case-hardened wrought steel from 310 to 525 MPa [36].

Non-metallic inclusions only affect a component's fatigue limit when located in a loaded area, where they decrease the local admissible load level for non-propagation of cracks below the fatigue limit of other potential failure sites in a component. This means that in addition to the sizes of the inclusions, it is also important to take into account their locations and the likelihood that they will be found in critical loaded regions. The statistical size effect discussed in section 2.1.e is therefore one of several further aspects that must be taken into account when evaluating how material defects affect fatigue strength.

2.1.c. Mean stresses and residual stresses

The fatigue strength is significantly influenced by mean stresses. While compressive mean stresses increase the allowable load stress amplitude, tensile mean stresses have the opposite effect. In order to describe the sensitivity of a material to mean load stresses, the parameter M_m is usually employed, which represents the slope of the limit curve described by the fatigue limit σ_D in the Haigh diagram between stress ratios of $R = -1$ and $R = 0$ as described by the following equation [8, 7]:

$$M_m = \frac{\sigma_D(R=-1) - \sigma_D(R=0)}{\sigma_D(R=0)}. \tag{2.2}$$

A generally conservative estimate is provided by the Goodman line combined with a flat line in the compressive stress range, as shown hatched green in figure 2.3. For tensile mean stresses, it is reported that the Gerber parabolic function of the mean stress is more accurate to determine the admissible stress amplitude. However, this method is also ineffective for describing the increase of fatigue strength under compressive mean stresses [16, 37]. In general, the mean stress sensitivity of a material increases with its hardness and tensile strength. This trend is explained by the decreasing tendencies for relaxation of cyclic stresses – which otherwise reduces the effective local mean stress corresponding to a defined cyclic load of the sample or component – with higher material strength [8]. Typical values

for the mean stress sensitivity of steels range from approximatively 0.1 to 0.6, but as with any value derived from several fatigue tests, there is a significant statistical scatter [7, 16]. Equation 2.3 is frequently used among the reported correlations [18]. Winderlich's equation 2.4 also describes the increased mean stress sensitivity of hard steels [22]:

$$M_m = R_m \cdot 3.5 \cdot 10^{-4}\,\mathrm{MPa}^{-1} - 0.1, \qquad (2.3) \qquad\qquad M_m = \frac{H_V}{1,000}. \qquad (2.4)$$

Within the whole range of stress ratios, mean stresses do not necessarily have the same impact on the admissible load amplitudes. The parameter M_m is only used in the FKM guidelines for negative stress ratios $R < 0$ [18]. Figure 2.3 illustrates the slope of the upper limit for permissible stress amplitudes in [18] as a function of the mean stress. A decreased coefficient $M'_m = \frac{M_m}{3}$ describes the slope between $R = 0$ and $R = 0.5$. In the FKM's hatched red Haigh diagram, other stress ratios are covered by a horizontal line.

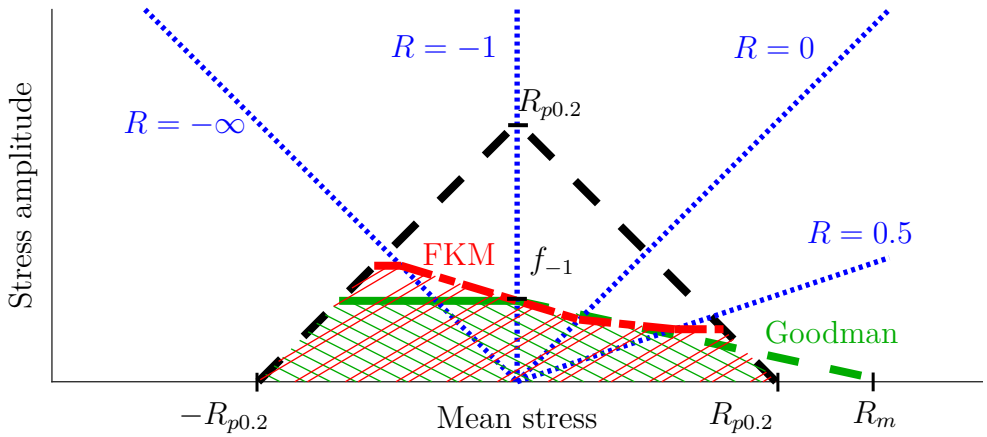


Figure 2.3: Haigh diagram with hatched safe domains according to Goodman (green) and FKM-guideline (red) for a fictitious material [7, 18].

Results of fatigue tests performed on samples with sharp notches and mean stresses must be interpreted carefully. Particularly for low strength steels, local plastic deformations may cause local compressive residual stresses due to stress relaxation. The latter are superimposed with the load stresses and help offset some of the impacts of the load's tensile mean stresses [7, 22].

Stresses known as residual stresses exist even in the absence of an external load. They have a considerable impact on the crack propagation and fatigue behavior of steel components. According to the length of the areas in which they are evenly distributed, they are classified as residual stresses of kinds I, II, and III as shown in figure 2.4 [38].

Residual stresses of the first type are approximately uniform over wide areas, which typically include many grains of a material, and are balanced with respect to the entire body. Secondary residual stresses exhibit homogeneous magnitude and direction over microscop-

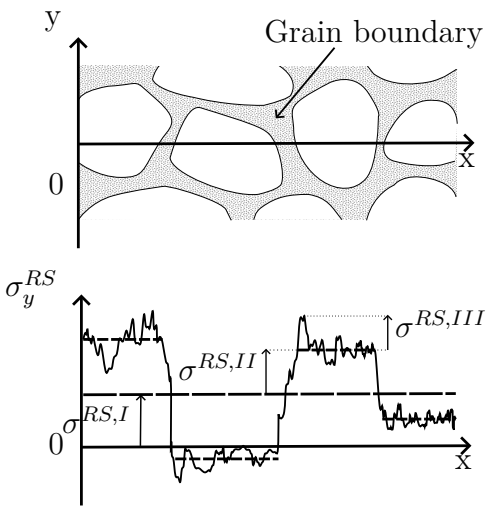


Figure 2.4: Classification of residual stresses depending on the scale of observation, adapted from [38].

ically small domains of one grain or sub-granular regions. As opposed to the first kind of residual stresses, only major disruptions of their equilibrium may result in macroscopic changes in the dimensions of a volume element [39]. Third-kind residual stresses are in equilibrium over subgranular sections but are heterogeneous throughout regions with diameters of multiple atomic distances within single grains. Second and third kind residual stresses are frequently referred to as micro-residual stresses, whereas the first kind residual stresses are also known as macro-residual stresses. Practical assessment of the fatigue strength of structural components usually only involves the first kind of residual stresses, rarely the second kind. Despite the fact that the total residual stresses result from the superposition of all three sorts of residual stresses, third kind stresses are averaged out and never taken into account in calculating approaches at a macro scale [16].

The sum of the forces and moments produced by all of the residual stresses spread throughout the component is zero since they are all in mechanical equilibrium. For any cross-section surface A of the whole body and for any reference line l, this can be described by equation 2.5 and equation 2.6 [39], where r represents the reference line distance for an element dA:

$$\int_A \sigma^{RS,I}\, dA = 0, \qquad (2.5) \qquad\qquad \int_A \sigma^{RS,I} \cdot r\, dA = 0. \qquad (2.6)$$

The entire process chain, from the steel production to the last manufacturing stage, affects the residual stress state of a finished component. All steel parts, with the exception of those that have undergone specific relaxation heat treatment, exhibit certain residual stresses [9]. Residual stresses are caused by uneven distributed strains. These can be attributed to localized volume or shape changes brought on by chemical composition, phase

transformation, thermal expansion or plastic and viscoplastic yielding [8, 9].

Thermal strains result from temperature gradients in a component coupled with yield stresses that depend on temperature or position. Large temperature variations between the surface and the core can cause local plastic deformations of the highest temperature regions, *e.g.* for high heating or cooling rates [40, 9]. In multi-phase materials, it is also possible for the volume changes brought on by thermal expansion to differ in each phase, which results in residual stresses caused by strain mismatches at the interface. Gradients in the chemical composition can generate inhomogeneous strains within the material, as is the case of carburized parts that have lattice distortions as a result of varying local carbon contents [40]. In steels, phase transformations are accompanied by a change in the material's density or shape. Such mechanisms can lead to significant irreversible strains and residual stresses under non-uniform temperature conditions by causing a mismatch in shape or volume between transformed and non-transformed regions. Finally, plastic deformations induced by applied mechanical forces will result in a strain mismatch upon load removal since the elastic drawback of areas that undergo different plastic strains has varying magnitudes.

In the surface layer, carburized parts typically have substantial compressive residual stresses. The mechanisms underlying this characteristic residual stress profile are discussed in more detail in the following section 2.3. All three types of residual stresses shown in figure 2.4 occur and, much like in many finished steel products, they include all of the previously listed mechanisms as well as some additional complex interactions. Depending on their magnitude and direction, residual stresses can be either beneficial or detrimental to fatigue behavior. Carburized components, thanks to high compressive residual stresses on the surface layer, often have exceptional fatigue strength properties [9]. Even though the fatigue behavior of typical quenched components can be evaluated considering only the surface residual stresses, the increased surface strength and high compressive residual stresses at the surface of carburized components make it necessary to also take into account the local loads and material strength in the subsurface regions [22, 37].

Residual stresses and mean stresses act similarly. While tensile residual stresses promote crack propagation, compressive residual stresses increase the fatigue strength [9]. However, there are some distinctions between the impacts of residual stresses and mean stresses on the fatigue behavior of steel parts [40]:

- Even for unnotched samples, residual stresses are distributed unevenly throughout a component's volume because they must comply to internal equilibrium equations 2.5 and 2.6, which let compressive residual stresses and tensile residual stresses to balance one another. Residual stresses are typically bi-axial at the surface and tri-axial in the volume, in contrast to mean stresses, which are frequently uni-axial in components with simple geometries [37].

- Cyclic loads can alter residual stresses. In most cases, this results in a reduction of the residual stress magnitude.
- Residual stresses, as opposed to mean stresses, cannot be easily replicated. Quantitative studies of the impacts of residual stresses on the fatigue behavior are particularly challenging because of the high sensitivity to process and material variations as well as issues with the measuring techniques.

In order to assess the fatigue behavior of steels, it is usual practice to take residual stresses into account like mean stresses, however the aforementioned features of residual stresses may necessitate more thorough analysis [16]. It is possible to define a residual stress sensitivity M_{RS} which is similar to the mean stress sensitivity M_m. M_{RS} is reported to correlate with the material strength, as does M_m, but exhibits slightly lower values, as displayed in figure 2.5 [41, 42]. While the experimentally observed differences between M_m and M_{RS} in the low-strength range can be explained by a different spatial distribution of residual stresses in the cross-section compared to the mean stresses, the reasons leading to a near constant value of residual stress sensitivity for hard steels in figure 2.5 remain largely unexplained [8].

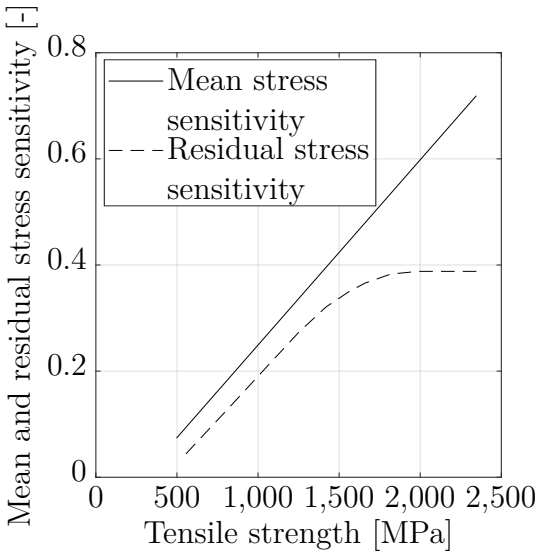


Figure 2.5: Mean stress sensitivity and residual stress sensitivity of steels depending on the static strength properties according to [41, 42].

If local plastic deformations take place, a reduction in residual stresses under fatigue loading is to be anticipated. Dislocation movements result in a redistribution of residual stress by transforming the elastic strains associated to the residual stresses into microplastic strains [37]. The onset of plastic deformation marks the start of the stress redistribution. If the local upper or lower stress exceeds the cyclic yield point, a redistribution of residual stresses has to be assumed. The equation $\sigma_{p,cyc} = 0.6 \cdot R_m$ can be used to estimate the cyclic yield point from the tensile strength of the material [18].

Local stress levels that match to the part's fatigue strength can exceed the local cycle yield limit, which lessens the impact of residual stresses on fatigue behavior, especially when combined with sharp notches [9]. The stress levels required for residual stress relaxation rise further with increasing strength, which results in a greater influence of residual stresses on fatigue behavior [8]. For medium strength steel, factors other than the magnitude of the surface residual stresses, such as the amount or depth of the process-dependent work hardening that frequently accompanies the development of residual stresses in the surface and subsurface material layer, may be important [9]. Still, the Goodman approximation and the consideration of residual stresses as additional mean stresses are found to produce satisfactory results when these factors are taken into account [9].

Because the cyclic yield point typically corresponds to stress levels that are higher than those for mechanical applications with technically relevant lifetimes, residual stress relaxation for hard steels only occurs in rare situations where sharp notches and high load levels are combined [9]. Therefore, the effects of relaxation can be neglected there, the mean stress and residual stress sensitivity may be assumed to be almost equal and the fatigue strength under mean stresses and residual stresses can be assessed through $\sigma_D = f_{-1} - M_m \cdot \sigma_m - M_{RS} \cdot \sigma_{RS}$ [8].

An exception to the aforementioned rules for stability of residual stresses may occur, however, when the steel's microstructure is metastable and may be altered by mechanical loads. After finishing, steels with a high carbon content or austenite stabilizing elements might exhibit a microstructure with a significant austenite phase fraction. The remaining austenite may transform into martensite when subjected to contact loads. This is commnly accompanied with a redistribution of the residual stress field because this phase change is linked to a local change in the material's density. For carburized parts, it is expected that the residual stresses are rather stable under cyclic loads below the fatigue strength [43]. Carburizing normally results in the formation of high hardness martensitic surface layers that exhibit very little plastic deformation. It is expected that case-hardened surface layers will crack and fail before significant plastic deformations are visible. As a result, residual stresses in case-hardened layers' martensitic microstructures remain stable in the fatigue strength range when subjected to cyclic loading [37, 44, 9].

Significant increases in fatigue strength are brought on by residual stresses in carburized components. In addition to the residual stress profiles induced by carburizing heat treatment, highly loaded mechanical components often undergo a shot blasting process, during which small hard particles cause plastic deformations and compressive residual stresses in a thin surface layer. Along with other positive effects like the removal of potential superficial oxide layers, work hardening and compressive residual stresses are linked to significant increases in fatigue strength. As an illustration, Shaw *et al.* [45] report up to 75% increases in the tooth root bending fatigue strength of carburized gears by shot blasting, which cannot be solely attributed to a lowered level of grain boundary oxidation.

Determining the precise quantitative impact of residual stresses on the fatigue behavior is challenging. This can be attributed to at least two factors. First, slight changes in the chemical composition of steels, hardenability or process conditions may have major effects on the magnitude of residual stresses. Variability may still arise even when the production route is precisely controlled. In [9], identical gears made of AISI 5120 steel that were carburized, quenched, and tempered showed typical variations in tooth root surface residual stresses up to 150 MPa when compared within a heat treatment lot and up to 300 MPa when compared across different heat treatment batches. As previously explained in 2.1.a, high strength steels are more sensitive to mean and residual stresses due to the extremely small permissible size range for cracks and defects that are not associated with crack propagation. As a result, the negative impact of local peak values in tensile residual stresses on fatigue strength might be further enhanced. Since residual stresses cannot be consistently reproduced, it is expected that some variations of the residual stress field lead to locally increased tensile residual stresses which are particularly detrimental to the fatigue strength of hard steels. Challenges in determining the influence of residual stresses on the fatigue behavior of steel components may also be reinforced by the complexity and limits of the available methods for measuring residual stress fields. The majority of residual stress determination methods work indirectly by measuring the elastic strains brought on by a residual stress field or its relaxation and occur in a constrained area in immediate proximity to the component surface. When a surface layer is removed, measurements in deeper layers are usually attainable at the expense of changing or redistributing the remaining stresses, necessitating sophisticated correction procedures or further assumptions [46, 47]. This subject is covered in more detail in section 4.1.d.

Many of the conclusions shown above were based on stresses that are described with a scalar value. As this is only applicable to uni-axial loads, transferring these results to multi-axial situations is not straightforward. The majority of residual stress systems do, however, exhibit multi-axiality. Only the addition of an appropriate multi-axial fatigue criterion can be used to treat these types of situations [8].

2.1.d. Multi-axiality and time evolution of load

Single loads or a combination of loads can both result in multi-axial stress states. Even uni-axial loads result in multi-axial stress states at the base of a notch. As in situations with residual stresses, the load on a component is frequently composed of multi-axial static components that are superimposed with cyclic stresses [17]. Since scalar strength criteria are employed to dimension components, the multi-axial stresses for each stress condition must be converted into a fictitious comparative uni-axial stress which corresponds to an equivalent damage.

In general, the cyclic stresses can be out of phase and out of frequency. The stress

distribution in the component cross-section then not only depends on time but also on the cross-section plane considered. During a loading cycle, the orientation of the section plane with the highest risk of damage may vary as well. Situations where the directions of the principal stresses remain constant during a loading cycle are called proportional stress states. For proportional stress states, common hypotheses derived from static strength theory such as the normal stress hypothesis, the shear stress hypothesis and the distortion energy hypothesis are accurate enough for practical applications. For surface-hardened components, however, stress components do not change in the same ratio due to the presence of residual stresses. Therefore, the directions of the principal stresses change with time and more elaborate stress hypotheses are required [37]. For this purpose, a description of the sectional planes by means of a unit sphere with azimuth (ϕ) and pole (θ) coordinates may be used. The coordinate system (x y z) of the unit volume is transformed into the rotated coordinate system (x' y' z') of the (ϕ, θ) section plane via the rotation angles $\theta \in [0, \pi]$ and $\phi \in [0, 2\pi]$, as shown in figure 2.6 [48]. The stress vector acting in the plane (ϕ, θ) can then be calculated using equations 2.7, 2.8 and 2.9 [49]:

$$\vec{u}(\phi,\theta) = \begin{pmatrix} -sin(\theta) \\ cos(\theta) \\ 0 \end{pmatrix}; \vec{v}(\phi,\theta) = \begin{pmatrix} -cos(\theta)\ cos(\phi) \\ cos(\theta)\ sin(\phi) \\ sin(\theta) \end{pmatrix}; \vec{n}(\phi,\theta) = \begin{pmatrix} sin(\theta)\ cos(\phi) \\ sin(\theta)\ sin(\phi) \\ cos(\theta) \end{pmatrix} \tag{2.7}$$

$$\sigma_n(\phi,\theta,t) = \vec{n}^T(\theta,\phi)\ \overline{\overline{\sigma(t)}}\ \vec{n}(\theta,\phi) \tag{2.8}$$

$$\tau_n(\phi,\theta,t) = \vec{u}^T(\theta,\phi)\ \overline{\overline{\sigma(t)}}\ \vec{u}(\theta,\phi) + \vec{v}^T(\theta,\phi)\ \overline{\overline{\sigma(t)}}\ \vec{v}(\theta,\phi). \tag{2.9}$$

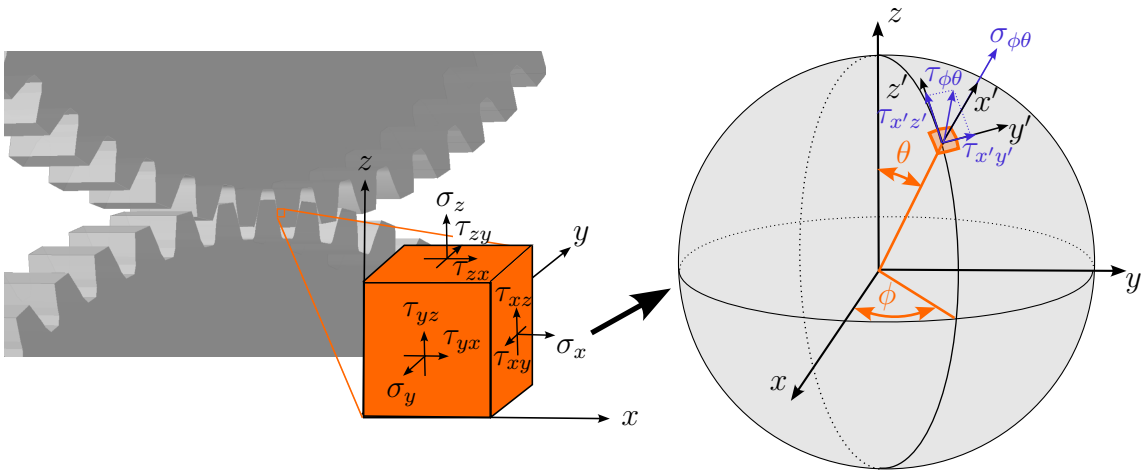


Figure 2.6: Coordinate transformation for an arbitrary cross-section plane (ϕ, θ). $\vec{\sigma}_{\phi\theta}$ represents the stress vector normal to the cross-section plane and $\vec{\tau}_{\phi\theta}$ is the shear stress vector in this plane [48].

A wide range of methods have been proposed in order to assess the fatigue behavior of materials under multi-axial stress conditions. In nearly all calculation methods, the normal and shear components of the stress tensors are determined for a defined cross-section plane. Based on their time variation, each of these stresses can be further subdivided into mean and amplitude values. The damage caused by both normal and shear loads is usually weighted. This often relies on an assumption regarding the kind of mechanism anticipated for fatigue failure, which can be influenced by both material aspects and load characteristics. For instance, ductile fatigue behavior significantly depends on damage brought on by shear stresses, whereas brittle behavior is associated with more noticeable impacts of the normal stresses compared to the shear stresses. In [50] and [20], the authors suggest to make a more precise distinction between brittle materials or ductile materials with defects on the one hand, and defect-free ductile materials on the other. The second type is associated to damage from shear stress-induced plastic strains, with the orientation of the slip plane playing a crucial role. In contrast, brittle materials and materials with crack initiation at defects like non-metallic inclusions are reported to be rather sensitive to normal stresses [16]. Thus, in addition to the material's ductility, the determination of the damage proportion caused by shear and normal stress also depends on other factors like the material's cleanliness. Geometric elements like notches, for instance, may also favor transgranular crack propagation driven by normal stresses over intergranular fractures [8].

There are many different ways to perform the calculations, and these changes might affect the accuracy of the results as well as the numerical effort. Since only a few aspects are covered in this work, reference materials like [49] or [51] may be consulted for additional details. Even the calculation of equivalent stress amplitudes and mean values from the stress tensor's time evolution can be carried out in a variety of approaches. In contrast to normal stresses, shear stresses in the plane (ϕ, θ) of a material's cross section change during a loading cycle in both direction and magnitude, describing a closed curve on the plane (see figure 2.7). In order to determine equivalent shear stress mean and amplitude values, the smallest circle enclosing the shear stress curve may be chosen, with its center serving as the mean point and its radius serving as an amplitude [46, 16, 52]. However, it is also common practice to merely specify the mean and amplitude values of shear stresses based on the distance to the origin [48, 53, 54].

A distinction between critical plane approaches, integral approaches, and empirical criteria can be made among the calculation methods that are available and applicable to general multi-axial cyclic stresses. In critical plane approaches, only the material plane with the greatest calculated damage risk is taken into account as contributing to the local failure. As stated previously, the criteria for determining which plane has the highest damage risk can be based on normal stresses, shear stresses, or a combination of both, with additional weighting factors depending on local hardness, ductility ratio, etc. On the other hand, in integral approaches, the stresses in all material planes contribute to the local damage,

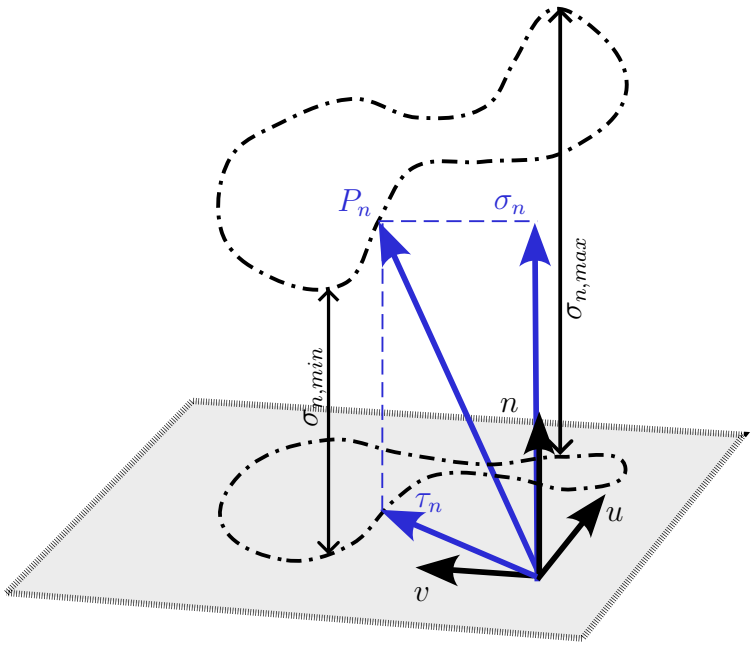


Figure 2.7: Definition of the normal and shear stresses and their time evolution during a load cycle on an arbitrary cross-section plane, adapted from [53].

and a single characteristic value is built through the quadratic or arithmetic mean of the stresses in all planes. One of the most popular integral techniques is the shear stress intensity hypothesis (SIH), which originally was developed by Simburger [55] and modified by authors like Liu and Zenner [50], Oster [54], and Hertter [56], among others. In its formulation in [54], the root mean square of an effective shear stress in all planes, as defined by equation 2.10, is used to predict failure. With various examples of use in the context of gear contact [54, 46, 56, 57, 58, 34], this technique has been shown to produce satisfactory results for contact situations that involve ductile materials:

$$\tau_{eff} = \sqrt{\frac{1}{4\pi} \int_{\phi=0}^{\pi} \int_{\theta=0}^{2\pi} \tau_{\phi\theta}^2 \, sin(\phi) \, d\phi \, d\theta}. \tag{2.10}$$

There are many different types of empirical criteria that have been formulated, which vary in both complexity and precision. The Dang Van technique [59, 60] is among the most commonly adopted [8, 61, 62, 63, 64]. This method, which was first based on microscopic-scale considerations, can be slightly modified or extended to macroscopic stresses and assumes a linear relationship between the hydrostatic stress σ_h and the principal shear stress τ_{12} for the maximum allowable cyclic load, as stated in equation 2.11:

$$\tau_{12} + a_{DV} \, \sigma_h = b_{DV}. \tag{2.11}$$

Uni-axial and torsional tests may be used to determine the Dang-Van model's parameters a_{DV} and b_{DV} [52].

All of the aforementioned examples serve mainly to demonstrate how challenging it is to relate the results of a uni-axial fatigue test to a multi-axial stress state. There have been significant efforts made over the past few decades, and a variety of methods are now available. Nevertheless, depending on the application considered, the accuracy and validity of various methods may be questioned since no single strategy appears to consistently outperform the others.

2.1.e. Size effect and further aspects

Size effects describe the differences in the fatigue behavior of geometrically similar samples which have different sizes. In most cases, experimental results from fatigue tests that are conducted on variously sized specimens or components do not agree. When results from smaller specimens are applied to larger ones, this frequently results in an overestimation of the behavior of the material, *i.e.* the fatigue strength decreases with increasing component size [7]. The evaluation of material and structural part fatigue properties may yield substantial inaccuracies if the size effect is not properly taken into account [65], especially when the fatigue behavior of small samples is extrapolated for very large components.

Size effects on the fatigue strength can be regarded as composed of the following three categories: geometrical size effect, statistical size effect and technological size effect [7].

The geometrical and the statistical size effects are related to the gradients and the stress distribution in the part, whereas the technological size effect combines a number of further influencing factors that vary together with component size. In most cases, different kinds of size effects coexist and interact with one another, making independent investigations nearly impossible [66].

Both the geometrical size effect and the statistical size effect describe how components or samples with a larger stressed region exhibit lower fatigue strength properties. However, there are differences between the assessment methods and the mechanisms underlying these effects.

The geometrical size effect describes the effects of notches on the fatigue strength. Notches reduce the fatigue strength, but for ductile materials not to the same extent as the predicted increase of linear elastic stress. In the case of sharp notches, plastic flow can take place on a microscale on grains that are favorably orientated without being able to propagate to the next grains. This local yield coincides with a decrease in stress and, hence, of the notch effect [8]. This is based on the hypothesis that some of the load is transferred to the material layers beneath the most severely loaded area. This is supported by the fact that samples' fatigue strength in torsion or rotating bending tests – where the load is concentrated in the surface layers – are generally higher than in axial tension-compression tests, where the stresses are uniformly distributed [17, 37]. Several methods have been proposed in order to assess the geometrical size effect on the fatigue strength [67, 68], which

rely on empirical relationships based on the dimensionless stress gradient χ. Equation 2.12 can be used to express this gradient, which is a measurement of the inhomogeneous stress distribution and is derived from the stresses normalized by the notch root stress $\sigma = \frac{\sigma^*}{\sigma_{max}}$ in the direction $\vec{x}$ perpendicular to the notch root:

$$\chi = \left.\frac{\mathrm{d}\sigma^*}{\mathrm{d}x}\right|_{x=0}. \tag{2.12}$$

These methods predict the same fatigue strength for samples with notches that are geometrically comparable but varying in size. The findings from experimental investigations, however, show that the fatigue strength loss caused by notches is more severe for large specimens than for small ones [37, 8]. In fact, even flat specimens made of the same material and with the same notch but with different thickness or length might exhibit noticeably different fatigue strength values. The geometrical size effect cannot fully explain these results [66, 16].

Higher stressed volumes increase the probability of finding a flaw or crack in the microstructure that is large enough to trigger crack propagation. This is the statistical size effect [8]. The highly stressed volume (HSV), which is closely related to the stress gradient, has been shown to produce accurate assessments for both the geometrical size effect and the statistical size effect [66]. The HSV is often defined as the region in which 90 % of the actual maximum stress is exceeded. According to reports, the HSV correlates well with the anticipated decrease in fatigue strength due to scaling of a specimen or part [8, 69, 70]. The selection of an appropriate HSV region, however, requires several assumptions regarding stress levels that are not associated to crack initiation and propagation. In contrast to the gradient approaches for the geometrical size effect, computer-based finite element simulations are often needed to identify the volume where the largest stresses are generated. Threshold values of 90 % or 95 % have frequently been utilized, depending on the material and load under investigation. With the majority of fatigue failures starting in highly stressed locations, this approach may work for most of the technical applications, but certain situations call for a more thorough and cautious evaluation. Technical cracks may also initiate in low loaded areas in the presence of occasional very large defects, such as in samples made using recent additive manufacturing methods [66, 71]. Similarly, in order to accurately forecast fatigue strength, the selection of the HSV must take into account aspects like residual stresses, an heterogeneous distribution of fatigue strength properties, stress multi-axiality or steel cleanliness [71]. Due to increased hardness and compressive residual stresses of the surface region, fracture initiation in case-hardened components may happen in a subsurface layer with stresses well below the threshold of 90 or 95 percent [16]. While the HSV method often yields satisfactory results, there exist many applications where applying this method requires prior knowledge of the expected failure regions and mechanisms in order to take the proper equivalent stress and threshold into account in the

calculation approach [71].

This issue can be solved by analyzing the distribution of stresses and fatigue strength throughout the component. The Weibull *weakest-link* model, which was initially developed for brittle materials, assumes a statistical distribution of defects in the volume or on the surface of a component, with the largest defect being responsible for the start of a fatigue crack that can propagate and eventually cause the component to fail [72]. With the help of a simplified relationship between defect size and allowable stress amplitude, this method takes into account the likelihood of having defects greater than a specified size and enables to estimate the survival probability $P_S^{(V_i)}$ for a volume V_i provided by equation 2.13 [40, 8]:

$$P_S^{(V_i)} = 2^{-\frac{V_i}{V_0}\left(\frac{\sigma_{a,eq}}{\sigma_D}\right)^{\kappa}}. \tag{2.13}$$

V_0 and σ_D represent the volume of a reference sample and the corresponding fatigue strength for 50 % failure probability at a specified cycle number. κ is the Weibull modulus and characterizes the scatter of the strength. It is obtained by inserting the experimental fatigue test data into a Weibull probability plot and depends, at least, on effects related to both the material and the production process [17]. $\sigma_{a,eq}$ is the local equivalent stress amplitude derived using the methods described in sections 2.1.c and 2.1.d. This relationship is not directly applicable to carburized steel components since it only holds true for homogeneous stresses and fatigue characteristics in the volume V_i. The equation for the survival probability P_V of a volume V under heterogeneous distribution of stress and material properties can be written as follows [46]:

$$P_S^{(V)} = 2^{-\frac{1}{V_0}\int_V\left(\frac{\sigma_{a,eq}}{\sigma_D}\right)^{\kappa} dV}. \tag{2.14}$$

Splitting V into a set of n_V sufficiently small partial volumes V_i with nearly homogeneous stress and material states yields equation 2.15 [48, 43].

$$P_S^{(V)} = 2^{-\frac{1}{V_0}\sum_{i=1}^{n_V}\left(\frac{\sigma_{a,v}^{(V_i)}}{\sigma_D^{(V_i)}}\right)^{\kappa^{(V_i)}}}. \tag{2.15}$$

As previously mentioned, there are shared characteristics between geometric and statistical size effects. Both of these effects can be quantified in terms of how they affect a component's fatigue strength, but *weakest-link* and volume-based approaches yield more precise results than those which only consider stress gradients. According to the information in sections 2.1.a and 2.1.b, it makes sense to assume that the geometrical size effect has a significant impact on ductile and low-strength materials, whereas the statistical size effect predominates in rather hard or brittle steels and fatigue failures triggered by defects [5, 16].

As the dimensions of a sample or part are scaled, some additional production-related

factors will change. Quenched and tempered steel parts rely on the transformation of austenite into a martensitic phase during cooling, which typically occurs only above a critical cooling rate. As a result, a process adjustment (such as using a different quenching medium) may be required to achieve the same martensitic microstructure on two pieces with different cross section sizes. Similarly, when the local thermal-mechanical histories between samples are not comparable due to differing diameters, properties including grain size, surface roughness, residual stresses, steel cleanliness and characteristics of the defects in the microstructure might vary substantially [16, 8]. Even though it is theoretically possible to evaluate all of these impacts using sophisticated metallurgical-physical models, they are typically accounted for by introducing an engineering factor for technical size effect for both production-related effects and surface-related effects [66, 73].

Regarding case-hardened components, the ratio of the hardened case's depth to the entire thickness of the cross-section may be one of the most significant variables related to the production process [74]. This feature is usually quantified by the Case Hardening Depth (CHD), which is defined as the minimum distance to the surface for which the hardness falls below 550 H_V [75]. This parameter does not properly add to the previously mentioned influencing factors on the fatigue properties of carburized parts, since the primary mechanisms causing fatigue strength variations due to different CHDs can typically be attributed to altered residual stresses or static strengths. On the other hand, the depth of the hardened case is a process-controllable parameter that has a direct and intuitive impact on the spatial distribution of residual stresses and hardness, making it especially relevant for practical applications.

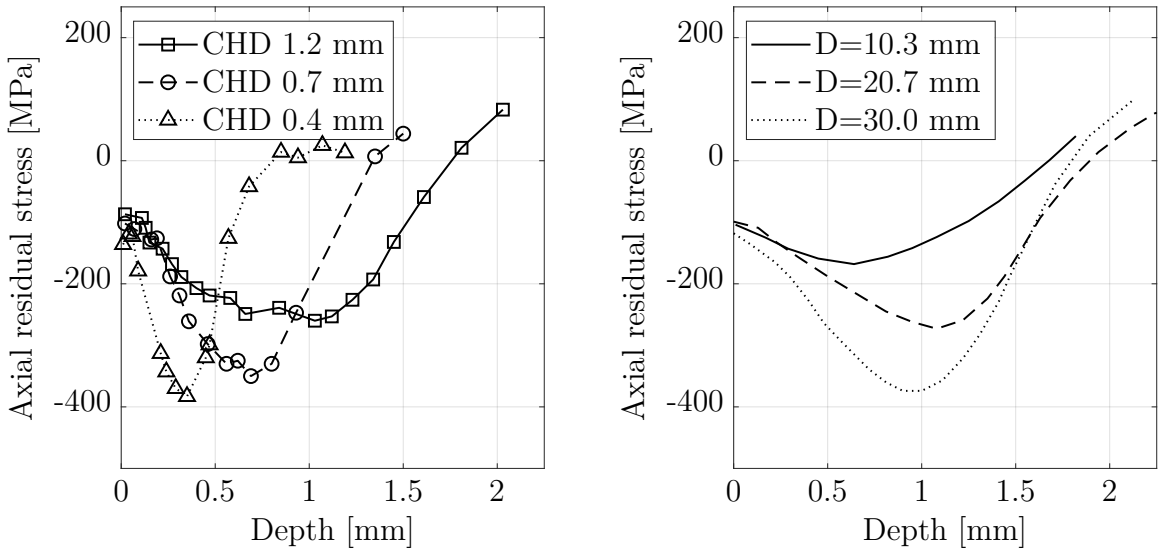


Figure 2.8: Left: Residual stress profiles of unnotched round samples of steel 20MoCrS4 with diameter 20.7 mm [37]. Right: Residual stress profiles of unnotched round samples of steel 20MoCr4 with similar case hardness depth (CHD) and different diameters [76].

Compressive stresses in the surface and subsurface region will be large in magnitude when the CHD is small compared to the cross-section, as shown in the examples of figure 2.8. When the opposite is true, the near-surface compressive stress is lower. Core tensile residual stress, which are only partially displayed in figure 2.8, can then be significant [74]. The combination of compressive residual stresses and increased hardness in the surface layer brought on by appropriate carburizing heat treatment is very effective for increasing the fatigue strength, especially for applications where the maximum tensile stresses are anticipated at the surface of a part, such as in bending or torsional loading [74]. The beneficial residual stress condition is primarily responsible for the majority of the fatigue strength improvement, while the part's tribological properties are enhanced by the hardness increase. Compressive residual stresses in the subsurface layer and surface can limit the ability of cracks to propagate and hence prevent the component from failing [77]. Crack initiation is shifted towards the core material or the transition between the case and the core by a successful case-hardening heat treatment. An increase in CHD implies that more of the cross-section is subjected to compressive stresses, which should lead to an increase in fatigue strength. Still, as previously indicated, the ratio of core to case thicknesses also affects the residual stresses' magnitude, therefore a balance between these two opposing effects needs to be achieved. This is shown in figure 2.9, where the strengthening effects of the carburizing heat treatment increase rapidly with the CHD at first, and then gradually decrease. This is in line with testing results on samples [13] or gears [78, 79, 80] as well as ISO 6336-5's guidelines for the optimal CHD of carburized gears based on module m_n [36]. The link between the increase in fatigue strength resulting from carburizing heat treatment and the notch geometry is another noteworthy feature of figure 2.9. The beneficial effects of carburizing relative to the fatigue strength of the part or sample without heat treatment increase with notch sharpness or geometry factor α_k [77]. Although notched samples also imply slight changes in the multi-axiality and amplitude of the residual stresses [37], this behavior can rather be mostly explained by the geometrical and statistical size effects. When there is a sharp notch, cracks are only likely to start and propagate in the region around the notch root because of the high stress concentration. In such cases, carburizing heat treatment enables the introduction of a compressive residual stress field throughout the entire loaded zone, even with a low CHD, avoiding tensile mean or peak stresses and significantly restricting the propagation possibilities of cracks [16].

Oxidation of carburized parts in the surface area is another result that typically varies with the CHD. Gas carburizing atmospheres containing carbon monoxide allow oxygen to diffuse into the steel in addition to carbon atoms. Since the intentionally produced diffusion of carbon is significantly faster than the unintentional diffusion of oxygen in the austenite microstructure at carburization temperature, the depth of oxidation is typically several orders of magnitude below the CHD, ranging from a few micrometers to about $50\,\mu$m [81]. Nevertheless, this superficial modification can have a substantial impact on

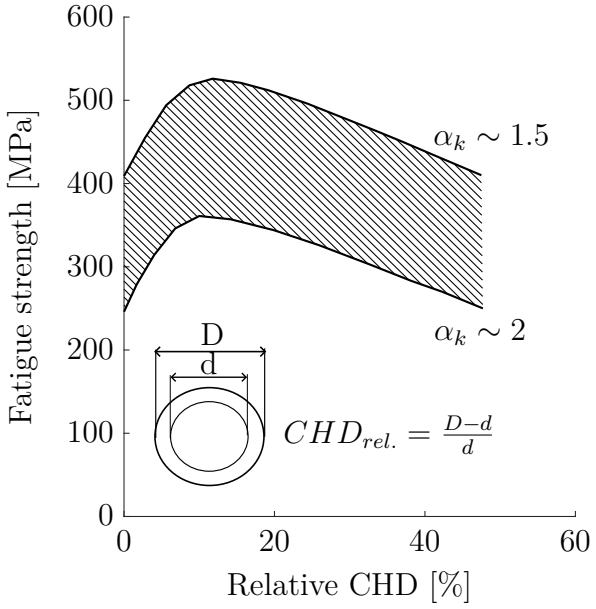


Figure 2.9: Effect of the Case Hardness Depth (CHD) on the rotating bending fatigue strength of round notched samples with different geometry factors α_k, where D is the cross-section diameter and $d = D - 2 \cdot \text{CHD}$ [12].

a carburized part's fatigue properties [16]. Preferential oxidation of alloying elements like silicon, manganese, chromium or aluminum will result in a local concentration decrease of these elements in the matrix. The ability of the steel to form hard martensite upon cooling can be strongly diminished, so that oxidized carburized parts often exhibit a thin layer of non-martensitic transformation products such as bainite, pearlite or troostite [81, 9]. Multiple variables, including the depth of oxidation [16], the impact on the residual stress field [9, 11, 24] and the propensity of oxides to precipitate at grain boundaries [43], determine how harmful oxidation can be. In rare cases, the effect might be negligible. Reduced sensitivity to micro-notches is a benefit of low-strength microstructures, which can thus potentially outweigh hardness losses at the surface [81]. Additionally, subsequent finishing operations like grinding, shot peening or shot blasting can completely or partially remove oxidation layers and the detrimental effects they have on fatigue strength [9, 16]. Surface oxidation therefore typically has no effect on the tooth flank load capacity of case-hardened gears with adequate grinding stock [57].

Carburized parts are frequently subjected to a shot peening or shot blasting procedure, which involves projecting tiny particles onto the surface to cause a thin exterior layer to deform plastically. Because they produce local compressive residual stresses and a shift in the total mean stresses towards lower values, processes based on a transverse pressure that causes plastic strains on the surface of highly loaded regions are generally associated with positive effects on the fatigue strength properties [8, 9]. Considerable compressive residual stresses can be created through shot peening. Furthermore, the work hardening brought

on by the plastic deformations causes a localized increase in hardness, which improves the part's fatigue performance even more. Optimal shot peening procedures can improve the fatigue strength by up to 100 %, depending on the properties and speed of the shot particles [8].

The presence of austenite after heat treatment is a further noteworthy feature of carburized parts. The austenite phase is strongly stabilized by additional carbon atoms in the surface and subsurface layers, and some of the typical alloying elements like nickel and manganese can also lead the microstructure fractions to shifting in favor of increased austenite. Carburized components usually exhibit volume fractions of 10 to 30 % retained austenite because the low-temperature tempering, which is commonly done at temperatures below 200 °C, is not high enough to induce the transformation of austenite [11]. The presence of residual austenite reduces the fraction of martensite, which in turn lowers hardness and compressive residual stresses, thus negatively impacting the fatigue properties. On the other hand, because of its capacity to absorb plastic deformation and to change into martensite under severe load, providing significant compressive residual stresses that inhibit the propagation of fatigue cracks, retained austenite can be considered as beneficial in rolling operations [82, 13, 74, 24]. Decreases in hardness are also associated to a reduction of the wear resistance, whereas additional negative impacts are potentially attributed to the dimensional stability: part distortions that exceed the necessary geometric tolerances may result from the volume expansion caused by the phase change of residual austenite in martensite [83]. Changes in the chemical composition, plastic deformation, tempering heat treatment or subzero cooling can all have an impact on the stability of residual austenite [82]. The prediction of fatigue strength of parts with metastable residual austenite is particularly challenging as it requires additional assumptions about the evolution of the hardness and residual stress field due to the potential transformation into martensite during service.

Surface roughness may be the most investigated property of a surface that influences a component's fatigue strength. In numerous applications, the surface experiences the highest stress. Because it raises local stress, surface roughness can serve as a preferential site for fatigue crack initiation. Hard materials will be more impacted by rough surface states because the sensitivity of steels to micro-notch correlates positively with the tensile strength or hardness, as previously noted. However, for case-hardened parts, high strength and compressive residual stresses at the surface can effectively suppress or postpone the onset and propagation of cracks in the surface region, shifting the critical region for fatigue failure deeper into the material. Roughness usually exhibits values below 5 μm for relevant finished product surfaces, indicating that it is not a primary contributing factor to fatigue fracture initiation [37].

Other surface parameters potentially influencing the fatigue properties of carburized parts such as corrosion, wear or temperature changes during service, are not covered in this work.

2.2. Tooth flank fracture of carburized gears

2.2.a. Experimental findings

The purpose of a gear is to transfer torque. The sophisticated stress states linked to this function are dependent on a wide range of factors, including gear design, operating circumstances, lubricant and tribological characteristics, gear material and hardness or case depth from the heat treatment procedure. As a result, several failure types with various underlying mechanisms can arise [84, 11]. The teeth of mating gears make contact along the active flank profile, beginning at the driven gear tooth tip, continuing across the pitch line and ending at the driving gear tooth tip. Rolling contact occurs at the pitch position, whereas relative sliding is involved as well on either side [85]. The most important stresses include contact stresses (which may be calculated using Hertzian theory), surface stresses associated with lubrication state and asperities, bending stresses brought on by the teeth's elastic deformation, and residual stresses from heat treatment or other procedures like grinding and shot peening.

Depending on where the failure initiates, a distinction can be drawn between the different fatigue failures of gears, which do not include some of the damages caused by tribological conditions such as scuffing [84]. Classical fatigue failure mechanisms for gears include pitting and tooth root breakage. The first can be attributed to surface contact pressures and involves material loss from the flank surface. Pitting damages appear as shallow craters that typically arise at the highest point of single-tooth contact for pinion or at the lowest single-tooth contact position of mating gear, because of high combined values of both contact and sliding loads. Cracks may initiate at the surface or at a slight depth below and they usually branch towards the surface after propagating a short distance in a direction roughly parallel to the tooth flank. Consequently, a pit forms when a piece of the material separates from the surface [11, 86, 87]. Micropitting is the term for pitting damage on a smaller scale of roughly 0.01 mm, whereas larger pits generated from many cracks growing together are known as spall [58]. These fatigue failures can be attributed to surface cracks or significant wear caused by unfavorable lubrication conditions between mating surfaces and excessively high pressures. Variables affecting these include the applied load, flank geometry, hardness, surface quality, operating temperature, and lubrication [24, 11]. Tooth root fracture also usually initiates at the root's surface and propagates deeper into the material. This type of failure is associated with bending stresses in the tooth root fillet, which may be amplified by notch effect, surface roughness or grain boundary oxidation [84]. In presence of sufficient compressive residual stresses in the case, however, fatigue crack initiation might occur at non-metallic inclusions or coarse matrix grains below the surface [88, 4].

With increasing research efforts to reduce the risk of failure due to surface and near-surface-induced mechanisms such as pitting and tooth root fracture, the importance of

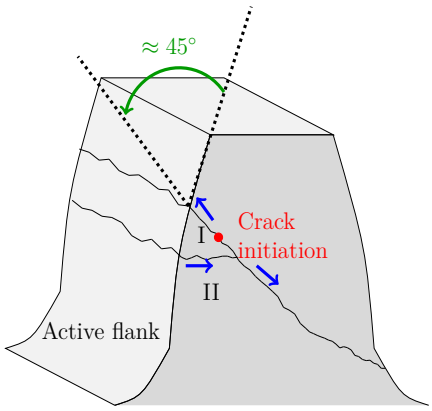


Figure 2.10: Schematic characteristics of a tooth flank breakage. Indicated are the primary I and secondary II cracks and their direction of propagation.

volume-induced fatigue damage has greatly increased in recent decades [46, 52, 89]. Tooth flank fracture (TFF), also referred to as tooth flank breakage, is a fatigue failure mechanism for case-hardened gears which initiates in the material depth below the tooth flank surface. TFF can reduce the lifetime of carburized spur gears, but carburized helical or bevel gears, as well as gears that have been nitrided, carbonitrided or induction-hardened, have also been reported to be affected by this kind of failure [89]. The crack initiation site is usually located at approximately half the height of the tooth, in the transition area between the case and core regions. Prior to TFF, surface damage indicators like pitting or micro-pitting on the active flank may not always be observed. Non-metallic inclusions can almost systematically be identified as TFF crack initiation sites. These can be either sulfides, hard oxides, oxisulfides or clusters formed from several non-metallic inclusions. Fractographic analyses reveal a fish-eye appearance and a crack lense surrounding the initiation site, which indicate a slow crack propagation under vacuum conditions. The crack propagates both toward the core and toward the surface, however the rate of propagation in either direction can vary significantly due to gradients of hardness and residual stresses. Since the fracture originates deep below the surface, surface and near-surface inspection methods may not detect the damage until the final hundreds or thousands of cycles prior to the gear's sudden failure. The angle at which the primary crack typically forms in relation to the flank surface is between 40 and 50°. Secondary and tertiary cracks may also develop. These may be brought on by the stiffness changes and stress redistribution due to the primary crack, as shown by Witzig [34] through FE simulations. The secondary cracks propagate approximately parallel to the tooth tip, thus possibly leading to the separation of wedge-shaped particles from the flank once reaching the main crack (see figure 2.10).

In the 1990's, several isolated reports of damage in industrial applications described gear failures of carburized gears initiated in the material depth below the active flank [90, 91, 92]. Mackaldener investigated tooth flank fracture in addition to a related failure mechanism referred as tooth interior flank fracture (TIFF). This particular gear failure type only affects

idler gears, for which both flanks are loaded during service [93, 94, 95]. Even if TIFF also originates in the core-case transition zone, the specific load conditions imposed on both flanks give rise to a distinct fracture morphology. The main cracks have a fairly symmetric pattern, starting at the mid-height of the fractured tooth and proceeding parallel to the flank along the hardened case profile until branching out towards the surface in the root area. In the process, the tooth tip is entirely separated. As in TFF, crack initiation preferentially occurs at a microstructure heterogeneity. The damage mechanism is therefore thought to be identical to tooth flank fracture, with the only difference being the crack propagation caused by reciprocal loading [46, 96]. Mackaldener attributes the formation of TFF and TIFF to the slender design of the gears, whereby the decreased tooth thickness causes higher shear stresses and increased tensile residual stresses in the tooth's subsurface layer [93]. Using FE simulation, Mackaldener shows that the position of crack initiation correlates with the maximum shear strains from both heat treatment and tooth flank load rather than with the maximum of hertzian pressure. This is consistent with the observations of Bauer that only cracks in line with the direction of the main shear stress seem to propagate [90].

Annast [97, 98] investigated the phenomenon of tooth flank fracture on carburized bevel gears of 16MnCr5 and identified through experimental tests the case hardness depth as a decisive influencing parameter in addition to the flank pressure. A higher occurrence of TFF failures was caused by low core hardness or elevated sulfur content, the latter of which correlates with an increased number and size of non-metallic inclusions. However, there was no discernible difference in the TFF risks caused by different shot peening, forging or surface finishing processes. Theoretical calculations also indicated a very limited effect of surface-related parameters such as lubricant or roughness. Stitch tests revealed that short-term overloads had an impact on TFF. Some bevel gears experienced tooth flank fracture during fatigue loading following purposeful overloads, while other gears showed pitting as a failure mechanism under the same loading conditions but without short-term overload. The experimental investigation with systematic parameter variation proved to be challenging to analyze, as the strength limits were not only determined by the mechanism of flank fracture but also by tooth root or pitting failures, thus limiting the possibilities for quantification of the various influences on TFF.

In his investigation on the impact of CHD on the load bearing capacity of carburized gears, Tobie encountered multiple TFF-caused failures on 16MnCr5 gears with a high centre-to-centre distance of 200 mm relatively to a small module of 3 mm [78, 79]. Flank fractures initiated on single or clustered aluminum oxides at depth between 1.5 and 2 mm under the active flank's surface. These failures occurred in a broad range of load cycle numbers, ranging from 10^6 to 10^8, and involved two distinct pairs of gears. The gear pair of module 5 mm with tooth number $z_1/z_2 = 40/41$ had a few TFFs at pinion with a majority of fatigue failure owing to pitting, whereas TFF was repeatedly observed on both the pinion and gear of the pair with module 3 mm and tooth number 67/69. Although

low case hardness depth tended to increase the failure rate due to TFF, increased CHD did not completely prevent tooth flank fracture. Bruckmeier and Witzig continued these experiments. In [34], Witzig conducted a systematic experimental variation to determine the most important parameters for TFF risks using two gear geometries with a center distance of 200 mm. He obtained the first S-N-curves of tooth flank fracture and systematic crack initiation below the surface of the flank at a depth slightly above twice the CHD, approximately corresponding to the microstructure transition between case and core. These cracks mostly originated from aluminum oxides and occasionally from manganese sulfides. While single-type inclusions were occasionally seen, the majority of cracks were associated with clustered inclusions. Relevant inclusion diameters were generally between 0.03 and 0.15 mm, with some larger single inclusions reaching maximum dimensions of up to 3.2 mm [89]. Witzig was able to measure the impact of the pressure angle, case hardening depth, and steel alloy. Compared to 20MnCr5, 18CrNiMo7-6 gears demonstrated significantly higher fatigue strength against TFF. This behavior is thought to be explained by higher material toughness and core strength, as well as potentially by a decrease in defect and non-metallic inclusion occurrences [46]. Slightly lower TFF risks are associated with deeper case hardening, though not as much as in the theoretical calculations. This may be because Witzig's model does not account for tensile residual stresses in the tooth's core cross-section. Gears with low pressure angle proved to be more resistant to TFF. This can be explained by a shift in the maximum of normal pressure from the hertzian contact towards the surface associated with the contact area's reduced curvature radii. This results in a shift in the maximum shear stresses to the hardened case, which has a correspondingly high shear stress resistance. This comprehensive and systematic experimental study provided validation results for various subsequent theoretical models regarding the computation of TFF risks, such as those developed by Wickborn [26] and Weber [46] or Ghribi [63]. Wickborn's subsequent bench testing campaigns on gears with a 10 mm module specifically made for TFF research did not yield data on tooth flank fractures; instead, they revealed subsurface failure in the tooth root region in the middle of the tooth gap, emphasizing the need for a more thorough understanding of the critical influencing factors for the underlying mechanisms of these failure types [99]. In a subsequent study on the subsurface failure of carburized gears caused by large grains or non-metallic inclusions in the tooth root region, VHCF stitch trials conducted by Fuchs were carried out and the results also verified a high fatigue strength against TFF for high-purity alloys [100, 4]. Remarkably, in these high-purity steels, TFF cracks initiated at seemingly defect-free locations. During his research into how the grinding stock and hardness profile affect the tooth flank's load bearing capacity, Konowalczyk came across numerous TFFs [101]. All gears used were identical in geometry, but variations in residual stress profiles and hardness led to tooth flank fracture failure in some and pitting damage in others. His findings indicated that the influence of heat treatment was critical in relation to the risks of TFF because it is

directly related to the spatial distribution of hardness and residual stresses in the tooth and belong to the very few parameters influencing carburized gears in areas deeply below the surface. In his research, tooth flank breakage caused the failure of both very high and very low stock removal gears. Despite having a surface hardness that was roughly 30 H_V lower, the variation with the highest ground depth also presented the highest fatigue strength. In following investigations, Konowalczyk created a test bench to measure the fatigue strength of gears against TFF, a task that Görgen subsequently took up. An economical and simple method to replicate the stress state in the subsurface of the tooth flank responsible for TFF would enable the generation of enough fatigue data to look into the key factors influencing this failure mechanism and support the development of design guidelines. This setup, which is based on the application of two time-dependent loads – one for contact-like stress states and the other for bending-like stress states – would be comparable to the pulsator setup used to precisely replicate the bending stress states in the tooth root of gears. However, no TFF could be generated by the developed method up to this point, possibly because of limitations in knowledge regarding the residual stress distribution, of the role of defects or due to the intrinsically narrowed loaded volume in this test setup (see statistical size effect section 2.1.e). In most recent experimental studies on the subject of tooth flank breakage, Böhme *et al.* published micrographs of early propagation stages of cracks that started in the active flank of carburized bevel gears for maritime applications below the surface, at depths of 2 to 3 mm, which roughly correspond to the transition area between the hardened case and the core material. These cracks had reached lengths of 0.45 to 0.65 mm and were parallel to the flank's surface. Uninterrupted cyclic loading of theses gears then resulted in classical TFF failure aspects, as described in *e.g.* [98].

2.2.b. Assessment methods for tooth flank fracture

In tooth flank fracture, a material with position-dependent fatigue strength and randomly distributed defects is subjected to a complex stress state produced by both residual and load stresses. Consequently, designing gear and processes against TFF is an exceptionally challenging task. However, due to its practical significance, a number of theoretical developments for evaluating TFF risks have been introduced over the past few decades, some of which have been done in association with the previously mentioned experimental studies. The list of authors who have contributed to this topic includes, but is not limited to: Mackaldener [95, 93, 94], Tobie [78, 79], Annast [97, 98], Bruckmeier [102], Witzig [34, 103], Wickborn [26, 99], Boijadjiev [104], Müller [105, 106], Octrue [64], Al [96], Ghribi [62, 63], Weber [46], Konowalczyk [57, 101], Görgen [107, 108], Leimann [109], Meis [16], Böhme [52, 61], Wirth and Höhn [110]. Only approaches that take into account the specific spatial distribution of the residual stresses, load and material strength can be suitable [111, 9]. Comparing an equivalent local stress with a local admissible stress is a

fundamental principle shared by all methods. However, there can be significant differences in the way these values are constructed and the effects they consider, which can have an impact on the validity or prediction accuracy domain. Moreover, some of the techniques are specifically designed to yield a closed, simplified solution that can be used in guidelines like ISO 6336. Although only a few examples are covered in detail in this work, this still allows for an overview of the various approaches that are available.

One of the earliest numerical methods for evaluating carburized gear TFF and TIFF failures was created by Mackaldener [93, 94, 95]. A 2D plane strain model is used to calculate the contact flank loads. Assumption of plane strain is common in modeling because it greatly minimizes the computational effort involved in calculating stresses and deriving a scalar equivalent stress value. The plane strain assumption seems well-suited for the load-induced stress state in many situations in which a spur gear's tooth width is much greater than its thickness or height [52], although the effects of crowning may also need to be taken into account. According to Konowalczyk [57], however, the plane strain hypothesis applied to helical gears yields unsatisfactory results. Moreover, for heat treated components with substantial residual stresses, the plane strain hypothesis is hardly ever applicable. In his research, Mackaldener [93, 94, 95] applies Findley's crack initiation criterion, which describes material failure as the threshold value for a combination of the maximum normal stress and the amplitude of shear stresses. The local variations in material strength are not taken into account in his work. One of the main features of the presented model is its consideration of residual stresses, which are determined using a very basic model of the transformation strains resulting from case hardening heat treatment. With the use of this straightforward model, Mackaldener is able to qualitatively describe the most likely location for crack initiation in the case-to-core transition area for both single-stage (TFF) and idler-usage (TIFF) gear applications. The slenderness of the gear tooth, the core's fatigue strength, and the contact loads are found to be the main factors influencing the risks of TFF and TIFF by the use of geometric variations in simulations. Based on these promising qualitative results, Al *et al.* [96, 112, 113] later modify this simulation model by adding local fatigue properties derived from the local hardness values. According to these studies, failure risks are significantly influenced by assumptions about residual stress profiles and tensile residual stresses in the core. The steel cleanliness or the presence of defects and non-metallic inclusions in the material are not taken into account in these models.

Researchers at FZG in Munich have created an alternative calculating approach for estimating the risks of tooth flank fractures. This method is based on the work of several authors, including Tobie [78, 79], Bruckmeier [102] and Witzig [34, 103]. This model, in its most comprehensive form, permits evaluation of flank fractures that start at the surface as well as in the subsurface areas. An equivalent local stress and an equivalent strength are compared in order to assess the cracking risk. The local stress is derived from the shear stress intensity theory, as developed by Oster [54] and Hertter [56] for rolling and sliding

contact and partially discussed in section 2.1.d. The load is described by using the normal and tangential contact stresses from Hertz theory in conjunction with the analytical effects of the lubrication state, thermal loads from localized heating caused by friction, and the specific stress state that develops between the flank surfaces' asperity peaks. For every volume element at and below the flank surface, the local material exposure A is taken into account as the ratio $A = \frac{\tau_{eff}}{\tau_{perm}}$, in which τ_{eff} is the effective shear stress calculated over all material planes at the position considered and τ_{perm} represents the corresponding admissible equivalent stress. In order to incorporate the effect of residual stresses, the local equivalent shear stress is derived using the following relationship:

$$\tau_{eff} = \tau_{eff,EL,RS} - \tau_{eff,RS}. \tag{2.16}$$

In equation 2.16, $\tau_{eff,RS}$ is the equivalent shear stress corresponding to the residual stress state, whereas $\tau_{eff,EL,RS}$ is the equivalent shear stress resulting from the superposition of both residual and load stresses. In a sense, the residual stresses are regarded as mean stresses in this context and are thus subtracted to determine the amplitude for the equivalent stresses; however, this subtraction occurs subsequently to the application of the SIH. Usually, a modified version of the formula from Lang's work is used to determine the residual stresses in the material depth y based on the local hardness $H_V(y)$ [114]:

$$\begin{cases} \sigma_y^{RS} = -1.25 \cdot (H_V(y) - H_{V,core}) & \text{if } H_V(y) - H_{V,core} \leq 300 \\ \sigma_y^{RS} = -0.2857 \cdot (H_V(y) - H_{V,core}) - 460 & \text{if } H_V(y) - H_{V,core} > 300. \end{cases} \tag{2.17}$$

Although this formula is based on many residual stress measurements and typically yields satisfactory results in the near-surface region for compressive residual stresses, it is not possible to account for tensile residual stresses using this approach. The assumption of negligible tensile residual stresses is reported to be only approximately valid when the core section is significantly larger than the case hardness depth [96]. It is not possible to fully examine the influence of the heat treatment conditions when designing gears using this method, since one of the parameters indicated as crucial for TFF is otherwise not taken into account [86]. Using equation 2.18, the material's strength limit is then determined by taking into account the local hardness:

$$\tau_{perm} = K_{\tau,perm} \cdot K_{mat} \cdot H_V(y). \tag{2.18}$$

Consequently, a proportionality between the admissible local equivalent shear stress and the local hardness is assumed by equation 2.18. This assumption has no theoretical support, yet values of $K_{\tau,perm} = 0.4$ have shown to generally yield acceptable accuracy. For the purpose of accounting for the impact of steel hardenability relative to tooth volume, Witzig introduced the factor K_{mat}. Depending on the alloy composition and tooth thickness,

gears are assigned empirical values for K_{mat} ranging from 0.7 to 1.13 [34]. Considering a load cycle corresponding to the different positions for the contact point on the tooth flank, a mapping of the material exposure is obtained for each material point. Based on experimental finding of gear running tests and industrial gear applications, a threshold value for material exposure A of $A_{crit} = 0.8$ has been found to describe the risks of tooth flank fracture with sufficient accuracy [104]. Although Witzig's model is able to determine the position of failure for the tested gears and achieves an adequate prediction accuracy for TFF [34], this method includes a significant amount of empirical elements, as demonstrated, among other things, by the seemingly arbitrary threshold value of 0.8 or by the definition of K_{mat} [115]. Steel cleanliness, inclusion size, and statistical size effect are not taken into account in this method, despite the fact that non-metallic inclusions and material defects are nearly always cited as the primary cause of fatigue crack initiation in TFF failures. According to the authors, the impacts of non-metallic inclusions on local stresses are implicitly accounted for by the threshold value of 0.8 for material exposure rather than 1, with a corresponding mean predicted stress increase due to inclusions of roughly 20 to 25 % [89]. This, however, is an extremely simplistic approach that disregards the crucial impact of the various sizes and positions of defects as outlined in section 2.1.b. Nevertheless, this concept or methods derived from it often serve as the foundation for gear design. In his work, Witzig [34] developed a practical-oriented method. With the exception of neglected effects in the near-surface region, this model yields very similar outcomes when calculating material exposure: the predicted risks for fracture initiation in the material depth are about the same as those for the previously detailed complex technique [34]. This means that this simplified model can only predict TFF and is no longer adapted for design againt pitting damage. However, this method has the important advantage of offering closed equations and does not require integration from SIH; for this reason, it forms the basis of the calculating method given in ISO/TS 6336-4 [3]. In recent years, the main shortcomings of the FZG-approach have been partially addressed. Müller calibrated analytical functions to characterize the residual stress profiles in carburized gear teeth using the output of FE simulation of heat treatment created by the author of this thesis [105, 47]. Both the compressive residual stresses at the surface of the flank and the tensile residual stresses in the core material may be predicted with satisfactory accuracy using input factors like the case hardness depth and the module. The created functions offer closed solutions and enable the integration of existing information from experimental residual stress measurements or expectations, including the height of surface residual stresses and the depth or value of maximal compressive stress. Müller demonstrated that, using this improved technique, the maximum material exposure threshold value for TFF failure shifts from 0.8 to 1.0 and that, in comparison to the approach using Lang's method for residual stress computation, the forecast accuracy can be significantly increased. Furthermore, he found that a crucial factor determining TFF hazards is the description of the hardness profile in the transition

zone between the case and the core, with notable variations between two widely used descriptions from Lang's and Thomas' models. Even though tensile residual stresses are taken into account, the chosen approach is evidently practical-oriented and only depends on simulated residual stress profiles at the pitch point and normal to the flank surface. Effects of residual stress gradients along the height of the tooth flank or along the gear width are not considered, although these may be significant *e.g.* for gear teeth with small radius of curvature or with low width. Wickborn extended the approach of Witzig and Bruckmeier by providing a framework to describe the effects of non-metallic inclusions [26]. Metallographic and fractographic analyses of the test gears from Witzig's work were performed in order to derive functions that characterize the size distribution and nature of non-metallic inclusions. The size of the gears and the size of the defects that caused the fracture do not correlate, according to the analysis. Small oxidic or oxisulphide inclusions, up to around 150 μm in diameter, are typically encountered at the crack initiation site in the base material 18CrNiMo7-6. Larger defects, up to 300 μm in diameter and of a sulphide type, are typically observed in the material 20MnCr5. In general, inclusion clusters are frequently recognized to be critical for crack initiation rather than individual defects. Most of the critical defects for TFF correspond to depths of about $2 \cdot \mathrm{CHD}$. Influences such as the production route or diameter of the bar material were not analyzed here. After testing several models, Wickborn [26] concluded that the logarithmic normal distribution is the most appropriate to characterize the size distributions of non-metallic inclusions, whereas extreme values are best described by means of a Gumbel distribution function. She suggests the introduction of a design factor K_{defect} in order to calculate the local admissible shear stress according to:

$$\tau_{perm} = K_{\tau,perm} \cdot K_{mat} \cdot K_{defect} \cdot H_V(y). \tag{2.19}$$

Here, K_{defect} is calculated by considering the reduced local shear strength of the material in the presence of defects, which can be derived from equation 2.1 and Murakami's work. Wickborn suggested a method to connect the parameters for the size distribution function with the results of standard cleanliness investigations. With a consideration of a reduced local fatigue strength in the presence of defects, Wickborn also reported a shift of the threshold value for material exposure before onset of TFF towards 1.0.

Using the experimental results from Witzig, Weber developed a model to assess subsurface crack initiation and TFF in carburized gears. An analytical model is used to calculate the contact and bending stresses and the results are verified using a 2D plane strain finite element simulation. In order to account for the local strength properties in the carburized tooth, the hardness profiles are described using Lang's equation:

$$H_V(y) = H_{V,core} + (H_{V,surface} - H_{V,core}) \cdot 10^{(-0.0381-0.2662 \cdot \frac{y}{\mathrm{CHD}}) \cdot \frac{y}{\mathrm{CHD}}}. \tag{2.20}$$

The local tensile strength is then calculated from the hardness using $R_m = 3.3 \cdot \mathrm{H_V}$ [22]

and the mean stress sensitivity according to the principles in [18]. The stress ratio R is used to perform this computation; however, the process of determining R for the complex multi-axial stress state is not specified. In his research, Weber highlights the critical role played by the residual stress field for tooth flank fracture risks. Using results of both X-Ray measurements and experimental data obtained with the contour method, he proposes to model the tensile residual stress profiles in the tooth core by modifying equation 2.17. Since Lang's approach usually provides satisfactory results for the compressive residual stresses in the near-surface area, Weber uses this equation up to a material depth of $0.5 \cdot \mathrm{CHD}$. From this point on, a third-order polynomial is used to characterize the evolution of the residual stress profile. The function's and its derivative's continuity at the transition point $0.5 \cdot \mathrm{CHD}$ are used to calculate the polynomial coefficients. By assuming a flat function when crossing the tooth's symmetry axis and compensation between the compressive and tensile residual stresses along a path normal to the flank's surface and up to the tooth's symmetry axis, the two missing equations are obtained. This assumption is very common and is also applied in a similar manner in the works of Konowalczyk [57], Ghribi [62, 63] and Böhme [52]. However, knowing the near-surface values of the residual stresses is not sufficient to directly obtain the residual stresses in the depth of a gear tooth using equations 2.5 and 2.6. Further assumptions are required, some of which may need to be questioned because they haven't been clearly stated or verified in the literature yet.

Like in the majority of available works on tooth flank fracture, Weber only considers the gear's axial and tangential residual stresses. While stresses in these two directions are taken to be equal, stress components in the radial or shear directions are neglected. After superimposing the load stresses and the residual stresses, a local equivalent stress is computed using either the SIH approach modified by Oster or a critical plane approach referred to as *KEV-Bosch*. This model describes the mean and amplitude value for normal stresses in each material plane characterized by the angles (θ, ϕ), as described in the following equation:

$$\begin{aligned} \sigma_{\theta\phi,m} &= \frac{max(\sigma_{\theta\phi}) + min(\sigma_{\theta\phi})}{2} \\ \sigma_{\theta\phi,a} &= \frac{max(\sigma_{\theta\phi}) - min(\sigma_{\theta\phi})}{2}. \end{aligned} \tag{2.21}$$

$\sigma_{\theta\phi,m}$ and $\sigma_{\theta\phi,a}$ are the mean and amplitude stress value in the material plane (θ, ϕ), respectively. The mean and amplitude values of shear stresses $\tau_{\theta\phi,m}$ and $\tau_{\theta\phi,a}$ are computed in a similar way and allow to determine equivalent mean and equivalent amplitude stresses in the material plane (θ, ϕ) according to equations 2.22 and 2.23, where $k_w = \frac{\sigma_w}{\tau_w}$ represents the local ratio between the axial fatigue strength and the torsion fatigue strength and sgn

is the sign function:

$$\text{For } k_w \leq 2: \begin{cases} \sigma_{\theta\phi,va} = \sqrt{\sigma_{\theta\phi,a}^2 + k_w^2 \cdot \tau_{\theta\phi,a}^2} \\ \sigma_{\theta\phi,vm} = sgn(\sigma_{\theta\phi,m}) \cdot \sqrt{\sigma_{\theta\phi,m}^2 + k_w^2 \cdot \tau_{\theta\phi,m}^2} \end{cases} \tag{2.22}$$

$$\text{For } k_w > 2: \begin{cases} \sigma_{\theta\phi,va} = \sqrt{k_w^2 \cdot (1 - \frac{k_w^2}{4}) \cdot \sigma_{\theta\phi,a}^2 + k_w^2 \cdot \tau_{\theta\phi,a}^2} \\ \sigma_{\theta\phi,vm} = sgn(\sigma_{\theta\phi,m}) \cdot \sqrt{k_w^2 \cdot (1 - \frac{k_w^2}{4}) \cdot \sigma_{\theta\phi,m}^2 + k_w^2 \cdot \tau_{\theta\phi,m}^2}. \end{cases} \tag{2.23}$$

The survival probability for each elementary volume is derived using the distribution function and the local critical sizes for material defects. Using the ideas from Murakami's work, Weber's method determines a position-dependent critical size, which depends on both the local hardness and the local equivalent stress, for defects like non-metallic inclusions to cause propagating cracks. A generalized extreme value (GEV) distribution function is used in each elementary volume to determine the probability of finding a defect larger than this critical size. Whether the parameters used for this distribution function were derived from fractographic analyses on Witzig's gears, from own rotating bending test data on carburized samples or from other assumptions is not clear, but Meis noticed significant differences between the modeled size of inclusions in Weber's and Wickborn's work [16]. He compared the expected maximum sizes for non-metallic inclusions as modelled by Weber with the defects corresponding to TFF failure in Witzig's work and concluded that Weber's model produced realistic size forecasts, whereas Wickborn's assumptions yielded excessively small defects [16]. Using the distribution function and the local critical sizes for material defects, Weber calculates the survival probability for each elementary volume and then obtains survival probability of the gear by multiplying all survival probabilities and raising them to the power of the number of teeth. In order to determine the survival probability of the gear stage, a similar calculation is carried out for the pinion and both survival probabilities are multiplied. Weber validates his model on the gear data from Witzig and predicts torque corresponding to a 50 % survival chance with a slight overestimation of about 10 %.

Böhme *et al.* proposed several approaches in order to assess the risks of tooth flank fractures in carburized gears. Motivated by the TFF-failures of large bevel gears intended for maritime use, they examined the fatigue strength of CrNiMo steel carburized samples. Using some of the elements from Murakami's work, a model for axial and torsion fatigue strength was created [33]. The alternate axial fatigue strength f_{-1} is defined in the lower range as proportional to the hardness, then takes a size of non-metallic inclusions representative for the material into account. The characteristic size of non-metallic inclusions in this work is taken to be 80 μm. Finally, fatigue strength reaches a constant value for high strength case material, thus illustrating the fact that the lower range of fatigue strength does not increase much with further hardness increases due to the higher notch effect of material defects. Using a combination of methods from FKM and own processed

equations, the remaining fatigue strength data is obtained as in the following equations:

$$t_{-1} = \frac{f_{-1}}{-5 \cdot 10^{-4} \cdot \mathrm{H_V} + \sqrt{3}}, \qquad (2.24)$$

$$f_0 = \frac{2 \cdot f_{-1}}{1 + \frac{M_m \cdot f_{-1}}{1.6 \cdot \mathrm{H_V}}}, \qquad (2.25)$$

$$t_0 = \frac{4 \cdot t_{-1}}{1 + \frac{2 \cdot f_{-1}}{f_0}}. \qquad (2.26)$$

Here, f_{-1} represents the alternate fatigue strength under axial load, f_0 the fatigue strength under axial load with stress ratio $R = 0$, t_{-1} and t_0 are the material strength under torsional load with $R = -1$ and $R = 0$ respectively. The fatigue behavior of samples with varying forging conditions prior to carburizing heat treatment could be modeled in the HCF and VHCF regimes using a continuous approximation for the SN curve for admissible stress amplitude versus number of cycles to failure. In the following investigation, the authors used this material model to predict the tooth flank failure of carburized bevel gears [52]. The contact loads were computed with analytical Hertzian calculations and a 2D plane strain assumption. Böhme's description of the local hardness was based on Thomas' work [116], whose model provides a more satisfactory agreement than Lang's formula. Since the CHD values in the tooth tip are typically higher than in the tooth root, the hardness in the tooth is implemented here with additional corrections based on the tooth height. Using Lang's equations, the residual stresses are modeled to a depth equivalent to the CHD. Similar to Weber's work, a fourth degree polynomial function and equilibrium conditions are then used to describe tensile residual stresses in the core. Several methods are used to assess the equivalent stress for multi-axial fatigue cycling loads, including Hertter, Papuga, Sines, Crossland, Liu-Zenner and Dang-Van models. A factor for the statistical size effect is also proposed, which consists of multiplying the predicted lifetime by a linear function of the gear's module. The numerical investigation showed that the integral calculation models from Liu-Zenner (LZ) and Papuga (PIN) *et al.* are not suitable for rolling contact problems and provide inaccurate fatigue strength estimations for the gears under study. However, adjustments made by the authors on the LZ and Hertter failure criteria concerning the effects of mean stresses resulted in a higher forecast accuracy for the examined bevel gears. The developed model could yield good agreement when used to recalculate crack initiation positions that were measured experimentally using ultrasonic detecting methods. In another study, Böhme proposes a new practical-oriented approach for predicting tooth flank fracture [61]. He proposes to modify Dang Van's criterion to consider only the planes parallel to the tooth flank, based on experimental results of subsurface cracks propagating parallel to the flank surface. With this adjustment, the computed equivalent stresses for contact load are found to be almost comparable to the original Dang-Van method, with deviations falling within a 3 % range. However, the expected accuracy in the presence of

residual stresses is not evaluated, and tensile residual stresses in the tooth core are not taken into account in this investigation. Still, the suggested framework offers a closed solution as it does not require integration or the search for material plane orientations. Böhme reports that the prediction accuracy for three tooth pairs from spiral bevel gears made of 18CrNiMo7-6 steel is similar to the models proposed by Witzig and Boiadjiev [34, 104]. Additionally, he discusses certain numerical issues that arise when calculating some of the intermediate coefficients in Witzig's approach. These issues can cause sudden and undesired increases in calculated material exposure when specific situations such as off-centered contact points are considered.

Based on the intrinsically statistical character of the influence of defects and non-metallic inclusions on the fatigue properties of carburized steel components, Konowalczyk proposed a probabilistic approach for the assessment of TFF on carburized gears [57, 101]. Derived from earlier work from Zuber for tooth root bending [43] and possibly from other models by Lai on bearing steels [29], Konowalczyk assumes a distribution of non-metallic inclusion sizes throughout the gear volume. A two-parameter Weibull function is used to describe the size distribution function. A local stress tensor is computed for every position in the gear's teeth using the finite element method and the STIRAK software. Similarly to Weber, Konowalczyk uses the equation from Lang's work and assumes some equilibrium conditions on a path normal to the flank surface in order to calculate tensile residual stresses in the core material with a fourth-order polynomial function. Konowalczyk applies Liu and Zenner's SIH hypothesis to account for the multi-axial stress condition. Using the local hardness and residual stress data, a Haigh diagram is created for each material point, and the local fatigue strength in the case of non-metallic inclusions is determined using equation 2.1 from Murakami [5]. Simulated staircase tests using virtual gears are used to calculate the strength of the carburized gears with varying grinding conditions. The created method is validated using both Witzig's work and the results of own experimental research. The accuracy for torque prediction corresponding to a 50 % failure probability is found within a deviation range of around 10 % and a satisfactory correlation is achieved for the most likely positions for crack initiation. Görgen continued this work later on, which also served as the foundation for designing the bench facility for TFF testing described in 2.2.a.

A similar approach is adopted by Meis in 2023 [16]. Meis establishes, in a purely theoretical work, a Monte-Carlo simulation model for the influence of non-metallic inclusions that is likewise based on probabilistic methods and Murakami's concepts. For the simplest load conditions, load stresses can be derived analytically; for TFF computations, load stresses are obtained via FE-models. Meis, in contrast to Konowalczyk, focuses on a thorough examination of the input data that is necessary for the simulation model. Large datasets from the literature are used to create hardness profiles. As surface oxidation depth has a strong correlation with the carburizing time, his model includes the description of depth of oxidation linked to the CHD. However, since the surfaces of the flanks are typically ground

and do not show significant levels of surface oxidation, this feature is not used for TFF assessment. Large datasets from several German research projects, among others, are used to describe residual stress profiles. Despite the fact that residual stresses in the material's depth are a crucial parameter for TFF mechanisms, Meis acknowledges that there are extremely few measurements available. He computes tensile residual stresses from equilibrium considerations along a path normal to the surface in his calculations, but he also concludes – as does Müller [105] – that these assumptions result in unreasonably high stress values when considering large case hardening depths and slender teeth. Additionally, he investigates the potential for selecting various polynomial functions based on tooth thickness, since experimental results indicate that, depending on the geometry, there may be either tensile residual stresses with a peak value in the area where the case and core transition or a steady profile that flattens in the core. He thus emphasizes the necessity for a more accurate quantitative and spatially resolved description of the residual stresses resulting from carburizing heat treatment. In his work, Meis also models the effect of shot peening through empirical modifications of the near-surface residual stresses. The equivalent stress for multi-axial stress states is derived using the same critical plane approach as in Weber's work. Meis first verifies the reasonableness of his simulation model and assumptions by comparisons with the FKM and DIN 743 guidelines for carburized round and notched samples. Using simulation techniques, he shows how impacts on the fatigue strength like strengthening from carburizing heat treatment or material quality may be more precisely predicted. Additionally, the couplings between these parameters can be better taken into account. Case-studies on tooth root bending demonstrate the applicability of the method for more complex carburized components, with a very good agreement with ISO 6336-3 [117]. With the simulation model, some additional predictions are made, such as some dependencies of the conversion factor between the results of the running tests and the pulsator tests for tooth root bending strength, which were subsequently verified by Fuchs' experimental work [4]. Finally, Meis investigates the assessment of TFF for carburized gears. Witzig's gears were chosen for a parameter analysis, which includes variations in material quality, core hardness and residual stress profiles. These input parameters have been selected due to uncertainties regarding the appropriate input parameters for a simulation. For the predicted torque and direction of the material planes on which failure initiates, very good agreement with the experimental results from Witzig can be obtained, depending on the input data. The material quality, which is represented in the simulation model by various distribution functions for the size of non-metallic inclusions, has been shown to create fatigue strength variations of up to $\pm 300\,\mathrm{MPa}$ and is clearly the most important investigated parameter. Though in smaller amounts, the core hardness also affects the gear's anticipated fatigue strength. Remarkably, Meis' simulation results are not drastically influenced by the location of the highest tensile residual stresses or the transition between compressive and residual stresses. On the other hand, through the equations adopted for modeling the residual stress profiles,

the core hardness also partially determines the residual stresses in the tooth, which is why a proper separation of these influences is not possible.

In addition to the previously mentioned studies on tooth flank fracture for carburized gears, a few models from other publications provide approaches and opportunities that may improve prediction abilities for TFF-risk assessment. With an emphasis on the ultra high cycle fatigue, Fuchs provides a technique for estimating the risks of tooth root bending failures started in the subsurface area of high-strength carburized gears [4]. He adopted concepts from Murakami's work to analyze fish-eyes and fractographic features at crack initiation in carburized gears to forecast the extent of Optical Dark Area around statistically dispersed defects like non-metallic inclusions and abnormally large grains. While the bending stress state in the tooth root differs drastically from the complex multi-axial stress state under the flank's surface, the underlying mechanisms responsible for subsurface fracture in these two examples might be similar enough to be integrated in a common assessment concept. Several models, like the gear contact model from Liu *et al.* [118], incorporate the effects of grain size and orientation distributions. While there is no experimental correlation between the size and orientation of microstructure grains and the probabilities of tooth flank fracture in gears, these techniques might be helpful if future developments in steel cleanliness result in TFF failure that mainly initiates at grain boundaries and apparently defect-free locations.

Combining FE models for both the case-hardening process simulation and the mechanical fatigue loading seems to be a potential strategy to better integrate the heat treatment-related factors in the fatigue strength prediction. The efforts associated with a polyvalent simulation model can easily compete with experimentally-based trial-and-error procedures, despite being computationally expensive and complex. Large degrees of geometrical change are possible with the finite element approach and material-oriented models. Building verified simulation models makes it possible to establish a direct connection between a wide range of characteristics, including the conditions of the heat treatment process, and the mechanical characteristics of the component in service. In his PhD-thesis, Diemar presents a concept for estimating the fatigue strength of carburized components using a finite element simulation of the heat treatment to predict the local hardness and residual stresses [40]. The multi-physics model computes the evolution of stresses due to various processes, including phase transformations and is based on coupled metallurgical, thermal, and mechanical field analyses. By imposing mechanical loads on the FE geometry produced by the heat treatment simulation, fatigue strength of the component is subsequently evaluated. To obtain a scalar equivalent stress, the stress tensor created by residual and load stresses is assessed using the Dang-Van criterion. Equations developed from FKM guidelines [18] and Murakami's work [5] on material defects are used to compute probabilities of local failure for both surface elements and volume elements. Next, the survival probability of the entire component is determined by multiplying the survival probability of each elementary volume

or surface. For a drilling hole with shoulder under cyclic internal pressure stress and a shaft undergoing axial bending, examples of fatigue strength estimation after carburizing heat treatment are provided. A satisfactory agreement between experimental data and simulation findings within a 10 % range is described for both cases. A more direct link between the parameters of the heat treatment process and the fatigue properties of the component is examined in [119], where Diemar uses the results of heat treatment simulation in conjunction with FE calculations for the mechanical fatigue loading to optimize the heat treatment process to a component's specific geometry. The optimization program uses the carburization parameters as input directly; the hardening temperature, duration, and temperature of the gas carburizing steps are varied to minimize the maximum value of the local material exposure in the component. The Dang-Van criterion is used to evaluate the stresses, and the material strength is derived from the calculated local hardness. A carburized shaft with a drilled hole that is subjected to bending loads is used as an example to demonstrate the optimization method for heat treatment design. The potentials for connecting FE results from heat treatment simulation to fatigue strength calculation with appropriate consideration of residual stress and hardness gradients are illustrated, even though no validation of the predicted results is provided. Tong *et al.* [120] use a comparable strategy for induction-hardened gears, although in a simplified formulation. The hardness and residual stresses arising from several dual-frequency induction surface hardening processes are first predicted using FE models. Next, contact loads are computed and superimposed to the residual stress tensors using FE methods in order to estimate the most likely location of fracture initiation during service. Similar approaches were previously employed by Li *et al.* to combine numerical models for both heat treatment and contact loads in order to estimate the impact of carburizing heat treatment on the tooth root fatigue parameters of carburized gears [121, 122].

Rajaei recently investigated the potential to optimize the carburizing and rolling processes for sintered steel gears' tooth root bending strength using simulation tools [48]. This offers a new way to consider the interaction between CHD and surface densification-induced heterogeneous density profiles. The carbon concentrations in the gears before quenching were computed using time and temperature data of low pressure carburizing heat treatment procedures in a diffusion model, whereas the densification depths were estimated from experiments or spatial distribution assumptions. The local residual stresses and hardness values can then be predicted using these results in a multi-physical FE simulation of the gear's quenching and tempering. In a following step on the FE model, the local time-dependent stress tensors for the load conditions corresponding to the pulsator test are generated and combined with the residual stresses produced by heat treatment. The highly loaded volume in the tooth root area is identified and the risks for surface and subsurface crack initiation are evaluated using different failure criteria. Iterations on the load magnitude for pulsator test simulation lead to a prediction for the tooth root bending strength corresponding to

50 % failure probability within a satisfactory margin as compared to experimental results. Additionally, the modeling approach revealed optimization potentials for the tooth root bending fatigue strength employing higher CHDs. In the final section of his work, Rajaei uses an analytical Hertzian model to simulate the contact loads on the surface of the tooth flank after heat treatment simulation. Reasonable qualitative agreements were found for both the pitting fracture risks of the carburized gears and the fracture patterns shown in gear running experiments.

Iss and Meis apply similar methods in [123] to determine the fatigue strength of carburized materials. FE-based prediction of the hardness and residual stress gradients were combined with the probabilistic approach described in [16]. Axial bending fatigue test data from other published experiments is used to validate the model. The original publication's comprehensive details of the heat treatment procedures allowed for a realistic reproduction of the microstructure and residual stresses in gas carburized 18CrNiMo7-6 samples. Accurate estimates of the sample's failure probability based on the applied bending load were obtained by making assumptions about the functions for size distributions of the defects that cause crack initiation. A simulative variation study was then conducted to examine various round notched and unnotched carburized sample geometries under rotational bending loads, whereby the samples investigated also featured varying case hardness depths and material quality. Although there was no experimental validation done there, the evolution of the hardness, residual stresses, fatigue strength values or crack starting positions with different CHDs and notch radii or characteristics of non-metallic inclusions, conform very well qualitatively with the expected behavior. In addition, the authors showed the possibility of predicting fatigue strength with more precision than the existing standards for designing heat treatment parameters optimally based on specific geometry or load conditions. The model was found to better account for the relationships between several mechanisms – such as CHD, statistical size effect and residual stress gradients – involved in fatigue failures of carburized components than virtually any other available assessment technique. The proposed approach's shortcomings were identified in the surface-related effects that were disregarded when calculating fatigue strength and in the uncertainty around the most adequate functions to describe the sizes of defects that are involved in crack initiation.

2.3. Residual stress development in carburized components

Carburizing is a thermochemical surface treatment method widely employed to enhance the fatigue strength, hardness and wear properties of steel components. This is achieved by the combination of three substeps. The surface layer is first enriched with carbon atoms, then hardened by the martensitic microstructure transformation through rapid quenching

and subsequently tempered [74]. In comparison to through-hardened gears and depending on the material quality, properly carburized and quenched gears can exhibit load capability increased by 30 to 50 % [11, 36]. Carburizing is therefore typically applied for heavily loaded components with high resistance requirements against wear, rolling or bending loads. Carburizing belongs to the broader category of case-hardening heat treatments, which increase the hardness of the surface and subsurface regions while leaving the components core mostly unchanged. This has an added benefit of allowing low-carbon steels with high machinability to be used to shape the component before heat treatment and provides the core material with sufficient toughness [124]. Steels usually used feature carbon contents between 0.15 and 0.30 %. The carbon content and alloying elements are selected based on the part geometry under consideration and the requirements for hardenability and core strength. These alloys include, for instance, the typical steels used in transmission gears, 18CrNiMo7-6 and 20MnCr5.

The most commonly used technique for carburizing is based on a gas medium. The introduction of carbon atoms in the surface and subsurface layer of a component mainly depends on three parameters: time, temperature and atmosphere composition. The temperature is always selected above the A_{c3} point, since the face-centered cubic lattice of austenite allows for the dissolution of substantial amounts of carbon atoms in the octahedral lattice interstices of up to a weight percentage of roughly 2.1 %C, depending on both temperature and alloy composition. For large components that must exhibit a deep hard layer after quenching, the process times can reach several days. However, long process times are associated with a number of disadvantages, such as high energy costs, low productivity, high distortion or disproportionately large grains, which is why shorter process times are typically preferred.

The diffusion of carbon in austenite can be described through Fick's first law of diffusion 2.27, which states that the flux $\vec{j}_c$ of the diffusing carbon atoms perpendicular to a plane surface with normal unit vector $\vec{n}$ is proportional to the local concentration gradient perpendicular to this surface area. Then, using Fick's second law 2.28, the time variation of the local carbon concentration is determined. Temperature and alloy composition both affect the diffusion coefficient D_c of carbon in austenite [48]:

$$\vec{j}_c = -D_c \, \frac{\mathrm{d}c_c}{\mathrm{d}\vec{n}}, \qquad (2.27) \qquad\qquad \frac{\mathrm{d}c_c}{\mathrm{d}t} = \nabla(D_c \, \nabla(c_c)). \qquad (2.28)$$

Carbon content is the main factor that determines case hardness. At about 0.6 %C, martensite reaches its maximum hardness; adding more carbon atoms only slightly raises martensite hardness and instead results in significant proportions of softer residual austenite. In addition to reducing the hardness of the surface region, this may have a detrimental impact on the dimensional stability. Depending on the service conditions, advantageous ef-

fects on the rolling fatigue properties may overweight, and proportions of residual austenite of 10 to 30 % are common in carburized gears [74]. Surface carbon concentrations between 0.6 and 0.9 % are typically targeted. However, in addition to surface hardness, the maximum values and gradient steepness for carbon content may need to consider the anticipated stresses beneath the surface as well as the removal of surface layers caused by grinding following heat treatment. Apart from significant residual austenite phase fractions, excessive carbon concentrations can also cause detrimental brittle carbides to develop at the grain boundaries or soot at the gear surface [74].

The mechanisms driving the absorption of carbon atoms at the component's surface can be highly complex and they will be explained here only in an exceedingly straightforward way. The difference in carbon activity between the workpiece and carburizing agent in the atmosphere induces the decomposition of carbon-rich gas at the surface [12]. The carbon supply at the surface can be regulated by controlling the proportions of different types of gases. The carbon potential C_p, which quantifies the amount of carbon that can dissolve in a pure iron foil, is used in gas carburizing for this purpose. To account for the impact of alloying elements, the achievable surface concentration C_a is corrected using the formula 2.29. Values for the alloying factor k_a depending on the steel's chemical composition can be found, for instance, in [125].

$$C_a = k_a \cdot C_p \tag{2.29}$$

The absorption of carbon at the outer surface influences the speed of carburization and can be described as a function of the current carbon concentration at the surface C_S by the transition number β. The mass flow of carbon $\frac{\mathrm{d}m_c}{\mathrm{d}t}$ then follows equation 2.30:

$$\frac{\mathrm{d}m_c}{\mathrm{d}t} = \beta \cdot (C_a - C_S). \tag{2.30}$$

In practice, values of β between $1.0 \cdot 10^{-5}$ and $4.0 \cdot 10^{-5}$ cm/s have been measured during gas carburizing [12]. A process referred as *boost-diffusion*, which is a two-stage saturation-equilibration procedure with a changing carbon potential and temperature, is typically used in gas carburizing. In order to maximize carbon transfer and reduce the overall process time, the carbon content in the austenite surface layer is maintained during the first phase slightly below its saturation limit. In the second stage, a rather continuous carbon depth gradient is achieved by diffusion of the high surface carbon content into the component with a carbon potential roughly corresponding to the desired surface concentration [40]. Adopting a strategy with low carbon concentration gradients in the outer surface layers has the additional advantage of reducing the surface hardness variability due to subsequent grinding operations.

In recent decades, methods for carburizing at very low pressure have been developed. The use of vacuum carburizing in case-hardening methods has expanded due to significant

benefits related to the simpler atmosphere composition, the elimination of oxidation issues or the ability to enable higher process temperatures and shorten process times. A sequence of short steps are conducted in non-equilibrium conditions. During the boost stages, small amounts of hydrocarbon gas are released, resulting in the rapid absorption of carbon at the surface. A further diffusion stage allows carbon atoms to diffuse further into the depth, preventing soot. The intended CHD determines the number and duration of boost and diffusion steps.

A carburized component's intended strength and hardness are first produced by applying the suitable quenching heat treatment after a carbon concentration gradient is introduced. This is accomplished by transforming the carbon-rich case region into martensite or, in specific scenarios, bainite. Carburizing can be followed promptly by quenching because the temperatures needed for carbon diffusion fall within the same range as those needed for hardening. This is referred to as direct quenching. Due to the graded carbon contents, the optimal temperatures for hardening vary across core and case regions. Temperatures between 780 °C and 860 °C are optimal for the surface's hardness properties, but may be too low for a fully austenitic microstructure in the core and thus lead to reduced core hardness [12]. Hardening temperatures tend to be lower than those of the carburizing process since the choice of hardening temperature affects the risk of distortion and cracking. For some special applications, quenching and reheating or isothermal transformation operations might be chosen in order to obtain optimal grain size and hardness throughout the component [11]. Given the fact that case-hardening steels micro-alloyed with Aluminum are rather insensitive to excessive grain growth, however, direct hardening is the most practical and extensively utilized method.

Conditions for the quenching process are designed to meet the case region's hardness requirements. Depending on the component's dimensions, geometry and steel hardenability, a variety of quenchants might be appropriate. High local hardness signifies that non-martensitic transformation products like ferrite, bainite or pearlite are prevented by a sufficient cooling rate. In the core region, large proportions of bainite may be acceptable for the low-carbon steel. The design of the quench can be estimated based on continuous cooling transformation (CCT) diagrams. However, the accuracy of such approaches may be affected by specific geometry-dependent cooling conditions and variations in the component's exact alloy composition or carbon content relative to the reference sample data available. In practice, liquid or gas quenching agents can be used to quench carburized parts. The use of nitrogen, argon or helium in gas quenching at pressures up to around 20 bars allows for uniform cooling and accurate control of the quenching intensity through the adjustment of gas pressure, velocity, nozzle number and position. However, for large components, the heat removal is typically not enough to provide the high near-surface cooling rates that are required. A heat transfer coefficient (HTC) h can be used to represent a quenching medium's ability to remove heat from a component's surface, as shown in equation 2.31:

$$h = \frac{Q}{A \cdot (T_s - T_q)} \tag{2.31}$$

Q is the heat flow from the workpiece to the quenchant, A is the component's surface area, T_s is the surface temperature and T_q the temperature of the quenchant. h typically encompasses the effects of radiation and conduction [39]. Values of h for various quenching media can be obtained in the literature, however the real heat transfer during quenching can be highly dependent on factors like the surface condition, the component shape, the steel composition or the agitation of quenching medium [74]. Higher cooling rates may typically be achieved using liquid quenchants, but the heat-transfer coefficient shows a noticeably stronger dependence on surface temperature. The various mechanisms underlying heat transport in different temperature ranges provide an explanation for this. Heat-transfer coefficients in the film-boiling, nucleate-boiling and convection-cooling stages can differ by an order of magnitude. Although water is the most straightforward and environment-friendly liquid quenchant, quenching with water is linked to extremely high cooling rates, which increase the likelihood of cracks or large distortions. Furthermore, heterogeneous and poorly reproducible cooling conditions result from the uncontrolled transition between the cooling stages in water quenching. Consequently, different techniques for quenching have been developed that rely on submersion in aqueous polymer solutions, oil or salt baths. The selection of a quenching medium for a given component geometry is invariably determined by finding a balance between the cooling rates needed for the case region to undergo martensitic transformation and the negative consequences of excessive cooling rates in terms of crack and distortion risks.

Quenching carburized parts typically results in significant residual stresses because of the remarkably heterogeneous distribution of both material properties and temperatures. A virtually stress-free state can be assumed prior to quenching, as flow stresses at the hardening temperature are orders of magnitude smaller than the residual stresses following quenching, and temperatures should be distributed rather evenly due to the relatively long carburizing times. Residual stresses during quenching can be attributed to differences in the local strains, which can have a variety of causes. Thermal strains result from the evolution of the local material density due to temperature variations. In the presence of large temperature gradients in a part, the thermal strains may lead to stresses greater than the local yield stress, thus causing the onset of plastic deformation. Thermal strains will also result from spatial variations in the thermal expansion coefficient in a hypothetical homogeneously cooled part, for instance as a result of a gradient in the concentration of carbon. Local density variations can also be created by the transformation of austenite in denser microstructures. In particular, the displacive transformation into martensite is linked to a volume increase. The local strain brought on by the martensitic transformation results in large residual stresses when constrained by the surrounding material. While the local

density also increases along with the transition between austenite and bainite or pearlite microstructures, the volume mismatch that results is usually significantly smaller. The residual stresses after quenching of carburized parts are the result of complex interactions between the local yield stresses, the spatial and temporal evolution of temperatures, the chronological order of the phase transformations and the carbon-dependent strain magnitudes associated to thermal dilatation and phase transformations.

Due to the increased local hardenability and decreased martensite start temperature, the carbon-rich surface region of carburized components usually stays austenitic longer than the core, despite being subjected to higher cooling rates. The core region first transforms into bainite, ferrite, pearlite or low-carbon martensite. The soft austenitic microstructure and relatively high temperatures lead the surface and subsurface to deform plastically to accommodate the core's volume expansion. Further cooling causes the surface temperature to drop below the temperature required for the martensitic transition M_S, which in turn causes the case region's volume to significantly rise. In contrast to the previous transformation, however, the yield stresses in the part are usually much higher because of the low temperatures and harder microstructures exhibited by the surrounding material. As a result, the martensite volume expansion essentially corresponds to elastic strains and usually produces compressive residual stresses in the vicinity of the surface, which are offset by tensile residual stresses in the core. Detailed considerations about the influence of thermal related and phase transformation related strains on the residual stress depth profile of carburized cylindrical samples are available in [9, 39]. Nevertheless, the residual stresses upon quenching cannot be inferred directly from the combination of the factors mentioned earlier. When a phase transformation occurs under stress, even though the local yield stress is not exceeded, inelastic strains are formed. This phenomenon is known as transformation-induced plasticity or TRIP. TRIP-strains during martensitic phase transformation have been found to have a significant impact on the residual stresses in carburized parts [39]. The dependence of these inelastic strains on the stress directions and magnitudes during phase transformation further emphasizes the influence of the time sequence in which the microstructure changes occur. Overall, a wide range of variables – some of which are intricately coupled – affect the residual stresses in carburized and quenched parts. Local carbon concentration affects the extent of dilatation due to martensite transformation and the differences in thermal expansion coefficients. Yield stresses, hardenability and sequence of the phase transformations are also significantly affected by the carbon content. From a non-local perspective, the CHD and the ratio between a part's case and core are directly impacted by the distribution of carbon atoms, with implications for the residual stress depth profiles that have been partially covered in section 2.1.e. Cooling conditions determine the extent of thermal strain mismatches through the homogeneity of the temperature distribution in the part, as well as the sequencing of the different phase transformations. Part geometry can also be held responsible for similar effects, besides determining the global conditions for

residual stress equilibrium. Although they are not covered in this study, further influencing elements that have an impact on the evolution of residual stresses include, for instance, the alloy composition or grain size.

Carburized items are typically subjected to a tempering heat treatment following quenching in order to provide them the toughness needed for several applications and to eliminate the brittleness of martensite. Suitable temperatures range from about 150 °C to 200 °C and tempering times of 1 to 2 hours are commonly used. During the process, the tetragonality of martensite is lowered through short-range diffusion of carbon atoms and precipitation of ϵ transition carbides in regions with carbon contents above approximately 0.25 %C. The moderate temperatures are anticipated to cause only minor declines in surface hardness and no appreciable changes in the levels of residual austenite [74]. Surface residual stresses of carburized and quenched parts can be reduced by tempering. In carbon-rich steels, the precipitation of carbides is linked to a reduction in material density, which partially offsets the expansion of the case region during quenching. Reports of residual stress variations during tempering vary significantly; they range from scarcely noticeable changes [12] to offsets of several hundred MPa of surface residual stresses in the direction of tensile stresses [9, 126, 127]. This may suggest some significant effects from the different alloy compositions, carburizing and quenching conditions or the geometry of the parts used. Tempering heat treatment can also change the micro-distribution of residual stresses between neighboring martensite and residual austenite areas [126, 127]. A possible residual stress redistribution in the core due to the shifted equilibrium conditions is not discussed in the literature.

In conclusion, the evolution of residual stress in carburized parts is a highly complex matter involving multiple interrelated variables. A number of factors are involved, including the carbon profile, temperature history, sequence and spatial distribution of the various phase transformations. In the simplest circumstances, theoretical analysis can yield some basic principles or trends, but evaluating actual processes on complex-shaped components is a very challenging task. Methods based on finite elements have been developed for this purpose. Assuming small deformations, the behavior of the material can be separately modeled for each of the several sources of strains, as stated in equation 2.32:

$$\overline{\overline{\epsilon^{total}}} = \overline{\overline{\epsilon^{el}}} + \overline{\overline{\epsilon^{pl}}} + \overline{\overline{\epsilon^{th}}} + \overline{\overline{\epsilon^{tr}}} + \overline{\overline{\epsilon^{tp}}} + \overline{\overline{\epsilon^{cr}}}. \tag{2.32}$$

The total strain tensor $\overline{\overline{\epsilon^{total}}}$ is obtained by superposition of the elastic strain $\overline{\overline{\epsilon^{el}}}$, the plastic strain $\overline{\overline{\epsilon^{pl}}}$, the strains due to thermal expansion $\overline{\overline{\epsilon^{th}}}$, phase transformations $\overline{\overline{\epsilon^{tr}}}$, transformation-induced plasticity $\overline{\overline{\epsilon^{tp}}}$ and creep $\overline{\overline{\epsilon^{cr}}}$. The resulting stresses are linked to the elastic strains via Hooke's law. To describe the plastic strain, a yield condition (*e.g.* von Mises) must be assumed for the local multi-axial stress state. Thermal strains, transformation strains and strains associated to transformation-induced plasticity can be determined by means of dilatometric investigations. Creep mechanisms can reduce the residual stresses

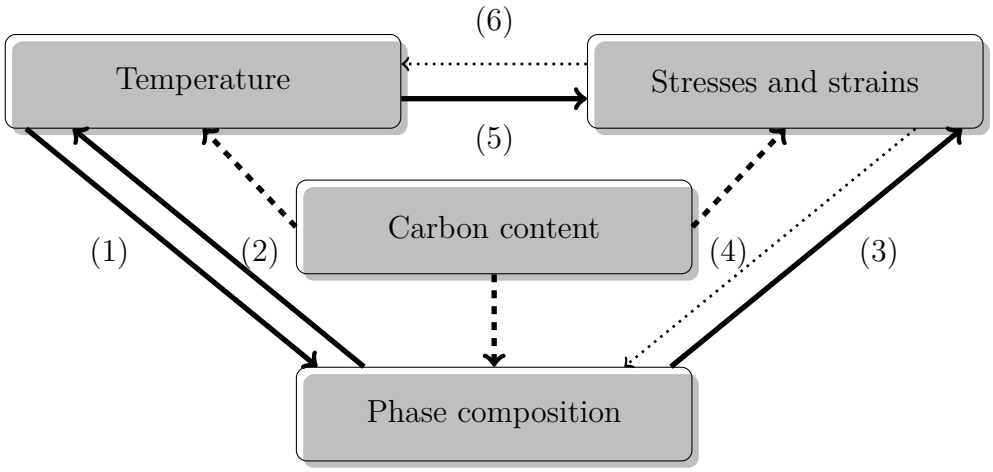


Figure 2.11: Main interactions considered in FE-simulation of a carburizing heat treatment. The description of interactions corresponding to each arrow is available in the text. Dotted arrows can usually be neglected.

at temperatures above $0.4 \cdot T_L$, where T_L is the melting temperature in Kelvin. In many heat treatment operations, however, creep is of secondary importance and is therefore typically neglected. The material data utilized is the cornerstone for the simulation. For instance, the elastic constants and thermal expansion coefficients of all microstructures involved are needed as a function of temperature. The flow curves must also be determined for each phase in order to take plastic deformation into account, which occurs primarily at high temperatures. Another crucial parameter is the transformation plasticity. For the 18CrNiMo7-6 gear steel, data is available for this purpose from the research projects CASH (Computer-Aided Simulation of Heat Treatment) [128, 129, 130] and FVA 501 I and III [131, 132]. The approaches of Johnson-Mehl-Avrami-Kolmogrow (equation 2.33) and Koistinen-Marburger (equation 2.34) for diffusion-controlled and martensitic transformations are extensively used models in the state of research today [133, 134, 135]:

$$\dot{\xi}_k \;=\; n \cdot \tfrac{\overline{\xi}_k - \xi_k}{\tau} \cdot \left[\ln\left(\tfrac{\xi_k}{\overline{\xi}_k - \xi_k}\right)^{\frac{n-1}{n}} \right] \cdot f_k(\dot{T}) \tag{2.33}$$

$$\xi_M \;=\; \overline{\xi}_M \cdot (1 - e^{b_{KM} \cdot (T - M_S)}). \tag{2.34}$$

The volume fraction of the product phase k is denoted by ξ_k, its derivative with respect to time is $\dot{\xi}_k$. The maximum transformed phase fraction at equilibrium is $\overline{\xi}_k$, while τ represents the time at which 63 % of the transformation is completed and n is an exponent characterizing the transformation rate. f_k is a calibration factor to accomodate for non-isothermal conditions, since equation 2.33 was originally formulated to determine the kinetics of phase transformations without any variation of temperature. In equation 2.34, the martensite volume fraction is directly calculated as a function of the martensite start temperature M_S, the current temperature T and a material parameter b_{KM}.

The fundamental ideas behind the numerical approaches are described in [136] and [133].

Once constructed and verified, a simulation model enables a very cost-effective investigation of the main influences of geometry, process or material features on the residual stresses. The combined calculation of mechanical and thermal fields is enabled within many commercially available FE softwares. Carburizing heat treatment-specific material behavior is typically only very partially available, however it may be included in user-defined plug-ins or subroutines. The FE approach offers considerable flexibility in the component's geometry. Numerous studies have successfully used FE simulations to study residual stresses caused by heat treatment in steel components. These studies include models for quenching [137, 138, 139], induction hardening [140, 120, 141], laser surface hardening [142], carbonitriding [143], and tempering [144, 145]. With FE methods, realistic predictions of residual stresses and hardness following carburizing and quenching heat treatment can be regarded as state-of-the-art. Numerous studies have effectively evaluated carbon profiles produced by gas or vacuum carburizing [125, 146, 147, 40]. FE-based prediction models for residual stresses in carburized and quenched components have been developed, for instance, in the work of Diemar [40], Rajaei [48], Castens [132], Franz *et al.* [129] and Nusskern [147]. The majority of models have a shared structure and comparable algorithms. Still, each model is unique in terms of material data, the specific modeling of the different mechanisms and the coupling between them. The various fields taken into account in numerical simulation models for carburizing and quenching, along with the most significant couplings between them, are shown in figure 2.11. The phase transformations during the quenching of an alloy depend on the temperature history and quenching rates (1). Phase transformations generate heat and can locally increase the temperature (2). Volume differences between the decomposed and produced phases induce strains during phase transformations (3). The effects of stresses on the kinetics of phase transformations (4) or on the thermal field through mechanical work (6) can generally be neglected, which is indicated by dotted lines in figure 2.11. The temperature variations impose thermal strains and strongly impact the mechanical properties of the material (5). Furthermore, the carbon concentration of the steel has an influence on both thermal and mechanical properties and changes the temperatures and kinetics characterizing the decomposition of austenite during the quenching. Since accurate results need a description of the material behavior under various thermal, metallurgical and mechanical circumstances, acquiring a large amount of specific material data is necessary. Other challenges to build and validate simulation models include the very scarcely available residual stress measurements in material depths of carburized parts or the high computation time for large or complex geometries [47].

2.4. Summary and objectives of this work

Tooth flank fracture is a fatigue failure that originates beneath the surface of a loaded tooth flank and is of critical importance for carburized gears. The substantial advancements in the field of gear fatigue research over the past few decades have enabled the optimization of gear design and heat treatment to effectively mitigate surface-initiated damages. By reducing or delaying surface-initiated damage, the proportional importance of fracture initiation in the volume of the material is increased. Moreover, certain techniques aimed at mitigating pitting concerns can potentially adversely affect the risks associated with TFF [115]. Due to the depth of crack initiation and the influence of residual stresses on the propagation pattern, there is currently no experimental approach available for reliable non-destructive inspection of TFF cracks. As a result, TFF frequently leads to the sudden failure of gear or gear stage.

Many different factors can affect the risks of TFF. Various techniques exist for evaluating the likelihood of TFF in carburized gears; however, these techniques exhibit significant shortcomings. A substantial amount of empirical approaches and coefficients are included in commonly used methods for TFF risk assessment, which may show discontinuities or lose validity when changes are made to the gear design, gear material or heat treatment procedure [61, 115, 16]. A few major influences, such as the statistical size effect or the coupling between different impacting factors, are not satisfactorily accounted for [16]. Every available approach makes use of certain input parameters that, depending on the specific component, production, heat treatment or finishing process, are either mostly unknown or subject to large deviations. The role of non-metallic inclusions, particularly the numerical evaluation of their influence on TFF, remains unsettled even though this question has been addressed in works from the past decade. Most importantly, while it is widely acknowledged that residual stresses in the material depth have a significant impact on the TFF, the existing assessment methods for TFF are extremely simplistic in their consideration of the residual stresses. Often made assumptions about equilibrium of residual stress depth profiles also need to be questioned. Variations of residual stresses and hardness along the tooth flank in the axial or height directions are either disregarded or given an extremely simple consideration. The state of the art does not allow for a satisfactory quantification of the effects of influencing parameters like CHD, carbon surface concentration or carbon depth profile and quenching medium on the TFF risks because of their largely unknown influences on the residual stresses and their interactions with one another.

On the other hand, it has been established that FE models are capable of accurately predicting the development of hardness and residual stresses generated by heat treatment procedures. Appropriate material models allow to calculate the local properties in a heat treated component nearly regardless of its shape and with a high degree of process condition flexibility. Aside from very elaborate experimental measurements with limited explanatory

power, simulation models may be the only possibility to evaluate the residual stresses in the depth of carburized and quenched components. Since residual stress and hardness are among the most influential variables on the risks of TFF fatigue failure, FE methods appear to be particularly suitable for a quantitative, physics-based approach to predicting TFF. Simulation models can be used for heat treatment as well as service or testing load conditions to determine connections between parameters such as CHD, quenching conditions, tooth shape and the risks of fatigue failure. Because of the substantial efforts involved in determining the essential materials and process data and the specific know-how required to carry out the simulations successfully, residual stress modeling has only been utilized in isolated problems and there hasn't yet been systematic investigations on the variables affecting residual stresses in carburized and quenched gears.

This work intends to address the shortcomings of the existing methods of assessing the risk of tooth flank fracture in carburized gears, with an emphasis on generally overlooked aspects related to residual stresses in the subsurface and core regions of the gear tooth.

The following formulation can be used to propose the main research hypotheses:

- Finite-element based modeling enables a precise prediction of the hardness and residual stresses in carburized gears, not only in the case region but also in the material depth under the tooth flank and with consideration of various heat treatment parameters such as CHD, carbon depth profile or quenching conditions.

- Assessment methods for the risks of tooth flank fracture in carburized gears can be significantly improved by the finite element based prediction of local hardness and residual stresses from heat treatment operations.

In order to address this topic, the investigation is structured in three main sections. First, the material behavior during carburizing, quenching and tempering heat treatment is modeled in chapter 3. For this purpose, extensive experimental characterization based on dilatometry is used in conjunction with available material data from published works. A simulation model is constructed in chapter 4 in order to calculate the effects of heat treatment on gear components while accounting for variations of process parameters and gear geometry. The prediction models are validated using experimental campaigns on gears conducted at IWT Leibniz-Institute Bremen as part of the research project FVA 835 I [47]. In order to identify trends and key influencing parameters in the evolution of residual stresses in carburized gears, some additional simulative studies are conducted. The surface carbon diffusion during the gas or vacuum carburizing process is only minimally addressed in this work and the carbon depth profiles are rather considered as known inputs for the quenching simulation than as subjects for a deep investigation. The impact of post-heat treatment procedures, such as shot peening or grinding, on the residual stresses in the surface region is not directly considered. Using FE models that integrate heat treatment

simulations for local hardness and residual stresses with the numerical computation of stresses under service or fatigue testing load conditions, chapter 5 finally addresses the fatigue and TFF properties of heat treated gears. Aspects of multi-axiality, statistical size effect, and non-metallic inclusions are explored, and several assessment techniques for TFF prediction are compared. Witzig's experimental results [34] serve as the main basis for evaluating the accuracy of the various calculation approaches.

Chapter 3

Material model for carburizing heat treatment

3.1. Material investigation

In order to determine the necessary material parameters for the modeling of the material behavior during heat treatment, dilatometer samples are produced in different carburized states. The material states are selected in such a way that, together with the existing data for the steel 18CrNiMo7-6, a statistically validated data set is created that covers all technologically relevant boundary conditions. The samples are produced from the same batch that was already used in the FVA 501 III research project [132]. Using vacuum carburizing, approximately 400 hollow cylindrical samples with carbon weight percentages of 0.32 %C, 0.44 %C, 0.50 %C, 0.53 %C, 0.66 %C, 0.75 %C, 0.82 %C and 0.89 %C are produced. Each individual sample is 10 mm long and exhibits homogeneous carbon concentration within its cross section defined by outside and inside diameters of 4 mm and 2 mm, respectively. In addition, approximately 50 samples are produced with a carbon concentration of 0.18 %C. This gradation allows an adequate description of the typical carbon profile observed after carburizing, and the resolution is sufficient to map the graded transformation behavior of the carburized material in a realistic manner. In this work, samples and gears from different material batches with base carbon contents between 0.17 %C and 0.19 %C are included. The chemical composition of the alloys can be found in appendix A1. As a simplification, the alloy carbon content nominal value of 0.18 %C is utilized for the following diagrams. The material characterization based on dilatometry includes the determination of plastic flow characteristics, transformation behavior, thermal and transformation-induced strains, transformation plasticity and tempering behavior. The corresponding tests are performed using a quenching and deformation device DIL 805A/D. The material properties are determined as functions of the carbon concentration, the temperature and the microstructure.

3.1.a. Yield stress and flow properties

Methods: The determination of the flow properties of 18CrNiMo7-6 in the carburized and non-carburized state aims to supplement the data set from the CASH project [130]. The objective is to validate these material parameters and to obtain a finer resolution of

the description of the flow properties, particularly with respect to the dependence on the carbon concentration. The desired microstructure is set in the dilatometer samples by applying adequate time-temperature profiles and the samples are then tested at the desired temperature under uni-axial compressive loads. Table 3.1 provides the full test plan.

Measured flow curve	Test temperature [°C]									
Carbon content [%C]	20	100	150	200	300	400	500	625	750	850
0.18	B M				B M	B M	B	A	A	A
0.32	B M	B M		B M	B M	B				
0.50	B M	M		B M	B M		A		A	A
0.66	B M	M	B	M		B				
0.82	M	M		M			A		A	A

Table 3.1: Test plan to determine the temperature, carbon and microstructure-dependent flow behavior. A stands for austenite, B for bainite and M for martensite.

The dilatometer samples are heated to 950 °C within 3 minutes. Following a ten-minute holding period, the temperature is lowered to 850 °C, the hardening temperature, and maintained there for another minute. The samples are quenched in the dilatometer in 5 seconds from the hardening temperature to the required test temperature in order to evaluate the flow behavior of the austenite phase. In order to achieve the intended microstructural change for the bainitic and martensitic microstructures, the samples are heated again to the test temperature after being quenched to room temperature. Cooling rates ranging from 30 to 150 K/s are required to enable martensite transformation, depending on the transformation kinetics of the samples (*i.e.* the carbon concentration). After quenching, samples containing more carbon than 0.50 %C are held in liquid nitrogen for a further 60 minutes in an effort to minimize the impact of the residual austenite on flow behavior. The bainite transformation is conducted with an isothermal holding phase above the carbon-dependent M_S-temperature, between 300 °C and 450 °C. In the course of experimental research, a number of trials were temporarily halted at relatively low strain values. This occurrence, however, was not due to the fracture of the samples. Rather, the cause was either a problem in the experimental setup or an externally applied force limit on the DIL805 device. The latter is a protective measure implemented to safeguard the integrity of the punches and the rods.

Results: In this work, the flow curves of the austenite phase were planned to be determined at temperatures of 500 °C, 700 °C and 850 °C with carbon contents of 0.18 %C, 0.50 %C and 0.82 %C. Since the bainitic transformation of the base material at 500 °C takes place already after a few seconds, the test temperature is increased to 625 °C for this variant. The results of the stress-strain curves of austenitic phases of 18CrNiMo7-6 under uni-axial compressive loading and as a function of carbon content are shown in figure 3.1.

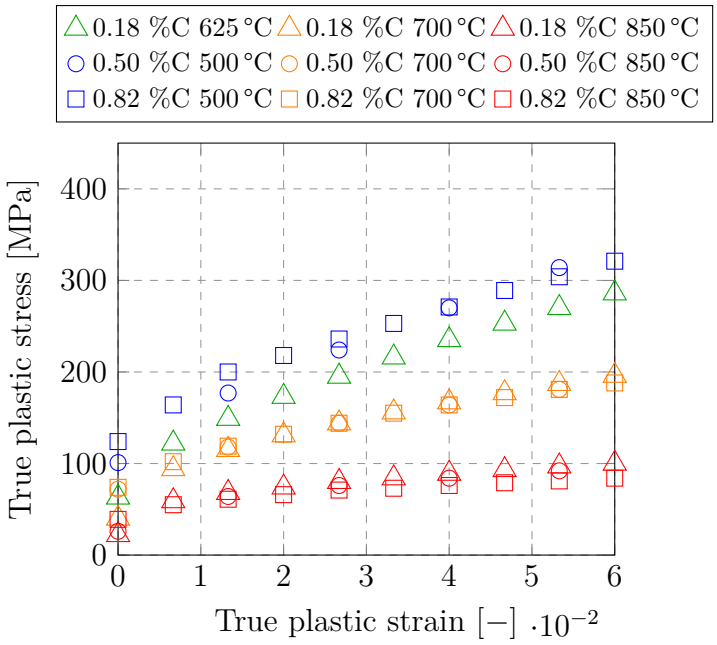


Figure 3.1: Flow properties of austenitic 18CrNiMo7-6 under compressive load for different temperatures and carbon concentrations.

As expected, the yield point of the austenite phase decreases with increasing temperature. In agreement with [130], the influence of the carbon concentration on the flow behavior of austenitic 18CrNiMo7-6 is negligible, so that a consideration of the dependence of the yield point of the austenite phase solely based on the temperature is sufficient.

Determining the flow properties of a bainitic microstructure with different carbon contents is also part of the material investigation. In bainitic microstructures, both temperature and carbon concentration effects can be determined. In all tested conditions, the yield point decreases with increasing temperature and tends to increase with carbon content. For reasons of clarity, the results are listed in tabular form in the appendix A3. Since the samples were transformed into bainite under isothermal conditions at different temperatures depending on the carbon concentration, the observed effects at a given testing temperature are not only due to the carbon content, but also because of the temperature-dependent morphology of the bainitic microstructure. Results of the investigation of the flow properties for martensitic and martensitic-austenitic microstructures are available in appendix A4. As expected, the martensitic case-hardening steel achieves higher strength values than in the bainitic state. The carbon content has a strengthening effect, especially up to approximately 0.50 mass percent. An increase in temperature, on the other hand, promotes the plastic deformation of the martensite.

3.1.b. Transformation behavior, thermal expansion and transformation strains

Transformation behavior

Methods: To investigate the phase transformation behavior of 18CrNiMo7-6 steel at different carbon contents, continuous cooling tests are carried out in the quenching dilatometer. The dilatometer tests are conducted specifically with cooling curves that correspond to the quenching of carburized gears and were determined using thermal FE simulations. Among other things, the focus is on the carbon and cooling rate dependence of the transformation kinetics and transformation strains. Between 5 and 15 continuous quenching tests are carried out per carbon content, depending on how high the cooling rate dependence of the transformation behavior is determined in technically relevant cooling conditions. The cooling times $t_{8/5}$ between 800 °C and 500 °C are between 20 s and 20,000 s. The transformation temperatures and volume fractions are determined using temperature vs. length change curves and systematic microstructural analysis with optical microscopy. In addition, hardness and energy-dispersive X-ray spectroscopy (XRD) measurements are carried out on selected dilatometer samples. For instance, the residual austenite content of carbon-rich samples after quenching was determined. A total of approximately 100 dilatometer tests are evaluated to characterize the transformation behavior of the case-hardening steel during quenching. The kinetics of the bainitic and ferritic-pearlitic transformations are characterized using isothermal dilatometer experiments in addition of continuous quenching investigation.

Results: The conducted tests to characterize the transformation behaviour in the quenching dilatometer can be displayed in the form of continuous cooling transformation (CCT) diagrams. The start and end points of the bainitic, ferritic-pearlitic and martensitic transformations are shown for the tested cooling processes. The starting point for the time axis is set for all carbon contents at a temperature below 780 °C, which corresponds approximately to the A_{c3} point of the base material. The figure 3.2 shows the CCT diagrams of the materials with 0.32 %C, 0.44 %C, 0.50 %C, 0.66 %C, 0.82 %C and the base material with 0.18 %C.

The martensite start temperature for the base material 18CrNiMo7-6 is slightly below 400 °C. Under typical quenching circumstances, some bainitic transformation is almost inevitable due to its rapid nature in the non-carburized steel. At lower cooling rates, ferritic-pearlitic microstructures are seen. When cooling time increases, the carbon atoms diffuse into the remaining austenite grains with increasing proportions of ferrite and bainite. This results in a drop in the martensite start temperature. Increased carbon contents cause the martensite start temperature to decrease and the diffusive phase transformations to move downward and toward longer time periods. At high carbon concentrations, the bainitic

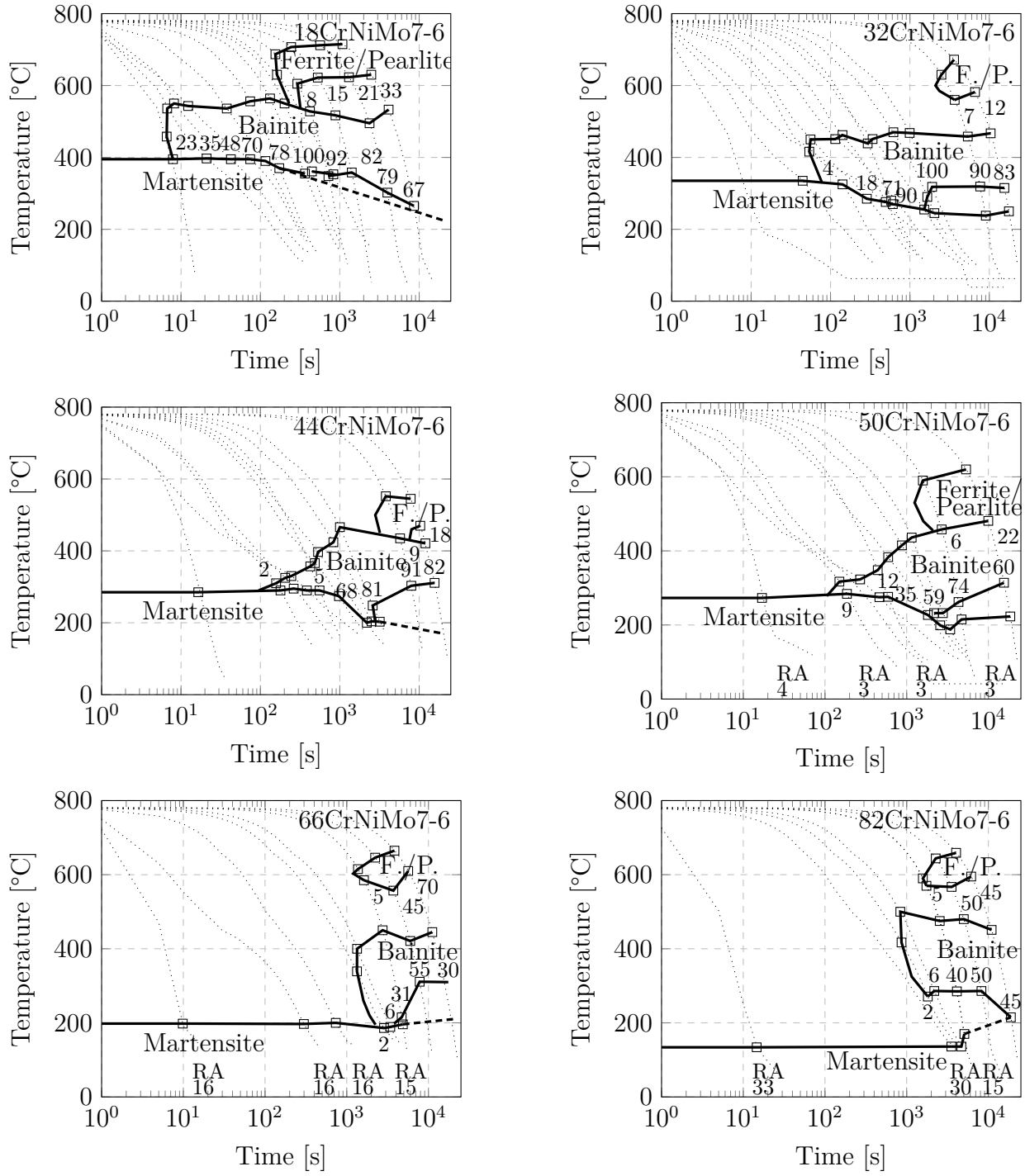


Figure 3.2: Experimentally determined continuous time-temperature-transformation diagrams of the case-hardening steel 18CrNiMo7-6 with different carbon contents.

and pearlitic transformations are no longer of any technical significance, as they require very slow cooling, which is typically not present in the carburized, near-surface regions. For carbon concentrations above approximately 0.44 %, retained austenite is present in the material because the martensite transformation is not entirely completed upon cooling to room temperature. The volume fraction of residual austenite rises with increasing carbon concentration and can reach up to around 30 % for the carburized samples. The findings of

isothermal dilatometer experiments for bainite transformation kinetics are included in the appendix in figure A5.1.

Thermal expansion and transformation strains

Methods: In addition to analyzing the phase transition kinetics, the dilatometric investigation assesses the strains caused by temperature and microstructure changes. These are represented by transformation strains and thermal expansion coefficients. The procedure for calculating transformation strains and thermal expansion coefficients from dilatometer experiments is illustrated in figure 3.3. The austenitic microstructure reference state of the steel samples at 850 °C serves as the basis for the transformation strains reported here. For instance, when the curve is vertically shifted so that cooling from the austenite microstructure begins at 0 % length change, the coefficient b_{FP} – the thermal strain associated with the ferrite/pearlite microstructure – corresponds to the Y-intercept of the linear fitting curve computed for 100 % ferrite/pearlite. These coefficients are established in relation to the carbon content and the phase being studied. A linear mixing rule is used to obtain the characteristic values of a microstructure when only mixed microstructures can be identified.

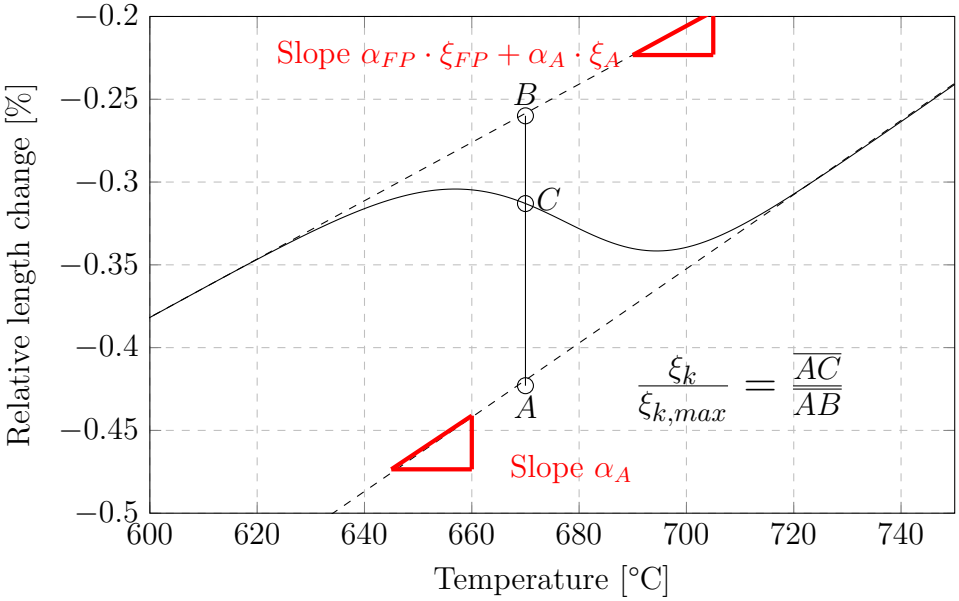


Figure 3.3: Determination of transformed fractions and thermal expansion coefficient α on the basis of dilatometer curves using the example of an incomplete transformation of austenite in ferrite and pearlite[148].

Results: The thermal expansion coefficient and transformation strains recorded for each phase and for each carbon content can be represented as shown in figure 3.4, where the transformation strains represent the intercept of linear fit of temperature *vs* strain curve for full homogeneous phase at 0 °C.

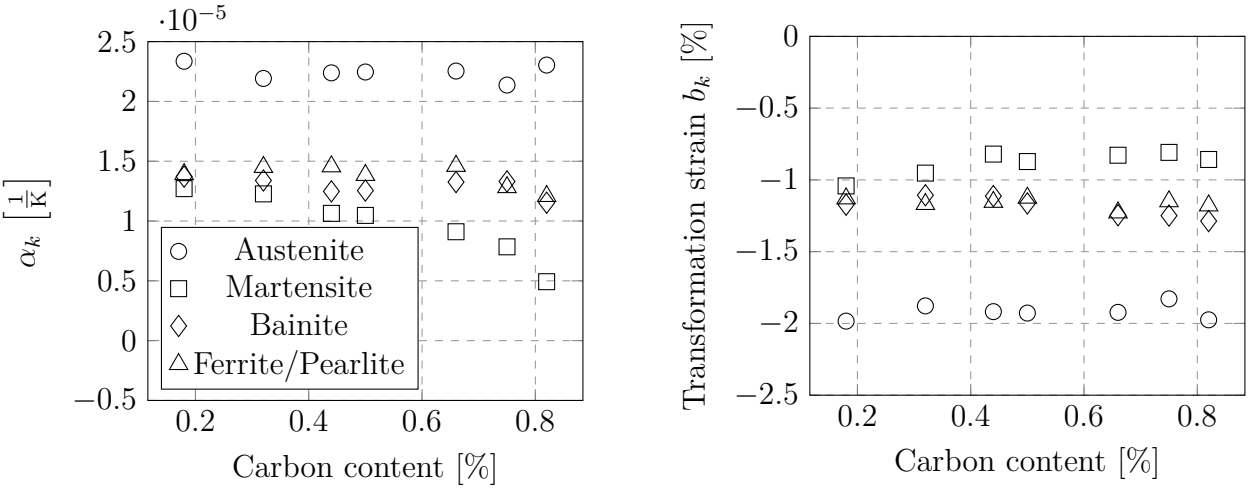


Figure 3.4: Experimentally determined thermal expansion coefficient α_k and transformation strains b_k, with the definition of α_k and b_k following the above description.

Due to the high number of quenching tests, not all data of the continuous cooling curves can be shown. Figure 3.5 shows examples of the dilatometer curves for $t_{8/5} = 18\,\mathrm{s}$ and $t_{8/5} = 900\,\mathrm{s}$ for the different carburized materials. The exact respective cooling conditions are given on the right-hand side.

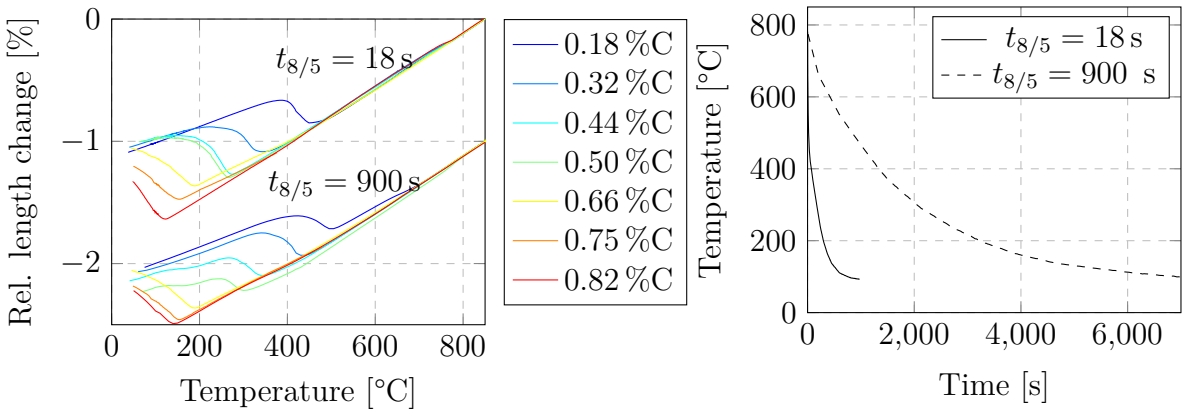


Figure 3.5: Dilatometer curves of 18CrNiMo7-6 samples (left) under selected cooling conditions (right) and with different carbon contents. The dilatometer curves of cooling with $t_{8/5} = 900\,\mathrm{s}$ are shifted downwards by 1 % relative length change for clear visualization.

These results can be analyzed using the micrographs obtained by optical microscopy of quenched dilatometer samples etched with alcoholic nitric acid (Nital) solution.

The carbon content influences the microstructure formation during rapid cooling. Figure 3.6 shows the resulting microstructures for selected carbon contents after cooling with $t_{8/5} = 18\,\mathrm{s}$. The bainitic transformation takes place at a basic carbon content of 0.18 mass percent even with rapid cooling. In the carburized states, martensite is increasingly formed instead. The martensite transformation is not fully completed with increased carbon concentration and leads to the preservation of residual austenite contents. For defined cooling

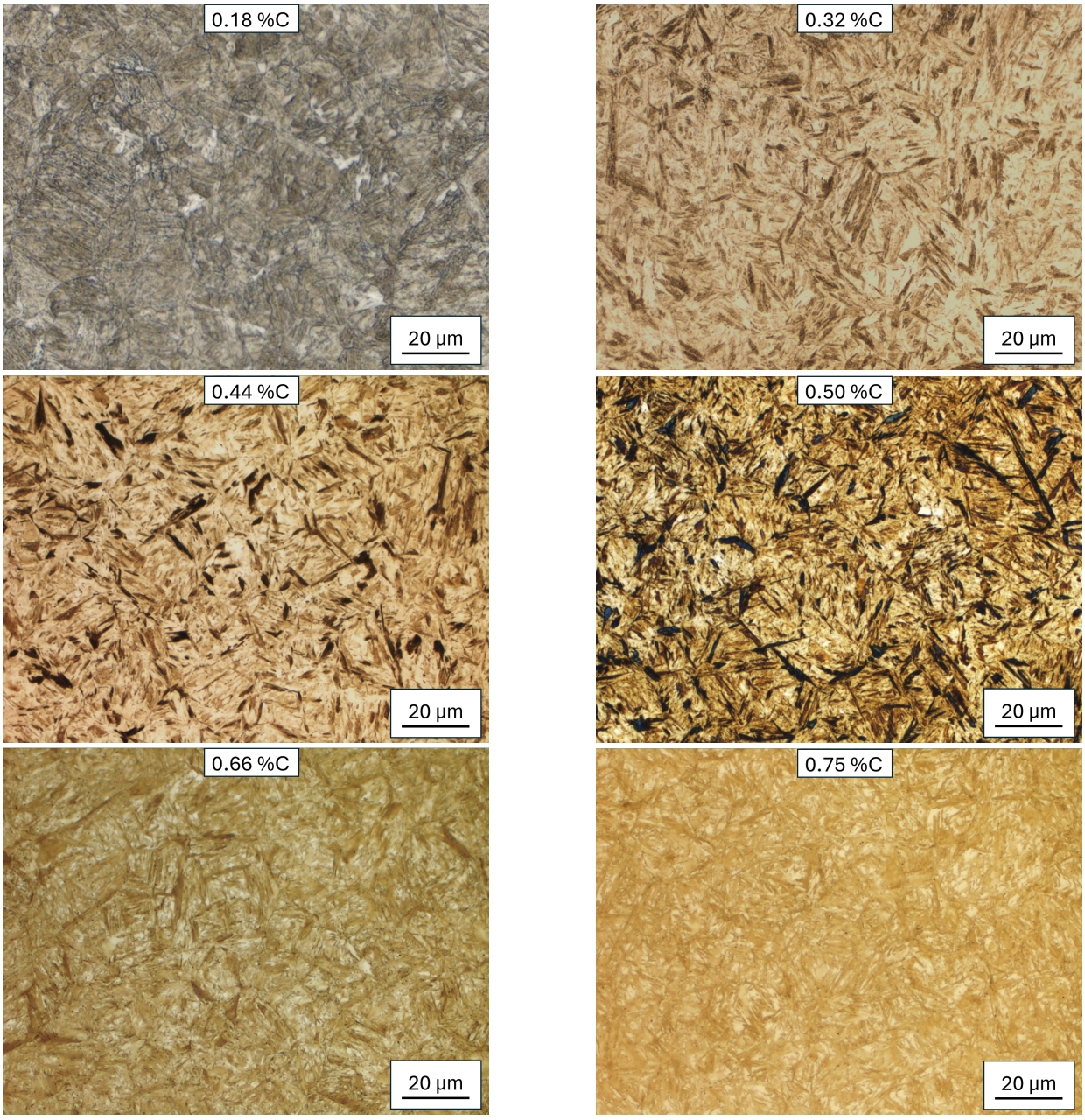


Figure 3.6: Resulting microstructure after rapid cooling with $t_{8/5} = 18\,s$ in the dilatometer as a function of the carbon content.

conditions, the carbon content also affects the morphology of both martensite and bainite phases. With increasing carbon content, the martensitic structure is expected to change from lath to plate, although this is not obvious from the micrographs in figure 3.6. Carbon concentration also has a significant impact on the transformation behavior under slower cooling conditions, as shown in figure 3.5 for a cooling time $t_{8/5} = 900\,\mathrm{s}$. The formation of a small percentage of ferrite and pearlite can be observed in samples which were not carburized, as indicated by the length evolution of the dark blue curve at about 680 °C. A sample with 0.32 %C, on the other hand, transforms completely bainitic. With increasing carbon concentration, bainite formation takes place at lower temperatures, which leads to

an evolution of the bainite structure from upper bainite to lower bainite. In carbon-rich materials, hardly any bainite is formed even at very low cooling rates. The most carbon-rich samples (0.66 %C, 0.75 %C and 0.82 %C) have a predominantly martensitic structure with retained austenite. At the moderate carbon contents of 0.44 %C and 0.50 %C, a shift in the martensite start temperature compared to faster cooling due to the back diffusion of carbon atoms into austenite during bainite transformation can be observed. This transformation behavior is also strongly influenced by segregation in the samples, as described in the section 3.1.d.

3.1.c. Transformation-induced plasticity

Methods: During a phase transformation under stress, inelastic strains occur, which are due to the so-called transformation plasticity. This property has a significant influence on the residual stresses, which are calculated by means of a heat treatment simulation [149] and is therefore investigated here. For this purpose, a constant compressive stress is applied and maintained during quenching in the dilatometer before the phase transformation starts, and the resulting strain of the sample is compared with the strains in the stress-free reference state. This investigation is carried out for the different carbon contents and phase transformations. The transformation-induced plastic strains under uni-axial compressive loading during martensite transformation were investigated for the carbon contents 0.18 %C, 0.32 %C, 0.50 %C, 0.66 %C, 0.75 %C and 0.82 %C under stresses from 0 MPa to 250 MPa. In contrast to the martensitic transformation, the investigation of transformation plasticity in a bainitic transformation is carried out under isothermal conditions. Hereby, carbon contents of 0.18 %C, 0.32 %C, 0.50 %C and 0.66 %C under stress levels between 0 MPa and 100 MPa were investigated.

Results: The results of the measured transformation-induced plastic strains during transition from austenite to martensite are presented in figure 3.7. For all carbon concentrations, an approximately linear relationship between the uni-axial stress and the transformation strain can be determined. A rather low dependence of the TRIP-strain on the carbon content is found. However, it should be noted that the observed strains are related to different transformed phase fractions of martensite, as high carbon contents prevent from a complete transformation of austenite into martensite. Thus, the derivation of adequate material models requires a more thorough analysis.

In a similar manner, the transformation from austenite to bainite exhibits an approximate linear relationship between uniaxial stress and transformation plastic strain. The dependence of the transformation-induced plasticity on the carbon concentration is more pronounced and can be clearly seen in figure 3.7. Under the tested conditions, the transformation plasticity reaches a maximum at 0.32 % carbon content.

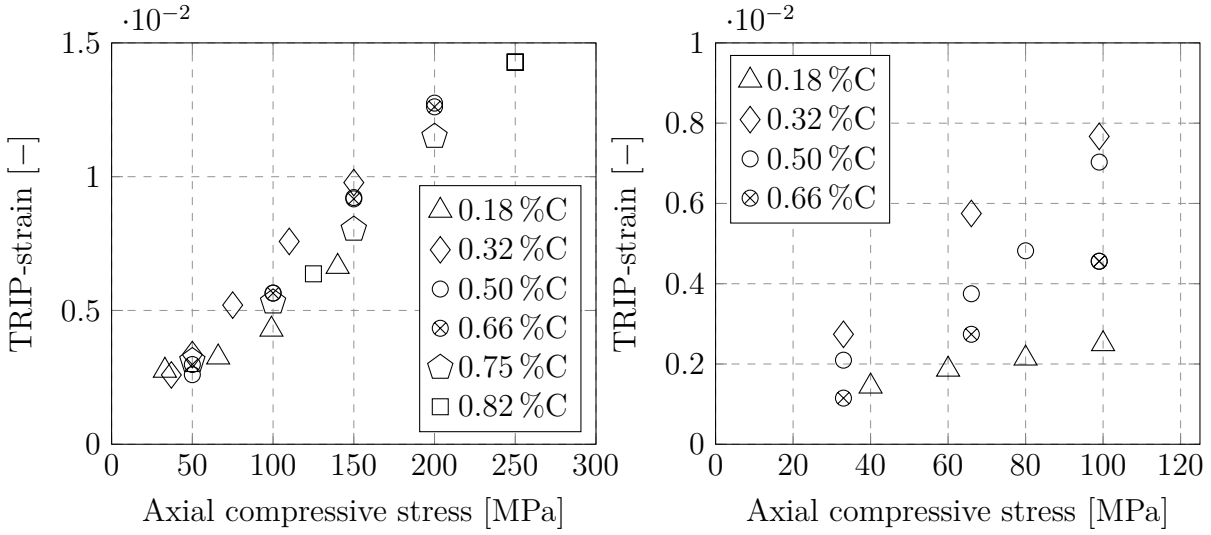


Figure 3.7: Transformation-induced plastic strains of martensitic transformation (left) and bainitic transformation (right) for different carbon contents.

3.1.d. Tempering behavior

Methods: After quenching, case-hardened gears are usually tempered. This reduces the brittleness of martensite and relieves the induced residual stresses by allowing the diffusion of carbon atoms. This behavior is investigated in dilatometer samples as a function of the carbon content. In this work, dilatometer samples are quenched rapidly and tempered at 170 °C for one hour. The contraction of the carbon-rich samples in the dilatometer due to formation of transition carbides is recorded and the (negative) strains resulting from the tempering process are then used in the material model for calculating the residual stresses of tempered gears. The retained austenite contents before and after the tempering step for the different carbon contents are determined for selected variants using XRD-analysis. During tempering tests under compressive stress in the dilatometer, the strains are affected by the existing uni-axial stress, so that a TRIP-like behavior during tempering can be described. This behavior is rarely discussed in the literature, but is characterized here and taken into account in material modeling. For this purpose, the strains that occur during a 1-hour tempering of dilatometer samples with carbon concentrations above 0.32 %C at 180 °C under 0 MPa, 150 MPa and 300 MPa are measured.

Results: The strains that occur when tempering martensitic-austenitic dilatometer samples for 1 h at 170 °C are recorded and shown in figure 3.8. After approximately 60 minutes at this tempering temperature, no measurable further length changes are detected for any of the carbon contents investigated.

Similar to quenching, these test data can be used to derive characteristic thermal expansions and *transformation strains*. The *transformation strains* here refer to the relative reduction in length caused by the tempering treatment. The evaluated values are shown

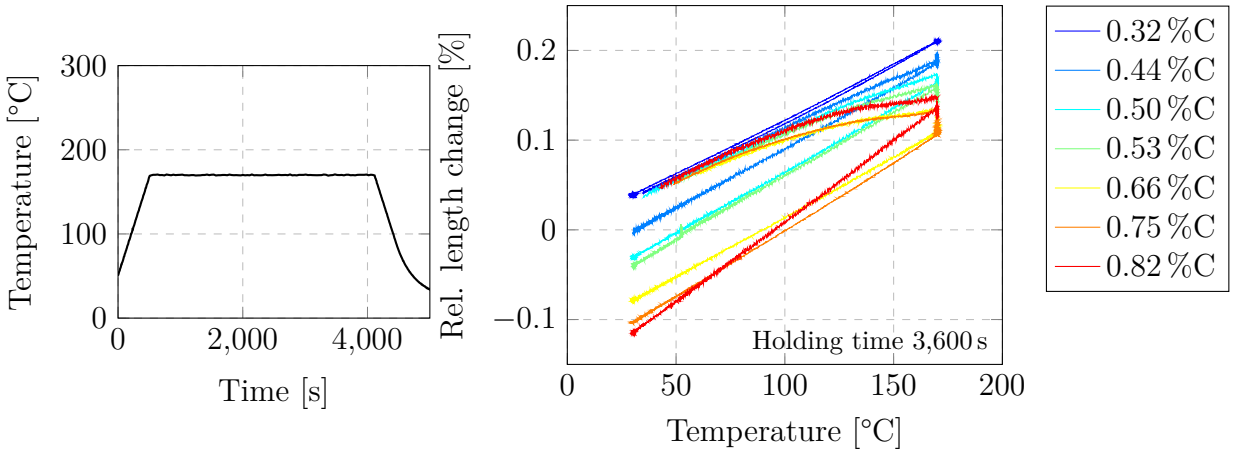


Figure 3.8: Tempering cycle used in dilatometric experiments on martensitic-austenitic samples of 18CrNiMo7-6 with different carbon contents (left) and strains induced during this tempering cycle (right).

in figure 3.9. For this representation, the zero point of the strains is selected with an extrapolation of the respective tempering heating curves at a temperature of 0 °C. For carbon concentrations below 0.32 %C, no persistent strain changes are observed due to the tempering process. At higher carbon contents, an almost linear dependence of the tempering-induced strains with the carbon content is observed. The thermal expansion coefficient of a tempered martensitic-austenitic sample is largely independent of the carbon concentration, but seems to increase from a carbon content of approximately 0.75 %C.

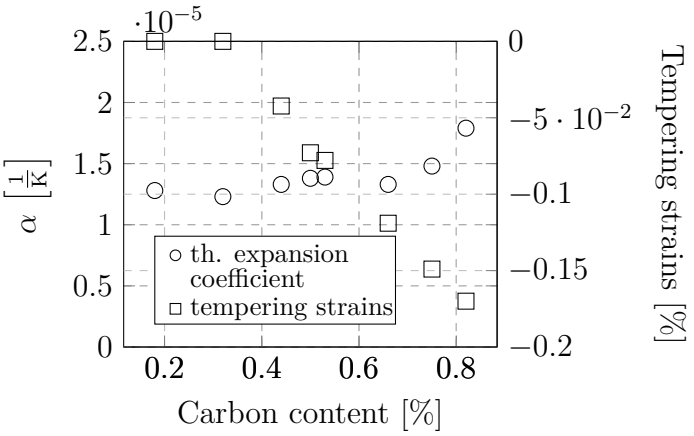


Figure 3.9: Measured expansion coefficients and tempering-induced strains of martensitic-austenitic dilatometer specimens during a tempering treatment of one hour at 170 °C.

For tempering heat treatments of 1 hour at 170 °C, no significant changes of the residual austenite phase fraction were detected by XRD-analysis. In contrast, vickers measurements showed some reduction of the hardness after tempering as compared to the quenched microstructure. These results are displayed in figure 3.10.

Tempering tests of martensitic-austenitic dilatometer specimens under axial compres-

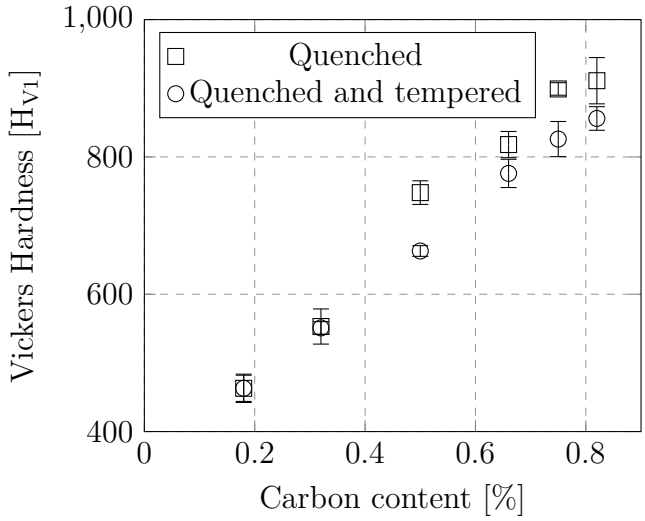


Figure 3.10: Hardness of martensite in samples of 18CrNiMo7-6 quenched in dilatometer and after 60 minutes at 170 °C as a function of carbon content.

sive load are also used to record transformation plastic strains. Depending on the carbon concentration, the tempering-induced changes in length are influenced by the stress state. Figure 3.11 (left) shows this effect as an example for a martensitic-austenitic sample with 0.66 % carbon during a tempering time of 1 h in the dilatometer. After evaluating the raw test data, the transformation plasticity during tempering can be summarized as shown in figure 3.11 (right). For these representations, the measured length of the respective samples at 55 °C in the heating phase of tempering is selected as the reference length.

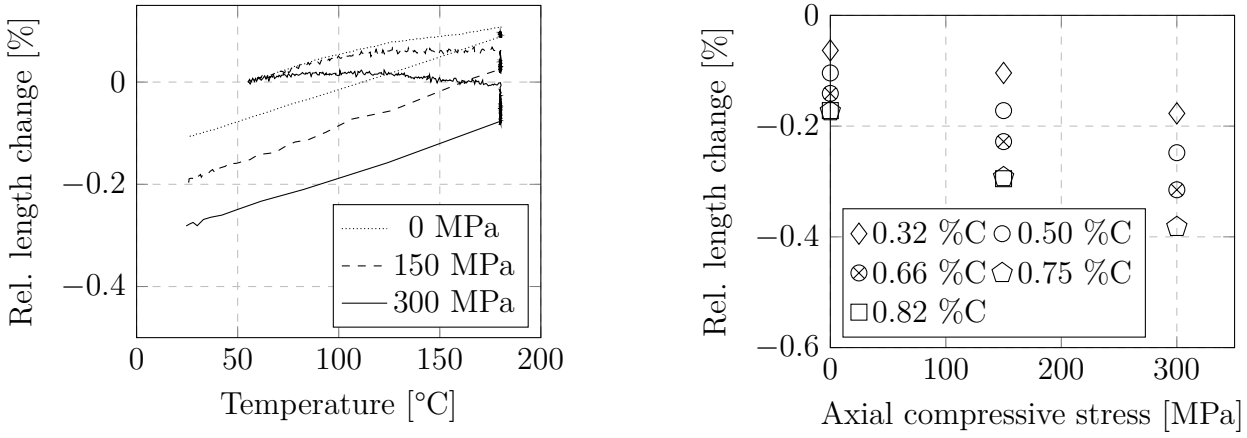


Figure 3.11: Dilatometer curves of carburized 18CrNiMo7-6 samples with 0.66 %C under uni-axial compressive load (left); Measured strains during tempering as a function of compressive stress and carbon concentration (right).

Microsegregation of the sample material

The dilatometer samples exhibit a segregated aspect in the as-delivered state (quenched and tempered microstructure), which can also impact the transformation behavior of the material. Figure 3.12 shows the etched microstructure of a dilatometer sample of the material 18CrNiMo7-6 as supplied (left) and after quenching in the dilatometer, which leads to a mixed bainitic-martensitic microstructure (right). In the image on the right, the dark areas consist mainly of bainite, while high proportions of martensite are found in the light areas. Figure 3.13 provides a more detailed view of these segregated areas. In general, the sequence in which the phase transformations take place during quenching of the samples follows the segregation pattern. Due to small deviations in the local concentrations of carbon and alloying elements such as Cr or Mn, nucleation of phase transition can occur preferentially in certain segregation domains. During bainitic and ferritic transformations of low-carbon steels, carbon atoms are released, which diffuse into the non-transformed microsegregations and thus further delay the phase transformation locally, leading to transformation products that are unequally distributed and follow the segregation pattern. For further explanations on the influence of microsegregations on the transformation behavior of case-hardening steels, reference can be made to the work of Hunkel *et al.* [150, 148].

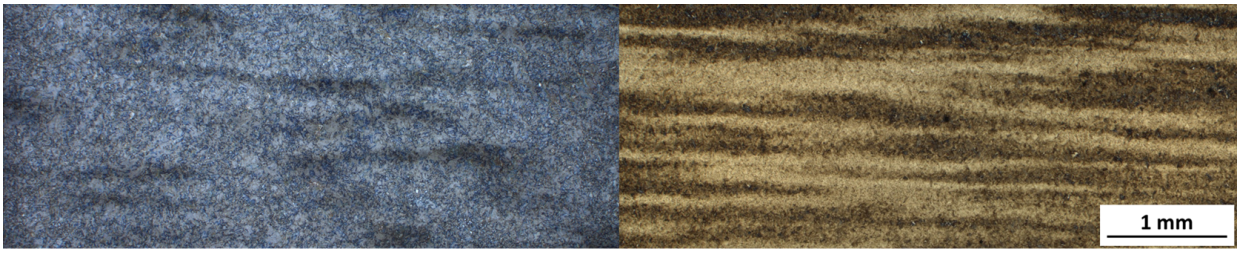


Figure 3.12: Micrograph of the segregation structure of dilatometer samples with 0.18 %C in the as-delivered and etched state (left) and after a bainitic-martensitic transformation in the quenching dilatometer (right).

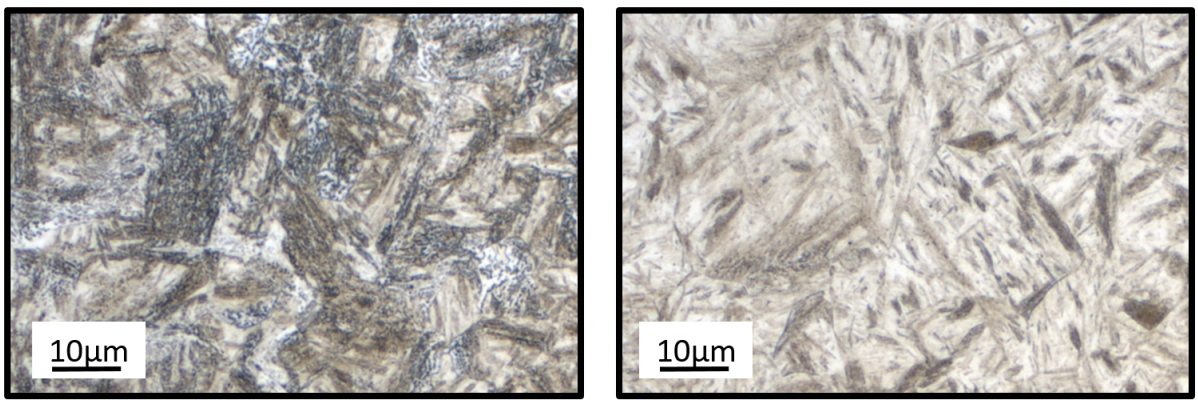


Figure 3.13: Micrograph of the dark (left) and light (right) segregated areas from the heat treated sample in figure 3.12.

In addition to the specific appearance of the segregated steel, residual stresses occur on the micro-scale between the segregation lines during the phase transformations of the samples, as the segregated areas cannot expand freely due to delayed transformation behavior in their direct vicinity. Thus, microstructural transformations can occur under stress during the quenching tests and the observed transformation strains are influenced by transformation plasticity effects. Detailed studies on the characterization and modeling of this material behavior – which is crucial in the context of anisotropic distortion – were carried out by Hunkel *et al.* [151, 152, 150, 148]. In order to avoid misinterpretation of the results due to segregation when determining the microstructure in continuous quenching tests, the evaluation of the transformation strains is systematically matched with the determination of phase fractions using optical microscopy. In order to assess the effects of the orientation of segregation lines on the phase transformations and strains of the material, dilatometer samples of the base material were produced with different main directions. As the transformation strains in quenching dilatometric tests were shown to be similar for all three tested orientation, this supports the modeling assumption of isotropic transformation strains in this material.

3.2. Material modeling

The modeling of the material 18CrNiMo7-6 in carburized and non-carburized states is based on the combination of the material investigations of this work and already available material parameters. The results of the CASH project [130] are used to describe Poisson's ratio and modulus of elasticity, density, thermal conductivity, heat capacity and heat generated by phase transformations. This data is available for 18CrNiMo7-6 as functions of temperature and microstructure with three different carbon concentrations. The material models derived from the combination of available data and own experiments are presented in the following.

3.2.a. Modeling of flow properties

The flow behavior of the material is described by a simple isotropic and strain rate-independent definition of the yield surface with the equivalent stress according to von Mises. The flow curves of each tested combination of microstructure composition and carbon content are defined as a function of temperature. These properties are entered into the FE model in tabular form and determined using linear mixing and interpolation rules at the integration points of the elements. In addition, literature data from the CASH project [128, 130] is used for the flow curves of the ferritic-pearlitic microstructure.

3.2.b. Modeling of transformation behavior

Methods: The transformation behavior of the steel in different carburized and non-carburized states is modeled using equations 2.34 and 3.1. The phase transformation kinetics are modeled using semi-empirical approaches, with equation parameters derived based on dilatometric investigations from section 3.1.b. The phase transformation kinetics is first implemented in MATLAB [153] for flexible calibration and then turned into FORTRAN subroutines for the FE simulation. In equation 2.34, the parameter $\overline{\xi}_M$ corresponds to the austenite content available before the martensite transformation. The martensite start temperature M_S is described by a linear dependence on the carbon concentration according to figure 3.14. The material-dependent parameter b_{KM} is simply set equal to 0.011 based on [135].

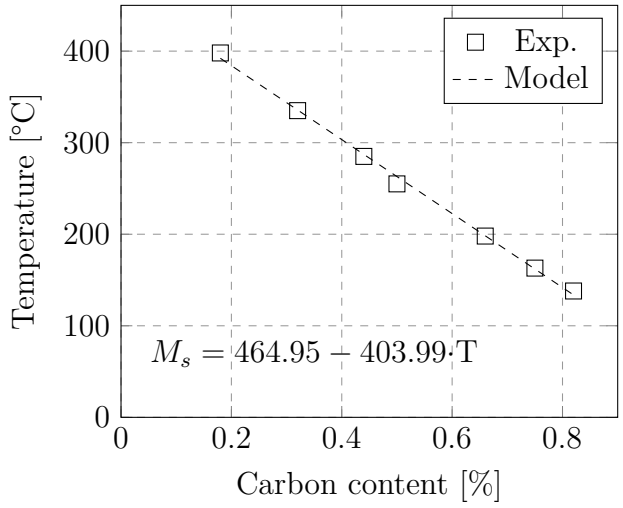


Figure 3.14: Martensite start temperature as a function of carbon content.

A differential method is used to calculate the diffusive phase transformations, which is based on a phenomenological modification of the Johnson-Mehl-Avrami-Kolmogrow equation to account for non-isothermal conditions [132]. The transformed volume phase fractions are calculated incrementally by the following equation 3.1:

$$\dot{\xi}_k = n \cdot \frac{\overline{\xi}_k - \xi_k}{\tau} \cdot \left[\ln\left(\frac{\xi_k}{\overline{\xi}_k - \xi_k}\right)^{\frac{n-1}{n}} \right] \cdot f_k(\dot{T}). \tag{3.1}$$

Equation 3.1 calculates the rate of change of the phase fraction $\dot{\xi}_k$ as a function of the current phase fraction ξ_k. To calculate $\dot{\xi}_k$, the Avrami parameters τ and n are required, which are determined by isothermal experiments. The maximum achievable product phase fractions $\overline{\xi}_k$ are taken from the CASH data set [130] as a function of the carbon content and temperature and interpolated for the missing carbon concentrations. The correction term $f_k(\dot{T})$ to account for the cooling rate is determined by an inverse fit procedure of the experimentally determined transformation kinetics in continuous quenching dilatometer

tests. The enrichment of carbon in the austenite grains due to the precipitation of the bainitic and ferritic phases is taken into account by empirical coefficients, which are defined as a function of phase fractions and cooling rate. All coefficients of the transformation kinetics models are given in the appendix A6. The determination of the transformation processes during quenching of the material is carried out until room temperature is reached according to the flow diagram in figure 3.15.

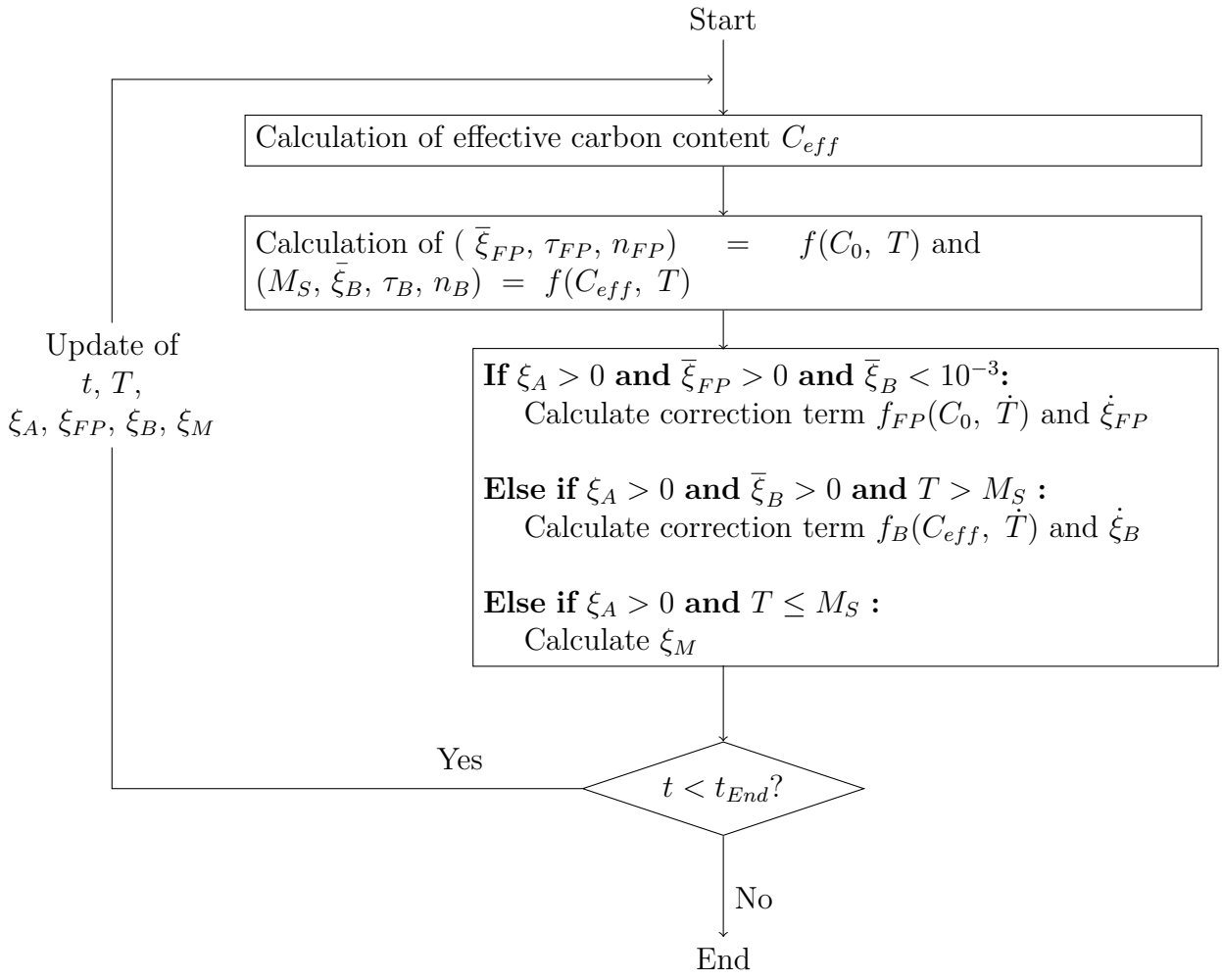


Figure 3.15: Schematic sequence of the calculation of phase transformations during quenching in the FE model.

The effective carbon content C_{eff} is calculated empirically according to the equation 3.2 as a function of the nominal carbon content C_0 and is used to improve the agreement between the experimental results in section 3.1.b and the predicted phase transformations. According to the determined transformation behavior of the low-carbon samples, the effective carbon content increases with increasing proportions of ferrite and bainite that is already formed:

$$C_{eff} = \frac{C_0}{1 - k_{FP} \cdot \xi_{FP} - k_B \cdot \xi_B}. \tag{3.2}$$

The effective carbon content is used to calculate the martensite start temperature M_S ac-

cording to figure 3.14, the transformation parameters $\overline{\xi}_B$, τ_B and n_B and the correction term $f_B(\dot{T})$. The parameters for ferrite/pearlite phase transformation τ_{FP}, n_{FP}, $\overline{\xi}_{FP}$ and $f_{FP}(\dot{T})$ are determined using the nominal carbon concentration C_0. The complete description of the kinetics model and the model parameters are available in the appendix A6. The model described above can be used to calculate the phase transformation kinetics of the case-hardening steel as a function of the cooling conditions and the carbon concentration. The model parameters are determined on the basis of the test data from 3.1.b.

Results: The accuracy of the simulation model is evaluated by comparing the calculated microstructure volume fractions and the experimentally determined data as shown in figure 3.16. In general, the phase transformation model achieves very good agreement with the existing experimental data and reproduces the main influences well. For carbon concentrations above approximately 0.66 %C, bainite formation is underestimated in the model. However, these deviations should not be considered critical. The carbon-rich regions in gear teeth are located exclusively near the surface, which correspond to rapid cooling conditions (left in the diagram). Thus, the prediction accuracy for bainitic transformation in high carbon materials is mostly irrelevant for application in carburized gears.

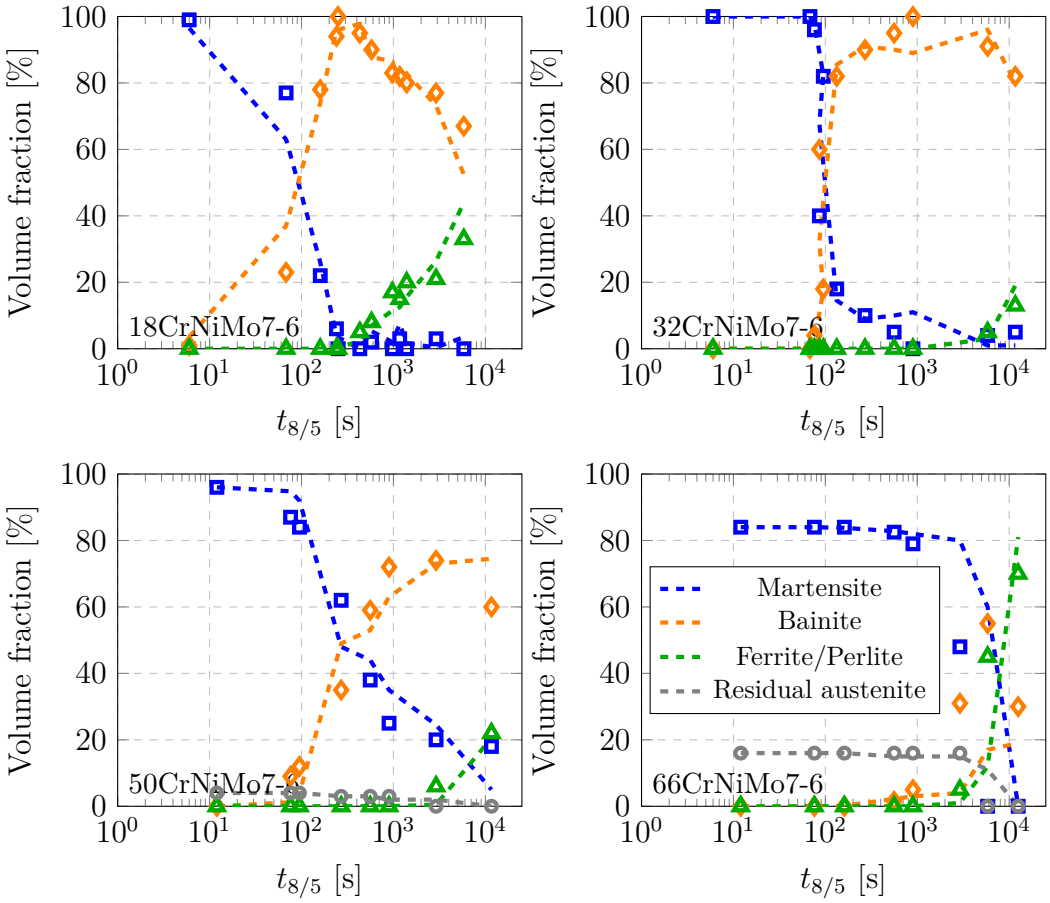


Figure 3.16: Comparison of the simulated volume fractions (dashed lines) with the experimentally determined microstructure (data points) for the steel 18CrNiMo7-6 as a function of the cooling conditions and for different carbon concentrations.

3.2.c. Modeling of thermal expansion and transformation strains

Methods: Based on the experimental data from 3.1.b, equations are set up to describe the thermal expansion coefficients and the transformation strains and are provided in the appendix A7. The carbon dependence of these parameters is fitted by polynomial functions. With these characteristic values, the strains in the material induced by the temperature changes and by the phase transformations can be calculated for a mixed microstructure of the phases k using the equation 3.3:

$$d\epsilon_{ii}^{th} = \sum_k (\alpha_k \cdot dT \cdot \xi_k + b_k \cdot d\xi_k). \tag{3.3}$$

$d\epsilon_{ii}^{th}$ is the strain increment due to thermal expansion and phase transformations, α_k and b_k are the thermal expansion coefficient and the transformation strains of the phase k as described in figure 3.4. ξ_k represents the volume fraction of phase k and dT is the temperature increment.

By linking the previously detailed phase transformation model with equation 3.3, the thermal and transformation-related strains of the material can be calculated under any

cooling conditions. The simulation model of the material can be validated by comparing the predicted strains and the experimental length changes obtained from dilatometer tests in 3.1.b.

Results: Figure 3.17 shows the comparison between predicted and measured length change of dilatometer samples for two selected cooling curves and different carbon contents.

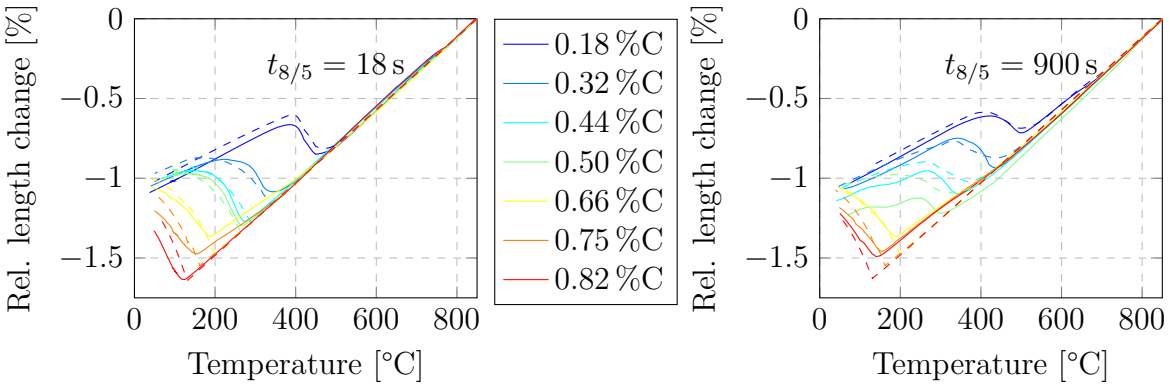


Figure 3.17: Comparison between simulated (dashed lines) and experimentally determined (solid lines) dilatometer curves of differently carburized 18CrNiMo7-6 samples under varying cooling conditions.

Overall, a high level of agreement is achieved. The experimentally determined trends can be reproduced well by the simulation model, both quantitatively and qualitatively.

Modeling of transformation-induced plasticity

Methods: To model the plastic strains that occur during phase transformations without exceeding the yield point, Leblond's approach [154] is used. In this approach, the strain increment induced by transformation plasticity under multi-axial stresses for the phase k is calculated following equation 3.4:

$$d\epsilon_{ij}^{tp} = -K_k^{tp} \cdot S_{ij} \cdot \dot{\xi}_k \cdot \ln(\xi_k). \tag{3.4}$$

S_{ij} is the component in position i, j of the deviatoric stress tensor and K_k^{tp} is a material parameter describing the roughly proportional relationship between stresses and TRIP-strains for the transformation of austenite into phase k. In this work, K_k^{tp} is defined as dependent on the carbon content for martensite and bainite phase transformation, whereas the transformation plasticity of ferritic-pearlitic transition is not considered. For high carbon contents, the proportionality factor for modeling the transformation plasticity in martensitic transformation is determined inversely with the calculation model, since the phase transformation does not take place completely and thus the factor must be adjusted with the actually transformed fraction.

Results: The transformation plasticity can be described with the equation 3.4. For instance, figure 3.18 shows the calculated changes in length in a dilatometer sample due to martensite transformation under different axial compressive loads and two selected carbon concentrations. The transformation plasticity for incomplete martensitic transformations

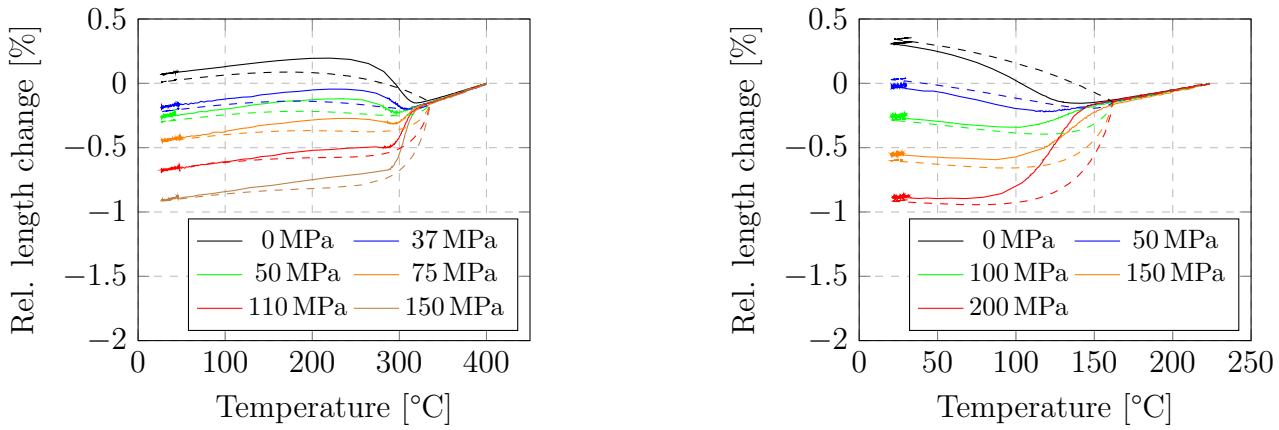


Figure 3.18: Comparison between simulated (dashed lines) and experimentally determined (solid lines) relative length changes due to transformation plasticity during martensite transformation under uni-axial compressive loading for carbon contents of 0.32 %C (left) and 0.75 %C (right).

is determined by adjusting the factor K^{tp}_{mart} in equation 3.4 to match the simulated transformation plastic strains with the experimental data. For the bainitic transformation, the transformation plasticity factors are derived directly from the experimental data from section 3.7. Figure 3.19 shows the evaluated carbon-dependent curves of the transformation plasticity constants. The equations used to model the transformation plasticity factors are available in appendix A7.

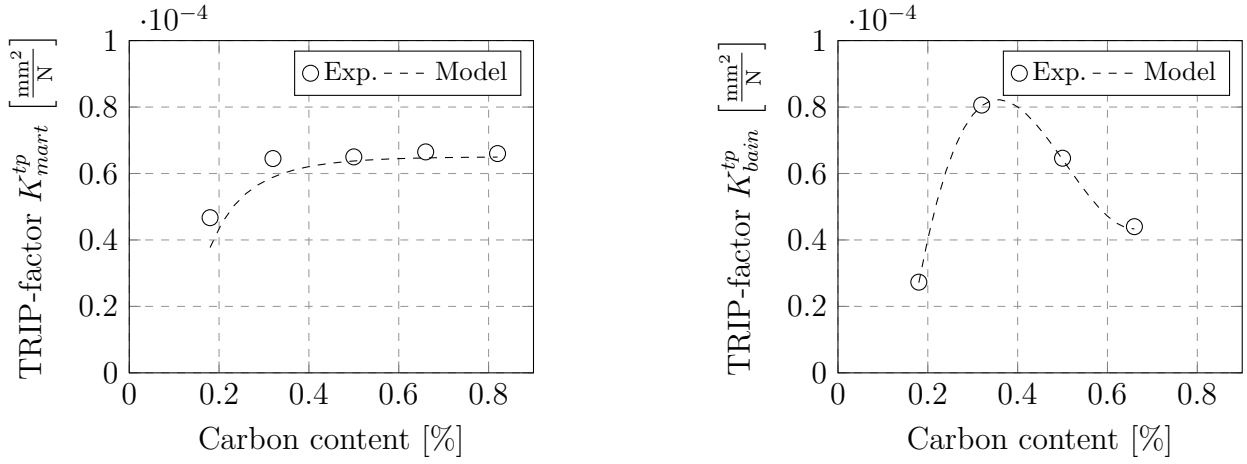


Figure 3.19: Carbon dependent transformation plasticity factors determined by experiment for martensitic (left) and bainitic (right) transformation. The dashed lines represent the model equations used in the FE model.

Table 3.2: Hardness values of bainite and ferrite-pearlite from [128, 130] used in the simulation model.

Bainite						
Carbon content [%]	0.18		0.50		0.80	
Transformation temperature [°C]	425	550	300	450	300	500
Hardness [H_{V1}]	340	300	504	229	529	319
Ferrite-Pearlite						
Carbon content [%]	0.18		0.50		0.80	
Transformation temperature [°C]	550	700	450	650	500	650
Hardness [H_{V1}]	224	155	448	283	434	292

3.2.d. Hardness model

Based on the predicted phase transformations, the hardness of the bainite and ferrite-pearlite phases is determined during the heat treatment as a function of the formation temperature and carbon content. The hardness model is based on hardness measurements of materials with three separate carbon contents that were obtained in [128, 130], where samples underwent isothermal transformations at varying temperatures. Based on the data in table 3.2, the hardness is linearly interpolated with respect to the transformation temperature and then to the carbon content. Conversely, the hardness of martensite is predicted based on own measurements from section 3.1.d and as a function of carbon concentration only. In order to consider materials with a mixed microstructure, a linear mixture rule is applied using the phase fraction and the calculated phase-specific hardness. Overall, the hardness model can be written as follows:

$$\begin{aligned} H_V^{total} &= \sum_k (\xi_k \cdot H_{V,k}) \\ &= H_{V,A} \cdot \xi_A + H_{V,M}(C_0) \cdot \xi_M + \sum_i (\Delta\xi_B^i \cdot H_{V,B}^i(C_0, T_i)) + \sum_j (\Delta\xi_{FP}^j \cdot H_{V,FP}^j(C_0, T_j)). \end{aligned} \tag{3.5}$$

With $H_{V,A} = 280\,\mathrm{H_V}$ and $H_{V,M}(C_0)$ from figure 3.10. $\Delta\xi_B^i$ is the volumic phase fraction of bainite that is transformed at the temperature T_i and corresponds to a hardness at room temperature $H_{V,B}^i(C_0, T_i)$ derived from table 3.2, while $\Delta\xi_{FP}^j$ and $H_{V,FP}^j(C_0, T_j)$ are defined in a similar manner for ferrite/pearlite.

3.2.e. Modeling of tempering effects

Methods: Although the tempering step influences the residual stresses in heat treated gears, only very few results and modeling approaches for tempering carburized and quenched steels are available so far. In this work, the experimentally determined volume reduction of the dilatometer specimens during tempering at 170 °C of carburized martensitic speci-

mens is empirically modeled. A simplified model is proposed which describes the tempering process by means of a tempering variable X and equivalent thermal and *transformation* strains. This tempering variable runs between 0 and 1 and is calculated as a function of the tempering time and the volume fractions of martensite and residual austenite. Figure 3.20 schematically shows the experimentally determined course of the proposed tempering variable. The evolution of X is derived similar to figure 3.3 by comparing the relative distance of measured strain with the linear fitting line obtained in the length change *vs* temperature plot both in the low-temperature range upon heating and with the linear fitting upon cooling down from tempering temperature. Based on this variable, the strain induced by tempering in the material can be calculated as in equation 3.6:

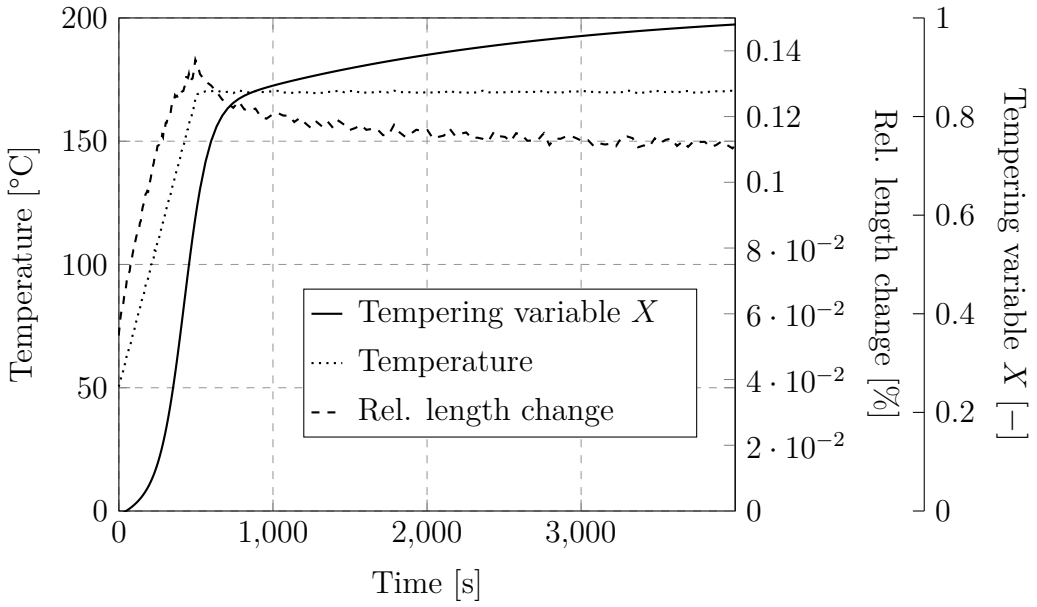


Figure 3.20: Schematic diagram of the variable describing the tempering process based on dilatometric data.

$$d\epsilon_{ii}^{th} = (\alpha_2 \cdot X - \alpha_1 \cdot X + \alpha_1) \cdot dT + ((\alpha_2 - \alpha_1) \cdot T + b_2 - b_1) \cdot X. \tag{3.6}$$

The parameters α_1 and b_1 describe the characteristic expansion coefficients and strains of the as-quenched mixed microstructure and are determined on the basis of the phase transformations calculated up to tempering. The characteristic values α_2 and b_2 are determined as a function of carbon on the basis of tempering tests of martensitic-austenitic samples and are given in the appendix A7.

Similar to quenching, carbon concentration-dependent transformation plastic strains are observed during tempering: the tempering-induced strains are influenced by the applied stress state. This mechanism is reported in the literature only very sporadically and almost exclusively from the experimental side [155, 48]. In this work, TRIP-strains during tempering are modeled analogously to the transformation plasticity during quenching. For this

purpose, as in equation 3.4, the transformation-induced plastic strain increments $d\epsilon_{ij}^{tp}$ are calculated proportional to the deviatoric part of the stress tensor, with a definition of the proportionality constant as a function of the carbon concentration. Here, the tempering variable X is used instead of a transformed volume fraction of the phase k, ξ_k:

$$d\epsilon_{ij}^{tp} = -K_{temp}^{tp} \cdot S_{ij} \cdot \dot{X} \cdot \ln(X). \tag{3.7}$$

The TRIP-strains during tempering for all carbon contents are modeled using a value of $K_{temp}^{tp} = 3.2 \cdot 10^{-6}\,\mathrm{MPa}^{-1}$, which could be found for carbon concentrations above 0.5 %C.

Based on the experimental results from section 3.1.d, the variations of hardness due to tempering are modeled through a simple empirical relationship between the hardness of martensite in quenched state $H_{V,m,quen}$ and its hardness after tempering:

$$H_{V,m,temp} = 1.936 \cdot {H_{V,m,quen}}^{0.8911}. \tag{3.8}$$

Results: Based on the measurement data from the chapter 3.1.d and the modeling approaches detailed previously, a prediction of the tempering-induced strains in the material as a function of the carbon content is made possible. In figure 3.21, the simulation results for the tempering-induced strains during a tempering process of one hour at 170 °C are compared with the experimental data from dilatometer investigations for three selected carbon contents.

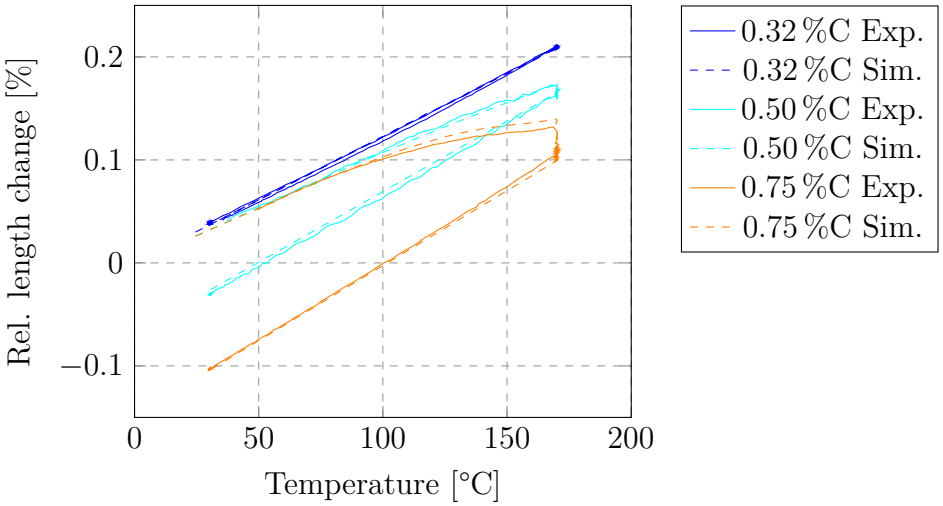


Figure 3.21: Comparison between selected simulated (dashed lines) and experimentally determined (solid lines) strains induced by tempering for 1 hour at 170 °C of differently carburized martensitic-austenitic 18CrNiMo7-6 dilatometer samples.

The experimental strains during the selected tempering process can be reproduced very accurately by the material model. The modeling of the tempering behavior is based on a tempering variable that is defined as a direct function of the time during the tempering

step. Accordingly, large variations in the tempering process conditions can't be simulated with this material model without the need to recalibrate the time evolution of the tempering variable. The time dependence in this modeling approach aims to represent the changes in length in material samples rather than for an exact calculation of the kinetics of microstructure changes in tempered components. For the calculation of residual stresses in case-hardened gears, it is assumed that the process time is sufficient to reach a stationary state in the whole model at the tempering temperature.

Modeling the material behavior of case hardening steel obviously requires a significant amount of material data and modeling parameters. This paragraph summarizes the origin of the various variables involved. All material data presented in section 3.1 were obtained by the author's own investigations. On the other hand, the simulation model also incorporates material parameters for temperature-dependent density, heat capacity, thermal conductivity, Young's modulus and heat of phase transformations that are obtained from the CASH project [128, 130]. The flow curves of ferrite/pearlite, the temperature-dependent maximum achievable phase fractions of the ferritic and bainitic phases in the kinetic model, and the hardness values for ferrite/pearlite and bainite were also taken from this cited work.

Chapter 4

Finite-element prediction of residual stress in carburized gears

Gears with varying sizes, quenching media, and carbon depth profiles were subjected to various heat treatment procedures in order to obtain the process data needed to verify the calculation models. The validation data originates from the research project FVA 835 I [47]. The gears were carburized, quenched and tempered. Measurements of residual stress depth and hardness were performed on the tooth flanks up to a depth that exceeds CHD. Optical emission spectroscopy (OES) was used to determine the carbon depth profiles. Selected gears were subjected to temperature measurements during the quenching process.

Multiple variations were investigated to evaluate the effect of specific parameters on the residual stresses in carburized gears. Two geometries that encompass a wide range of gear sizes were examined. The first is a 3 mm module gear with 69 teeth that was already extensively utilized in investigations related to tooth flank fracture [78, 34, 46]. The second geometry is a larger gear, which has already been studied in research project FVA 501 [132]. It has 24 teeth and a module of 18 mm.

The first set of three gears with a 3 mm module was not carburized but used in conjunction with thermocouples to monitor the cooling rates corresponding to different quenching media. Then, using a reference *sigmoidal* carbon depth profile, three more gears with the same geometry – V2-1, V2-2 and V2-3 – were gas carburized and quenched in an oil bath, polymer bath or salt bath. The series V3-gears were vacuum carburized and quenched using nitrogen gas at high pressure. Though it was carburized differently, gear V3-1 was intended to replicate the carbon depth profile of the gears in the V2-series. Experiments V3-2 and V3-3 were designed to determine the impact of varying carbon surface concentration on the residual stress state. A carbon depth profile with an overall lower gradient and slightly higher total carburized depth, but with a similar CHD, was obtained in the gear V3-4. For gears with an 18 mm module, comparable CHDs were targeted and quenching medium modifications were examined. A salt bath at 170 °C, an aqueous polymer solution bath and two distinct commercially available oil baths were used. Table 4.1 summarizes the experimental campaign conducted on gears.

Leibniz IWT in Bremen carried out the heat treatment of the gears with module 3 mm. The 18 mm module gears underwent heat treatment at the industrial carburizing and hardening facilities of partner companies in project FVA 835 I. Measurements of residual stress,

Table 4.1: Experimental heat treatment tests on gears.

Name	Module [mm]	Carbon depth profile	Targeted CHD [mm]	Carburizing	Quenching medium
V1-1	3	/	/	/	Oil bath
V1-2	3	/	/	/	Polymer bath
V1-3	3	/	/	/	Salt bath
V2-1	3	*sigmoidal*	0.5 - 0.7	Gas carburizing	Oil bath
V2-2	3	*sigmoidal*	0.5 - 0.7	Gas carburizing	Polymer bath
V2-3	3	*sigmoidal*	0.5 - 0.7	Gas carburizing	Salt bath
V3-1	3	*sigmoidal*	0.5 - 0.7	Low pressure	High-pressure Nitrogen gas
V3-2	3	Reduced surface concentration	0.5 - 0.7	Low pressure	High-pressure Nitrogen gas
V3-3	3	Increased surface concentration	0.5 - 0.7	Low pressure	High-pressure Nitrogen gas
V3-4	3	Flat runout after CHD	0.5 - 0.7	Low pressure	High-pressure Nitrogen gas
V4-1	18	*sigmoidal*	3.0 - 3.5	Gas carburizing	Oil bath - Marquench 875 (90 °C)
V4-2	18	*sigmoidal*	3.0 - 3.5	Gas carburizing	Polymer bath - Aquacool AC (15 %, 40 °C)
V4-3	18	*sigmoidal*	3.0 - 3.5	Gas carburizing	Oil bath - Isorapid 280 HM (50 °C)
V4-4	18	*sigmoidal*	3.0 - 3.5	Gas carburizing	Salt bath - AS135 (170 °C)

carbon depth profiles and hardness depth profiles were carried out at Leibniz IWT in Bremen. Since the experimental tests were conducted as a part of the research project FVA 835 I [47], the reader may consult the corresponding report for a more thorough explanation of the procedures followed and the outcomes of the experiments.

4.1. Methods

The FE simulation model results from the coupling of thermal, metallurgical and mechanical fields. The calculation of the residual stresses is based on the additivity of the strain components, which is described by equation 2.32 for small deformations and neglecting creep strains. The material modeling described in section 3 is transferred to a simulation model for the case-hardening of gears. This FE model takes as input information the gear geometry, the carbon depth profile and the quenching and tempering conditions. The results provided include the microstructure and the time- and spatially-resolved residual

stress state. The software Abaqus 2020 [156] is used for the simulation. The built-in FE solver is supplemented with user-defined subroutines that describe the material behavior in the form of FORTRAN commands.

The thermal-mechanical-metallurgical simulation is carried out by successively performing carburizing simulation, quenching simulation and tempering simulation. The main modeling steps are described below. From preliminary work, the prerequisites for successful simulation of the residual stress state were determined. For example, it was observed that two-dimensional (2D) modeling with the assumption of a plane strain state is satisfactory for the consideration of tangential residual stresses in case-hardened gears. However, it was shown that the deviations in the calculated stress values in the axial direction between 2D and 3D modeling are not negligible. Therefore, a design of experiments (DoE) has been set up in which the influencing factors of gear module, tooth shape, case hardening depth, quenching medium and the carbon depth profile were modeled using three-dimensional heat treatment simulations.

The simulative investigation of residual stresses is divided in two parts. First, a simplified cylindrical geometry is analyzed in order to test the model, identify some trends in the dependence of residual stresses in carburized components on the influencing factors and assess the validity of some basic principles on residual stress distribution.

For this purpose, variations of the geometrical features of hollow cylinders such as the outer diameter, inner diameter and height are investigated. Different carbon depth profiles are used to vary the CHD. Because of the simple geometry and subsequently moderate computational effort, a large number of simulations could be included in the Design of Experiment, enabling the identification of some of the interactions between influencing parameters and the outcomes of carburizing heat treatment. The examined configurations for the cylindrical geometry are summarized in table 4.2.

Secondly, the simulation model for carburizing heat treatment is validated by comparing the microstructure, hardness and residual stresses computed for different gear shapes and process parameters with the experimental data. Along with different geometries, the numerical study includes variations of the CHD. The gears that have been studied are given in table 4.3, where z represents the number of teeth, a is the center distance and m the normal module. Geometry of gears with 18 and 41 teeth are obtained from the works of [103] and [157], respectively.

4.1.a. Geometry

Three-dimensional geometry data of the gears is imported into the Abaqus software environment. The gear symmetries are modeled to minimize the computational time and effort required for the 3D simulations. For each shape, just half of a tooth segment is represented. It is assumed implicitly that the cooling conditions rely entirely on the gear's axial and ra-

Table 4.2: DoE for hollow cylindrical samples, with variations of the inner and outer diameters D_i and D_o, the height H and the case hardness depth CHD.

No.	D_o [mm]	D_i [mm]	$\frac{D_o}{D_i}$	H [mm]	$\frac{D_o}{H}$	CHD [mm]	$\frac{D_o}{\text{CHD}}$
1	300	171	1.75	100	3	1.2	250
2	300	171	1.75	100	3	1.875	160
3	300	171	1.75	100	3	2.5	120
4	300	171	1.75	100	3	3.75	80
5	300	171	1.75	100	3	5	60
6	300	240	1.25	100	3	2.5	120
7	300	200	1.5	100	3	2.5	120
8	300	120	2.5	100	3	2.5	120
9	300	75	4	100	3	2.5	120
10	300	171	1.75	600	0.5	2.5	120
11	300	171	1.75	300	1	2.5	120
12	300	171	1.75	50	6	2.5	120
13	300	171	1.75	30	10	2.5	120
14	50	29	1.75	17	3	0.20	250
15	50	29	1.75	17	3	0.31	160
16	50	29	1.75	17	3	0.42	120
17	50	29	1.75	17	3	0.63	80
18	50	29	1.75	17	3	0.83	60
19	50	40	1.25	17	3	0.42	120
20	50	12	4	17	3	0.42	120
21	50	29	1.75	100	0.5	0.42	120
22	50	29	1.75	5	10	0.42	120
23	175	100	1.75	58	3	0.70	250
24	175	100	1.75	58	3	1.46	120
25	175	100	1.75	58	3	2.92	60
26	425	243	1.75	142	3	1.70	250
27	425	243	1.75	142	3	3.54	120
28	425	243	1.75	142	3	7.08	60
29	550	314	1.75	183	3	2.20	250
30	550	314	1.75	183	3	3.4	160
31	550	314	1.75	183	3	4.58	120
32	550	314	1.75	183	3	6.88	80
33	550	314	1.75	183	3	9.17	60
34	550	440	1.25	183	3	4.58	120
35	550	138	4	183	3	4.58	120
36	550	314	1.75	1100	0.5	4.58	120
37	550	314	1.75	55	10	4.58	120

Table 4.3: DoE for gear heat treatment.

z	a [mm]	m_n [mm]	No.	CHD [mm]	Carbon depth profile	Quenching medium	Experiment
69	200	3	1	0.5	*sigmoidal*	Oil bath	V2-1
			2	0.3	*sigmoidal*	Oil bath	/
			3	0.4	*sigmoidal*	Oil bath	/
			4	0.6	*sigmoidal*	Oil bath	/
			5	0.7	*sigmoidal*	Oil bath	/
			6	0.5	*sigmoidal*	Salt bath	V2-3
			7	0.5	*sigmoidal*	Polymer bath	V2-2
			8	0.64	*sigmoidal*	Gas	V3-1
			9	0.6	Flat runout after CHD	Gas	V3-4
			10	0.65	Reduced surface concentration	Gas	V3-2
			11	0.65	Increased surface concentration	Gas	V3-3
			12	0.15	*sigmoidal*	Oil bath	/
			13	1.2	*sigmoidal*	Oil bath	/
24	478	18	14	3.26	*sigmoidal*	Oil bath	V4-1
			15	3.42	*sigmoidal*	Oil bath	V4-3
			16	1.8	*sigmoidal*	Oil bath	/
			17	4.8	*sigmoidal*	Oil bath	/
			18	3.28	*sigmoidal*	Salt bath	V4-4
			19	2.56	*sigmoidal*	Polymer bath	V4-2
41	200	5	20	0.65	*sigmoidal*	Oil bath	/
			21	1.5	*sigmoidal*	Oil bath	/
18	91.5	5	22	0.5	*sigmoidal*	Oil bath	/
			23	0.9	*sigmoidal*	Oil bath	/
			24	1.25	*sigmoidal*	Oil bath	/

dial positions. It would be sufficient to simulate just 25 % of a tooth segment for the heat treatment process. Here, however, the simulation models are then either utilized to calculate the fatigue characteristics of the gear under service and test loads, or they are used to calculate the impacts of material layer removal on residual stresses, as in X-ray based measurement. For the carburizing heat treatment simulations on cylindrical samples, an angular section equal to 5 ° is modeled and the symmetry with respect to the central plane orthogonal to the cylinder's axis is employed.

4.1.b. Model set up

Mechanical boundary conditions: The mechanical boundary conditions are derived from the specified symmetry conditions for a half tooth segment. In a cylindrical coordinate system fixed on the center of the gear or cylinder, the displacements of the lateral boundary planes are blocked in the tangential direction (see figure 4.1). The axial displacements are set to zero for the axial symmetry plane. Similar mechanical boundary conditions are applied to the cylinder segment models.

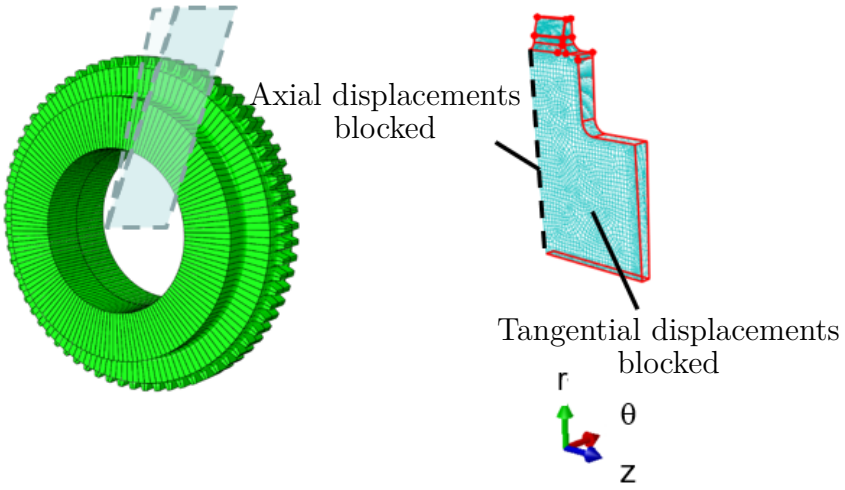


Figure 4.1: Definition of the mechanical boundary conditions for the heat treatment simulation of gears, shown schematically for a gear with module 3 mm and 69 teeth.

Carbon depth profile: This work does not primarily focus on simulating carbon diffusion, although the carbon profile has a significant impact on the residual stresses after quenching. Here, the required carbon profiles and case hardening depths on complex 3D gear geometries are generated using a simple gas carburization model. A two-stage procedure with different carbon potentials is used in the simulation. Carbon potentials, step duration and process temperatures are all fictitious and calculated iteratively in order to produce the targeted carbon depth profile. Here, complex factors like cementite precipitation are not taken into account. When carbon concentrations for the simulated configurations were measured experimentally, the model parameters are tuned to ensure agreement.

Furthermore, all external surfaces have the same carburization parameters. The carbon depth profile of the tooth's front and rear sides, or the inner hole of the cylinder, for example, is thus similar to that of the functional surfaces, with the exception of variations resulting from the different radii of curvature.

Thermal boundary conditions: As in the heat treatment experiments, 850 °C is chosen as the hardening temperature. Temperature-dependent heat transfer coefficients (HTCs) on the exterior component surface and within the central hole are introduced to define the quenching conditions. To determine these HTCs, available work – as for example in project FVA 501 III [132] – is used. On the quenched surface, the HTCs are assumed to be homogeneous. One notable exception is high-pressure gas cooling, for which a position-dependent description of heat transfer coefficients from [158] is assumed. An iterative procedure is used to match the temperature curves between simulation and experiment with the heat transfer values from the literature if experimental temperature curves are available, as in the case of the gears module 3 mm and module 18 mm. Until an acceptable agreement with the experimental temperature data is attained, the heat transfer coefficients from the literature on the inner and outer surfaces of the gear are multiplied by adjustment factors. Appendix A8 provides specific values of the HTCs that were utilized in the simulation model. A tempering process is modeled after quenching. For the simulation of tempering, a holding duration of 1 h was chosen since length variations were only seen within the first hour of tempering dilatometer samples. Homogeneous temperature conditions are also assumed for all gears during tempering, for the sake of simplification.

Meshing: The convergence and accuracy of the residual stress simulation are shown to be critically dependent on an accurate description of the carbon gradient in the near-surface area of the gears. Consequently, the meshing is produced on the corresponding geometries in a manner that significantly reduces the element size near the carburized surface. The overall number of finite elements in the 3D models is calculated by balancing simulation accuracy with computing time. While the meshing of some geometric features necessitates the extra usage of tetrahedral and wedge elements, C3D4T and C3D6T, respectively, hexahedral 8-node trilinear displacement and temperature elements, C3D8T, are used preferentially. The total number of integration points ranges from 90,000 for the cylindrical samples to 850,000 for gear models.

4.1.c. Evaluation of the simulation results

Extensive temporally and spatially resolved data for temperature, microstructure development and residual stress tensors are produced by the heat treatment simulation. Only the residual stress components along specific paths perpendicular to the component surface are consistently documented in order to maintain this work's clarity. Only the residual stresses in the main directions with regards to the paths are systematically provided because the

shear stress components are typically low.

On the cylindrical geometry, two paths are investigated. The first path *path 1* runs from the outer diameter to the inner diameter of the hollow cylinder. The path direction is indicated by the black arrow in figure 4.2 left, while the tangential and the axial direction vectors are described by a red and a green arrow, respectively. In contrast, *path 2* runs from the middle point of the front side of the cylinder up to the axial symmetry plane and parallel to its main axis. Directions described as tangential and axial to this path are indicated by red and green arrows, respectively. It should be noted that the terms *normal*, *tangential* and *axial* in the local coordinate system relate to the component surface being investigated as well as the direction of the path. For *path 1*, they also correspond to the directions *radial* (inwards), *tangential* and *axial* of a global cylindrical coordinate system positioned at the center of the hollow cylinder. However, for *path 2*, the *axial* direction does not coincide with the cylinder's main axis.

Similar descriptions are used in the post-processing of simulation results on gears. Four paths are used here, as displayed in figure 4.2 right. The first three paths belong to the axial symmetry plane of the gear and run perpendicular to the flank surface, while the position of the starting points differs. *Path 1* initiates at the pitch point, while the second and third paths start at tooth height of $\frac{1}{4}$ and $\frac{3}{4}$, respectively. Directions referred as tangential and axial to these paths are described with red and green arrows, respectively. In contrast, *path 4* runs from the point at half tooth height on the front side of the tooth and runs up to the axial symmetry plane and parallel to its main axis. The local coordinate system's directions here also refer to the direction of the path and of the flank surface that is being studied. They may not consistently correspond to the *radial*, *tangential*, and *axial* directions in a global cylindrical coordinate system that is positioned at the gear's center.

4.1.d. Correction of calculated residual stresses for comparison with measurement results

Stress redistribution occurs concurrently with material removal, which is required for X-ray measurements of the residual stresses beneath the component surface. High volume of removed material and high stress magnitudes in the removed material cause the most significant modifications of residual stress distribution. Additionally, the mass moment of inertia of the component affects the impact of material removal. The subsequent correction of residual stress values is thus essential for a meaningful evaluation of measurements that require the removal of a relatively high volume of material or of a part with high residual stresses [159]. Through integration over the residual stresses removed, the measurement correction may be found analytically for simple sample geometries and stress distributions. The method suggested by SAE HS-784 (2003) [160] can be used as an example and is based on Moore and Evans' procedure. The residual stresses that truly exist in the component

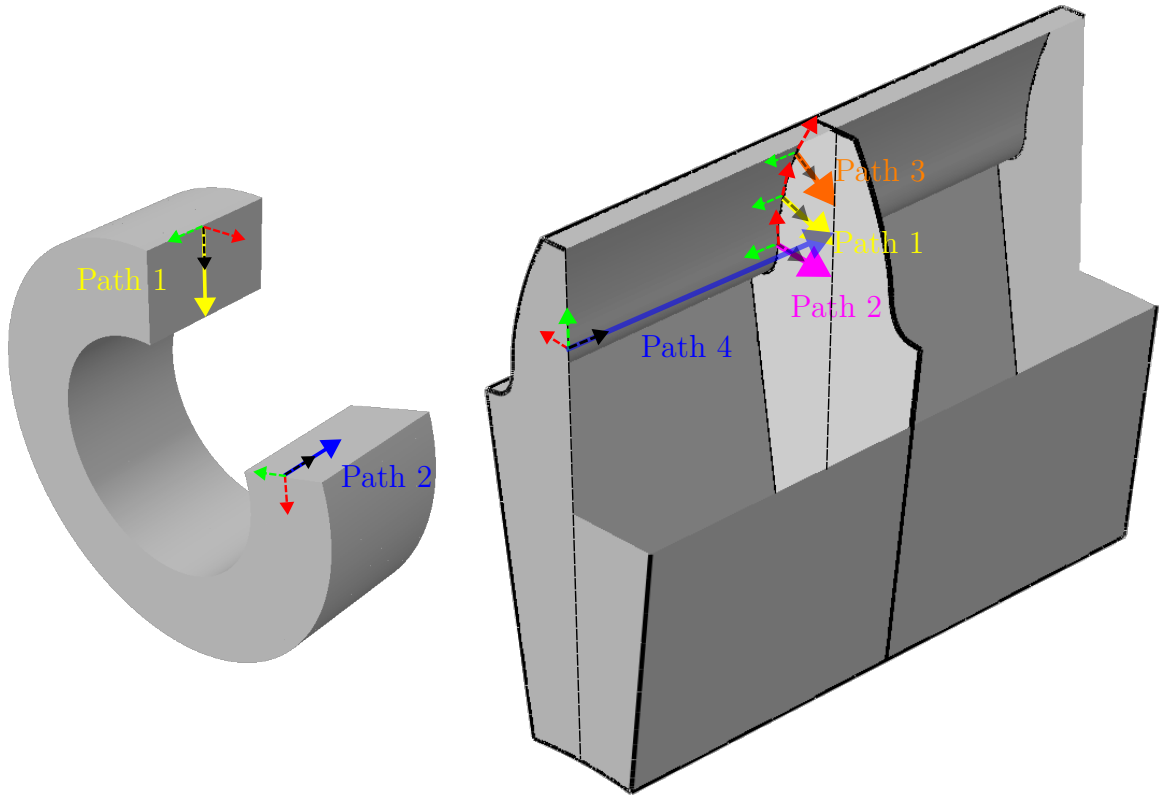


Figure 4.2: Definition of paths and local coordinate systems for hollow cylinder (left) and gear simulation models (right). The directions indicated by black, red and green arrows are referred as normal, tangential and axial with respect to the considered path, respectively.

in direction j at depth $H - z_i$ for a plate geometry with thickness H can be computed using equation 4.1, based on the measured residual stress values $\sigma_{j,m}$. It is assumed that the residual stresses in the plate – except at the side edges – only depend on the distance to the surface:

$$\sigma_j(z_i) \;=\; \sigma_{j,m}(z_i) + 2 \;\int_{z_i}^{H} \frac{\sigma_{j,m}(z)}{z}\, dz - 6 \; z_i \;\int_{z_i}^{H} \frac{\sigma_{j,m}(z)}{z^2}\; dz. \tag{4.1}$$

However, an analytical solution may only provide adequate correction of X-ray residual stress data for very simple geometries, which are rare in practice. In his work, Weber [46] assumes an analogous plate shape for the residual stress measurement on the tooth flank of a gear with module 3 mm, and then assesses the stress redistribution resulting from material removal with Moore & Evans' method. Still, the fundamental geometric assumptions of this method are difficult to verify. Alternative techniques are required for intricate component and removal geometries or when the position to measure requires cut operations on the component before measurement. A finite element based technique is more appropriate than analytical approaches, in order to account for stress relaxations associated to complex geometry [161, 162]. For this approach, a FE model of the component geometry is set up with a virtual residual stress field. The material is removed via stepwise deactivation of elements, with the removal geometry approximated as accurately as possible. Using the FE solver to calculate the new stress equilibrium yields the stress redistribution. This approach makes the assumptions that no new stresses are created by the material removal and that the stress relaxation is elastic. Furthermore, initial residual stresses inside a removed layer are assumed to be homogeneous. Reliability in the calculation of stress relaxation also depends on the assumption of a FE mesh resolution fine enough in the direction of material removal, such that the residual stress variations between two measurement locations may be considered linear. These assumptions are typically considered to hold in real measurements with limited removed volumes [46].

Consequently, a correction of the measured values is applied here to account for the material removal, rather than a direct comparison between the simulated and measured values. Using an analogous plate shape, the impact of material removal on the remaining stresses in the tooth is computed with the method of Moore & Evans (see figure 4.3 on the right) and formula 4.1. The integration is carried out in Matlab [153], where spline curves are used for numerical integration of the discrete measured residual stresses. FE models are used in a second approach to correct measured residual stress data. Layer by layer, the elements of the removed volume are eliminated after the heat treatment simulation and the new stress equilibrium is computed (see figure 4.3 on the left for an example of this process). The residual stress depth curves obtained with both correction approaches exhibit a generally satisfactory agreement. The results are nonetheless evaluated with both techniques because the adopted correction approach can have an impact on the

interpretation of experimental residual stress results.

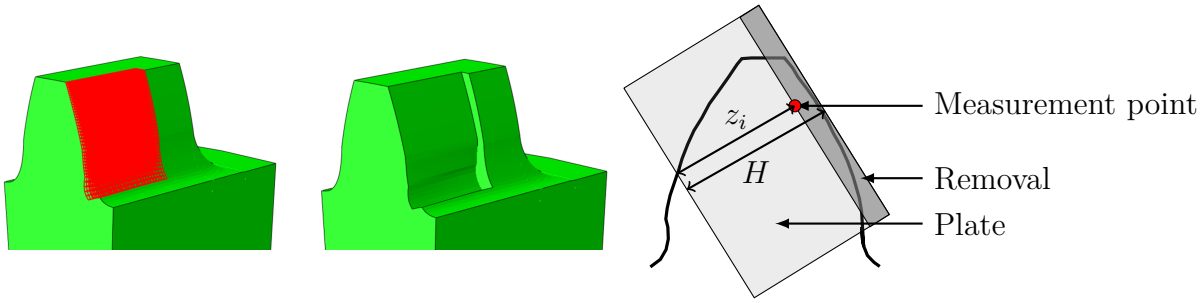


Figure 4.3: Schematic representation of the correction of residual stress measurements on the tooth flank with FE simulation of the material removal (left) and with the approach of Moore & Evans according to Weber [46].

4.2. Results

4.2.a. Analysis of calculated residual stresses on hollow cylindrical samples

Figure 4.4 presents the simulation results for the residual stresses on paths 1 and 2 for a hollow cylinder with external diameter $D_o = 300\,\text{mm}$, internal diameter $D_i = 171\,\text{mm}$, a height of $H = 100\,\text{mm}$ and a case hardness depth CHD $= 2.50\,\text{mm}$. The stresses in the directions tangential and axial to the paths exhibit compressive values in the surface regions. Surface values are about $-100\,\text{MPa}$, minimal values range between $-450\,\text{MPa}$ and $-500\,\text{MPa}$ and the transition to tensile stresses is reached at about 1.5 to $2 \cdot \text{CHD}$. Due to equilibrium conditions, the stresses normal to the paths are nearly zero at the outer surfaces. While the stress magnitudes in this direction remain lower than in the tangential and axial directions, some peak tensile values of up to $120\,\text{MPa}$ are predicted by the simulation model. On the first glance, stresses tangential and axial to the path directions seem to behave very similarly. However, because of the dependency of the cooling conditions on the radial coordinate in the cylinder, the tangential stresses show higher tensile stresses in the region near the inner surface than at the external diameter. In contrast, tensile axial stresses are stable in the whole core region of the component for the selected paths.

The effect of the CHD on the residual stresses in hollow cylinders is displayed in figure 4.5.

Depending on whether *path 1* or *path 2* is considered, stresses normal to the path's direction behave differently. As the CHD increases, the normal stresses for the first path with a radial orientation show higher compressive residual stresses. The maximal tensile stresses are not much impacted by the CHD and the surface stresses are always close to zero. As the CHD increases, the depths corresponding to the lowest and maximum residual stresses as well as the depth at which compressive stresses turn tensile are moved

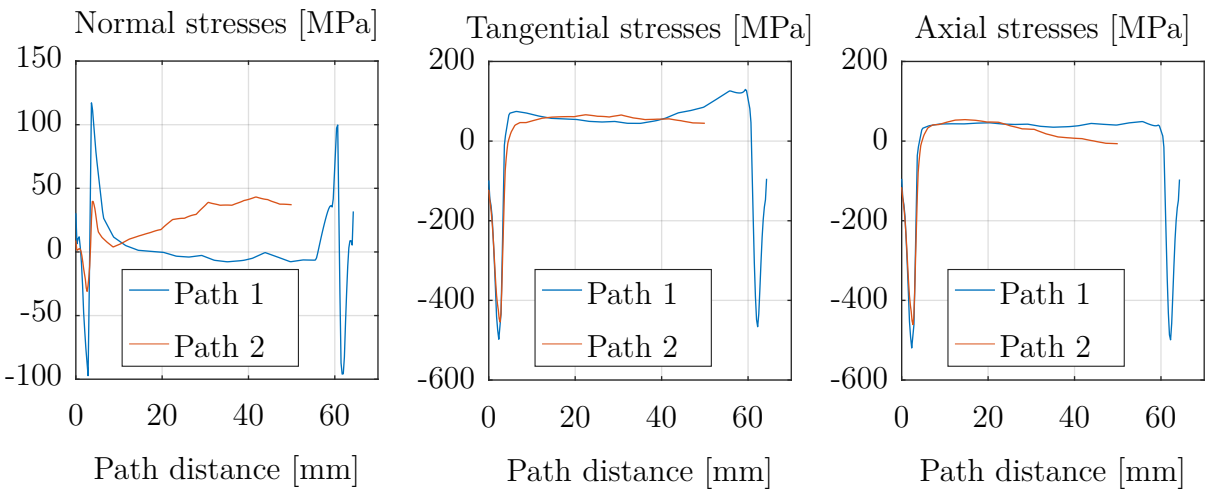


Figure 4.4: Computed residual stresses for a carburized hollow cylinder with outer diameter $D_o = 300\,\text{mm}$, inner diameter $D_i = 171\,\text{mm}$, height $H = 100\,\text{mm}$ and CHD = 2.5 mm. Stresses are displayed for directions normal, tangential and axial to paths 1 and 2, as defined in figure 4.2.

towards larger values. Similar findings apply to the second path, with the exception that the maximum tensile stresses normal to that path are located deeper below the surface and their magnitudes rise with increasing CHD.

Regarding the impact of the CHD on stresses in the tangential and axial directions for paths 1 and 2, distinct trends can be observed. CHD variations have little effect on surface stresses. Only minor differences in the maximum compressive residual stresses are computed, whereas the maximum tensile stresses obviously rise with increasing CHD. As CHD increases, the position of the compressive and tensile stress transition point, as well as that of the lowest and highest residual stresses, move towards larger depths.

Similar effects can be observed on the cylinders with substantially smaller or larger dimensions. Figure 4.6 displays CHD variations for various cylinder sizes, whereby only half of *path 1* is represented for clarity purpose. Overall, there is no clearly discernible relationship between the CHD and the highest residual compressive stresses or surface residual stresses. Conversely, as ought to be expected, there is a high correlation between the CHD and the depth in which the residual stresses change from between compression to tension. Elevated CHD values also result in greater residual tensile stresses within the component depth; however, this impact diminishes as component size increases. A discontinuous residual stress depth profile is produced by the calculation model when a cylinder diameter greater than approximately 400 mm is coupled with a relatively low CHD. More thorough simulation analyses have revealed that this situation arises when significant fractions of the carburized region undergo bainitic transformation rather than turn into martensite.

Figure 4.7, which displays the residual stresses for simulations 3, 6, 7, 8, and 9 from table 4.2 in the directions normal and tangential to paths 1 and 2, illustrates the effects of the

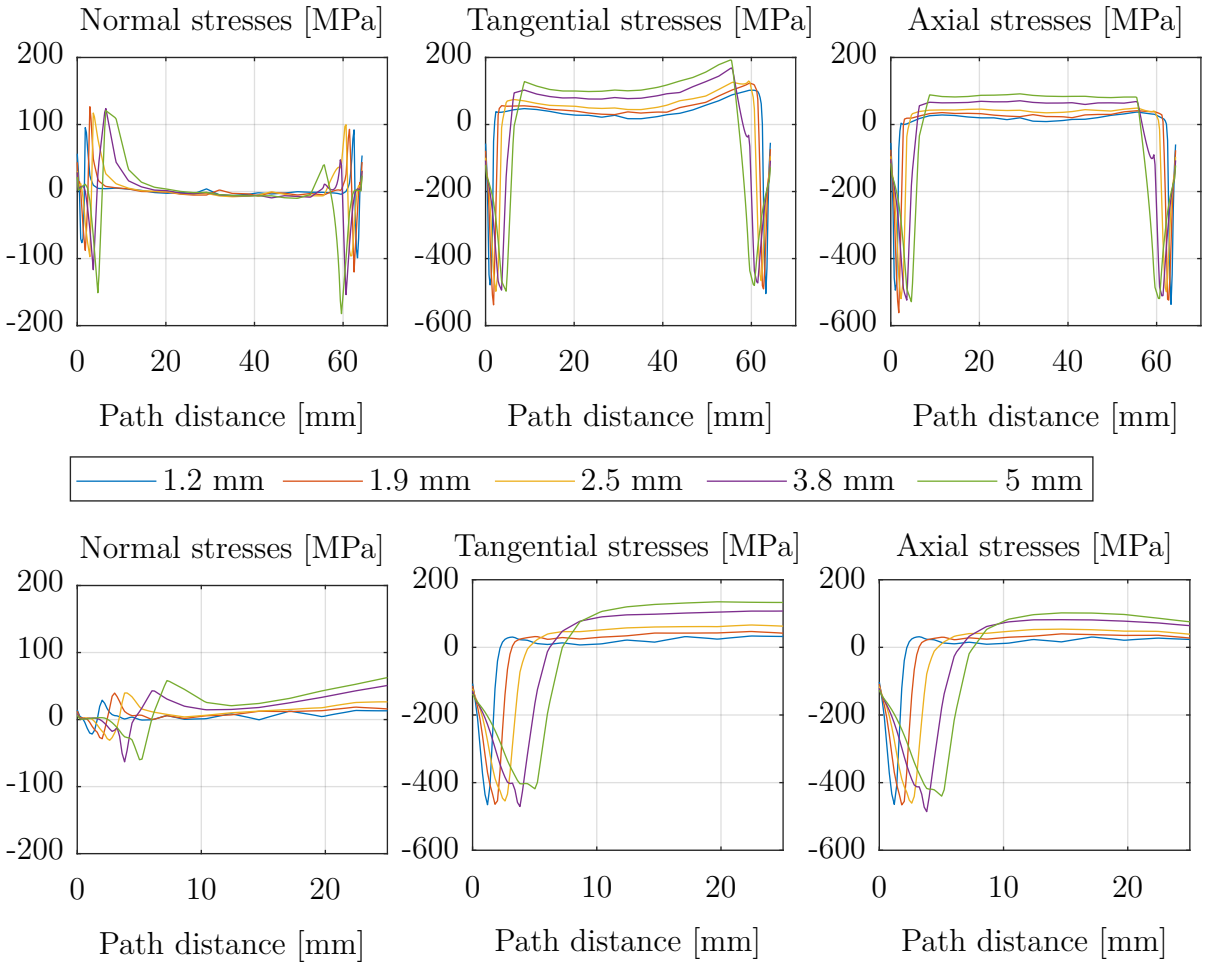


Figure 4.5: Computed residual stresses for a carburized hollow cylinder with outer diameter $D_o = 300\,\text{mm}$, inner diameter $D_i = 171\,\text{mm}$, height $H = 100\,\text{mm}$ and variations of the CHD between 1.2 mm and 5.0 mm and corresponding to simulations No. 1 to 5 in table 4.2. Stresses are displayed for along *path 1* (top) and *path 2* (bottom), where the directions normal, tangential and axial are defined with respect to each path as described in figure 4.2.

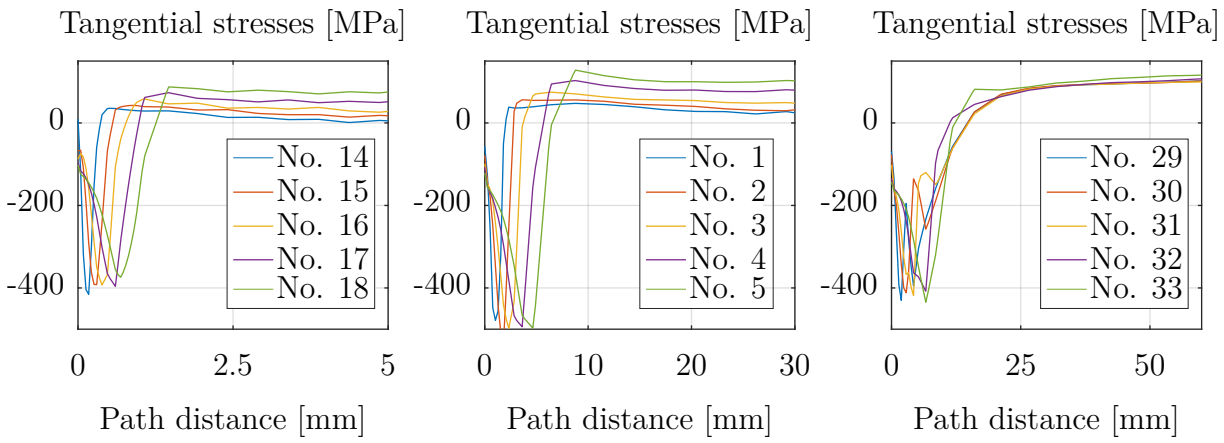


Figure 4.6: Computed tangential residual stresses for carburized hollow cylinders with different geometries and varying CHDs. Stress along *path 1* for an outer diameter D_o of 50 mm is shown in the left diagram. Results for $D_o = 300$ mm are presented in the center diagram, with the right diagram depicting $D_o = 550$ mm geometry. CHDs and sample dimensions are detailed in table 4.2.

cylinder wall thickness. Changes in the cylindrical samples' wall thickness have no predicted effect on either compressive residual stresses or surface residual stresses. Conversely, the dimensions of the cylinder hole have a substantial impact on the maximum tensile stresses below the surface. The transition point between compressive and tensile residual stresses moves towards higher depths with greater wall thickness in the directions tangential or axial to pathways 1 and 2.

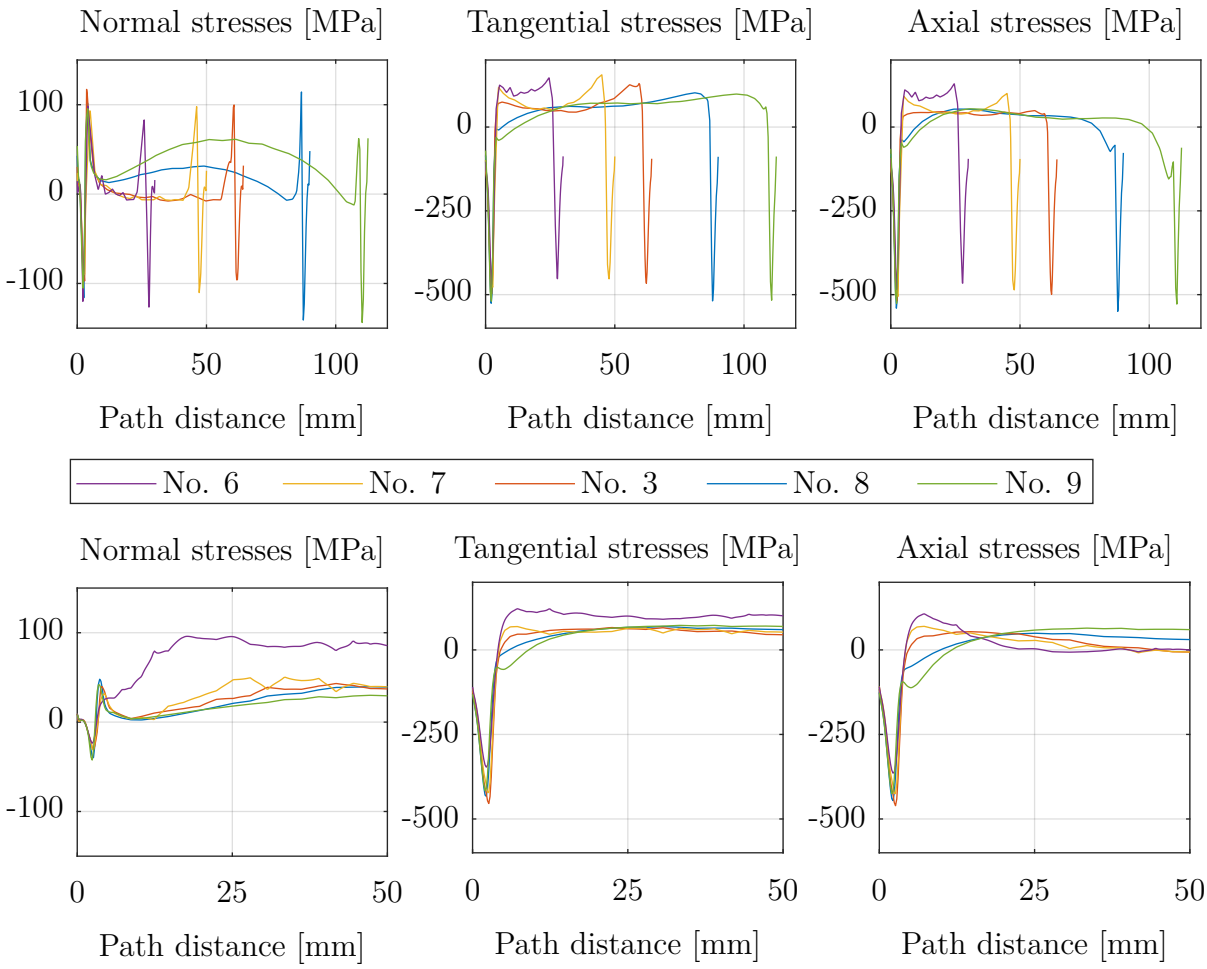


Figure 4.7: Computed residual stresses for a carburized hollow cylinder with outer diameter $D_o = 300\,\text{mm}$, height $H = 100\,\text{mm}$, CHD $= 2.5\,\text{mm}$ and variations of the wall thickness. Stresses are displayed for along *path 1* (top) and *path 2* (bottom), sample geometry of each simulation number is detailed in table 4.2.

4.2.b. Correlation analysis

In order to quantify the trends discussed in the previous subsection, the correlation matrix between varying input parameters (CHD, wall thickness and height of the cylinder) and the residual stresses are computed. The calculation is realized in MATLAB 2021 [153] using additional utilities for visualization that have been adapted from [163]. A positive correlation is depicted in blue and a negative correlation in red. The area of each circle is directly proportional to the squared value of R_{corr}. When the value p – which tests the hypothesis that there is no link between the two variables – is less than 0.05, the correlation coefficient values R_{corr} can be deemed significant. In order to concentrate on the effects of the carburizing heat treatment on the functional surface of the cylindrical samples, only the first half of *path 1* is taken into consideration for this study. The results suggest positive correlations between the maximum computed residual stresses in the direction normal to this path and radial wall thickness, height and CHD. It is anticipated that when wall thickness, height or CHD increase, compressive residual stresses in this direction would rise in amplitude. However, no obvious correlation can be found to determine the highest and lowest values of the stresses axial and tangential to *path 1*. Increasing cylinder height primarily affects the depth at which residual stresses switch between compressive and tensile, as well as the depth at which lowest and maximum values are found. Even though the surface tangential and axial stresses appear to be mainly determined by CHD, the effect size – which only varies in a moderate range of approximately 120 MPa despite very large CHD differences – should also be taken into account.

Similar tendencies for *path 2* in the main direction of the cylinder are seen in figure 4.9, however the strength of the correlations seem to differ slightly. The impact of the height of the cylinder on the maximum value of the stresses in the direction normal to *path 2* or on the depth of the maximum stresses in the tangential and axial directions is higher than for *path 1*. The depth of the transition between compressive and residual stresses, as well as the depth of peak and minimal residual stresses, are strongly positively correlated with the radial wall thickness of the cylinder, its height and CHD. For the lowest and surface values of stresses tangential and axial to *path 2*, the opposite tendencies are found. The maximum values of the residual stresses on *path 2* are only weakly correlated to the investigated input parameters.

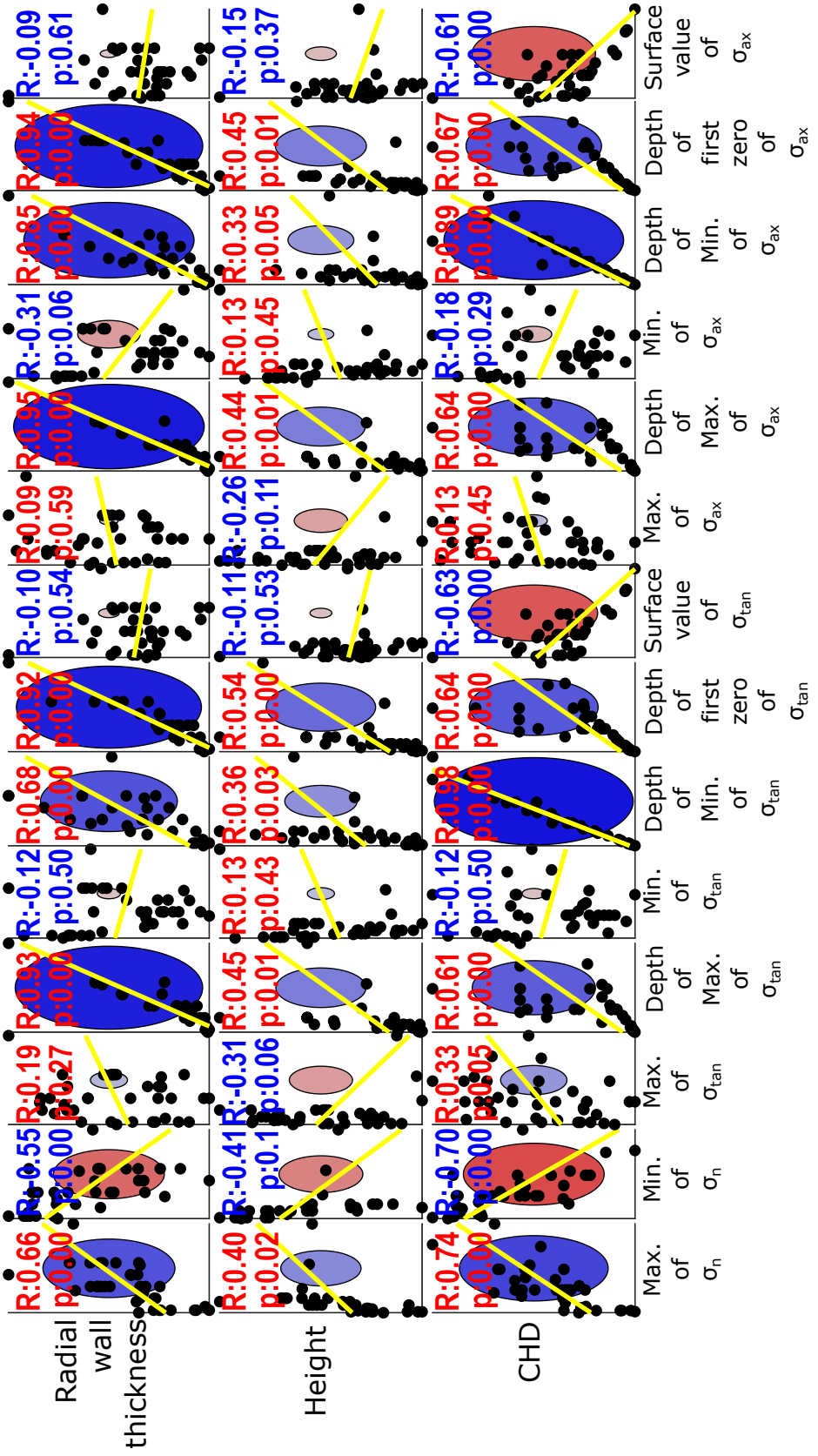


Figure 4.8: Correlation analysis of computed residual stresses in carburized cylindrical samples for *path 1*. Path definition and simulation details are available in figure 4.2 and table 4.2, respectively.

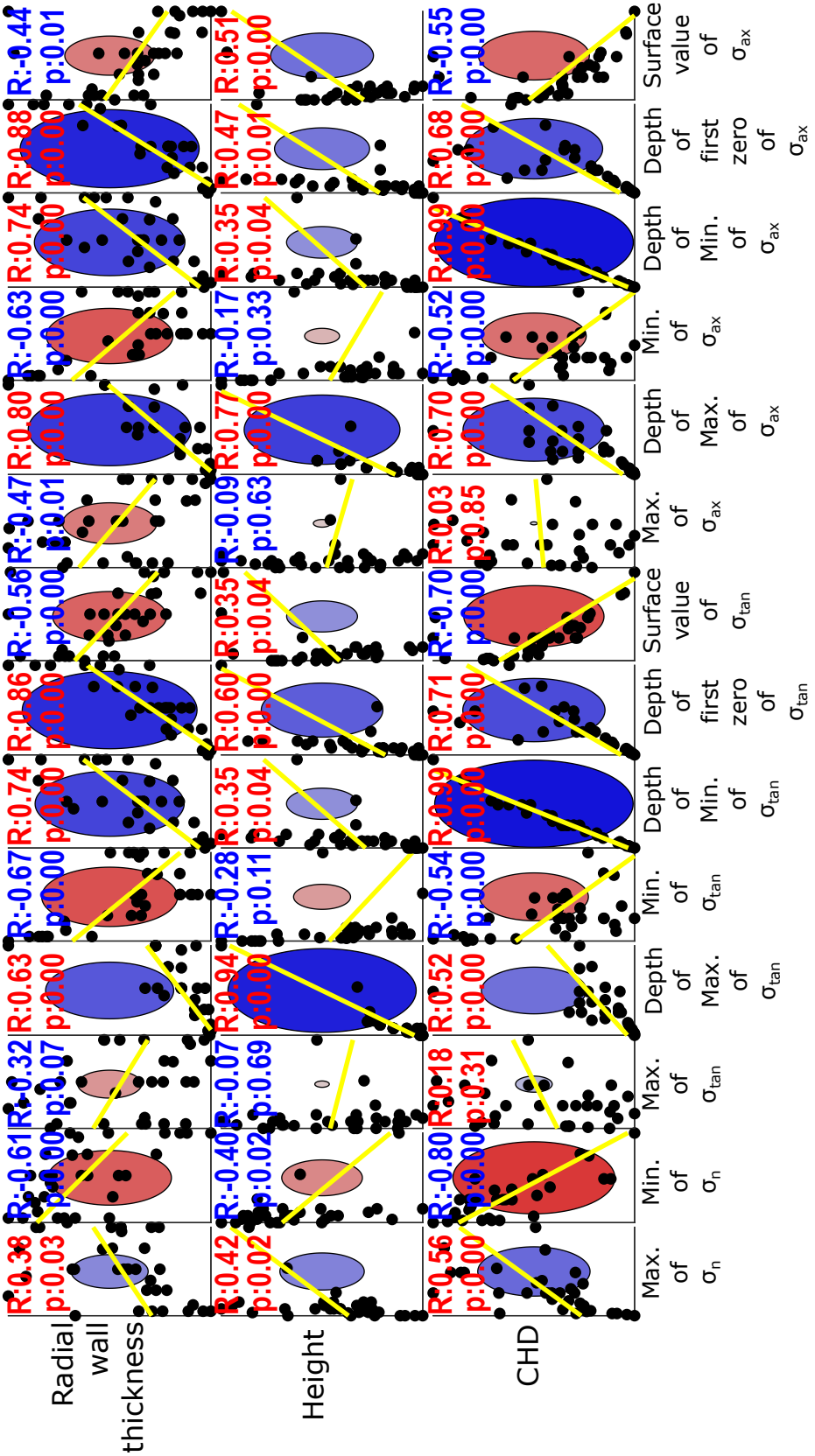


Figure 4.9: Correlation analysis of computed residual stresses in carburized cylindrical samples for *path 2*. Path definition and simulation details are available in figure 4.2 and table 4.2, respectively.

4.2.c. Detailed analysis of selected gear simulations

The FE model is utilized to predict the residual stresses in carburized gears. In this subsection, a detailed description of the outcomes of the first simulation in table 4.3 is given. Validation of the simulation model using experimental data is provided in section 4.2.d, whereas some selected effects on the residual stress depth profiles are described in 4.2.f.

Figure 4.10 left depicts the carbon depth profile on the tooth flank for the basic variation, which has a CHD of 0.5 mm. On the right, the spatial distribution of carbon concentrations is shown for the 48,000 elements in the tooth region. At the surface, the carbon concentration reaches around 0.72 %C. The area close to the surface presents a short plateau, and as depth increases, the concentration of carbon decreases. The carbon concentration is approximately 0.32 %C at the specified CHD of 0.5 mm. The carbon concentration of the base material is reached at a depth of approximately 1 mm. This profile matches the carbon depth curves determined experimentally in [47] for this configuration.

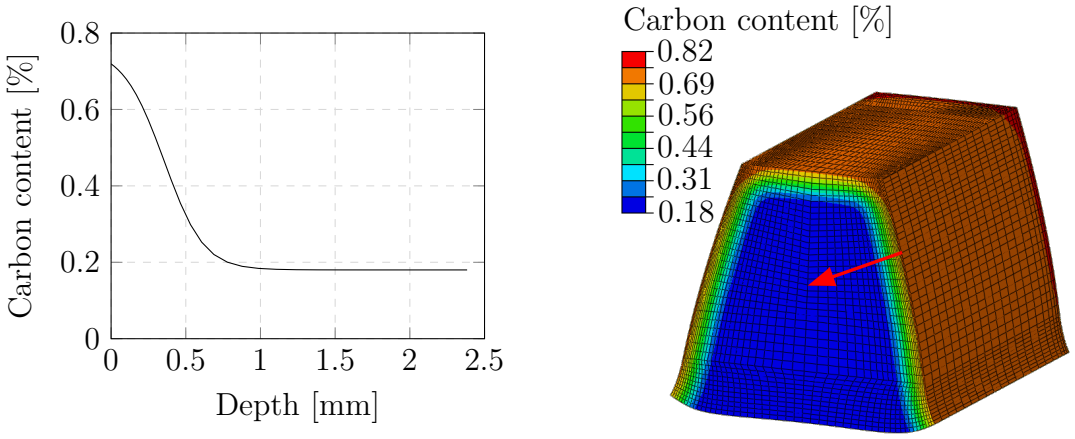


Figure 4.10: Calculated spatial distribution of carbon in tooth region prior to quenching for gear simulation 1 with module 3 mm and CHD 0.5 mm.

The temperature distribution at each time point is determined using the temperature-dependent heat transfer coefficient for a quench using 90 °C oil bath, as detailed in appendix A8. The calculated temperatures and the experimental measurements from [47] for the two thermocouples placed in the tooth flank and core area may be compared in figure 4.11. Overall excellent agreement is found, although the experimental quenching is slightly slower than predicted by the model in temperature ranges below 350 °C.

The FE model provides the time- and spatially resolved microstructure development in the gear. The tooth region is cooled fastest during quenching. When the temperature reaches approximately 400 °C, the first austenite phase fractions transform into martensite. Because carburizing lowers the martensite start temperature locally, the martensite does not initially develop at the tooth's surface. The case area is first subjected to tensile stresses. At about 150 °C, the surface also starts to transform into martensite, which results in

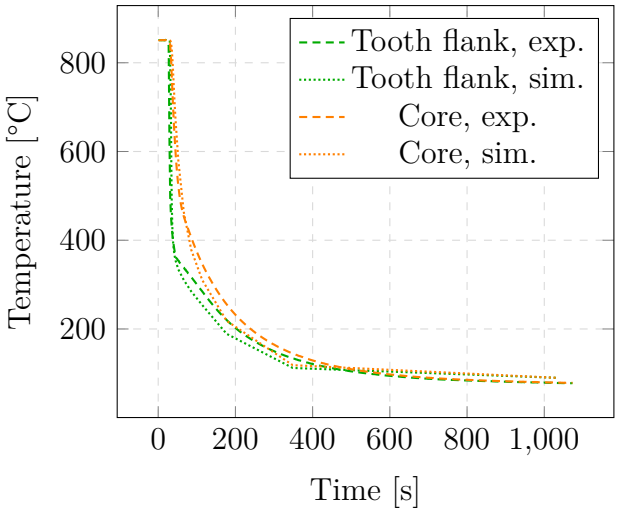


Figure 4.11: Comparison of the simulated and measured temperature curves during oil quenching of the gear with module 3 mm.

significant residual compressive stresses at the flank. In the tooth core, martensite fraction tends to stay lower because bainite has already been formed. Tempering step follows and lowers the magnitude of the residual stresses. The FE-calculated distribution of the different microstructures and the carbon content resulting from this gear's oil quenching is displayed in figure 4.12. The tooth core has a mixed martensite and bainite microstructure, with varying proportions based on the distance to the tooth tip. As one gets farther away from the material surface, the proportion of bainite rises because of lower cooling rates and carbon concentration, and bainite can form before the onset of martensite transition. On the surface of the tooth flanks, residual austenite concentrations are estimated to reach up to 20 %; however, these contents rapidly diminish as one moves toward the tooth core.

The position-dependent cooling conditions, phase transformations and material properties in the gear result in residual stresses. These stresses are evaluated in accordance with section 4.1.c at the pitch point along *path 1*, which is perpendicular to the tooth flank surface. The maximal principal stresses (in absolute values) in the tooth following tempering are displayed in figure 4.13 together with the von Mises equivalent stress. The maximum residual stresses are predicted for the surface in the tooth root area. In contrast, the maximal equivalent stress in the tooth flank region, as determined by von Mises, occurs around 0.5 mm below the material surface. Comparing both stress distributions, however, reveals that von Mises' residual stress maxima are situated in regions with compressive residual stresses. From a depth of approximately 0.95 mm, the principal residual stresses act tensile and grow with increasing distance from the tooth flank surface until they reach a maximum value, after which no significant variations are observed up to the tooth's core. Figure 4.14 presents the individual components of the simulated residual stress tensors in reference to the local coordinate system at the pitch point, both after quenching and after tempering.

The stress state is dominated by residual stresses in the direction axial and tangential

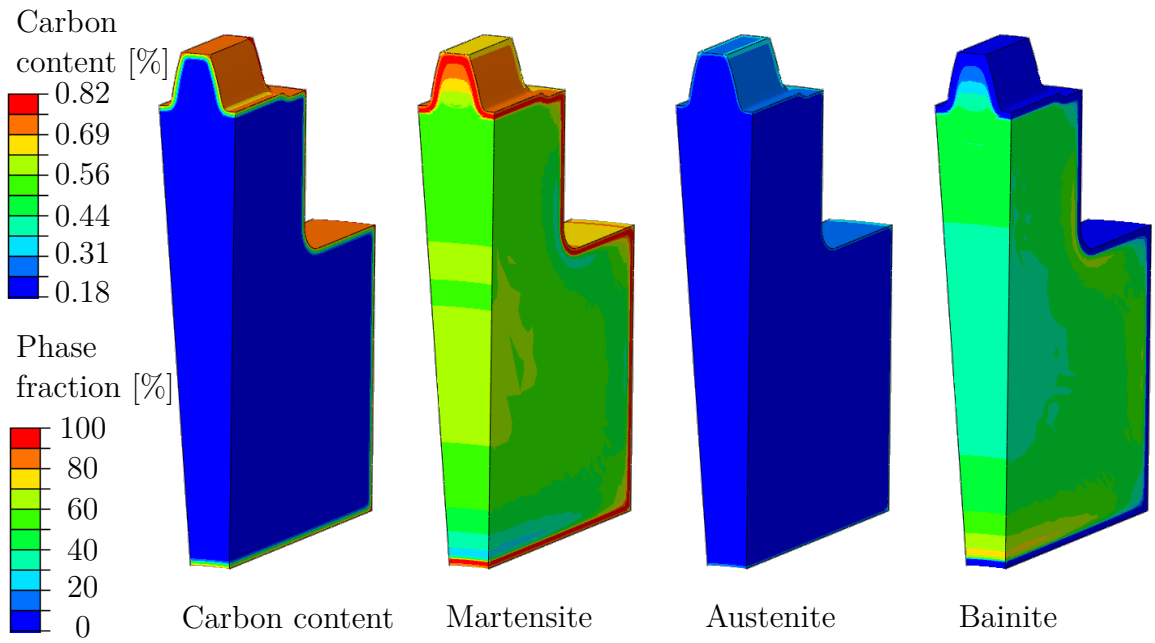


Figure 4.12: Calculated phase fractions and carbon content after oil bath quenching of gear with module 3 mm and case hardening depth 0.5 mm from simulation 1.

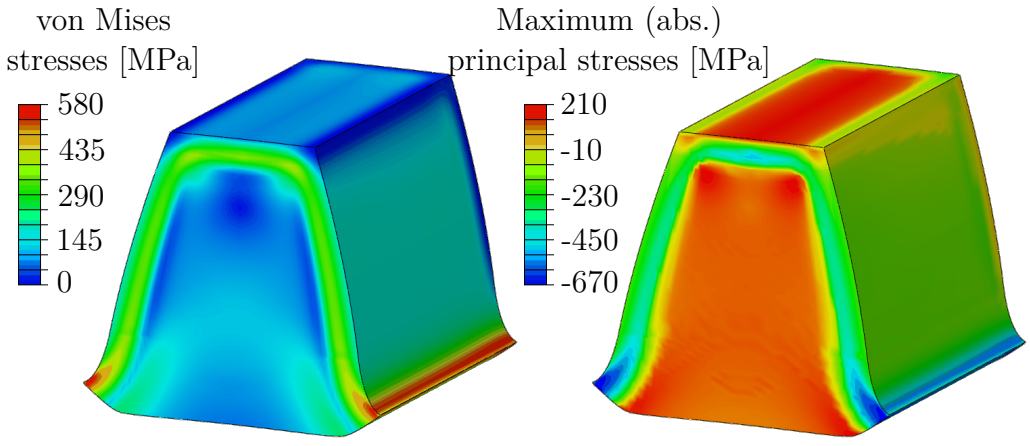


Figure 4.13: Predicted von Mises equivalent residual stresses and principal residual stresses with the maximal absolute value for gear with module 3 mm and CHD 0.5 mm after oil quenching and subsequent tempering.

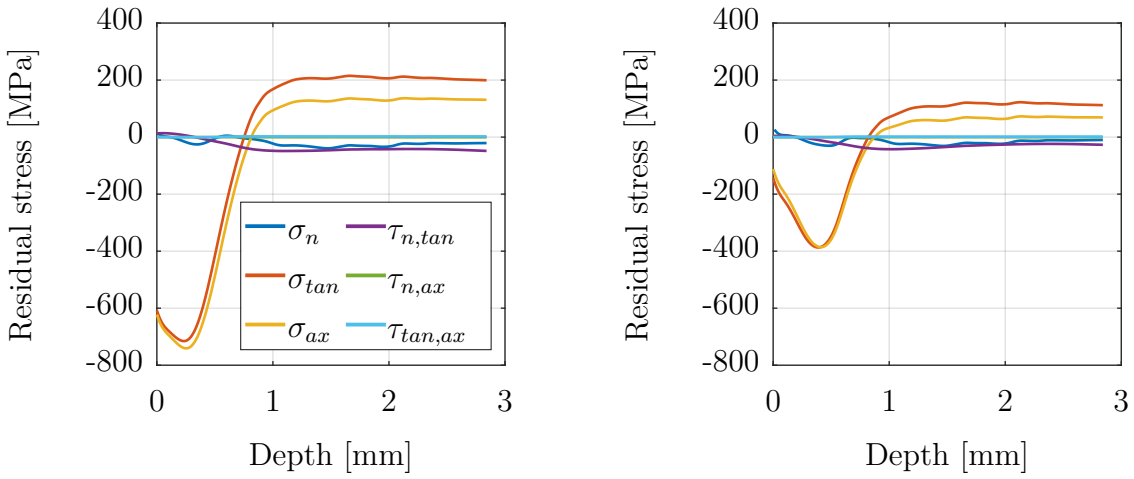


Figure 4.14: Predicted residual stresses in the gear with module 3 mm and CHD = 0.5 mm along *path 1* after oil quenching (left) and subsequent tempering (right).

to *path 1*, as seen in figure 4.14. As a first approximation, the shear stresses and residual stresses in the radial direction can be neglected since they fall between 0 and 30 MPa. The depth curves for the tangential and axial residual stresses are comparable, although tangential stresses reach higher tensile values. Surface compressive stresses of around 140 MPa are computed as a result of the heat treatment. Compressive residual stresses peak between 0.35 and 0.45 mm below the surface. The zero crossing is attained at around 0.8 mm. A plateau with tensile stress levels of 110 MPa and 70 MPa, respectively, is observed for residual stresses in the tooth depth. It is noteworthy that the tempering stage creates significant changes in the residual stress levels, with a clear decrease in overall stress magnitudes. The stress shift is up to around 450 MPa in the surface area, but it also affects the residual stresses at larger depths. The maximum tensile residual stresses in the tooth core are decreased and the zero crossing is moved slightly deeper as a result of tempering.

Figure 4.15 shows the stresses in the normal and tangential directions of paths 1, 2, 3 and 4, as defined in figure 4.2. For this configuration, residual stresses in the tangential direction are very similar for all the paths that start from the tooth's functional surface. While residual stresses in the normal direction are higher when approaching the tooth tip, the predicted stresses in the tangential direction show magnitudes only up to about 50 MPa lower for the path starting at $\frac{1}{4}$ of the tooth height than for the upper region. Overall, similar depth profiles but with greater absolute values are predicted for *path 4* that is aligned with the gear's main axis.

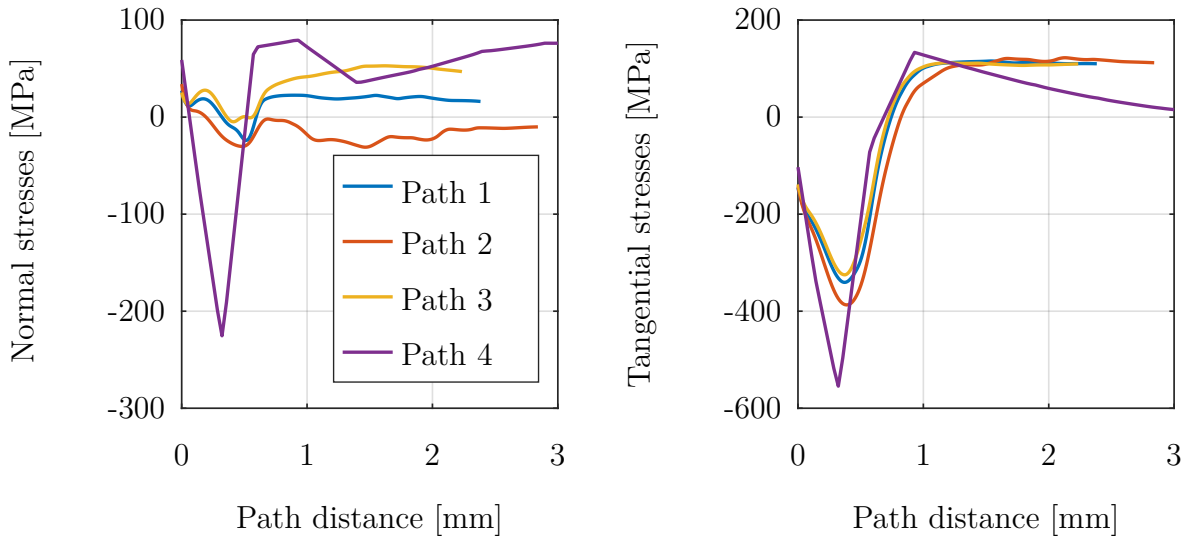


Figure 4.15: Predicted residual stresses of gear with module 3 mm and CHD = 0.5 mm in directions normal and tangential to different paths after oil quenching and tempering.

4.2.d. Validation of the heat treatment simulation model

As stated in section 4.1.d, both an FE-based stress correction and the Moore & Evans correction technique are applied in order to compare the simulated residual stress profiles with measurements. For the latter, equation 4.1 is used with parameter $H = 4.5$ mm and $H = 30.5$ mm for the gears with module 3 mm and 18 mm, respectively. Using the heat treatment simulation model, the FE correction is performed by sequenced deactivating of element layers after case hardening for a removed volume that corresponds to the geometry used in experimental X-ray measurement. The stress values on the tooth flank's exposed surface are extracted and the FE solver determines how the material removal impacts the stress equilibrium. The variation of residual stress brought on by material removal can be expressed for each direction as a function of the depth. The corrected residual stress curve is then calculated by applying this scalar function multiplied by -1 to the experimentally obtained values. The comparison between the observed and corrected residual stress curves and the calculated ones for the gear with module 3 mm and CHD of 0.5 mm after oil quenching and tempering is presented in figure 4.16.

Figure 4.16 illustrates how the residual stress correction affects the residual stress curves. The observed values are generally moved in the direction of tensile stress, and there is high consistency between the Moore & Evans correction and the FE technique. As the distance from the flank surface rises, the corrected amount also increases. Overall, the simulated residual stress curves correlate very well with the corrected measurement values. In comparison to the measurement, the simulation model slightly underestimates the highest tensile residual stresses, with deviations of up to 70 MPa at the tooth core.

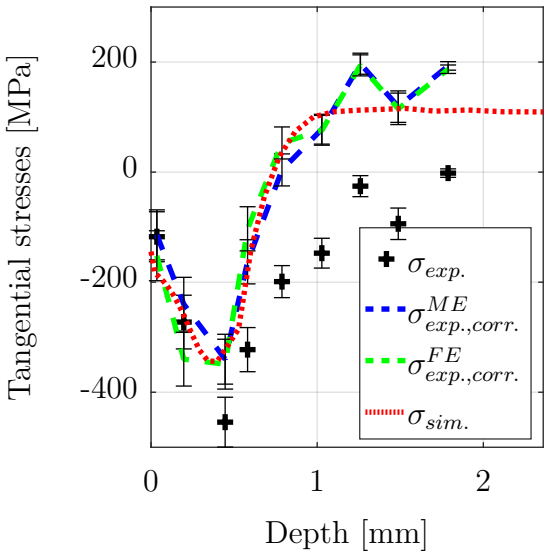


Figure 4.16: Comparison between residual stress calculation, residual stress measurements and corrected residual stress measurements for gear with module 3 mm and CHD = 0.5 mm after oil quenching and tempering. Residual stress correction is done with Moore & Evans (ME) and finite element based (FE) modeling.

Every simulation outcome is extensively assessed, similar to section 4.2.c. For simulations corresponding to experiments conducted in [47], the comparison between (corrected) residual stress measurement and calculation results enables to validate the simulation model. This comparison is shown in figure 4.17 for the gear module 3 mm quenched with high-pressure gas from simulation 8 that has a case hardening depth of 0.64 mm.

For this variation, residual stress measurements in both tangential and axial directions are provided. There is fairly strong agreement between the corrected and simulated curves for the tangential residual stresses. The residual stress curves produced using the two correction techniques agree well with each other and with the simulation outcomes. In all scenarios, the transition region between compressive and tensile residual stresses is located around 0.8 mm. According to corrected measured data and heat treatment modeling, the tensile tangential stresses in the tooth core are approximately 160 MPa. Uncorrected stress measurements for this configuration never reach tensile values. The compressive near-surface residual stresses in the axial direction are higher when using the FE method in comparison to the Moore & Evans method. The simulation model's computed residual stresses, the Moore & Evans-corrected measurements, and the FE correction approach all produce fairly similar curves but differ in the axial stress values attained in the tooth core. Although the FE correction yields a maximum tensile residual stress of around 60 MPa, the Moore & Evans technique results in tensile residual stresses of approximately 115 MPa in the core, still 30 MPa below the heat treatment simulation outcomes.

The residual stress curves from simulations 6 and 7 are displayed in figure 4.18 and are

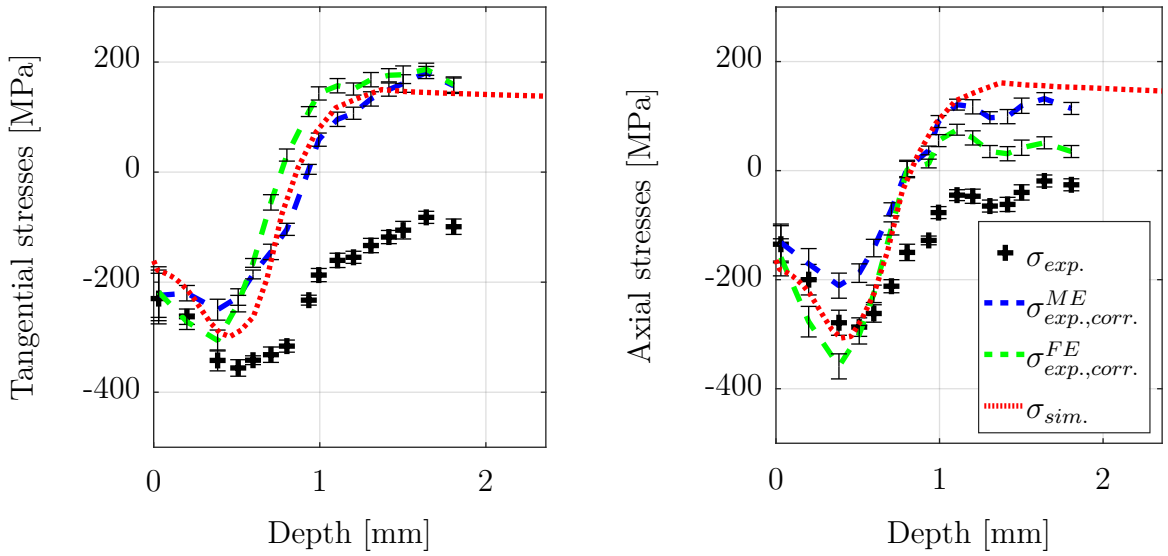


Figure 4.17: Comparison between residual stress calculation, residual stress measurements and corrected residual stress measurements in the tangential (left) and axial (right) directions for gear with module 3 mm and $CHD = 0.64$ mm after gas quenching and tempering.

compared to the measured and corrected residual stresses after the gear with module 3 mm and CHD = 0.5 mm has been carburized and quenched using either a polymer bath (left) or a salt bath (right). The corrected measured values and the simulation findings of the residual stress depth curves agree well in both situations. Differences between both methods applied for the correction of residual stress measurements can be observed, which can reach up to 150 MPa in the region with steep gradient. For these configurations, the computed residual stresses from the simulation model are very close to the Moore & Evans corrected experimental findings.

The simulation model is further validated by looking at the impact of changes in the carbon depth profile on the residual stress depth profile for the gear with module 3 mm. The simulated, measured and corrected residual stress curves under various carburizing conditions are displayed in figure 4.19. The simulation model captures most of the tendencies that were seen in the experiment. The form of the tangential residual stress curve for these variations can generally be predicted. For the gear with reduced surface carbon concentration of 0.65 %C, the compressive surface residual stresses are overestimated by about 150 MPa. For the variation with increased carbon concentration, the predicted residual stresses at the surface are only slightly below zero and therefore show significant differences with the measured and corrected values. In the experiments from [47], the residual stress measurements were conducted in the α-lattice. Volume fractions of residual austenite over 25 % following quenching and tempering may be expected for surface carbon concentrations above 0.8 %C. Comparing simulation results with residual stresses

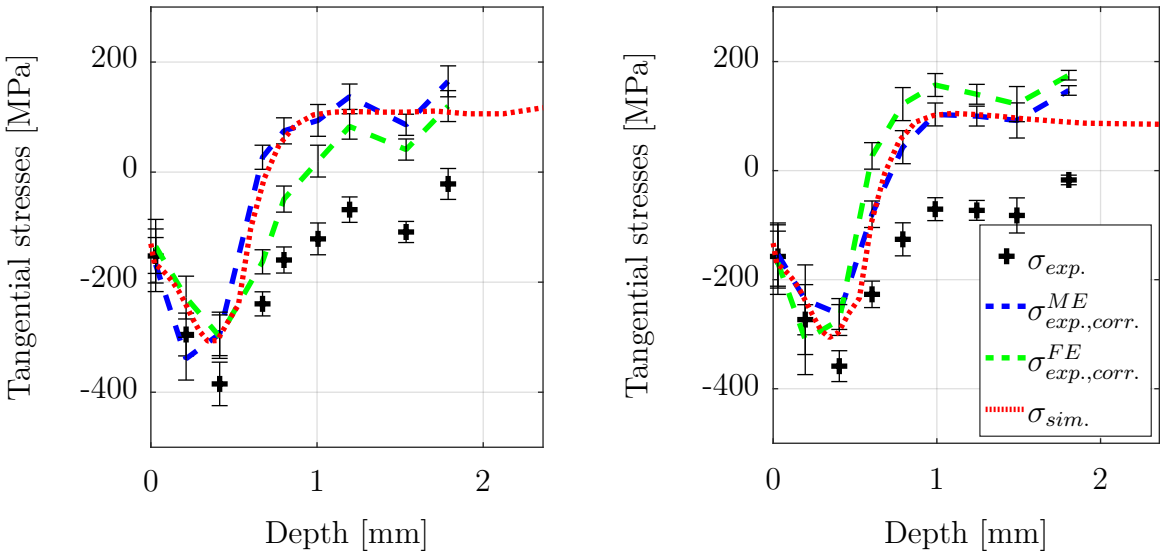


Figure 4.18: Comparison between residual stress calculation, residual stress measurements and corrected residual stress measurements in the tangential direction for gears with module 3 mm and CHD = 0.5 mm after quenching and tempering, using salt bath (left) and polymer bath (right) for quenching.

based on the lattice strains just in the α-phases may be deceptive for such heterogeneous microstructures. According to [126] and [82], mixed surface microstructures of carburized or carbonitrided components may exhibit compressive stresses in the martensite and tensile stresses in the remaining austenite, whereas the simulation model solely computes averaged stresses in each FE-element. For the areas corresponding to transition or tensile stresses, the predictions of the simulation model mostly agree with the measured and corrected tangential stresses. It is noteworthy that the FE-based correction and the Moore & Evans method differ significantly in the surface area for this configuration, with maximal deviations of up to 280 MPa. The simulation model's predictions mostly match the observed and corrected tangential stresses for the regions corresponding to transition or tensile stresses.

For the module 3 mm gears, residual stress depth curves at the pitch point (*path 1*) can generally be predicted with an appropriate level of accuracy. The experimentally obtained and corrected measurement results match with the calculated maximum residual tensile stresses in the core and the depth of the transition area between compressive and residual tensile stresses. It is also possible to validate the residual stress prediction in the axial direction. The simulated residual stresses in the surface region occasionally show larger deviations and should only be utilized cautiously, especially in the event of surface carbon concentrations that differ from the typical values.

Results of residual stress measurements for the module 18 mm gears were provided in [47] and they may be used to validate the simulation model. The calculated residual stress curves for the gears V4-1 and V4-3 (simulation 14 and 15, respectively) quenched in an oil bath are

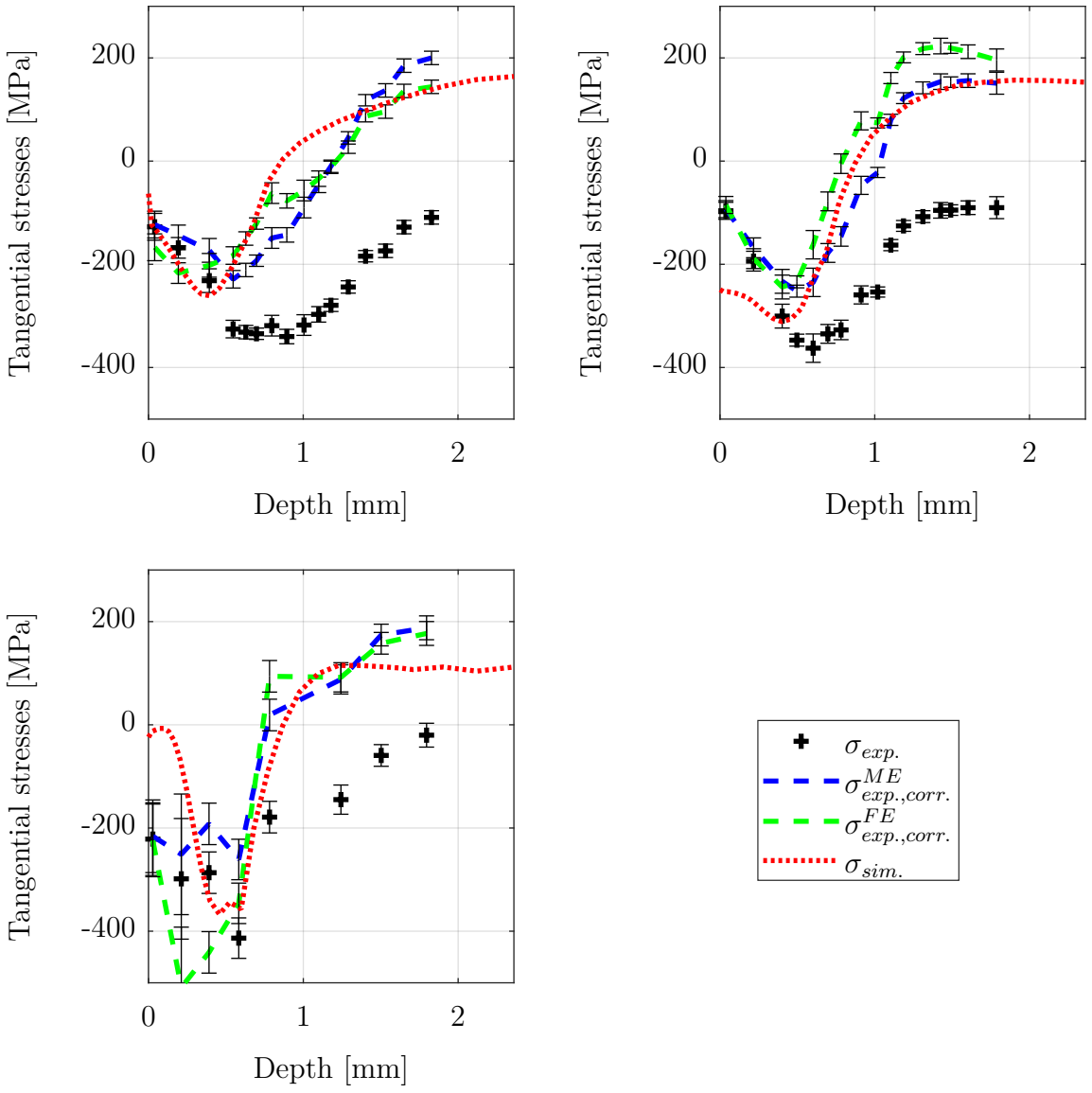


Figure 4.19: Comparison between measured and simulated residual stress curves at the pitch point of the gears with module 3 mm, case hardening depth 0.65 mm, gas quenched and with variations of the carbon profile in tangential direction: profile with flat runout after CHD (top left), profile with surface carbon content of 0.65 %C (top right) and profile with increased surface carbon content of 0.88 %C (bottom). The diagram also shows the corrected measured values according to Moore & Evans and with FE method.

displayed in figure 4.20. For this gear geometry, the ME-correction method is conducted using $H = 30.5\,\text{mm}$ in equation 4.1.

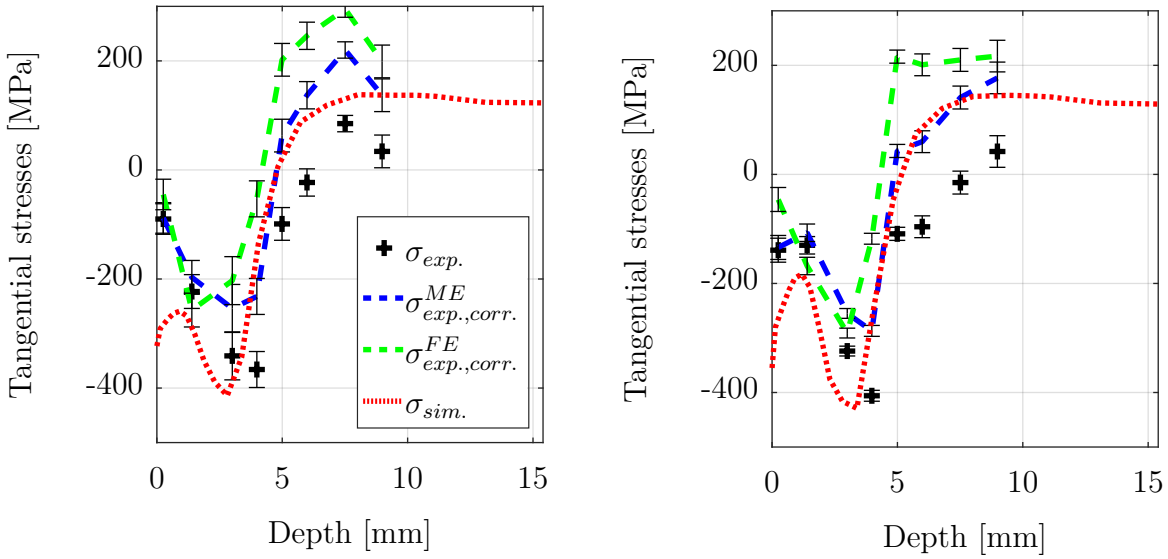


Figure 4.20: Comparison between residual stress calculation, residual stress measurements and corrected residual stress measurements in the tangential direction for gears with module 18 mm and CHD = 3.26 mm (left) and CHD = 3.42 mm (right) after oil quenching and tempering.

Overall, an acceptable modeling of the tangential residual stresses during oil quenching of the 18 mm module gear is achieved. However, the simulation results appear to have a systematic bias of about 100 MPa towards compressive residual stresses in the tangential direction. The residual compressive stresses on the tooth flank surface are not reliably reproduced by the simulation model, with deviations of up to 200 MPa. The prediction of the maximum residual tensile stresses in the tooth core and in the transition region between case and core, on the other hand, corresponds to the corrected experimental results with an acceptable degree of accuracy. The depth of the zero crossing is only very slightly overestimated by the simulation model compared to the experimental findings.

The simulation and the experimentally obtained and corrected residual stress curves show larger deviations for the case hardening with polymer bath quenching or with salt bath quenching of the module 18 mm gear. The simulation model well reproduces the general shape of the experimental residual stress curves. Nevertheless, significant discrepancies are noted in the depth range of 5 mm to 8 mm. The deviations observed are smaller for the gear quenched with polymer bath, but the calculated residual stress profile appears to be slightly shifted towards the flank surface, leading to an underestimation of the predicted depth for transition between compressive and residual tangential stresses.

The accuracy of the FE-based prediction model varies depending on the gear module, depth and heat treatment that are taken into consideration, even if its quality seems to

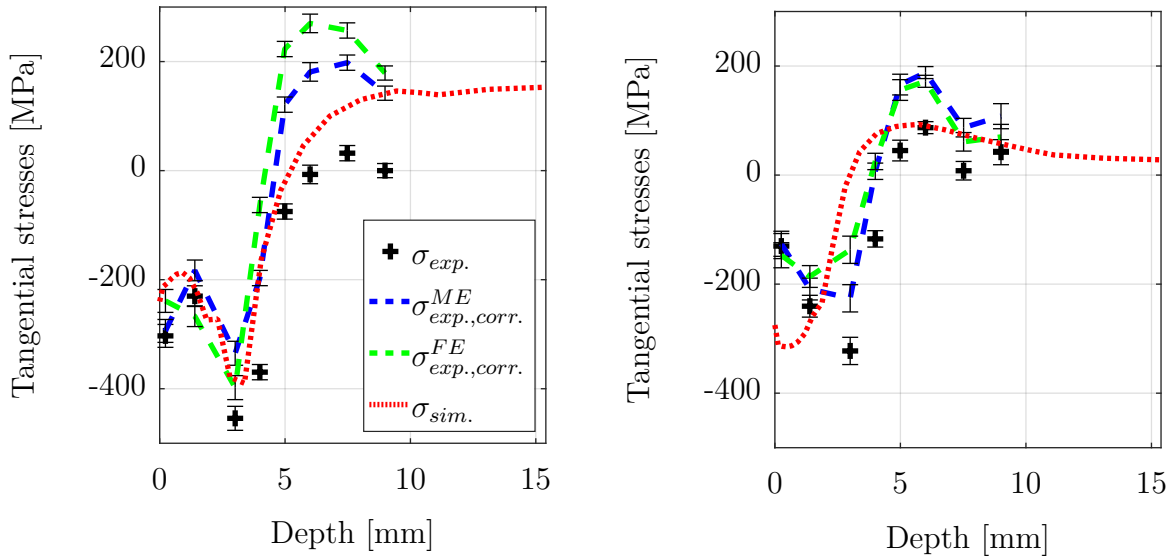


Figure 4.21: Comparison between residual stress calculation, residual stress measurements and corrected residual stress measurements in the tangential direction for gear with module 18 mm and CHD = 3.28 mm quenched with salt bath (left) and gear with module 18 mm and CHD = 2.56 mm quenched with polymer bath (right).

be satisfactory for the majority of evaluated scenarios. By comparing all experimentally measured residual stress measurements with their corresponding predictions, an overview and a quantitative indication of the prediction model's accuracy may be obtained. This analysis is performed in figure 4.22. All points would fall on the $y = x$ line in a perfect prediction model, with the exception of scattering brought on by the heat treatment or measuring technique. The color of each measuring point also indicates its depth with respect to the CHD of the gear. This makes it possible to identify the depth ranges where prediction accuracy is best. The majority of the anticipated residual stresses, as can be observed, are located close to the diagram's diagonal, suggesting high accuracy. Additionally depicted are lines that correlate to +50 MPa and −50 MPa systematic biases. The quality of the model may be evaluated using the R correlation value and the mean absolute error MAE given on the graphic. The residual stresses corrected using the Moore & Evans technique are shown by the x-axis in figure 4.22. A similar linear trend and correlation coefficient $R = 0.86$ are shown in the same figure when the FE-based correction is applied. The mean absolute error then rises to MAE = 76.02 MPa, mostly due to a few severe deviations in the surface region for the gear experiment with module 3 mm and an increased surface concentration of carbon. The case region (depth < CHD) in figure 4.22 shows the highest deviations, suggesting that the simulation model regularly predicts compressive residual stresses that are about 100 MPa overstated. On the other hand, practically all points corresponding to a depth larger than approximately $1.5 \cdot$ CHD fit within a relatively narrow range of the

diagonal line, showing a good prediction accuracy for the residual stresses anticipated in the tooth core area.

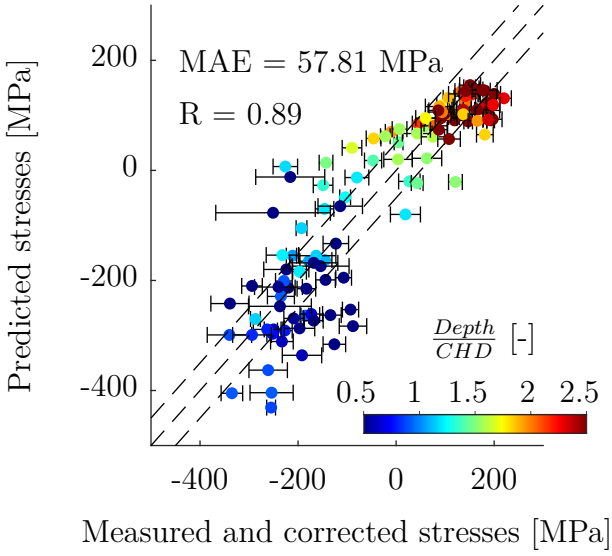


Figure 4.22: Evaluation of the accuracy of prediction model. Each available measurement data in [47] is plotted against the simulated value. Residual stress correction is done with Moore & Evans (ME) as defined in equation 4.1.

Comparing the FE results with other existing residual stress prediction methods for case-hardened gears is an instructive way to assess the accuracy of the model and its reliability. The results obtained using the approach from Weber's work [46] mentioned in section 2.2.b and using equation 2.17 derived from Lang's work are both visualized using the same method, as shown in figure 4.23.

Tensile residual stresses are not included in calculations using Lang's model, as explained in 2.2.b. As a result, it is evident that the residual stress estimates for the tooth core region are unsatisfactory. Remarkably, Lang's equation shows larger errors than the heat treatment simulation model and overestimates the compressive residual stresses even in the near-surface area corresponding to dark blue spots in figure 4.23. Weber's model appears to capture general trends effectively; the correlation coefficient between the anticipated and experimental results is $R = 0.84$. On the other hand, residual stresses tend to be underestimated in all tooth regions, with a mean absolute error of around 97.5 MPa.

A similar analysis may be performed on the hardness predictions derived from the simulation model, as figure 4.24 illustrates. With a high correlation coefficient and nearly all of the points falling within a 10 % margin, the computed hardness values generally accord well with the measurements in [47]. Equation 2.20 yields very similar results for a path located at the pitch point and without the need of overly complex simulation tools, but requires previous information of surface and core hardness values as well as CHD.

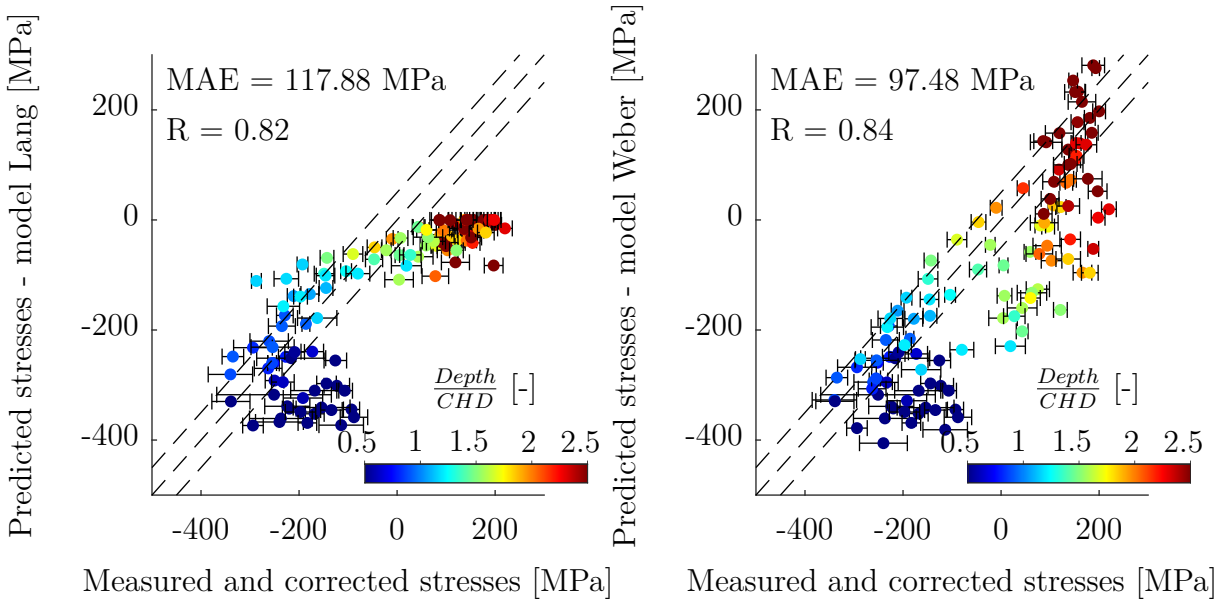


Figure 4.23: Evaluation of the accuracy of alternative prediction models. Each available measurement data in [47] is plotted against the predicted values for equation 2.17 (left) and for calculation model from Weber [46] (right). Residual stress correction is done with Moore & Evans (ME) as defined in equation 4.1.

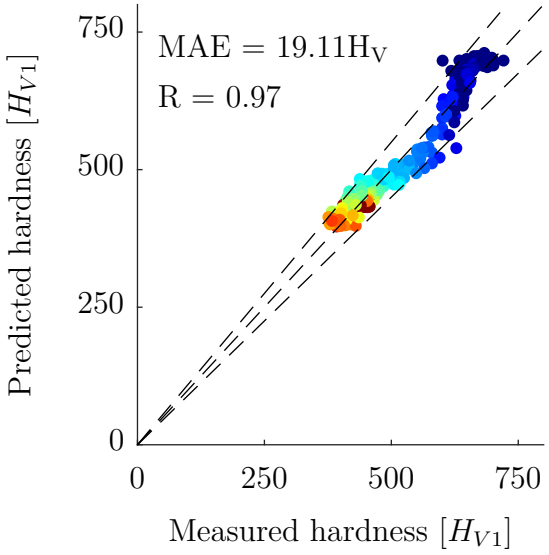
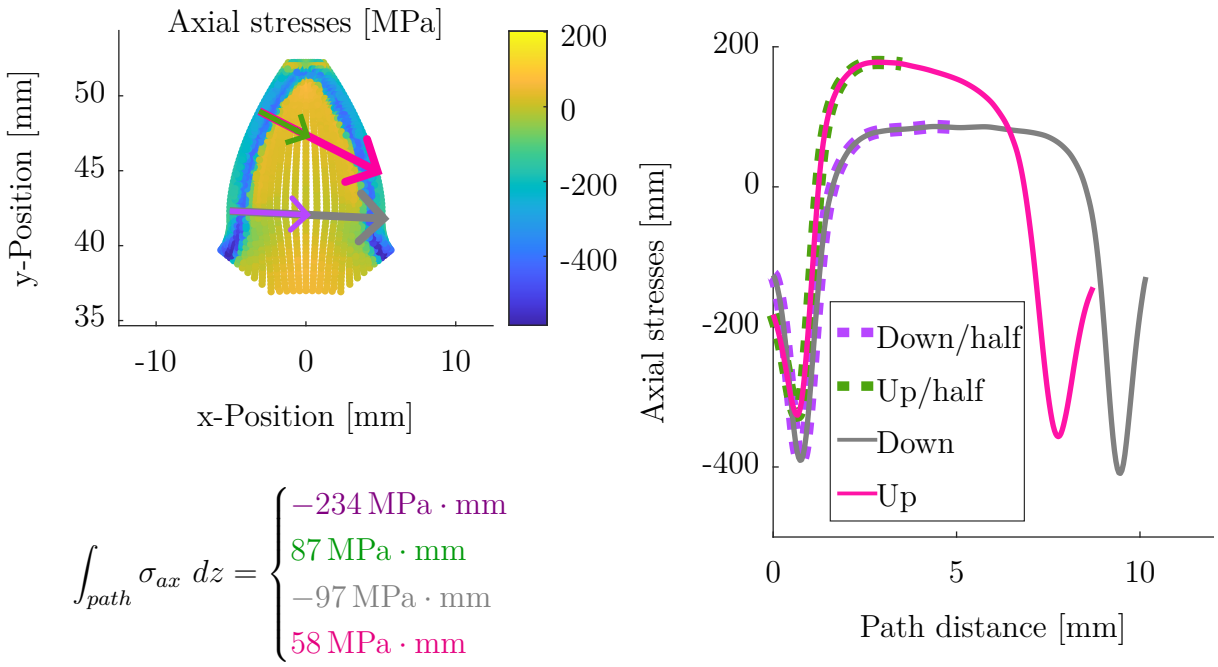


Figure 4.24: Evaluation of the accuracy of hardness prediction model. Each available measurement data in [47] is plotted against the predicted value.

4.2.e. Analysis of the residual stress equilibrium

As stated in section 2.1.c, the integral sum of residual stresses over the cross section on a line that crosses the entire component must result in a zero value. To determine the unknown tensile residual stresses at the gear tooth's depth from known stress values in the near-surface region, several authors actually employ a slightly modified version of equation 2.5. The signed area under the curve of a chosen stress tensor component for a path normal to the flank's surface and up to the symmetry axis is frequently assumed to equal zero. This is only true, though, if certain requirements for the stress state over the entire cross section are satisfied. As figure 4.25 illustrates, this hypothesis is not supported by the simulation results – experiment data from this work is not available in sufficient depth and necessitates a correction measurement and thus is not suitable for this purpose. In figure 4.25, axial residual stresses from the carburizing heat treatment finite element simulation on the gear with module 5 mm and 18 teeth are evaluated for two pathways that are normal to the flank's surface and at various heights. The convergence requirements of the FE solver imply that the global equilibrium of the residual stresses is respected. While the higher path's integral summation of the axial stress values through the whole tooth yields a relatively low value of $58\,\mathrm{MPa} \cdot \mathrm{mm}$, the value up to the tooth symmetry axis shows an even greater excess of tensile residual stresses over compressive residual stresses. This can be explained by irregular geometry of the cross section considered and heterogeneous stress distribution. In addition, the total length and stress values differ between the path up to the symmetry axis and its continuation on the other side of the tooth. By comparison, the lengths of the left and right sections of the lower path are less different, still the first path's axial stresses appear to be mainly compressive. This means that, as opposed to equations 2.5 and 2.6, the above-mentioned equilibrium hypothesis with area under the stress curve is not always true; rather, it depends on the tooth shape, the existing residual stress gradients and the path's location and direction. This is an important precision, since this simplifying assumption is the only known analytical tool for modeling the residual stress profiles in the material depth and is employed in numerous works on TFF such as [62, 63, 46, 52] or [57].



$$\int_{path} \sigma_{ax}\, dz = \begin{cases} -234\,\text{MPa} \cdot \text{mm} \\ 87\,\text{MPa} \cdot \text{mm} \\ -97\,\text{MPa} \cdot \text{mm} \\ 58\,\text{MPa} \cdot \text{mm} \end{cases}$$

Figure 4.25: Example of FE-simulation results of axial residual stresses after case-hardening heat treatment in a gear with module 5 mm, 18 teeth and CHD = 0.9 mm. The graphic on the right depicts the stress profiles along designated colored paths, while the left displays the spatial distribution of the axial stresses. Each path's computed area under the stress curve is then presented.

4.2.f. Investigated influencing parameters on the residual stresses in carburized gears

The heat treatment simulations from table 4.3 can be used to investigate the effect of gear geometry, CHD, carbon depth profile or quenching medium on the residual stress profiles. Experiments in [47] and previously described simulation results have shown a limited effect of the quenching conditions on the residual stress depth profiles in carburized gears. In contrast, surface concentration in carbon impacted the magnitude of the compressive residual stresses at the flank surface and near-surface. It was also shown that the shape of the carbon depth profile influences the residual stress depth profile, with the transition between compressive and tensile residual stresses being shifted towards larger depths when the total diffusion depth of carbon was increased while keeping the CHD constant.

Calculations on gears show very clear trends for the impact of CHD on the residual stress profiles. Figure 4.26 left displays the predicted tangential residual stresses along *path 1* for different CHDs ranging from 0.3 mm to 0.7 mm on the gear geometry with module 3 mm. Stress profiles are shifted towards larger depths with increasing CHD. Both the maximal compressive stresses and the maximum tensile stresses are shifted in the direction of positive stresses. The effect on the position of transition between compressive and tensile stressed region is obvious, whereas no significant effect on the surface residual stresses can

be observed. Although they are not reported here, axial stresses show identical behavior in these simulations.

Very similar effects of the CHD appear on the large-sized gear with module 18 mm in figure 4.26 right. In some configurations with low CHD as compared to the gear dimensions, the tangential residual stresses exhibit a peak tensile value shortly below the transition region, whereas larger CHDs correlate with a plateau with constant tensile stresses in the whole tooth core area.

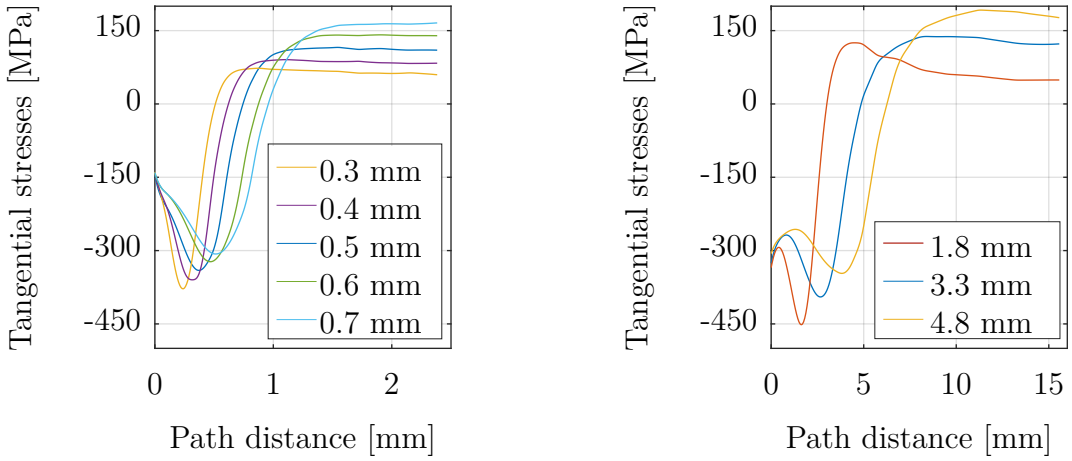


Figure 4.26: Impact of variations of CHD on the predicted tangential residual stresses on path 1 for a module 3 mm gear with 69 teeth (left) and for a module 18 mm gear with 24 teeth (right).

The residual stress profiles at pitch point are highly dependent on the tooth shape and gear size. The predicted tangential and axial residual stresses for *path 1* are shown in figure 4.27, where the x-axis of each simulation result is normalized by dividing the path distance by the CHD. The investigated gears have similar case hardness depths relative to their sizes, with $0.13\ m_n \leq \text{CHD} \leq 0.19\ m_n$. For every example under investigation, the depth that corresponds with the lowest residual stresses matches up closely. The distinctive profile of the gear with module 18 mm indicates that the gear size appears to have a considerable impact on surface stresses. The residual stresses' maximum and minimum levels of the different gears don't seem to follow any obvious patterns.

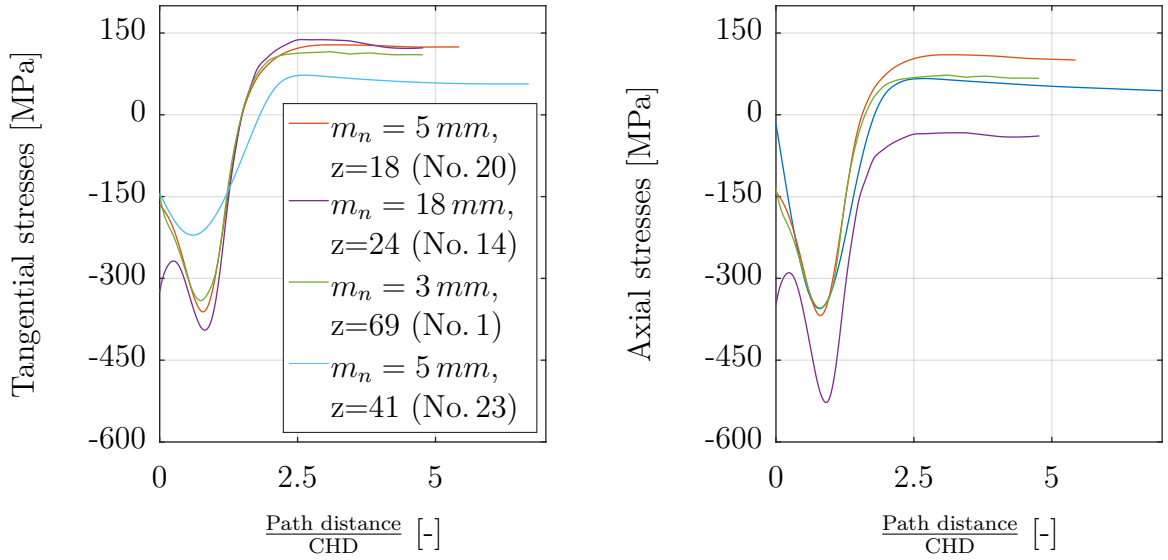


Figure 4.27: Impact of differences in shape and size of gear on the predicted tangential (left) and axial (right) residual stresses on *path 1*. Gear geometries and heat treatment conditions of the displayed simulations are detailed in table 4.3.

Chapter 5

Calculation of tooth flank fracture risks

5.1. Prediction model for load stresses

Methods

Contact loads between meshing gears can be quite complex, as they arise from the combination of several factors, including surface roughness, lubrication and dynamic conditions. Since local loads much below the flank surface primarily dictate tooth flank fracture, simpler concepts are utilized in this work. Hertzian theory-based analytical calculation models can produce satisfactory results in this case. The meshing gears in this process are described as two elastic contacting cylinders with a radius of curvature determined by the local geometry at the contact position. Equation 5.1 [58] yields the hertzian pressure $p_{h,CP}$ at the contact point CP:

$$p_{h,CP} = \sqrt{\frac{F_N}{\pi \cdot L \cdot \rho_{red,CP}} \cdot \frac{E_r}{2\pi} \cdot X_{CP}}. \tag{5.1}$$

L is the contact width. The equivalent radius of curvature $\rho_{red,CP}$ is determined from the curvature radii of both mating gears, $\rho_{1,CP}$ and $\rho_{2,CP}$, at the contact point:

$$\rho_{red,CP} = \frac{\rho_{1,CP} \cdot \rho_{2,CP}}{\rho_{1,CP} + \rho_{2,CP}}. \tag{5.2}$$

The reduced modulus of elasticity E_r can be calculated from the elastic modulus E and the Poisson coefficient ν of gears 1 and 2 through equation 5.3:

$$E_r = \frac{2}{\frac{1-\nu_1^2}{E_1} + \frac{1-\nu_2^2}{E_2}}. \tag{5.3}$$

The load sharing factor X_{CP} indicates how the contact load decreases when two pairs of teeth mesh at the same time. In this work, adequate tooth profile modifications are assumed. Thus, the load sharing factor X_{CP} as defined in ISO 6336-4 [3] runs continuously from 0 to 1 and back to 0 along the contact path, where X_{CP} is equal to 1 for contact points corresponding to single tooth contact. By using equation 5.4, one may determine

the contact pressure profile $P(x')$ in the area surrounding the contact point:

$$P(x') = \begin{cases} p_{h,CP} \cdot \sqrt{1 - \left(\frac{x'}{b_{h,CP}}\right)^2}, \text{ if } |x'| \leq b_h \\ 0, \text{ if } |x'| > b_{h,CP}, \end{cases} \tag{5.4}$$

where x' is the distance from the location of the surface point to the position of maximum applied pressure and $b_{h,CP}$ represents half of the Hertzian contact width at the contact point CP. According to equation 5.5, the parameter $b_{h,CP}$ may be expressed as a function of the load, the elastic characteristics of the gears, and the geometry of the contact:

$$b_{h,CP} = \frac{4 \cdot p_{h,CP} \cdot (1 - \nu^2) \cdot \rho_{red,CP}}{E}. \tag{5.5}$$

Using the input torque of a driving pinion on a driven gear M_1, equation 5.1 can be formulated as follows:

$$p_{h,CP} = \sqrt{\frac{M_1}{\pi \cdot L \cdot R_{b,2} \cdot \rho_{red,CP}} \cdot \frac{E_r}{2\pi} \cdot X_{CP}}, \tag{5.6}$$

where $R_{b,2}$ is the base circle radius of the driven gear. Using equations 5.4 and 5.6, the analytical pressure exerted on a surface point of the driven gear may be estimated dependent on the gear and flank geometry, the material's elastic properties and the driving torque of the pinion.

With a FORTRAN function in the Abaqus software environment, the analytical contact stresses may be imposed on the flank surface using the same geometry and three-dimensional FE-mesh as in section 4. As this procedure uses the same mesh as the heat treatment simulation, projected hardness and residual stress tensors may be easily included for the equivalent stress and failure risk calculations that follow. The load cycle is applied via a moving contact pressure and with fifty intermediate positions. Begin and end of active profile as well as positions of the lower and higher points of single pair teeth contact are calculated with a 2D contact simulation and utilized for application of the contact pressure as well as for calculation of the load sharing factor X_{CP}. Although comprehensive three-dimensional FE contact simulations can yield more accurate contact stress results, they necessitate significant computational resources and geometric aspects that are not compatible with the existing residual stress calculation technique. An example calculation of 3D FE contact stresses on the gear pair with 67/69 teeth and module 3 mm from [34] is performed and compared to the simplified calculation procedure to confirm the correctness of the used analytical approach. Surface-to-surface contact and the enhanced Lagrange method are used in the contact formulation and 0.04 is chosen as the friction coefficient.

Results

The normalized von Mises stresses obtained on *path 1* when the contact point is positioned at the gear's pitch point are shown in figure 5.1. The analytical approach can accurately replicate the contact loads, as illustrated by the comparison with simulation results produced under the identical driving torque placed on the pinion and with a full 3D contact calculation between pinion and gear. Specifically, only minor variations between the two modeling techniques are seen at depths greater than b_h ($\approx 0.42\,\text{mm}$ for the gear, load and contact point displayed in figure 5.1).

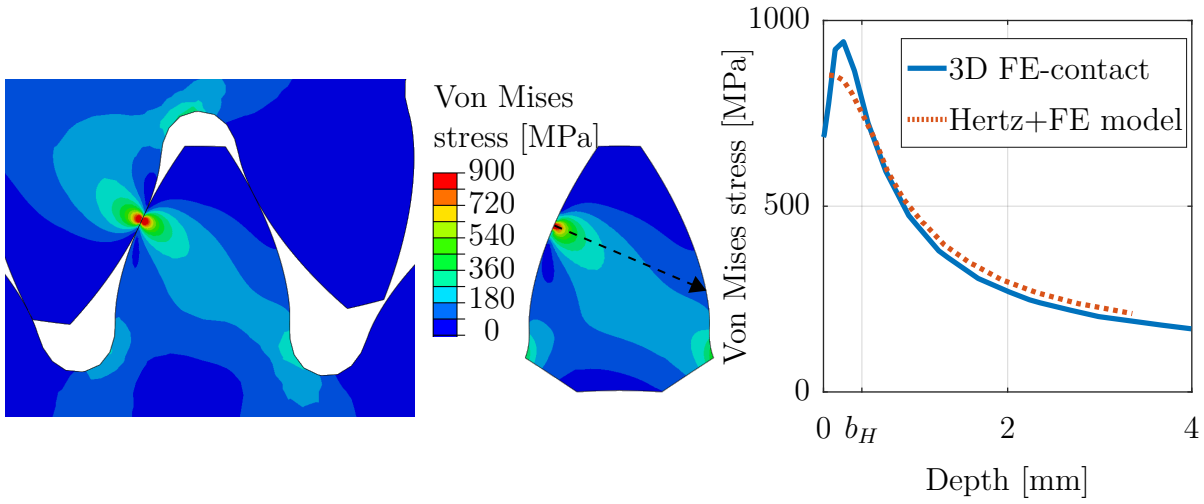


Figure 5.1: Comparison of stresses obtained in the tooth of gear with module 5 mm and 18 teeth from [157] when a 510 Nm torque is applied on the driving pinion, using either full 3D contact simulation or a combination of Hertzian theory and FE calculation.

5.2. Prediction model for tooth flank fracture

This section compares and evaluates various methods' capacities to identify the effects of some of the main influencing factors and predict TFF failure in carburized gears. Methods described in the works of Witzig [34], Böhme [52] and Meis [16] are implemented for the gear pair 67/69 with module 3 mm from [34]. The procedure outlined in section 5.1 is used to derive the contact stresses. By contrasting the fatigue prediction derived using either the Lang-model (equation 2.17) or the outcomes produced by 3D FE heat treatment simulation, the impact of the carburizing process on the TFF risks is evaluated. Making use of the simulation model, additional impacts are examined, such as those related to gear shape, case hardness depth and carbon depth profile. Using scripts written in Python and Matlab, the techniques outlined in the subsequent subsections are applied to implement the various TFF assessment methodologies. In practice, fatigue strength calculations are done

Table 5.1: Gear pairs for numerical investigation of TFF.

Source	z_1/z_2	a [mm]	m_n [mm]	α_M [°]	L [mm]	ϵ_α	d_1 / d_2 [mm]	CHD [mm]	Main failure mechanism
[103]	67/69	200	3	20	18	1.5	201.2 / 207.2	0.5	TFF
[103]	40/41	200	5	20	18	1.5	205.6 / 210.2	0.65	TFF
[157]	17/18	91.5	5	20	14	1.38	99.8 / 104.5	0.9	Pitting

for all elements located on the axial symmetry plane of the tooth segment, assuming this slice to be representative for the whole tooth. In that approach, a significant reduction in computational expenses is achieved when calculating equivalent stress or material exposure from a multi-axial non-proportional stress condition. Nevertheless, as section 4.2 illustrates, residual stresses resulting from carburizing heat treatment in gears can show significant variations in both direction and magnitude along the gear's main axis. For this reason, example calculations are also carried out for the entire tooth volume. The carburized 18CrNiMo7-6 spur gears that are examined in this section and for which fatigue and TFF data is available from literature are summarized in table 5.1. The reader can consult table 4.3 for the further CHD modifications that were explored through simulation.

5.2.a. Model based on Witzig's approach

Methods: The calculation principles presented in section 2.2.b and derived from the works of – among others – Witzig [34] are applied here. First, the equivalent shear stress is calculated for each integration point of the FE model $\tau_{eff,EL,RS}$, using the shear stress intensity hypothesis (SIH) as described in equation 2.10 for a cycle with flank contact loads superimposed with the residual stresses from heat treatment. This operation is then repeated for the last frame of the heat treatment simulation, in order to determine $\tau_{eff,RS}$. Subtracting the latter to $\tau_{eff,EL,RS}$ gives the local effective shear stress τ_{eff}, as described in equation 2.16. The calculation of the local admissible equivalent stress τ_{perm} is done with equation 2.18, where the coefficient K_{mat} is computed as in ISO 6336-4 [3] from the tooth chordal thickness and a tensile strength greater than 900 MPa and the local hardness comes from the prediction of the FE heat treatment model. The local material exposure $A = \frac{\tau_{eff}}{\tau_{perm}}$ is then computed and can be analyzed for different regions of the loaded tooth.

Similarly to equation 2.15, a *weakest-link* approach can be proposed to consider the size effect in addition to the calculated local material utilization in order to predict the failure probability $1 - P_S^{(V)}$ of the component. The equation 5.7 is used for this purpose:

$$P_S^{(V)} = 2^{-\frac{1}{V_0}\sum_{i=1}^{n_V}\left(A_i^{(V_i)}\right)^{\kappa^{(V_i)}}} . \tag{5.7}$$

V_i is the elementary volume associated with a FE integration point, A_i the local mate-

Table 5.2: Weibull module values for calculation of failure probability.

Source	Label	V_0 [mm^3]	κ [-]
Diemar [40]	A	1,272	35
Löpenhaus [58]	B	1	$\frac{8 \cdot 10^6}{\mathrm{Hv}^2}$

rial utilization and $\kappa^{(V_i)}$ the corresponding Weibull module. Weibull module values for carburized steels have rarely been documented and should only be used with considerable caution. This study tests two distinct sets of parameters, which are described in table 5.2, were applied in Diemar's and Löpenhaus's respective work and will be later referred as A and B.

Results: Figure 5.2 shows the material exposure calculated for the gear with module 3 mm from [103], CHD = 0.5 mm and a driving torque at pinion of 1, 460 Nm based on simulation results for hardness and residual stresses in the tooth's axial symmetry. The material exposure computed using Lang's approach for residual stress and hardness prediction is also given for comparison. Although the two methods provide results that are quite similar, the FE-simulation technique produces a maximal TFF-risk in a zone that is more constrained and slightly closer to the surface.

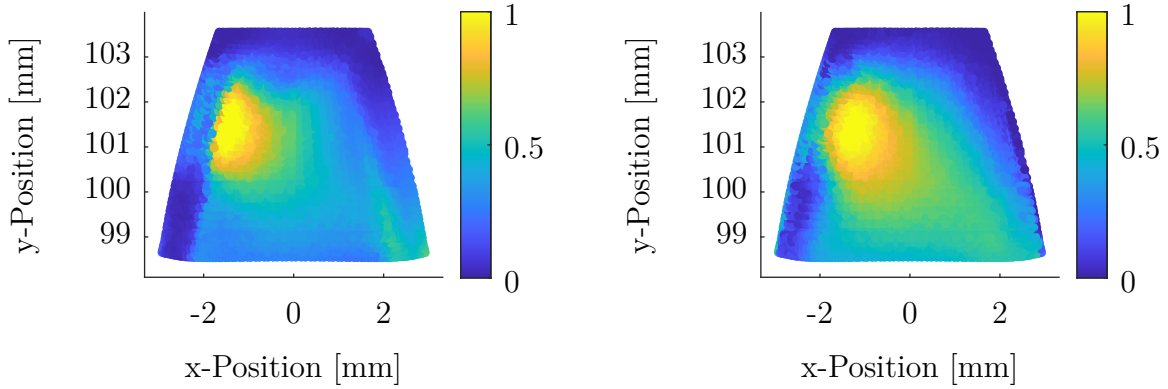


Figure 5.2: Material exposure of the gear module 3 mm and CHD = 0.5 mm from [103] when a 1, 460 Nm torque is applied on the driving pinion, using the local hardness and residual stresses from the developed simulation model (left) and from Lang's approach (right).

Figure 5.3 illustrates how both methods react similarly to variations in contact loads or in the CHD. While the material exposure reduces with increasing CHD, the primary fracture risks are well identified in the material depth under the active flank and rise with increasing driving torque.

Calculations on the gears with module 5 mm from [103] and [157] show that these gears are likely to present TFF risks when the CHD is low, as shown in figure 5.4. On the other hand, the highest material exposure shifts in the surface region when the CHD rises.

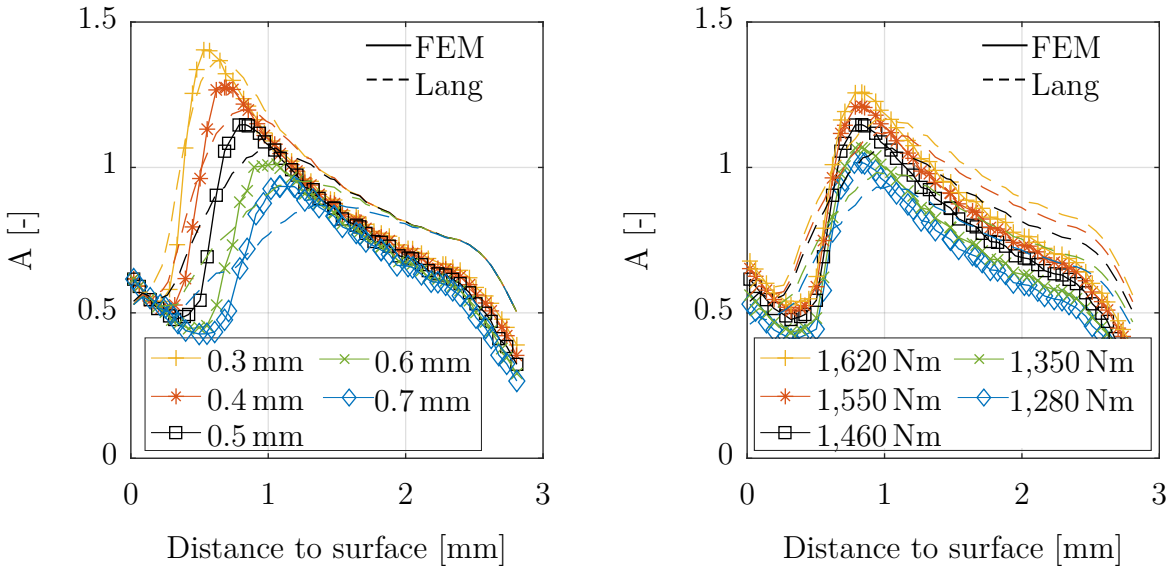


Figure 5.3: Material exposure of the gear module 3 mm from [103] when varying the case hardness depth (left, with driving moment at pinion 1, 460 Nm) and the applied torque on pinion (right, with CHD = 0.5 mm). Results from the local hardness and residual stress calculation using the developed simulation model are represented by continuous lines, whereas dashed lines are outcomes from Lang's approach.

These results are consistent with the experimental results reported in [164] and [103, 157]. TFF risks are computed for torques as low as 1, 550 Nm for the gear with 41 teeth and CHD = 0.65 mm, whereas experimental TFF-failures were only observed above 1, 700 Nm applied on the mating pinion. This suggests that the presented method may be overly conservative.

The approach from Witzig's work appears to have a good correlation with TFF-risks, based on a qualitative assessment. Moreover, considering residual stresses from heat treatment simulation increases the estimated peak of material exposure, which could push the typical threshold value of 0.8 toward the more significant critical value of 1.0. All things considered, however, the prediction accuracy of the suggested technique remains incomplete until a large-scale set of experimental TFF and non-TFF failures is examined, which is outside the scope of this work.

Using Weibull module to calculate the failure probability of gears delivers very different results, depending on the assumptions used and the gear considered. These results are shown for the gear with module 3 mm and 69 teeth with a CHD = 0.5 mm in figure 5.5. The outcomes of calculations using a constant Weibull module (A) are in good agreement with the currently available experimental data [34], with deviations in the range of 1 to 7 %. In contrast to Lang's approach, the inclusion of residual stresses and hardness from FE simulation produces a slightly overly conservative fatigue prediction. Conversely, Weibull module values based on hardness (B) as stated in [58] greatly underestimate fatigue strength

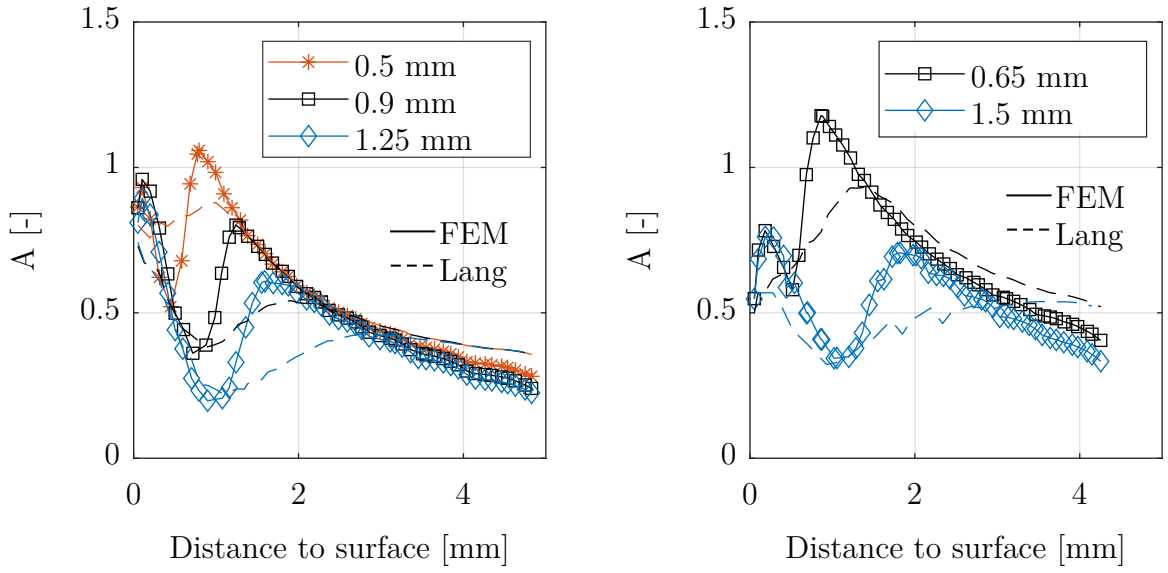


Figure 5.4: Material exposure of the gears module 5 mm from [157] (left) and [103] (right) with varying CHD and applied torque on pinion 460 Nm and 1, 720 Nm, respectively. Results from the local hardness and residual stress calculation using the developed simulation model are represented by continuous lines, whereas dashed lines are outcomes from Lang's approach.

of the gear. Because the hardness and residual stress gradients in the axial direction are relatively low, it is possible to assume that the tooth's axial symmetry plane represents the entire tooth volume in this configuration when using the simulated data as an input for the TFF calculation. This is indicated by the very slight shift of the dotted lines in the fatigue prediction compared to the continuous lines.

Applying the Weibull coefficients A from table 5.2 to the gear with module 5 mm, 41 teeth and CHD = 0.65 mm from [34] results in about 12 % understated fatigue strength against TFF when the outcomes from FE simulation are considered, figure 5.6. Interestingly, the estimated TFF risks rise further when taking into account the local hardness and residual stresses in the entire tooth volume rather than supposing them to be identical to their values in the axial symmetry plane. This may be explained by the higher stress and hardness gradients in the axial direction compared to the previously studied gear with module 3 mm. Except in situations where they are paired with residual stress and hardness profiles from Lang's method, Weibull coefficients B consistently result in a significant overestimation of TFF risks. It is not unexpected that this Weibull module only provides an adequate prediction when the residual stress calculation is done using Lang's approach, since these values were originally provided by Löpenhaus by calibrating his model to Lang's residual stress calculations and ignoring tensile residual stresses [58]. In addition, it is important to note that the experimental TFF data available are based on an extremely limited number of gear tests, so that especially results for the module 5 mm are not statistically validated.

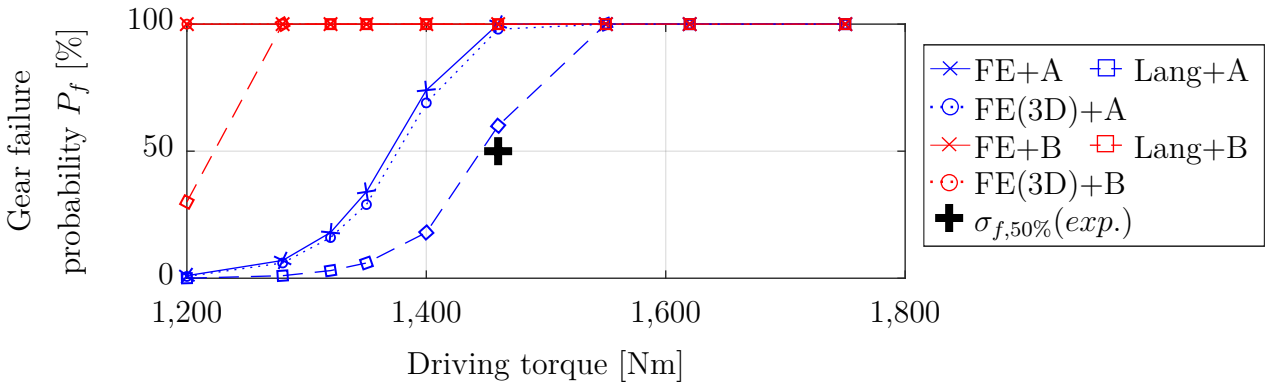


Figure 5.5: Computed failure probability of the gear module 3 mm and CHD = 0.5 mm from [34] for Witzig-based method as a function of applied torque on pinion and calculation assumptions. Results using FE-computed local hardness and residual stress for the tooth's axial symmetry plane are represented by continuous lines, calculation using simulation results from the entire tooth correspond to dotted lines, whereas dashed lines are outcomes from Lang's approach. Blue and red colors indicate Weibull coefficients A and B from table 5.2, respectively.

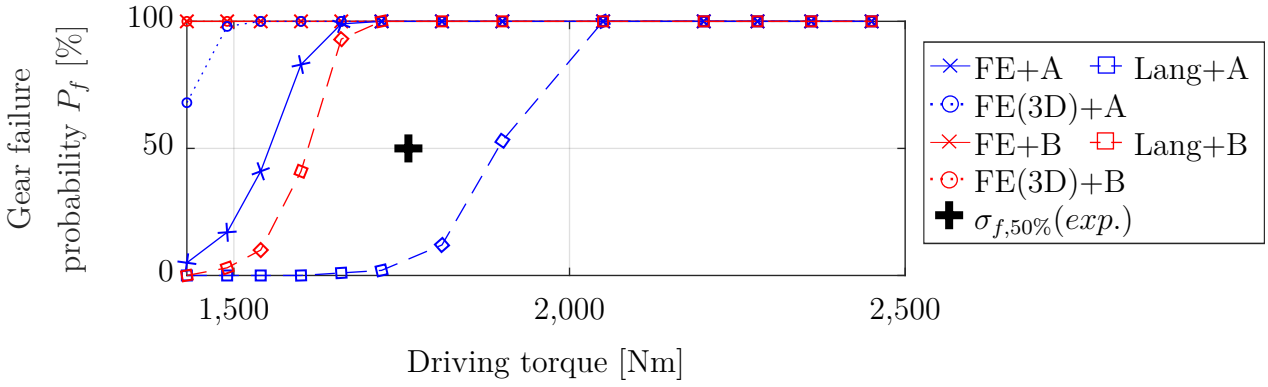


Figure 5.6: Computed failure probability of the gear module 5 mm and CHD = 0.65 mm from [34] for Witzig-based method as a function of applied torque on pinion and calculation assumptions. Results using FE-computed local hardness and residual stress for the tooth's axial symmetry plane are represented by continuous lines, calculation using simulation results from the entire tooth correspond to dotted lines, whereas dashed lines are outcomes from Lang's approach. Blue and red colors indicate Weibull coefficients A and B from table 5.2, respectively.

5.2.b. Model based on Böhme's approach

A model analogous to the one presented in [52] for the prediction of TFF is adopted here. First, the local fatigue strength under uni-axial alternating stress is determined with equation 5.8:

$$f_{-1} = \begin{cases} 1.6 \cdot H_V, \text{ for } H_V < 300 \\ \frac{1.56 \cdot (H_V + 120)}{\sqrt{area}^{\frac{1}{6}}}, \text{ for } H_V > 550 \\ 505 \text{ MPa else.} \end{cases} \tag{5.8}$$

$\sqrt{area}$ is a characteristic size of non-metallic inclusions that is assumed to be equal to $80\,\mu$m here, as in Böhme's work. Equation 2.24 enables to calculate the fatigue strength under torsional loads. Then, the developed fatigue damage criterion D_{Bo} is computed using a modification of integral models from Liu-Zenner as stated in the equations below, where $\lambda = -5 \cdot 10^{-4} \cdot H_V + \sqrt{3}$:

$$\begin{aligned} D_{Bo} &= \frac{\sqrt{\frac{15}{8\pi} \int_{\phi=0}^{\pi} \int_{\theta=0}^{2\,\pi} (a_{Bo} \tau_{\theta\phi,a}^2 + b_{Bo} \sigma_{\theta\phi,a}^2)\ (1 + c_{Bo} \sigma_{\theta\phi,m})^2 + d_{Bo} \tau_{\theta\phi,a} \tau_{\theta\phi,m})\ sin(\phi)\ d\phi\ d\theta}}{f_{-1}} \\ a_{Bo} &= \frac{1}{5}(3\lambda^2 - 4) \text{ and } b_{Bo} = \frac{1}{5}(6 - 2\lambda^2) \\ c_{Bo} &= \frac{3 f_0}{70 C}(2\lambda^2 - 11) + \sqrt{\left(\frac{3 f_0}{70 C}(11 - 2\lambda^2)\right)^2 + \frac{1}{C}\left(\left(\frac{2 f_{-1}}{f_0}\right)^2 - 1 - \frac{\lambda^2}{3}\left(\left(\frac{2 t_{-1}}{t_0}\right)^2 - 1\right)\right)} \\ d_{Bo} &= \frac{\lambda^2}{3}\left(\left(\frac{2\ t_{-1}}{t_0}\right)^2 - 1 - \frac{C^2\ t_0^2}{35\ \lambda^2}(8 - \lambda^2)\right) \text{ with } C = \frac{f_0^2}{84}(17 - 4\lambda^2) - \frac{t_0^2}{105}(8 - \lambda^2). \end{aligned} \tag{5.9}$$

By substituting A_i with the local damage parameter $D_{Bo,i}$ in equation 5.7, a failure probability of the gear can be computed. The Weibull modules that are used are the same than for the previous method and can be found in table 5.2.

Results: The material exposure obtained in the gear tooth with module 3 mm and CHD = 0.5 mm when the pinion is subjected to a torque of 1,460 Nm is shown in figure 5.7. Using Böhme's methodology, the failure risks associated with TFF are expected to be much lower than with the previously computed method from Witzig's work, irrespective of whether the FE model established here is used to calculate the hardness and local residual stresses or Lang's work. While this gear should provide significant TFF risks under the examined heat treatment and load conditions, D_{Bo} values peak below 0.8. The region where the greatest damage is anticipated is shifted to greater depths by FE-computed residual stresses in comparison to Lang's equations, and the TFF risks are somewhat increased (see figure 5.8).

The gears with module 5 mm from [157] and [103] are expected to have maximum failure risks at the surface region and in the case-core transition region, respectively. Figure 5.9

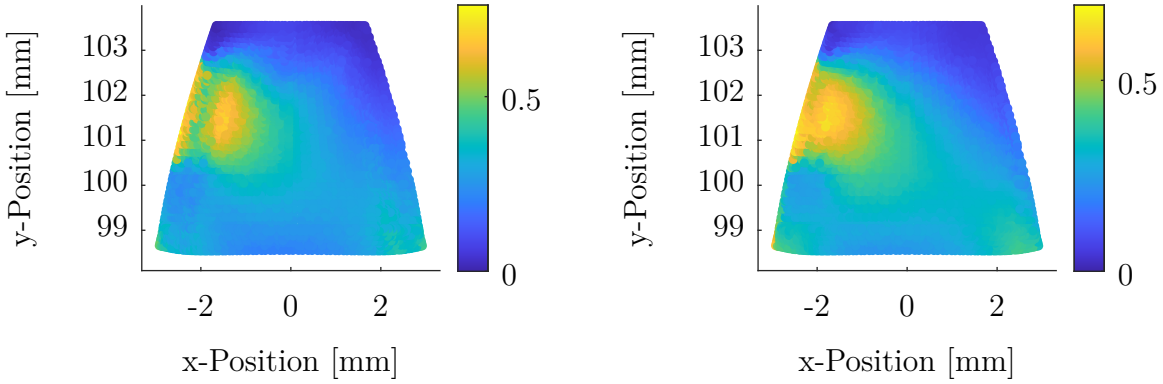


Figure 5.7: Damage parameter D_{Bo} of the gear module 3 mm and CHD = 0.5 mm from [103] when a 1,460 Nm torque is applied on the driving pinion, using the local hardness and residual stresses from the developed simulation model (left) and from Lang's approach (right).

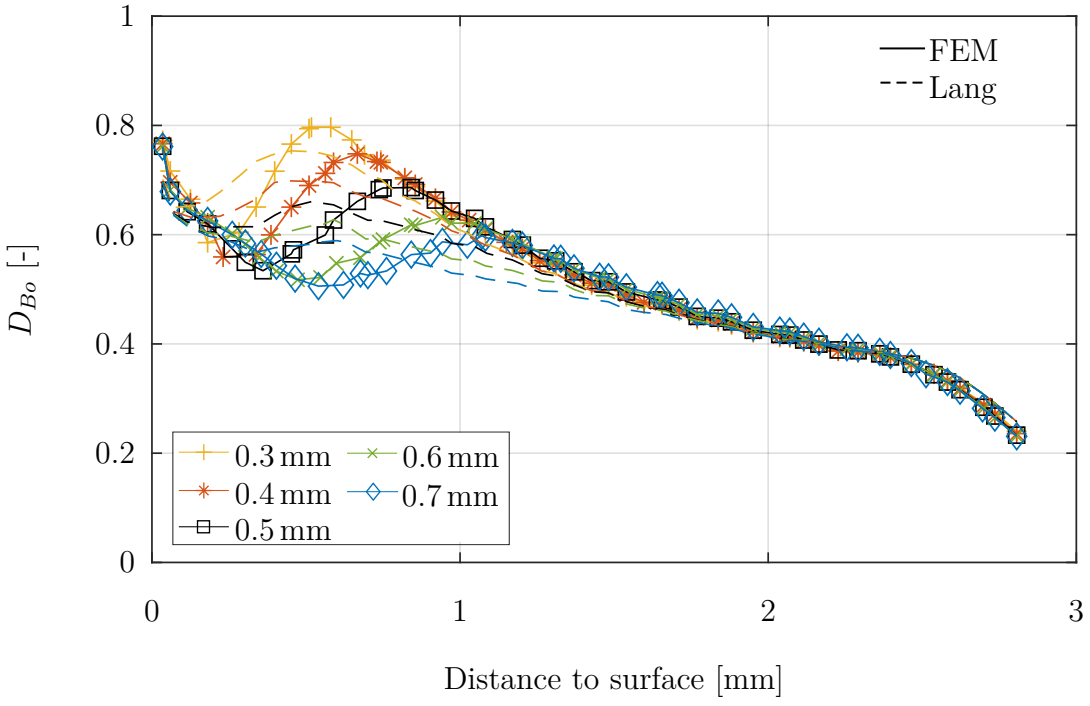


Figure 5.8: Damage parameter D_{Bo} of the gear module 3 mm from [103] when varying the case hardness depth and a 1,460 Nm torque is applied on the driving pinion. Results from the local hardness and residual stress calculation using the developed simulation model are represented by continuous lines, whereas dashed lines are outcomes from Lang's approach.

displays the local damage parameter in these gears. The predictions show a good correlation with experimental results. Nonetheless, for the investigated driving torques at the mating pinion, the corresponding damage indicator values D_{Bo} are situated far below 1, and TFF is only anticipated for contact loads significantly higher than those observed in tests.

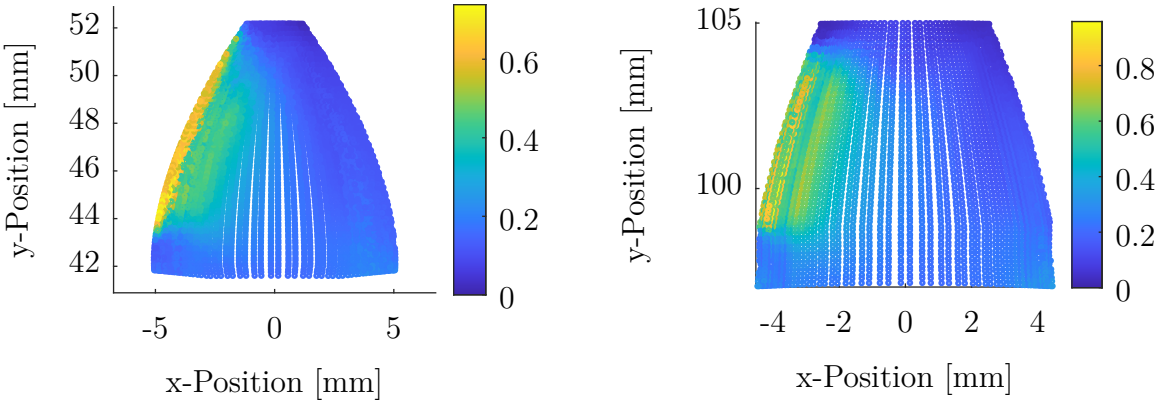


Figure 5.9: Damage parameter D_{Bo} of the gear module 5 mm from [157] with CHD = 0.90 mm and applied torque on pinion 460 Nm (left) and of gear module 5 mm from [103] with CHD = 0.65 mm and applied torque on pinion 1, 720 Nm (right). Local hardness and residual stress calculation were obtained using the developed simulation model.

Similar to the method based on Witzig's work, a quantitative assessment of Böhme's calculating approach's predicted accuracy is not feasible here due to the very limited experimental data set and lack of quantifiable predictions delivered by this method. The damage profiles and the experiment match somewhat on a qualitative level, however in the few calculated examples, the approach produces non-conservative findings. Böhme's model enables to include a parameter describing a characteristic size of non-metallic inclusions. An inclusion size parameter larger than 80 μm can be used to adapt the model to Witzig's tested gears, as the material used in [52] might be of higher quality. However, this parameter only impacts the modeled fatigue strength for hardness greater than 550 H_V and it does not significantly alter the predicted TFF risks in the core and case-core transition region.

The gear failure probability calculated with the constant Weibull module only shows limited alignment with available experimental data. The results are shown for the gear with module 3 mm and 69 teeth with a CHD = 0.5 mm in figure 5.10. Regardless of the method used to calculate the local hardness and residual stresses, calculations using a constant Weibull module predict a 0 % failure rate at load values that are substantially higher than the measured fatigue strength. A greater accuracy is produced using the hardness-dependent Weibull model, particularly when the residual stresses originate from FE simulation. According to Lang's approach, the load level has relatively little effect on the failure probability. It is important to keep in mind, nevertheless, that precise assessment of surface-initiated failures – which are not properly addressed in this work because of

the adopted contact load modeling approach – may increase the input torque's effect and improve the agreement with experimental results. Using simulated data of the entire tooth volume for TFF calculation slightly shifts the results to higher failure probabilities compared to extrapolated data from a slice of elements in the axial symmetry plane, which indicates that this method predicts failure to be more likely to happen in other regions of the tooth than near the symmetry plane.

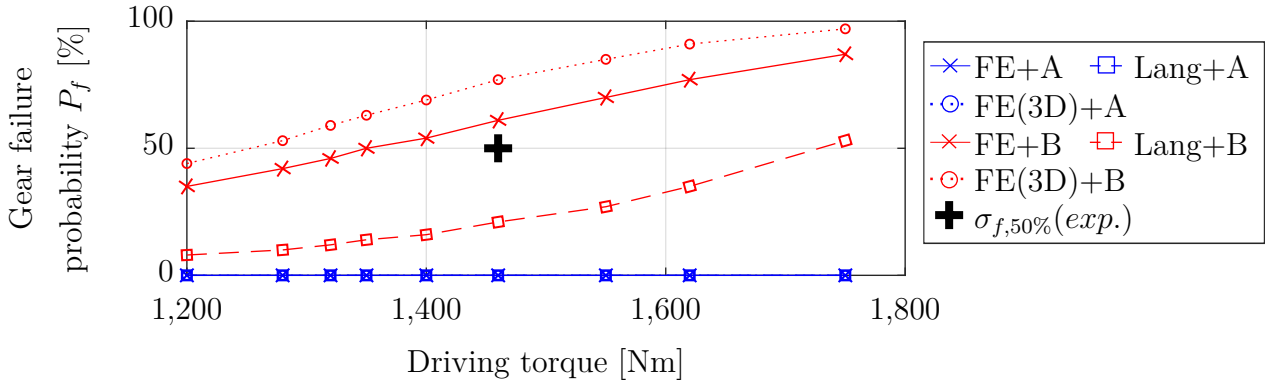


Figure 5.10: Computed failure probability of the gear module 3 mm and CHD = 0.5 mm from [34] for method from Böhme's work as a function of applied torque on pinion and calculation assumptions. Results using FE-computed local hardness and residual stress for the tooth's axial symmetry plane are represented by continuous lines, calculation using simulation results from the entire tooth correspond to dotted lines, whereas dashed lines are outcomes from Lang's approach. Blue and red colors indicate Weibull coefficients A and B from table 5.2, respectively.

Residual stresses and statistical size effect assumptions have a major impact on the results of calculations performed on the gear with module 5 mm, 41 teeth and CHD = 0.65 mm from Witzig's work [34]. Combining a hardness-dependent Weibull coefficient (B) with Lang's technique for residual stresses and hardness yields the most accurate fatigue prediction, with deviations of the predicted torque corresponding to 50 % failure probability that are under 3 %. Although taking into account the hardness and residual stress gradients from the entire 3D tooth volume somewhat improves the result, using the constant Weibull module (A) consistently overestimates the fatigue strength of this gear.

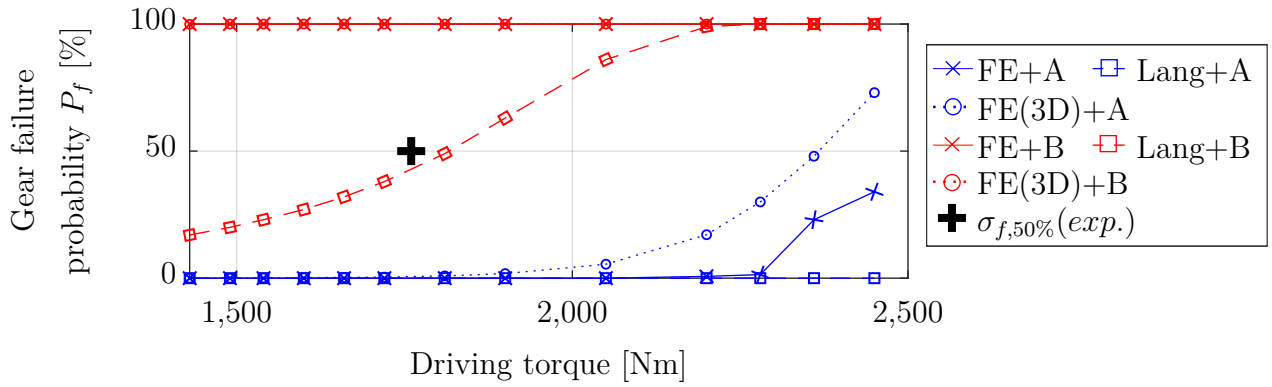


Figure 5.11: Computed failure probability of the gear module 5 mm and CHD = 0.65 mm from [34] for method from Böhme's work as a function of applied torque on pinion and calculation assumptions. Results using FE-computed local hardness and residual stress for the tooth's axial symmetry plane are represented by continuous lines, calculation using simulation results from the entire tooth correspond to dotted lines, whereas dashed lines are outcomes from Lang's approach. Blue and red colors indicate Weibull coefficients A and B from table 5.2, respectively.

5.2.c. Model based on Meis' approach

Methods: For capturing the statistical characteristics of fatigue processes like TFF caused by non-metallic inclusions, Monte-Carlo approaches offer considerable potential [57, 16]. The method of Meis [16, 123] is used for TFF prediction in this work. Using the critical plane model *KEV-Bosch* as outlined in equations 2.21, 2.22 and 2.23, the equivalent stress amplitude and equivalent mean stress are first computed for each integration point in the gear tooth. The local alternating fatigue strength of the material is approximated in a first step using $\sigma_{w0} = 1.6 \cdot \mathrm{H_V}$, under the assumption that the material is defect-free. It is also necessary to estimate the torsion fatigue strength, which may be done with equation 2.24. In the second calculation stage, assumptions are made on the function characterizing size distribution of non-metallic inclusions and on their volume concentration. Three distinct hypotheses are examined in this work:

- Case 1: Generalized extreme value distribution with mean size $\mu_{dist} = 10\,\mu$m, shape parameter $\zeta_{dist} = 0.3$, scale parameter $\sigma_{dist} = 0.75 \cdot \mu_{dist}$ and volume concentration for defects $C_d = 0.035\,\mathrm{mm}^{-3}$.
- Case 2: Generalized extreme value distribution with mean size $\mu_{dist} = 25\,\mu$m, shape parameter $\zeta_{dist} = 0.3$, scale parameter $\sigma_{dist} = 0.75 \cdot \mu_{dist}$ and volume concentration for defects $C_d = 0.05\,\mathrm{mm}^{-3}$.
- Case 3: Lognormal distribution with mean size $\mu_{dist} = 60\,\mu$m, shape parameter $\zeta_{dist} = 0.3$, standard deviation $\bar{\sigma}_{dist} = 0.75 \cdot \mu_{dist}$ and volume concentration for defects $C_d = 0.035\,\mathrm{mm}^{-3}$.

Equation 5.10 provides the probability density function of the generalized extreme value distributions for size variables $x > 0$, given the previously defined parameters [165]. Equation 5.11 expresses the lognormal probability density function [153].

$$P(X \leq x) = \begin{cases} \frac{1}{\sigma_{dist}} exp\left\{ -\left(1 + \zeta_{dist} \frac{x-\mu_{dist}}{\sigma_{dist}}\right)^{\frac{-1}{\zeta_{dist}}} \right\} \cdot \left(1 + \zeta_{dist} \frac{x-\mu_{dist}}{\sigma_{dist}}\right)^{\frac{-\zeta_{dist}-1}{\zeta_{dist}}} , \text{ if } \zeta_{dist} \neq 0 \\ \frac{1}{\sigma_{dist}} exp\left\{ -exp\left(-\frac{x-\mu_{dist}}{\sigma_{dist}}\right) - \frac{x-\mu_{dist}}{\sigma_{dist}} \right\} \text{ else} , \end{cases} \tag{5.10}$$

$$P(X \leq x) = \frac{1}{x \cdot \sigma_{dist} \cdot \sqrt{2\pi}} exp\left(\frac{-log(x - \mu_{dist})^2}{2 \cdot \sigma_{dist}^2} \right). \tag{5.11}$$

It should be mentioned that the choices of parameters for description of the distribution of material defects in this work are somewhat arbitrary and are only being made in order to see if the simulation models can anticipate how fatigue strength behaves in relation to the presence of non-metallic inclusions. To acquire quantitatively valid computation findings, future studies should fine-tune the parameters for the size distribution of defects. The distribution functions used in cases 1, 2 and 3 are shown in figure 5.12. The total number of defects considered is scaled with the number of loaded teeth. The permissible stresses are locally decreased by the presence of non-metallic inclusions. Equation 2.1 describes how the fatigue strength loss depends on the size of the inclusion and the local material hardness. Using the updated local fatigue strength values and taking non-metallic inclusions into account, the position and material exposure of the most critically loaded point in the tooth are established. The result data is recorded and the previously established size distribution functions are then used to assume new random number, position and size assignments for defects. This process is repeated until convergence and statistically significant findings are achieved. In this work, a number of 3,000 iterations is shown to be sufficient and corresponds to a computing time of around 1 minute for 500,000 material points. This method enables the prediction of the most critical positions and defect sizes for tooth flank fracture in the gear, as well as the anticipated failure percentage for the investigated load.

Results: Figure 5.13 illustrates the anticipated failure probability of the gear with module 3 mm from Witzig's investigations [34], based on assumptions made on the size distribution of non-metallic inclusions, local hardness, and residual stresses. With FE simulated stresses and *case 2* assumptions, a near-perfect agreement between the experimental data and the computed results is obtained. The fatigue strength of the gear is overestimated when alternate size distribution functions for material defects are used. The size distribution function's kind and specific parameters have a significant impact on the slope and level of the expected failure *vs* load level curve. Low mean size, concentration, and dispersion of the non-metallic inclusions greatly enhance the gear's expected fatigue strength. Because Lang's approach neglects the tensile residual stresses in the tooth core, all other factors

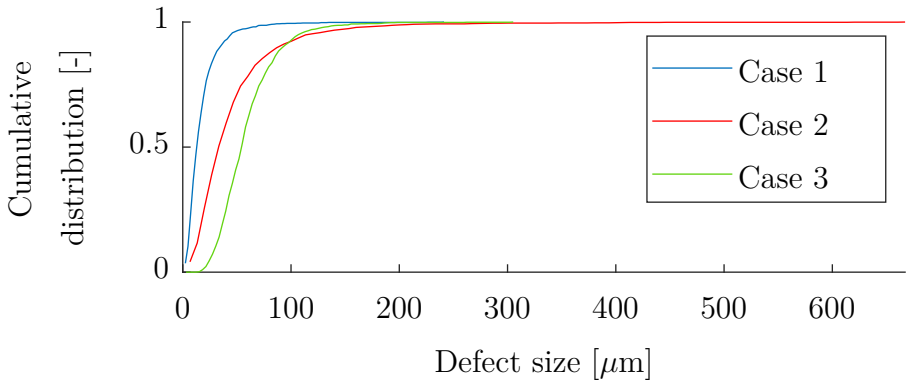


Figure 5.12: Example of size distribution of defects for the different cases investigated and a total material volume of 45,000 mm^3.

being equal, the results are substantially less conservative.

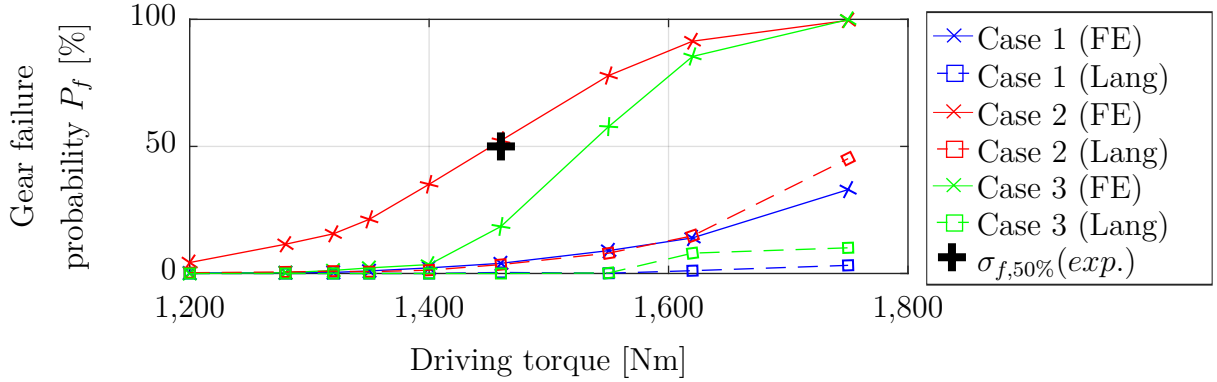


Figure 5.13: Computed failure probability of the gear module 3 mm and CHD = 0.5 mm from [34] for probabilistic method from Meis's work as a function of applied torque on pinion and calculation assumptions for non-metallic inclusions, hardness and residual stresses. FE-produced local hardness and residual stress results for the tooth's axial symmetry plane are represented by continuous lines, whereas dashed lines are outcomes from Lang's approach.

The properties of every critical defect found in 3,000 gear simulations with module 3 mm and CHD = 0.5 mm for the various size distribution assumptions are shown in figure 5.14, using the local hardness and residual stresses derived from FE heat treatment simulation. Across all materials studied for this load level, the median size of the critical defects ranges from 150 μm to 250 μm. The second assumption *case 2* results in several outliers with dimensions greater than 1 mm, whereas *case 3*'s lognormal function correlates with a smaller variation range. Although these extraordinarily large defect sizes are uncommon in fatigue tests and may suggest that the description functions being used need to be adjusted, other authors report defect areas exceeding 1 mm^2, especially when assessing optical dark area (ODA) or clusters of adjacent non-metallic inclusions [4, 16, 34]. These results are also not in direct contradiction with the comparatively small tooth thickness, as the tooth width

of 18 mm is considerably larger and is geometrically compatible with the occurrence of such defect sizes. The critical defect position for failure initiation is consistent throughout every scenario under investigation and is most likely within the range of 1.75 to 2.0 · CHD. However, *case 2*'s distribution indicates low probability failures at significantly greater depths. Figure 5.15 illustrates additional outputs from the simulation approach, such as the orientation of the critical planes determined by the *KEV-Bosch* multi-axial stress criteria and the position of these critical defects. It is anticipated that the transition between the tooth core and the carburized surface would experience the majority of failures. When exceptionally large inclusions occur in low-loaded locations, rare failures at higher depths are predicted. For a large percentage of all predicted failures, the material plane orientations at the positions identified for crack initiation (blue lines in figure 5.15) present an angle between 25° and 45° with the horizontal axis, which is slightly lower than the experimental TFF observations.

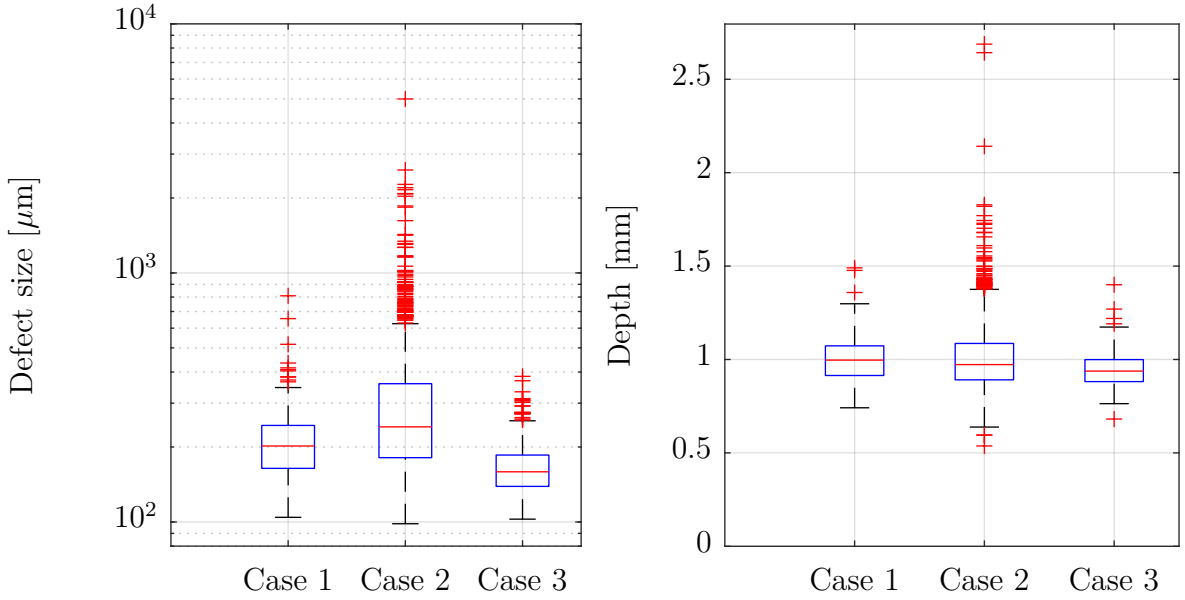


Figure 5.14: Size and depth of the defects that have been identified as critical in 3,000 simulations of the gear with module 3 mm and CHD = 0.5 mm under a load of 1,460 Nm on the pinion and for different assumptions of size distribution of non-metallic inclusions.

For the gear with module 5 mm, CHD = 0.65 mm, and 41 teeth, the observations from figure 5.13 can also be applied to figure 5.16. When coupled with hardness and residual stresses from heat treatment simulation, the second set of assumptions for the size distributions of defects results in a highly accurate estimation of the fatigue strength of the gear. The anticipated failures due to non-metallic inclusions are significantly influenced by the size distribution functions, wherein the largest defects in the heavily loaded area play a critical role. Primarily due to the disregard of tensile residual stresses in the core and

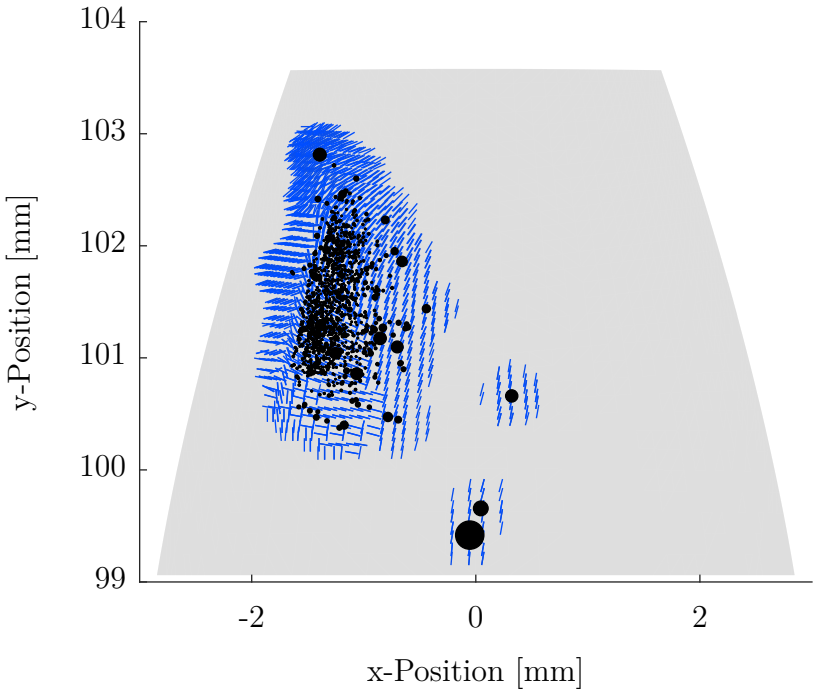


Figure 5.15: Example of computed critical planes and superimposed critical defects of 3,000 simulations on the gear module 3 mm from [34] with CHD = 0.5 mm and applied torque 1,460 Nm on pinion. Size distribution for defects is from *case 2* and the local hardness and residual stresses are predicted by FE heat treatment simulation. For clarity, the displayed defect size is multiplied by 0.05 in relation to the gear.

case-core transition area, Lang's method results in an overestimation of the gear's fatigue strength.

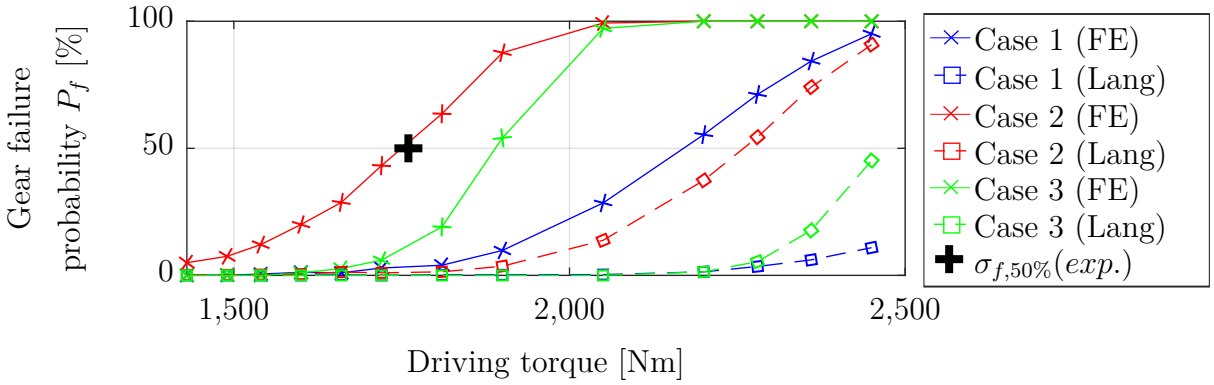


Figure 5.16: Computed failure probability of the gear module 5 mm and CHD = 0.65 mm from [34] for probabilistic method from Meis's work as a function of applied torque on pinion and calculation assumptions for non-metallic inclusions, hardness and residual stresses. FE-produced local hardness and residual stress results for the tooth's axial symmetry plane are represented by continuous lines, whereas dashed lines are outcomes from Lang's approach.

Overall, the effects of the non-metallic inclusions, statistical size effect and contact loads seem reasonable when the probabilistic technique and the chosen critical plane approach are coupled. Extensive data can be produced on the position, defect size, load levels and failure probability or material orientation of the predicted failure initiation, which can be validated or contradicted by fatigue tests. When the hardness and residual stress are provided by the developed FE heat treatment model, using the suggested parameter set with plausible input data *case 2* results in extremely good agreement on both 18CrNiMo7-6 gears from Witzig's investigations [34]. Neglecting tensile residual stresses in the carburized tooth, on the other hand, yields significantly understated probabilities of gear failure.

5.2.d. Summary of the tested TFF prediction approaches

Three different approaches were tested in this work, which were adapted from the works of Witzig [34], Böhme [52] and Meis [16] and tested under several different assumptions. The two first methods are based on integral calculation of equivalent stress values and evaluate a damage or material exposure parameter in comparison to a threshold value. For the three tested 18CrNiMo7-6 carburized gears in table 5.1, maximum exposure values for depth that approximately match to the observed gear failures may be determined using Lang's method for local hardness and residual stress calculation. It also seems that valid predictions may be made regarding the impacts of contact stress, CHD, and gear shape. Additionally, for an entire FE tooth model with 100,000 to 300,000 integration points, the local equivalent stress may be calculated in a matter of minutes, making it possible to take into account

factors like crowning or axial position-dependent hardness and residual stresses. The FE model developed for carburizing heat treatment allows for improved consideration of residual stresses and local hardness. The damage parameter D_{Bo} in Böhme's technique, or the material exposure in Witzig's method, rise when the tensile residual stresses in the core and transition area are taken into consideration. The depth profiles are different in both residual stress calculation methods, but the shift of material exposure or damage parameter is purely quantitative and not qualitatively noteworthy. Since this work covers only limited gear fatigue data and the two aforementioned methods do not predict the failure rate but instead rely on a threshold value that is, for Witzig, largely empirical, it is not possible to assess the effects of the modifications caused by the FE calculation model on the prediction accuracy for TFF. Essentially, these methods ignore material defects and the statistical size effect, despite the fact that these are two of the most important factors determining tooth flank fracture. A *weakest-link* approach has been presented to try to obtain quantitative conclusions for the failure probability of carburized gears under contact load. Gear failure probabilities were calculated using various Weibull coefficients from Diemar [40] and Löpenhaus [58]. For the two gears under investigation, none of the examined combinations produce satisfactory results. The combination of Diemar's constant-value Weibull coefficient with Witzig's approach produced the best results. In this instance, utilizing FE-computed hardness and residual stresses results in a 11 % underestimation of the load corresponding to 50 % failures for the gear module 5 mm from Witzig's tests [34] and 6 % for the fatigue strength of the gear module 3 mm. With understated fatigue strength estimates of 6 % for the module 3 mm gear and overestimation of 8 % for the second tested geometry, Lang's method produced slightly lower errors. Although taking into account the changes in hardness and residual stresses in the axial direction of the gear is expected to increase forecast accuracy, this could not be demonstrated. This parameter did not affect the TFF risks of the smallest gear for the versions and hypotheses that were studied for the statistical size effects. However, the module 5 mm gear computation with complete 3D hardness and residual stress fields from heat treatment simulation produces findings that are excessively conservative. For a given load and gear configuration, the probabilistic approach based on Meis' work [16] provides more quantitative fatigue prediction outputs, such as the failure probability or the locations and sizes of the most critical defects. This approach allows for a realistic anticipation of the impact of statistical size effect and non-metallic inclusions. Here, a combined method is suggested using the hardness and local residual stresses from the developed FE carburizing model. For the two gears under investigation, nearly complete agreement with the available TFF experimental data may be obtained under reasonable assumptions regarding the size distribution of material flaws. By contrast, the fatigue strength is much overstated when hardness and residual stress data from Lang's empirical formulae are used. There was no consideration of hardness and residual stress changes along the main axis of the gear in this probabilistic framework, due to the signifi-

cant computational cost of the critical plane approach used for equivalent stress estimation from multi-axial contact load.

Chapter 6

Conclusion

This work addresses the crucial problem of tooth flank fracture (TFF), which has become increasingly prevalent, especially in large gears used in the wind energy industry. Different TFF evaluation approaches exist, but their performance is still restricted because of the central role played by empirical considerations, statistical size effects or non-metallic inclusions that are not adequately taken into account. Among the most important shortcomings is the very simplistic consideration of the residual stresses from the carburizing heat treatment, which is specifically addressed here. To address these issues, this research proposes a novel approach combining finite element (FE) simulation of carburizing heat treatment with established TFF assessment methods. A sophisticated thermal-mechanical-metallurgical heat treatment FE model was built by utilizing extensive dilatometric experiments and material data from published research. This model incorporates essential mechanisms such as carbon-dependent phase transformations, thermal strains and strains from phase transformations and tempering, and the TRIP-effect during quenching and tempering. A large simulative parameter analysis on cylindrical samples is conducted to get an in-depth understanding of residual stresses in carburized components. The study analyzes the effects of changes in case-hardening depth (CHD), wall thickness, and height of the samples. In addition, a thorough validation of the FE heat treatment model for prediction of residual stresses in carburized gears is conducted with different sizes of gears, CHDs, quenching media and carbon depth profiles. While discrepancies are noted in certain configurations, the model consistently outperforms other existing approaches, particularly in accurately predicting tensile residual stresses in the tooth depth and the transition region between case and core. The findings from the simulation have exposed concerns regarding the residual stress equilibrium assumptions implemented in the most commonly utilized prediction methods. Integration of these simulation outcomes into existing TFF assessment frameworks, as those derived from Böhme's and Witzig's works, increases the anticipated risks of TFF. However, the exact prediction accuracy remains challenging to ascertain due to the absence of quantitative results on failure probability provided by these approaches, the possible need for updated threshold values for failure onset and the limited TFF fatigue data covered in this work. On the other hand, the probabilistic method investigated provides a realistic impact estimation of changes in contact load, CHD, gear shape and size, and material quality. Notably, near-perfect agreement with available TFF experimental data is achieved for the investigated gear pairs with plausible assumptions regarding the

size distribution of non-metallic inclusions.

Several improvement potentials and further developments can be identified. The accuracy of the residual stress prediction can still be improved, since the model yields deviations in the surface and near-surface residual stresses on some specific heat treatment configurations that are only partially understood. Applying machine learning techniques and neural networks based on extensive FE simulation studies using the heat treatment model built, it might be possible to achieve precise residual stress predictions in a more flexible and time efficient way. Additionally, extending the framework to encompass nitrided gears, induction-hardened gears, or incorporating the effects of shot peening procedures would broaden its applicability and relevance. Furthermore, enhanced modeling for TFF prediction in helical gears, which are frequently employed in heavy-duty tasks within the wind energy sector, could present a significant improvement. More importantly, it would be valuable to extend the focus beyond conventional high-cycle fatigue (HCF) concerns to include the very-high-cycle fatigue (VHCF) regime and finite fatigue life with cycles $N < 10^6$. Given the practical implications of TFF across a wide range of life cycles, such an enhanced approach is essential to advance knowledge and reduce the risks of tooth flank fracture in gear systems.

Bibliography

[1] International Energy Agency. “Net Zero Roadmap: A global pathway to keep the 1.5 °C goal in reach - 2023 Update”. In: *International Energy Agency* (2023).

[2] Global Wind Energy Council. “GWEC Global Wind Report 2023”. In: *Global Wind Energy Council: Brussels, Belgium* (2023).

[3] *ISO/TS 6336-4 Calculation of Load Capacity of Spur and Helical Gears - Part 4: Calculation of Tooth Flank Fracture Load Capacity*. International Organization for Standardization, 2019.

[4] Daniel Fuchs. “Einfluss mikroskopischer Fehlstellen auf die Zahnfußtragfähigkeit”. PhD thesis. Technische Universität München, 2023.

[5] Yukitaka Murakami. *Metal fatigue: Effects of small defects and nonmetallic inclusions*. Elsevier, 2002.

[6] Uwe Zerbst, Mauro Madia, Christian Klinger, Dirk Bettge, and Yukitaka Murakami. “Defects as a root cause of fatigue failure of metallic components. I: Basic aspects”. In: *Engineering Failure Analysis* 97 (2019), pp. 777–792. DOI: 10.1016/j.engfailanal.2019.01.055.

[7] Volker Läpple. *Einführung in die Festigkeitslehre - Lehr- und Übungsbuch*. Springer Vieweg, 2016.

[8] Dieter Radaj and Michael Vormwald. *Ermüdungsfestigkeit Grundlagen für ingenieure*. Springer, 2007.

[9] George Totten. *Handbook of residual stress and deformation of steel*. ASM International, 2008.

[10] Hideo Kitagawa. “Applicability of fracture mechanics to very small cracks or the cracks in the early stage”. In: *Proc. 2nd Int. Conf. on Mechanical Behaviour of Materials*. 1976, pp. 627–631.

[11] Joseph R. Davis. *Gear materials, properties, and manufacture*. ASM International, 2005.

[12] Dieter Liedtke. *Merkblatt 452: Einsatzhärten*. Wirtschaftsvereinigung Stahl, 2008.

[13] Shengwei Qin, Chenghao Zhang, Bang Zhang, Haiyang Ma, and Minghao Zhao. “Effect of carburizing process on high cycle fatigue behavior of 18CrNiMo7-6 steel”. In: *Journal of Materials Research and Technology* 16 (2022), pp. 11361149. DOI: 10.1016/j.jmrt.2021.12.074.

[14] Ashutosh Sharma, Min Chul Oh, and Byungmin Ahn. "Recent advances in very high cycle fatigue behavior of metals and alloysa review". In: *Metals* 10.9 (2020), p. 1200. DOI: 10.3390/met10091200.

[15] Hubert Bomas, Klaus Burkart, and Hans-Werner Zoch. "VHCF behaviour of case-hardened specimens made of two grades of steel SAE 5120 differing in microstructure". In: *International Journal of Fatigue* 60 (2014), pp. 63–73. DOI: 10.1016/j.ijfatigue.2012.10.001.

[16] Jean-André Meis. "Probabilistische Modellierung der Dauerfestigkeit randschichtverfestigter Stahle". PhD thesis. RWTH Aachen University, 2023.

[17] Matthias Spickenreuther. "Untersuchungen zur Berechnung der Dauerfestigkeit von Randschichtgehärteten Dieseleinspritzdüsen". PhD thesis. Technische Universität Ilmenau, 2007.

[18] Roland Rennert. *Rechnerischer Festigkeitsnachweis für Maschinenbauteile, 6. Überarbeitete Ausgabe*. VDMA-Verlag, 2012.

[19] *DIN 743 calculation of load capacity of shafts and axles*. Deutsches Institut für Normung, 2012.

[20] Erwin Haibach. *Betriebsfestigkeit*. Springer-Verlag Berlin Heidelberg, 2006.

[21] M. F. Garwood. *Interpretation of tests and correlation with service*. ASM, 1951.

[22] Bernd Winderlich. "Das Konzept der Lokalen Dauerfestigkeit und seine Anwendung auf martensitische Randschichten, Insbesondere Laserhärtungsschichten". In: *Materialwissenschaft und Werkstofftechnik* 21.10 (1990), pp. 378–389. DOI: 10.1002/mawe.19900211006.

[23] Masae Sumita, Iku Uchiyama, and Toru Araki. "The Effect of Inclusions on Fatigue Properties of Steels with Various Matrixes". In: *Tetsu-to-Hagane* 57.2 (1971), pp. 298–334. DOI: 10.2355/tetsutohagane1955.57.2_298.

[24] Fouad Belgassem Abudaia. "Microstructure and fatigue strength of High Performance Gear Steels". PhD thesis. University of Newcastle upon Tyne, 2003.

[25] Steffen Rödling, Jürgen Fröschl, Manfred Hück, and Matthias Decker. "Einfluss nichtmetallischer Einschlüsse auf zulässige HCF-Bemessungskennwerte". In: *Materials Testing* 53.78 (2011), pp. 455–462. DOI: 10.3139/120.110250.

[26] Carolin Wickborn. "Erweiterung der Flankentragfähigkeitsberechnung von Stirnrädern in der Werkstofftiefe Einfluss von Werkstoffeigenschaften und Werkstoffdefekten". PhD thesis. Technische Universität München, 2017.

[27] *DIN 10247 Metallographische Prüfung des Gehaltes nichtmetallischer Einschlüsse in Stählen mit Bildreihen: Deutsche Fassung Pren 10247:2017*. Deutsches Institut für Normung, 2017.

[28] *SEP 1571-1 Bewertung von Einschlüssen in Edelstählen auf Basis der Einschlussflächen - Teil 1: Grundlagen*. Beuth Verlag, 2017.

[29] Junbiao Lai, Thore Lund, Karin Rydén, Antonio Gabelli, and Ingemar Strandell. "The fatigue limit of bearing steels part I: A pragmatic approach to predict very high cycle fatigue strength". In: *International Journal of Fatigue* 38 (2012), pp. 155–168. DOI: 10.1016/j.ijfatigue.2011.09.015.

[30] Chong Wang, Johann Petit, Zhiyong Huang, and Danièle Wagner. "Investigation of crack initiation mechanisms responsible for the fish eye formation in the very high cycle fatigue regime". In: *International Journal of Fatigue* 119 (2019), pp. 320–329. DOI: 10.1016/j.ijfatigue.2018.06.016.

[31] Uwe Zerbst, Mauro Madia, Christian Klinger, Dirk Bettge, and Yukitaka Murakami. "Defects as a root cause of fatigue failure of metallic components. II: Non-metallic inclusions". In: *Engineering Failure Analysis* 98 (2019), pp. 228–239. DOI: 10.1016/j.engfailanal.2019.01.054.

[32] Junbiao Lai and Yuri Kadin. "Towards a better understanding of material imperfections". In: *Evolution SKF* 3 (2018), pp. 26–30. DOI: 10.3390/cryst12020200.

[33] Stephan André Böhme, Alexei Vinogradov, Horst Biermann, Anja Weidner, Alexander Schmiedel, and Sebastian Henkel. "Fatigue of carburised CrNiMo Steel: Testing and Modelling Concept". In: *Fatigue & Fracture of Engineering Materials & Structures* 44.3 (2020), pp. 788–804. DOI: 10.1111/ffe.13394.

[34] Jochen Witzig. "Flankenbruch - eine grenze der zahnradtragfähigkeit in der Werkstofftiefe". PhD thesis. Technische Universität München, 2012.

[35] Chao Gu, Junhe Lian, Ziyu Lv, and Yanping Bao. "Microstructure-based fatigue modeling with residual stresses: Effect of inclusion shape on very high cycle fatigue life". In: *Crystals* 12.2 (2022), p. 200. DOI: 10.3390/cryst12020200.

[36] *ISO 6336-5 Calculation of load capacity of spur and helical gears - Part 5: strength and quality of materials*. International Organization for Standardization, 2016.

[37] Eberhard Velten. "Entwicklung eines Schwingfestigkeitskonzeptes zur Berechnung der Dauerfestigkeit thermochemisch randschichtverfestigter Bauteilähnlicher Proben". PhD thesis. Technische Hochschule Darmstadt, 1984.

[38] Eckard Macherauch, Helmut Wohlfahrt, and Ulrich Wolfstieg. "Zur zweckmäßigen definition von Eigenspannungen". In: *HTM Journal of Heat Treatment and Materials* 28.3 (1973), pp. 201–211. DOI: 10.1515/htm-1973-280305.

[39] Božidar Liščić. *Quenching theory and Technology*. CRC Press, 2010.

[40] Andreas Diemar. "Simulation des Einsatzhärtens und Abschätzung der Dauerfestigkeit Einsatzgehärteter Bauteile". PhD thesis. Bauhaus-Universität Weimar, 2007.

[41] Eckard Macherauch and Helmut Wohlfahrt. “Eigenspannungen und Ermüdung”. In: *Ermüdungsverhalten metallischer Werkstoffe*. Deutsche Gesellschaft fur Metallkunde, 1983.

[42] Helmut Wohlfahrt. *Einfluss von Mittelspannungen und Eigenspannungen auf die Dauerfestigkeit*. 661. VDI- Berichte, 1988.

[43] Daniel Zuber. “Fußtragfähigkeit einsatzgehärteter Zahnräder unter Berücksichtigung lokaler Materialeigenschaften”. PhD thesis. RWTH Aachen University, 2008.

[44] Matthias Schleicher, Hubert Bomas, and Peter Mayr. “Berechnung der Dauerfestigkeit von gekerbten und mehrachsig beanspruchten Proben aus dem einsatzgehärteten Stahl 16MnCrS5*”. In: *HTM Journal of Heat Treatment and Materials* 56.2 (2001), pp. 84–94. DOI: 10.1515/htm-2001-0024.

[45] Brian Shaw. “The role of residual stress on the fatigue strength of high performance gearing”. In: *International Journal of Fatigue* 25.911 (2003), pp. 1279–1283. DOI: 10.1016/j.ijfatigue.2003.08.014.

[46] Ralf Weber. “Auslegungskonzept gegen Volumenversagen bei einsatzgehärteten Stirnrädern”. PhD thesis. Universität Kassel, 2015.

[47] Valérian Iss, Nicolai Haupt, and Daniel Müller. *FVA 835 I: Erweiterte Berechnung der Flankenbruchgefährdung einsatzgehärteter Zahnräder unter besonderer Berücksichtigung des Eigenspannungszustands in größerer Werkstofftiefe*. Heft 1507. Forschungsvereinigung Antriebstechnik e.V., 2022.

[48] Ali Rajaei. “Integrierte Wärmebehandlungssimulation und Berechnung der Fußtragfähigkeit von Sinterzahnrädern”. PhD thesis. RWTH Aachen University, 2023.

[49] Darrell Socie and Gary Marquis. *Multiaxial fatigue*. SAE International, 1999.

[50] Jiping Liu and Harald Zenner. “Berechnung der Dauerschwingfestigkeit bei mehrachsiger Beanspruchungteil 1”. In: *Materialwissenschaft und Werkstofftechnik* 24.7 (1993), pp. 240–249. DOI: 10.1002/mawe.19930240706.

[51] Andrea Carpinteri, Andrea Spagnoli, and Sabrina Vantadori. “A review of multiaxial fatigue criteria for random variable amplitude loads”. In: *Fatigue & Fracture of Engineering Materials & Structures* 40.7 (2017), pp. 1007–1036. DOI: 10.1111/ffe.12619.

[52] Stephan André Böhme, Alexei Vinogradov, Jan Papuga, and Filippo Berto. “A novel predictive model for multiaxial fatigue in carburized bevel gears”. In: *Fatigue & Fracture of Engineering Materials & Structures* 44.8 (2021), pp. 2033–2053. DOI: 10.1111/ffe.13475.

[53] Franco Concli, Lorenzo Maccioni, Lorenzo Fraccaroli, and Luca Bonaiti. "Early crack propagation in single tooth bending fatigue: Combination of finite element analysis and critical-planes fatigue criteria". In: *Metals* 11.11 (2021), p. 1871. DOI: 10.3390/met11111871.

[54] Peter Oster. "Beanspruchung der Zahnflanken unter Bedingungen der Elastohydrodynamik". PhD thesis. Technische Universität München, 1982.

[55] Armin Simbürger. "Festigkeitsverhalten zäher Werkstoffe bei einer mehrachsigen, phasenverschobenen Schwingbeanspruchung mit körperfesten und veränderlichen Hauptspannungseinrichtungen". PhD thesis. Technische Hochschule Darmstadt, 1975.

[56] Tobias Hertter. "Rechnerischer Festigkeitsnachweis der Ermüdungstragfähigkeit vergüteter und einsatzgehärteter Stirnräder". PhD thesis. Technische Universität München, 2003.

[57] Philip Konowalczyk. "Grübchen- und Zahnflankenbruchtragfähigkeit Großmoduliger stirnräder". PhD thesis. RWTH Aachen University, 2018.

[58] Christoph Löpenhaus. "Untersuchung und Berechnung der Wälzfestigkeit im scheiben- und zahnflankenkontakt". PhD thesis. RWTH Aachen University, 2015.

[59] Ky Dang Van, Bernard Griveau, and Olivier Message. "On a new multiaxial fatigue limit criterion: theory and application". In: *Biaxial and multiaxial fatigue, EGF* 3 (1989), pp. 479–496.

[60] Ky Dang-Van. "Macro-micro approach in high-cycle multiaxial fatigue". In: *ASTM Special Technical Publication* 1191 (1993), pp. 120–120.

[61] Stephan André Böhme, Joni Keski-Rahkonen, and Tami Komssi. "A standardizable approach for tooth flank fracture". In: *Forschung im Ingenieurwesen* 86.4 (2022), pp. 693–708. DOI: 10.1007/s10010-022-00599-7.

[62] Dhafer Ghribi and Michel Octrue. "Some theoretical and simulation results on the study of the tooth flank breakage in cylindrical gears". In: *International gear conference*. 2014, pp. 26–28.

[63] Dhafer Ghribi, Michel Octrue, and Philippe Sainsot. "Comparative study of the tooth flank fracture in cylindrical gears - Efficient method to asses the risk of the tooth flank fracture on the cylincrical gears". In: *International Conference on Gears*. 2015.

[64] Michel Octrue, Dhafer Ghribi, and Philippe Sainsot. "A contribution to study the tooth flank fracture (TFF) in cylindrical gears". In: *Procedia engineering* 213 (2018), pp. 215–226. DOI: 10.1016/j.proeng.2018.02.023.

[65] Tomasz Tomaszewski. "Statistical size effect in fatigue properties for mini-specimens". In: *Materials* 13.10 (2020), p. 2384. DOI: 10.3390/ma13102384.

[66] Shun-Peng Zhu, Yang Ai, Ding Liao, José AFO Correia, Abílio MP De Jesus, and Qingyuan Wang. "Recent advances on size effect in metal fatigue under defects: a review". In: *International Journal of Fracture* (2021), pp. 1–23. DOI: 10.1007/s10704-021-00526-x.

[67] Erich Siebel. "Ungleichformige Spannungsverteilung bei Schwingender Beanspruchung". In: *VDIZ* 97.5 (1955), pp. 121–126.

[68] Cord Petersen. "Die Vorgänge im zügig und wechselnd beanspruchten Metallgefüge III: Der technische Größeneinfluß glatter und gekerbter Stäbe bei Wechselbeanspruchung als Wirkung des Spannungsgefälles". In: *International Journal of Materials Research* 42.6 (1951), pp. 161–170. DOI: 10.1515/ijmr-1951-420601.

[69] Roberto Kuguel. "Relation between theoretical stress concentration factor KT and fatigue notch factor KF according to highly stressed volume approach". In: *TAM R 184* (1960).

[70] Celtin Morris Sonsino. "Zur Bewertung des Schwingfestigkeitsverhaltens von Bauteilen mit Hilfe örtlicher Beanspruchungen". In: *Konstruktion* 45.1 (1993), pp. 25–33.

[71] Andrea Tridello, Carlo Boursier Niutta, Filippo Berto, and Davide S Paolino. "Size-effect in very high cycle fatigue: a review". In: *International Journal of Fatigue* 153 (2021), p. 106462. DOI: 10.1016/j.ijfatigue.2021.106462.

[72] Waloddi Weibull. "A statistical theory of strength of materials". In: *IVB-Handl.* (1939).

[73] Karl Heinz Kloos. "Einfluß des Oberflächenzustandes und der Probengröße auf die Schwingfestigkeitseigenschaften." In: *VDI- Berichte* (1976).

[74] *Heat Treating - ASM Handbook*. ASM International, 1991.

[75] *ISO 18203 Steel - Determination of the Thickness of Surface-Hardened Layers*. International Organization for Standardization, 2016.

[76] Eckard Macherauch and Otmar Vöhringer. "Residual stresses after quenching". In: *Theory and Technology of Quenching: A Handbook*. Springer, 1992, pp. 117–181.

[77] Karl Heinz Kloos. "Größeneinfluß und Dauerfestigkeitseigenschaften unter besonderer Berücksichtigung optimierter Oberflächenbehandlung". In: *Materialwissenschaft und Werkstofftechnik* 12.4 (1981), pp. 134–142. DOI: 10.1002/mawe.19810120406.

[78] Thomas Tobie. *FVA 271 I: Einfluss der Einsatzhärtetiefe auf die Grübchen- und Zahnfußtragfähigkeit großer Zahnräder*. Heft 622. Forschungsvereinigung Antriebstechnik e.V., 2001.

[79] Thomas Tobie. "Zur Grübchen-und Zahnfußtragfähigkeit einsatzgehärteter Zahnräder". PhD thesis. Technische Universität München, 2001.

[80] Christian Güntner, Thomas Tobie, and Karsten Stahl. *FVA 740 I: Einflüsse aus Baugröße, Härtbarkeit und Einsatzhärtungstiefe und deren Gesamtwirkung auf die Zahnfußtragfähigkeit einsatzgehärteter Stirnräder größerer Baugröße*. Heft 1303. Forschungsvereinigung Antriebstechnik e.V., 2018.

[81] Sacha Laue, Cchristian Thoben, Hubert Bomas, Roland Schröder, and Reinhold Kienzler. "Untersuchungen zum Einfluss des Aufkohlungsverfahrens auf die Dauerfestigkeit des Einsatzstahls 16MnCr5: Erster Teil: Einleitung–Werkstoff, Probenform und Wärmebehandlung–Charakterisierung der wärmebehandelten Proben-Literatur". In: *HTM Journal of Heat Treatment and Materials* 60.4 (2005), pp. 229–239. DOI: 10.3139/105.100345.

[82] Richard J. Katemi. "Influence of carbonitriding process on phase transformation during case hardening, retained austenite and residual stresses". PhD thesis. Universität Bremen, 2019.

[83] Patrick C. Kramer. "An investigation of rolling-sliding contact fatigue damage of carburized gear steels". PhD thesis. Colorado School of Mines, 2013.

[84] Thomas Tobie, Frank Hippenstiel, and Hardy Mohrbacher. "Optimizing Gear Performance by alloy modification of carburizing steels". In: *Metals* 7.10 (2017), p. 415. DOI: 10.3390/met7100415.

[85] Dennis P. Townsend. *Dudley's gear handbook*. McGraw-Hill, 1992.

[86] Vincenzo Vullo. *Tooth Flank Breakage Load Carrying Capacity of Spur and Helical Gears*. Springer, 2020.

[87] Matjaž Šraml and Jože Flašker. "Computational approach to contact fatigue damage initiation analysis of gear teeth flanks". In: *The International Journal of Advanced Manufacturing Technology* 31 (2007), pp. 1066–1075. DOI: 10.1007/s00170-005-0296-2.

[88] Alessandro Stenico. "Werkstoffmechanische Untersuchungen zur Zahnfußtragfähigkeit einsatzgehärteter Zahnräder". PhD thesis. Technische Universität München, 2007.

[89] Karsten Stahl, Bernd-Robert Höhn, and Thomas Tobie. "Tooth flank breakage: influences on subsurface initiated fatigue failures of case hardened gears". In: *International Design Engineering Technical Conferences and Computers and Information in Engineering Conference*. Vol. 55928. American Society of Mechanical Engineers. 2013. DOI: 10.1115/DETC2013-12183.

[90] Erwin Bauer. "Beispiele für Verzahnungsschäden, ausgehend von innenliegenden Fehlstellen". In: *Allianz Report* 68 (1995), pp. 230–238.

[91] J. Gärtner. "Betriebsverhalten Hochbelasteter Kegelradsätze in Traktoren". In: *Berichtsband zur Tagung Innovationen Rund ums Kegelrad* (1998).

[92] Erwin Bauer. “Flankenbrüche bei Hochleistungsgetrieben”. In: *Allianz Report* 71 (1998), pp. 79–87.

[93] Magnus Mackaldener and Mårten Olsson. “Interior fatigue fracture of gear teeth”. In: *Fatigue & Fracture of Engineering Materials & Structures* 23.4 (2000), pp. 283–292.

[94] Magnus Mackaldener and Mårten Olsson. “Tooth interior fatigue fracture - computational and material aspects”. In: *International journal of fatigue* 23.4 (2001), pp. 329–340. DOI: 10.1016/S0142-1123(00)00099-2.

[95] Magnus Mackaldener. “Tooth Interior Fatigue Fracture & Robustness of Gears”. PhD thesis. Royal Institute of Technology, Stockholm, 2001.

[96] Baydu Al and Paul Langlois. “Analysis of tooth interior fatigue fracture using boundary conditions from an efficient and accurate loaded tooth contact analysis”. In: *British Gears Association (BGA) Gears 2015 Technical Awareness Seminar, 12th of November*. 2015.

[97] Rainer Annast. *FVA 240 II: Flankentragfähigkeit und Laufverhalten von hart-feinbearbeiteten Kegelrädern, Schadensform Flankenbruch*. Heft 690. Forschungsvereinigung Antriebstechnik e.V., 2003.

[98] Rainer Annast. “Kegelrad-Flankenbruch”. PhD thesis. Technische Universität München, 2003.

[99] Carolin Wickborn. *FVA 556 II: Entwicklung eines erweiterten Berechnungsverfahrens zur Ermittlung optimaler Zahnflankentragfähigkeit bis in den Bereich großer Werkstofftiefen - Ergänzungsversuche zur Verifizierung an größeren Zahnrädern*. Heft 1069. Forschungsvereinigung Antriebstechnik e.V., 2013.

[100] Daniel Fuchs. *FVA 293 IV: Untersuchungen zum Fehlstellenversagen an Zahnrädern und deren Einfluss auf die Zahnradtragfähigkeit*. Heft 1439. Forschungsvereinigung Antriebstechnik e.V., 2021.

[101] Philip Konowalczyk. *FVA 695 I: Einfluss des Abschliffbetrags auf die Zahnflankentragfähigkeit großmoduliger einsatzgehärteter Zahnräder*. Heft 1267. Forschungsvereinigung Antriebstechnik e.V., 2021.

[102] Stefan Bruckmeier. “Flankenbruch bei Stirnradgetrieben”. PhD thesis. Technische Universität München, 2006.

[103] Jochen Witzig. *FVA 556 I: Entwicklung eines erweiterten Berechnungsverfahrens zur Ermittlung optimaler Zahnflankentragfähigkeit bis in den Bereich großer Werkstofftiefen*. Heft 1000. Forschungsvereinigung Antriebstechnik e.V., 2012.

[104] Ivan Boiadjiev, Jochen Witzig, Thomas Tobie, and Karsten Stahl. "Tooth flank fracture - basic principles and calculation model for a sub-surface-initiated fatigue failure mode of case-hardened gears". In: *Proceedings of the International Gear Conference, Lyon, France*. 2014, pp. 26–28.

[105] Daniel Müller, Thomas Tobie, and Karsten Stahl. "Enhanced Calculation Method for Tooth Flank Fracture Risk with Consideration of Tensile Residual Stresses in Larger Material Depths". In: *Gear technology* 40.6 (2023), pp. 58–71.

[106] Daniel Müller, Thomas Tobie, and Karsten Stahl. "Calculation of sub-surface-initiated fatigue fractures in gears". In: *COMPLAS XV: proceedings of the XV International Conference on Computational Plasticity: fundamentals and applications*. CIMNE. 2019, pp. 189–200.

[107] Fabian Goergen, Christian Brecher, and Jens Brimmers. "WZL-double pulsator analogy test rig for the generation of tooth flank fractures at large-module spur and helical gears". In: *Forschung im Ingenieurwesen* 85 (2021), pp. 77–87. DOI: 10.1007/s10010-020-00432-z.

[108] Fabian Goergen, Johannes Rolzhäuser, Dieter Mevissen, and Christian Brecher. "Analogy test rig for the generation of tooth flank fractures at large gears (WZL-double pulsator) commissioning and first test results". In: *Forschung im Ingenieurwesen* 87.1 (2023), pp. 51–60.

[109] Dirk-Olaf Leimann and Wim Smet. "Calculation of Tooth Flank Fracture Load Capacity acc. to the method of Leimann". In: *Conference for Wind Power Drives 2019: Conference Proceedings*. BoD–Books on Demand. 2019, p. 51.

[110] Christian Wirth, Bernd-Robert Höhn, and Christo Braykoff. "New methods for the calculation of the load capacity of bevel and hypoid gears". In: *AGMA Technical Paper 12FTM15* (2012).

[111] Viktor Hauk and Herfried Behnken. *Structural and residual stress analysis by Nondestructive Methods: Evaluation - Application - Assessment*. Elsevier, 2006.

[112] Baydu Al, Rupesh Patel, and Paul Langlois. "Finite element analysis of tooth flank fracture using boundary conditions from LTCA". In: *Gear Technology* 9.10 (2016), pp. 62–68.

[113] Baydu Al, Rupesh Patel, and Paul Langlois. "Comparison of tooth interior fatigue fracture load capacity to standardized gear failure modes". In: *FTM (Fall Technical Meeting)*. 2016.

[114] Otto R Lang and R Kernen. "Dimensionierung komplizierter Bauteile aus Stahl im Bereich der Zeit-und Dauerfestigkeit". In: *Materialwissenschaft und Werkstofftechnik* 10.1 (1979), pp. 24–29. DOI: 10.1002/mawe.19790100108.

[115] Stefan Beermann and Ulrich Kissling. "Tooth Flank Fracture - A Critical Failure Mode Influence of Macro and Micro Geometry". In: *KISSsoft User Conference, Pune, India, Nov.* 2015, pp. 25–26.

[116] Joachim Thomas. "Flankentragfähigkeit und Laufverhalten von hartfeinbearbeiteten Kegelrädern". PhD thesis. Technische Universität München, 1998.

[117] *ISO 6336-3 Calculation of Load Capacity of Spur and Helical Gears - Part 3: Calculation of Tooth Bending Strength.* International Organization for Standardization, 2019.

[118] Huaiju Liu, Wei Wang, Caichao Zhu, Chenxu Jiang, Wei Wu, and Robert G Parker. "A microstructure sensitive contact fatigue model of a carburized gear". In: *Wear* 436 (2019), p. 203. DOI: 10.1016/j.wear.2019.203035.

[119] Andreas Diemar, Jörg Hildebrand, Uwe Gerth, and Carsten Könke. "Simulation-based optimization of the local material state in the field of cyclically highly stressed case hardened construction details with notch effect". In: *Materialwissenschaft und Werkstofftechnik* 48.7 (2017), pp. 629–638. DOI: 10.1002/mawe.201600715.

[120] Daming Tong, Jianfeng Gu, and George Totten. "Numerical investigation of asynchronous dual-frequency induction hardening of spur gear". In: *International Journal of Mechanical Sciences* 142 (2018), pp. 1–9. DOI: 10.1016/j.ijmecsci.2018.04.036.

[121] Zhichao Li, Andrew M Freborg, Bruce D Hansen, and Tirumalai S Srivatsan. "Modeling the effect of carburization and quenching on the development of residual stresses and bending fatigue resistance of steel gears". In: *Journal of materials engineering and performance* 22 (2013), pp. 664–672. DOI: 10.1007/s11665-012-0306-0.

[122] Zhichao Li and B Lynn Ferguson. "Heat Treatment and Fatigue of a Carburized and Quench Hardened Steel Part". In: *Integrated Computational Materials Engineering (ICME) for Metals: Concepts and Case Studies* (2018), pp. 107–135. DOI: 10.1002/9781119018377.ch5.

[123] Valérian Iss, Jean-André Meis, Ali Rajaei, Bengt Hallstedt, and Christoph Broeckmann. "Fatigue strength evaluation of case-hardened components combining heat-treatment simulation and probabilistic approaches". In: *Fatigue & Fracture of Engineering Materials & Structures* 47.3 (2023), pp. 745–765. DOI: 10.1111/ffe.14208.

[124] Dieter Liedtke and Hansjürg Stiele. *Merkblatt 236: Wärmebehandlung von Stahl - Randschichthärten.* 2009.

[125] Matthias Steinbacher. "Thermogravimetrische Messungen beim Niederdruckaufkohlen als Grundlage für Simulationen". PhD thesis. Universität Bremen, 2012.

[126] Oliver Schwarz, Johann Grosch, Christoph Genzel, and Walter Reimers. "Gefüge und eigenspannungen tiefgekühlter und Angelassener Einsatzgehärteter Stähle". In: *HTM Journal of Heat Treatment and Materials* 49.2 (1994), pp. 134–141. DOI: 10.1515/htm-1994-490222.

[127] Christoph Genzel, Walter Reimers, Oliver Schwarz, and Johann Grosch. "Eigenspannungsentwicklung in einsatzgehärteten Stählen". In: *HTM Journal of Heat Treatment and Materials* 50.3 (1995), pp. 163–167. DOI: 10.1515/htm-1995-500311.

[128] Martin Ehlers, Jürgen Gütler, and Jochen Schwarzer. "Computer Aided Simulation of Heat Treatment (CASH) - Teil 1: Ein Überblick". In: *HTM Journal of Heat Treatment and Materials* 61(1) (2003), pp. 5–9. DOI: 10.3139/105.100358.

[129] Clemens Franz, Th Lübben, Jörn Lütjens, Frank Streicher, Nicolas Trapp, and Michael Vogel. "Computer Aided Simulation of Heat Treatment (CASH) Teil 3: Simulation der Einsatzhärtung komplexer Bauteilgeometrien durch Abstraktion". In: *HTM Journal of Heat Treatment and Materials* 61.1 (2006), pp. 19–24. DOI: 10.3139/105.100360.

[130] Jörn Lütjens, Volker Heuer, Thomas Lübben, Volker Schulze, and Nicolas Trapp. "Computer Aided Simulation of Heat Treatment (CASH) - Teil 2: Bestimmung von Eingabedaten zur FEM-Simulation des Einsatzhärtens". In: *HTM Journal of Heat Treatment and Materials* 61(1) (2006), pp. 10–17. DOI: 10.3139/105.100359.

[131] Matthias Steinbacher. *FVA 501 I: GroSSprobe I: Vergleichbarkeit von Couponprobe und GroSSzahnrad beim Einsatzhärten*. Heft 885. Forschungsvereinigung Antriebstechnik e.V., 2009.

[132] Matthias Castens, Matthias Steinbacher, and Hans-Werner Zoch. *FVA 501 III: Großprobe III: Vergleichbarkeit von Couponprobe und verzahntem Großgetriebebauteil*. Heft 1304. Forschungsvereinigung Antriebstechnik e.V., 2017.

[133] Jon Dossett and George Totten. "Modeling and simulation of steel heat treatmentprediction of microstructure, distortion, residual stresses, and cracking". In: *Steel Heat Treating Technologies, ASM Handbook, ASM International B* 4 (2014), pp. 409–466.

[134] Melvin Avrami. "Kinetics of Phase Change. II Transformation-Time Relations for Random Distribution of Nuclei". In: *The Journal of Chemical Physics* 8(2) (1940), pp. 212–224. DOI: 10.1063/1.1750631.

[135] D. P. Koistinen and R. E. Marburger. "A general equation prescribing the extent of the austenite-martensite transformation in pure iron-carbon alloys and plain carbon steels". In: *acta metallurgica* 7 (1959), pp. 59–60.

[136] Tatsuo Inoue. "Metallo-Thermo-Mechanics-Application to Quenching". In: *Handbook of Residual Stress and Deformation of Steel* 60 (2002), p. 296.

[137] Axel Höfter. "Numerische Simulation des Härtens von Stahlbauteilen mit verschleißbeständigen Schichten". PhD thesis. Ruhr-Universität Bochum, 2005.

[138] Caner Şimşir. "3D finite element simulation of steel quenching in order to determine the microstructure and residual stresses". PhD thesis. Middle East Technical University, 2008.

[139] Seong-Hoon Kang and Yong-Taek Im. "Three-dimensional thermo-elastic–plastic finite element modeling of quenching process of plain-carbon steel in couple with phase transformation". In: *International journal of mechanical sciences* 49.4 (2007), pp. 423–439. DOI: 10.1016/j.ijmecsci.2006.09.014.

[140] Maximilian Schwenk. "Numerische modellierung der induktiven ein-und zweifrequenzrandschichthärtung". PhD thesis. Karlsruher Institut für Technologie (KIT), 2014.

[141] Fabian Mühl, James Damon, Stefan Dietrich, and Volker Schulze. "Simulation of induction hardening: Simulative sensitivity analysis with respect to material parameters and the surface layer state". In: *Computational Materials Science* 184 (2020), p. 109. DOI: 10.1016/j.commatsci.2020.109916.

[142] Dominik Kiefer, Philip Schüssler, Fabian Mühl, and Jens Gibmeier. "Experimental and simulative studies on residual stress formation for laser-beam surface hardening". In: *HTM Journal of Heat Treatment and Materials* 74.1 (2019), pp. 23–35. DOI: 10.3139/105.110374.

[143] James Damon. "Experimentelle und numerische Untersuchungen resultierender Randschichtzustände und Eigenschaften Carbonitrierter Pulvermetallurgisch Hergestellter Bauteile". PhD thesis. Karlsruher Institut für Technologie (KIT), 2022.

[144] Attilim Eser, Christoph Broeckmann, and Caner Simsir. "Multiscale modeling of tempering of AISI H13 hot-work tool steel–Part 1: Prediction of microstructure evolution and coupling with mechanical properties". In: *Computational Materials Science* 113 (2016), pp. 280–291. DOI: 10.1016/j.commatsci.2015.11.020.

[145] Attilim Eser, Christoph Broeckmann, and Caner Simsir. "Multiscale modeling of tempering of AISI H13 hot-work tool steel–Part 2: Coupling predicted mechanical properties with FEM simulations". In: *Computational materials science* 113 (2016), pp. 292–300. DOI: 10.1016/j.commatsci.2015.11.024.

[146] Marco Kaffenberger. "Vorhersage des Einsatzhärtungsergebnisses aus dem Aufkohlungsprofil und den Abschreck-und Anlassbedingungen". PhD thesis. Universität Siegen, 2013.

[147] Philipp Nußkern. "Prozesssimulation der Herstellung einsatzgeharteter pulvermetallurgischer Bauteile". PhD thesis. Karlsruhe, Karlsruher Institut für Technologie (KIT), 2013.

[148] Martin Hunkel, Holger Surm, and Matthias Steinbacher. "Dilatometry". In: *Handbook of Thermal Analysis and Calorimetry* (2018), pp. 103–129. DOI: 10.1016/B978-0-444-64062-8.00019-X.

[149] Clemens Franz, Volker Schulze, Eckard Macherauch, and Detlef Löhe. "Simulation der Wärmebehandlung von Stählen am Institut für Werkstoffkunde I". In: *Materialwissenschaft und Werkstofftechnik: Entwicklung, Fertigung, Prüfung, Eigenschaften und Anwendungen technischer Werkstoffe* 34.1 (2003), pp. 162–171. DOI: 10.1002/mawe.200390009.

[150] Martin Hunkel, Friedhelm Frerichs, Christian Prinz, Holger Surm, Franz Hoffmann, and Hans-Werner Zoch. "Size change due to anisotropic dilation behaviour of a low alloy sae 5120 steel". In: *steel research international* 78.1 (2007), pp. 45–51. DOI: 10.1002/srin.200705858.

[151] Martin Hunkel. "Modelling of phase transformations and transformation plasticity of a continuous casted steel 20MnCr5 incorporating segregations". In: *Materialwissenschaft und Werkstofftechnik* 43.1-2 (2012), pp. 150–157. DOI: 10.1002/mawe.201100903.

[152] Caner Simsir, Martin Hunkel, Jörn Lütjens, and Rüdiger Rentsch. "Process-chain simulation for prediction of the distortion of case-hardened gear blanks". In: *Materialwissenschaft und Werkstofftechnik* 43.1-2 (2012), pp. 163–170.

[153] The MathWorks Inc. *MATLAB version 9.11.0 (R2021b)*. https://www.mathworks.com. 2021.

[154] Jean-Baptiste Leblond. "Mathematical modelling of transformation plasticity in steels II: coupling with strain hardening phenomena". In: *International journal of plasticity* 5.6 (1989), pp. 573–591. DOI: 10.1016/0749-6419(89)90002-8.

[155] Daniel Kaiser, Bernhard De Graaff, AM Jung, Stefan Dietrich, and Volker Schulze. "A dilatometric study on the influence of compressive stresses on the tempering of martensitic AISI 4140 steel-Evidence of transformation induced plasticity during cementite precipitation". In: *Materials Science and Engineering: A* 705 (2017), pp. 114–121. DOI: 10.1016/j.msea.2017.08.028.

[156] Dassault Systemes. *Abaqus 2020*. https://www.3ds.com/products-services/simulia/products/abaqus. 2020.

[157] Daniel Kadach and Jonas Pollascheck. *FVA 284 V: Einfluss der Lastverteilung auf die Grübchentragfähigkeit von einsatzgehärteten Stirnrädern*. Heft 1205. Forschungsvereinigung Antriebstechnik e.V., 2017.

[158] Volker Heuer and Klaus Löser. "Experimentelles Verfahren zur Ermittlung von Wärmeübergangskoeffizienten bei der Hochdruck-Gasabschreckung". In: *HTM Journal of Heat Treatment and Materials* 59.6 (2004), pp. 432–438. DOI: 10.3139/105.100316.

[159] Paul Prevéy. "X-ray diffraction residual stress techniques". In: *ASM International, ASM Handbook.* 10 (1986), pp. 380–392.

[160] Warrendale. "Residual stress measurement by X-ray diffraction - HS-784". In: *SAE International* (2003).

[161] Vincent Savaria, Florent Bridier, and Philippe Bocher. "Computational quantification and correction of the errors induced by layer removal for subsurface residual stress measurements". In: *International Journal of Mechanical Sciences* 64.1 (2012), pp. 184–195. DOI: 10.1016/j.ijmecsci.2012.07.003.

[162] Vincent Savaria, Hossein Monajati, Florent Bridier, and Philippe Bocher. "Measurement and correction of residual stress gradients in aeronautical gears after various induction surface hardening treatments". In: *Journal of Materials Processing Technology* 220 (2015), pp. 113–123. DOI: 10.1016/j.jmatprotec.2014.12.009.

[163] Weitingwlin. *MATLAB utility codes for correlation plots*. https://www.mathworks.com/matlabutility/tree/master/documents. 2015.

[164] Peter Koller. *FVA 521 I: Steigerung der Zahnflankentragfähigkeit durch Kombination von Strahlbehandlung und Finishingprozess*. Heft 957. Forschungsvereinigung Antriebstechnik e.V., 2010.

[165] Samuel Kotz and Saralees Nadarajah. *Extreme value distributions: theory and applications*. world scientific, 2000.

[166] *DIN EN ISO 683-3 Heat-treatable steels, alloy steels and free-cutting steels - Part 3: Case-hardening steels*. Deutsches Institut für Normung, 2022.

[167] Božidar Liščić and Tomislav Filetin. "Measurement of quenching intensity, calculation of heat transfer coefficient and global database of liquid quenchants". In: *Materiálové inžinierstvo* 19.2 (2012), pp. 52–63.

Appendix A

Appendix

A1. Chemical composition of alloys used in this work

Table A.1: Comparison of the chemical composition of steel 18CrNiMo7-6 used for dilatometer samples and carburized gears [47].

Material or standard		Element in mass percent									
		C	Si	Mn	P	S	Cr	Mo	Ni	Al	N
Gears module 18 mm		0.188	0.26	0.53	0.005	0.001	1.69	0.31	1.60	0.025	0.0101
Gears module 3 mm		0.170	0.24	0.55	0.004	0.001	1.69	0.30	1.57	0.030	0.0110
Dilatometer samples		0.170	0.30	0.55	0.003	0.002	1.71	0.30	1.58	0.036	0.0095
DIN EN	max	0.21	0.40	0.90	0.025	0.035	1.80	0.35	1.70	-	-
ISO 683-3[166]	min	0.15	-	0.50	-	-	1.50	0.25	1.40	-	-

A2. Austenite flow properties

Table A.2: Temperature-dependent flow properties of 18CrNiMo7-6 with austenite microstructure

True plastic strain [-]	True plastic stress [MPa]		
0	63	40	22
$6.67 \cdot 10^{-3}$	122	94	59
$1.33 \cdot 10^{-2}$	149	115	68
$2.00 \cdot 10^{-2}$	173	131	74
$2.67 \cdot 10^{-2}$	195	144	80
$3.33 \cdot 10^{-2}$	216	156	84
$4.00 \cdot 10^{-2}$	235	167	89
$4.67 \cdot 10^{-2}$	253	177	93
$5.33 \cdot 10^{-2}$	270	187	97
$6.00 \cdot 10^{-2}$	286	196	100
Test temperature [°C]	625	700	850

Table A.3: Temperature-dependent flow properties of 50CrNiMo7-6 with austenite microstructure

True plastic strain [-]	True plastic stress [MPa]		
0	101	72	26
$1.33 \cdot 10^{-2}$	177	118	64
$2.67 \cdot 10^{-2}$	224	144	76
$4.00 \cdot 10^{-2}$	270	164	84
$5.33 \cdot 10^{-2}$	314	181	92
$6.67 \cdot 10^{-2}$	357		98
$8.0 \cdot 10^{-2}$	398		105
$9.33 \cdot 10^{-2}$	438		111
$1.07 \cdot 10^{-1}$	477		118
$1.20 \cdot 10^{-1}$	516		124
Test temperature [°C]	500	700	850

Table A.4: Temperature-dependent flow properties of 82CrNiMo7-6 with austenite microstructure

True plastic strain [-]	True plastic stress [MPa]		
0	124	74	39
$6.67 \cdot 10^{-3}$	164	102	55
$1.33 \cdot 10^{-2}$	200	119	61
$2.00 \cdot 10^{-2}$	218	132	66
$2.67 \cdot 10^{-2}$	236	144	71
$3.33 \cdot 10^{-2}$	253	155	73
$4.00 \cdot 10^{-2}$	271	164	76
$4.67 \cdot 10^{-2}$	289	172	79
$5.33 \cdot 10^{-2}$	304	181	81
$6.00 \cdot 10^{-2}$	321	188	84
Test temperature [°C]	500	700	850

A3. Bainite flow properties

Table A.5: Temperature-dependent flow properties of 18CrNiMo7-6 with bainitic microstructure (isothermally transformed at 450 °C).

True plastic strain [-]	True plastic stress [MPa]			
0	530	525	523	520
$5.56 \cdot 10^{-3}$	1,005	970	924	806
$1.11 \cdot 10^{-2}$	1,109	1,060	998	858
$1.67 \cdot 10^{-2}$	1,172	1,109	1,041	886
$2.22 \cdot 10^{-2}$	1,214	1,141	1,074	906
$2.78 \cdot 10^{-2}$	1,225	1,174	1,099	922
$3.33 \cdot 10^{-2}$		1,202	1,121	937
$3.89 \cdot 10^{-2}$		1,228		951
$4.44 \cdot 10^{-2}$		1,251		965
$5.00 \cdot 10^{-2}$				977
Test temperature [°C]	20	300	400	500

Table A.6: Temperature-dependent flow properties of 32CrNiMo7-6 with bainitic microstructure (isothermally transformed at 400 °C).

True plastic strain [-]	True plastic stress [MPa]				
0	824	715	684	640	604
$5.56 \cdot 10^{-3}$	1,151	1,096	1,139	1,159	1,067
$1.11 \cdot 10^{-2}$	1,239	1,176	1,235	1,252	1,148
$1.67 \cdot 10^{-2}$	1,298	1,225	1,293	1,309	1,194
$2.22 \cdot 10^{-2}$	1,339	1,260	1,336	1,352	1,228
$2.78 \cdot 10^{-2}$	1,372	1,283	1,372	1,388	1,256
$3.33 \cdot 10^{-2}$	1,400	1,309	1,403	1,421	1,280
$3.89 \cdot 10^{-2}$	1,421	1,331	1,427	1,450	1,301
$4.44 \cdot 10^{-2}$	1,436	1,351	1,450	1,477	1,320
$5.00 \cdot 10^{-2}$	1,455	1,370	1,470	1,503	1,337
Test temperature [°C]	20	100	200	300	400

Table A.7: Temperature-dependent flow properties of 50CrNiMo7-6 with bainitic microstructure (isothermally transformed at 300 °C).

True plastic strain [-]	True plastic stress [MPa]		
0	1,145	715	684
$5.56 \cdot 10^{-3}$	1,712	1,096	1,139
$1.11 \cdot 10^{-2}$	1,842	1,176	1,235
$1.67 \cdot 10^{-2}$	1,911	1,225	1,293
$2.22 \cdot 10^{-2}$	1,960	1,260	1,336
$2.78 \cdot 10^{-2}$	1,998	1,283	1,372
$3.33 \cdot 10^{-2}$	2,029	1,309	1,403
$3.89 \cdot 10^{-2}$	2,055	1,331	1,427
$4.44 \cdot 10^{-2}$	2,077	1,351	1,450
$5.00 \cdot 10^{-2}$	2,095	1,370	1,470
Test temperature [°C]	20	200	300

Table A.8: Temperature-dependent flow properties of 66CrNiMo7-6 with bainitic microstructure (isothermally transformed at 300 °C).

True plastic strain [-]	True plastic stress [MPa]		
0	1,165	860	785
$5.56 \cdot 10^{-3}$	1,703	1,558	1,311
$1.11 \cdot 10^{-2}$	1,834	1,652	1,387
$1.67 \cdot 10^{-2}$	1,915	1,721	1,413
$2.22 \cdot 10^{-2}$	1,978	1,800	1,428
$2.78 \cdot 10^{-2}$	2,021	1,868	1,439
$3.33 \cdot 10^{-2}$	2,056	1,924	1,451
$3.89 \cdot 10^{-2}$	2,082	1,969	1,463
$4.44 \cdot 10^{-2}$	2,104	2,005	1,475
$5.00 \cdot 10^{-2}$	2,122	2,035	1,487
Test temperature [°C]	20	150	400

A4. Martensite flow properties

Table A.9: Temperature-dependent flow properties of 18CrNiMo7-6 with martensitic microstructure.

True plastic strain [-]	True plastic stress [MPa]		
0	672	710	508
$5.56 \cdot 10^{-3}$	1,279	1,237	1,054
$1.11 \cdot 10^{-2}$	1,386	1,324	1,127
$1.67 \cdot 10^{-2}$	1,445	1,371	1,161
$2.22 \cdot 10^{-2}$	1,486	1,403	1,182
$2.78 \cdot 10^{-2}$	1,517	1,427	1,199
$3.33 \cdot 10^{-2}$	1,544	1,446	1,213
$3.89 \cdot 10^{-2}$	1,567	1,458	1,226
$4.44 \cdot 10^{-2}$	1,588	1,472	1,238
$5.00 \cdot 10^{-2}$	1,606	1,482	1,249
Test temperature [°C]	20	300	400

Table A.10: Temperature-dependent flow properties of 32CrNiMo7-6 with martensitic microstructure.

True plastic strain [-]	True plastic stress [MPa]			
0	1,073	1,108	988	783
$8.89 \cdot 10^{-4}$	1,460	1,402	1,325	1,117
$1.78 \cdot 10^{-3}$	1,586	1,520	1,462	1,251
$2.67 \cdot 10^{-3}$		1,608	1,550	1,335
$3.56 \cdot 10^{-3}$				1,398
$4.44 \cdot 10^{-3}$				1,446
$5.33 \cdot 10^{-3}$				1,485
$6.22 \cdot 10^{-3}$				1,518
Test temperature [°C]	20	100	200	300

Table A.11: Temperature-dependent flow properties of 50CrNiMo7-6 with martensitic microstructure.

True plastic strain [-]	True plastic stress [MPa]			
0	1,610	1,713	1,225	879
$3.33 \cdot 10^{-4}$	1,932	2,002	1,574	1,101
$6.67 \cdot 10^{-4}$	2,097			1,216
$1.00 \cdot 10^{-3}$				1,300
$1.33 \cdot 10^{-3}$				1,364
$1.67 \cdot 10^{-3}$				1,414
$2.00 \cdot 10^{-3}$				1,456
$2.33 \cdot 10^{-3}$				1,495
$2.67 \cdot 10^{-3}$				1,525
$3.00 \cdot 10^{-3}$				1,560
Test temperature [°C]	20	100	200	300

Table A.12: Temperature-dependent flow properties of 66CrNiMo7-6 samples with martensitic (+ residual austenite) microstructure.

True plastic strain [-]	True plastic stress [MPa]		
0	1,741	1,535	1,258
$1.33 \cdot 10^{-3}$	2,085	1,822	1,525
$2.67 \cdot 10^{-3}$		1,912	1,562
$4.00 \cdot 10^{-3}$		1,956	1,592
$5.33 \cdot 10^{-3}$		1,973	1,619
$6.67 \cdot 10^{-3}$		1,991	1,650
$8.00 \cdot 10^{-3}$		2,027	1,689
$9.33 \cdot 10^{-3}$		2,080	1,737
$1.07 \cdot 10^{-2}$		2,146	1,799
Test temperature [°C]	20	100	200

Table A.13: Temperature-dependent flow properties of 82CrNiMo7-6 samples with martensitic (+ residual austenite) microstructure.

True plastic strain [-]	True plastic stress [MPa]		
0	1,795	1,526	1,134
$1.33 \cdot 10^{-3}$	2,124	1,862	1,554
$2.67 \cdot 10^{-3}$		1,933	1,641
$4.00 \cdot 10^{-3}$		1,961	1,687
$5.33 \cdot 10^{-3}$		1,984	1,714
$6.67 \cdot 10^{-3}$		2,014	1,746
$8.00 \cdot 10^{-3}$		2,053	1,796
$9.33 \cdot 10^{-3}$		2,100	1,850
$1.07 \cdot 10^{-2}$		2,157	1,915
$1.20 \cdot 10^{-2}$			1,980
Test temperature [°C]	20	100	200

A5. Characterization tests for isothermal bainite phase transformation kinetics

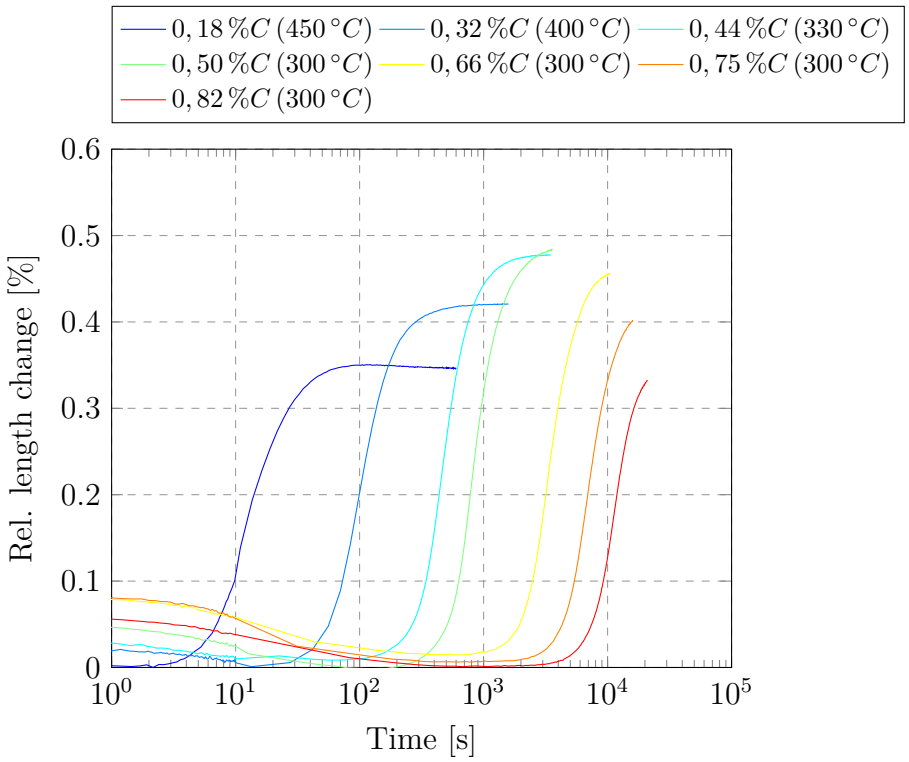


Figure A5.1: Time-length change diagram of isothermal bainite phase transformation as a function of carbon concentration.

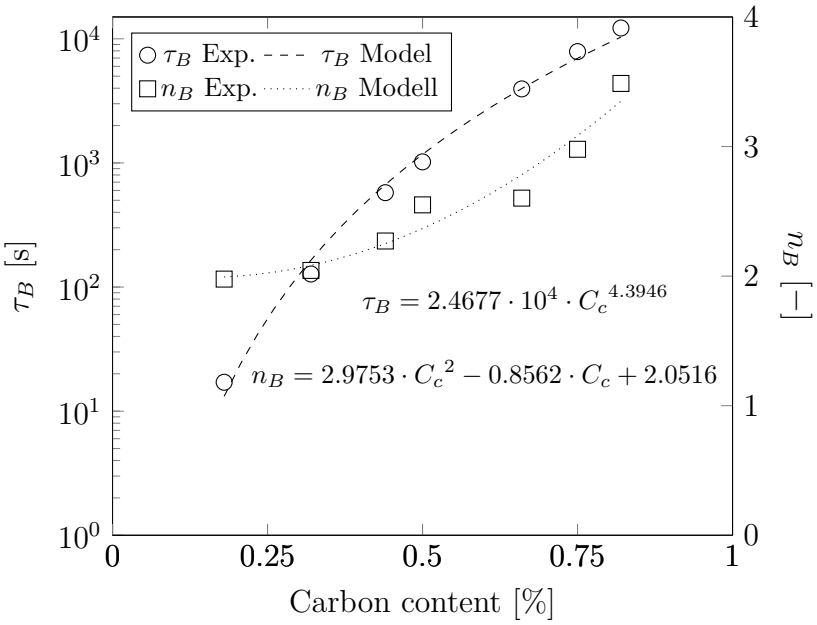


Figure A5.2: Post-processed kinetics parameters τ_B and n_B for equation 3.1 from isothermal bainite phase transformation trials in figure A5.1.

A6. Transformation kinetics model parameters

Model parameters applied for the kinetics of the transformation of austenite into ferrite/pearlite

τ_{FP} [s]	Carbon content [%]					
T [°C]	0.18	0.32	0.44	0.50	0.66	0.82
300	1,000,000	1,000,000	1,000,000	1,000,000	1,000,000	1,000,000
330	1,000,000	1,000,000	1,000,000	1,000,000	1,000,000	1,000,000
350	1,000,000	1,000,000	1,000,000	1,000,000	1,000,000	1,000,000
390	1,000,000	1,000,000	1,000,000	9,968,00	1,000,000	1,000,000
400	1,000,000	1,000,000	1,000,000	759,808	1,000,000	1,000,000
450	1,000,000	1,000,000	136,801	196,654	1,000,000	1,000,000
475	1,000,000	1,000,000	53,180	100,838	1,000,000	1,000,000
500	1,000,000	1,000,000	22,816	52,332	996,196	590,724
525	1,000,000	335,371	11,797	27,778	269,170	159,944
550	1,000,000	88,530	7,826	15,356	73,396	43,973
575	353,848	26,399	6,511	9,099	20,679	12,755
600	63,921	10,760	6,567	6,070	6,492	4,372
625	12,572	6,824	8,822	5,137	2,732	2,255
650	3,480	5,834	19,021	7,258	2,123	2,604
660	2,506	5,696	29,454	10,102	2,530	3,783
670	2,031	5,626	47,984	15,417	3,644	6,429
675	1,907	5,616	62,089	19,552	4,660	8,746
680	1,844	5,627	80,882	25,123	6,169	12,136
690	1,944	5,788	139,277	42,678	11,661	24,315
700	2,741	6,521	242,922	74,305	23,469	50,227
725	35,488	37,000	1,000,000	311,934	150,107	323,644
750	996,344	997,600	1,000,000	1,000,000	999,686	1,000,000
775	1,000,000	1,000,000	1,000,000	1,000,000	1,000,000	1,000,000

Table A.14: Parameter τ_{FP} for description of ferrite/pearlite transformation kinetics as a function of temperature and carbon content, from [130] and from own investigations.

$$n_{FP} = -335.19 \cdot {C_0}^4 + 659.15 \cdot {C_0}^3 - 468.06 \cdot {C_0}^2 + 145.05 \cdot C_0 - 13.527 \tag{A6.1}$$

Model parameters applied for the kinetics of the transformation of austenite into bainite

$$n_B = 2.9753 \cdot C_{eff}^2 - 0.8562 \cdot C_{eff} + 2.0516 \tag{A6.2}$$

$$\tau_B = 2.4677 \cdot 10^4 \cdot {C_{eff}}^{4.3946} \; [s] \tag{A6.3}$$

$\overline{\xi}_{FP}$ [-]	Carbon content [%]					
T [°C]	0.18	0.32	0.44	0.50	0.66	0.82
300	0	0	0	0	0	0
330	0	0	0	0	0	0
350	0	0	0	0	0	0
390	0	0	0	0	0	0
400	0	0	1	1	1	1
450	0	0	1	1	1	1
475	0	0	1	1	1	1
500	0	0	1	1	1	1
525	1	1	1	1	1	1
550	1	1	1	1	1	1
575	1	1	1	1	1	1
600	1	1	1	1	1	1
625	1	1	1	1	1	1
650	1	1	1	1	1	1
660	1	1	1	1	1	1
670	1	1	1	1	1	1
675	1	1	1	1	1	1
680	1	1	1	1	1	1
690	1	1	0	1	1	1
700	1	0	0	0	0	0
725	0	0	0	0	0	0
750	0	0	0	0	0	0
775	0	0	0	0	0	0

Table A.15: Parameter $\overline{\xi}_{FP}$ for description of ferrite/pearlite transformation kinetics as a function of temperature and carbon content, from [130] and from own investigations.

Model parameters applied for the transformation kinetics for the transformation of austenite into martensite

$$\xi_M = \overline{\xi}_M \cdot e^{0.011 \cdot (T - M_S)} \tag{A6.4}$$

$$M_S = -403.99 \cdot C_{eff} + 464.5 \tag{A6.5}$$

Calculation of the empirical effective carbon content parameter

$$C_{eff} = \frac{C_0}{1 - k_{FP} \cdot \xi_{FP} - k_B \cdot \xi_B} \tag{A6.6}$$

$$k_{FP} = 1 - \frac{1}{1 + e^{-50 \cdot (C_0 - 0.44)}} \tag{A6.7}$$

$$k_B = min(max((0.67 - 0.74 \cdot C_0) \cdot e^{-\dot{T}/5}, 0), 0.55) \tag{A6.8}$$

$f_{FP}(\dot{T})$ [-]	Carbon content [%]					
$\dot{T}$ [K/s]	0.18	0.32	0.44	0.50	0.66	0.82
0	1	1	1	1	1	1
0.03	1	1	1	1	1	1
0.06	1	1	1	1	1	1
0.12	1	1	1	1	1	1
0.3	1	1	1	1	1	1
0.6	1	1	1	1	1	0.1
1.2	0.1	0.1	0.1	0.1	0.1	0.01
1.6	0.01	0.01	0.01	0.01	0.01	0.01
2.5	0.01	0.01	0.01	0.01	0.01	0.01
5	0.01	0.01	0.01	0.01	0.01	0.01
10	0.01	0.01	0.01	0.01	0.01	0.01
16	0.01	0.01	0.01	0.01	0.01	0.01
25	0.01	0.01	0.01	0.01	0.01	0.01
50	0.01	0.01	0.01	0.01	0.01	0.01
100	0.01	0.01	0.01	0.01	0.01	0.01

Table A.16: Parameter $f_{FP}(\dot{T})$ for description of ferrite/pearlite transformation kinetics as a function of temperature and carbon content, from [130] and from own investigations.

$f_B(\dot{T})$ [-]	Carbon content [%]						
$\dot{T}$ [K/s]	0.18	0.32	0.44	0.50	0.66	0.75	0.82
170	0	0	0	0	0	0	0
200	0	0	0	0	0	0.56	1
230	0	0	0.67	0.67	0.84	0.93	1
250	0	0	1	1	1	1	1
300	0	0	1	1	1	1	1
350	0	0.5	1	1	1	0.97	0.95
390	1	1	0.856	0.856	0.91	0.78	0.69
395	1	1	0.838	0.838	0.76	0.7	0.65
400	1	1	0.82	0.82	0.73	0.67	0.62
410	1	1	0.747	0.747	0.68	0.58	0.5
425	1	1	0.710	0.710	0.6	0.5	0.43
450	1	0.89	0.637	0.637	0.53	0.41	0.31
475	1	0.37	0.317	0.317	0.31	0.14	0
500	0.37	0.235	0.09	0.09	0.09	0.02	0
525	0.235	0.1	0.03	0.03	0.03	0	0
550	0.1	0	0	0	0	0	0
565	0.1	0	0	0	0	0	0
575	0	0	0	0	0	0	0
590	0	0	0	0	0	0	0
600	0	0	0	0	0	0	0
1,000	0	0	0	0	0	0	0

Table A.17: Parameter $f_B(\dot{T})$ for description of bainite transformation kinetics as a function of temperature and carbon content, from [130] and from own investigations.

A7. Strain model parameters

Austenite:

$$\alpha_A = 2.285 \cdot 10^{-5}\ K^{-1} \tag{A7.9}$$

$$b_A = -1.95 \cdot 10^{-2} \tag{A7.10}$$

Ferrite/Pearlite:

$$\alpha_{FP} = -2.676 \cdot 10^{-4} \cdot C_c + 1.516 \cdot 10^{-3}\ K^{-1} \tag{A7.11}$$

$$b_{FP} = -6.91 \cdot 10^{-4} \cdot C_c - 1.13 \cdot 10^{-2} \tag{A7.12}$$

Martensite:

$$\alpha_M = -1.757 \cdot 10^{-5} \cdot {C_c}^2 + 6.762 \cdot 10^{-6} \cdot C_c + 1.189 \cdot 10^{-5}\ K^{-1} \tag{A7.13}$$

$$b_M = -1.021 \cdot 10^{-2} \cdot {C_c}^2 + 1.331 \cdot 10^{-2} C_c - 1.253 \cdot 10^{-2} \tag{A7.14}$$

Bainite:

$$\begin{aligned} \alpha_B = &- 3.209 \cdot 10^{-4} \cdot {C_c}^5 + 4.140 \cdot 10^{-4} \cdot {C_c}^4 - 3.259 \cdot 10^{-5} \cdot {C_c}^3 \\ &- 1.296 \cdot 10^{-4} \cdot {C_c}^2 + 4.800 \cdot 10^{-5} \cdot C_c + 9.088 \cdot 10^{-6}\ K^{-1} \end{aligned} \tag{A7.15}$$

$$b_B = 3.12 \cdot 10^{-2} \cdot {C_c}^3 - 5.40 \cdot 10^{-2} \cdot {C_c}^2 + 2.57 \cdot 10^{-2} \cdot C_c - 1.48 \cdot 10^{-2} \tag{A7.16}$$

Tempered martensitic-austenitic microstructures for carbon concentration over $0,32\,\%C$:

$$\alpha_2 = -1.279 \cdot 10^{-6} \cdot C_c + 1.265 \cdot 10^{-5} \tag{A7.17}$$

$$b_2 = b_1 - 8.728 \cdot 10^{-3} \cdot {C_c}^2 + 9.251 \cdot 10^{-3} \cdot C_c - 1.146 \cdot 10^{-2} \tag{A7.18}$$

TRIP coefficients for martensite and bainite phase transformations:

$$K^{tp}_{mart} = min(9.801 \cdot 10^{-6} \cdot ln(1.622 \cdot C_c)^3 + 6.503 \cdot 10^{-5}, 6.503 \cdot 10^{-5}) \tag{A7.19}$$

$$\begin{aligned} K^{tp}_{bain} = &2.81 \cdot 10^{-3} \cdot {C_c}^3 - 4.28 \cdot 10^{-3} \cdot {C_c}^2 \\ &+ 1.98 \cdot 10^{-3} \cdot C_c - 2.07 \cdot 10^{-4} \ \text{ for } C_c \leq 0.66 \end{aligned} \tag{A7.20}$$

A8. Heat transfer coefficients for quench simulation

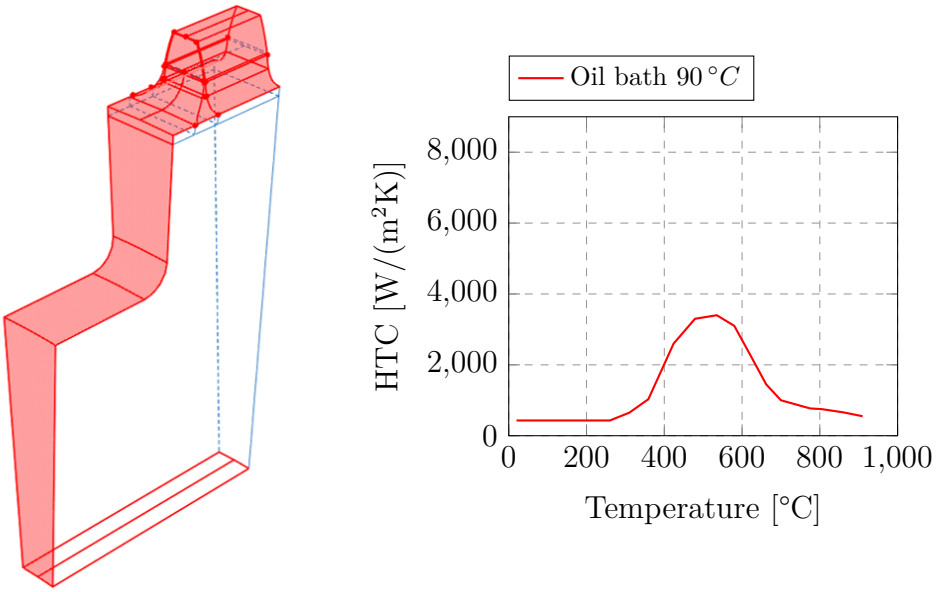


Figure A8.3: Applied heat transfer coefficient and quenched surfaces in heat treatment simulation: oil bath quenching Marquench 875 at 90 °C [132].

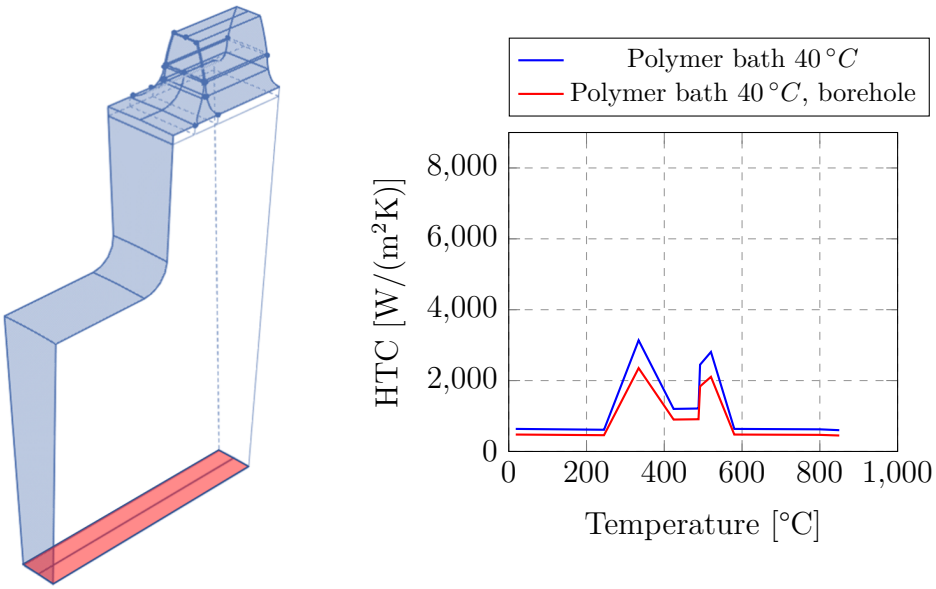


Figure A8.4: Applied heat transfer coefficient and quenched surfaces in heat treatment simulation: polymer bath quenching Aquacool AC (15%) at 40 °C, inverse fit with initial parameters from [132].

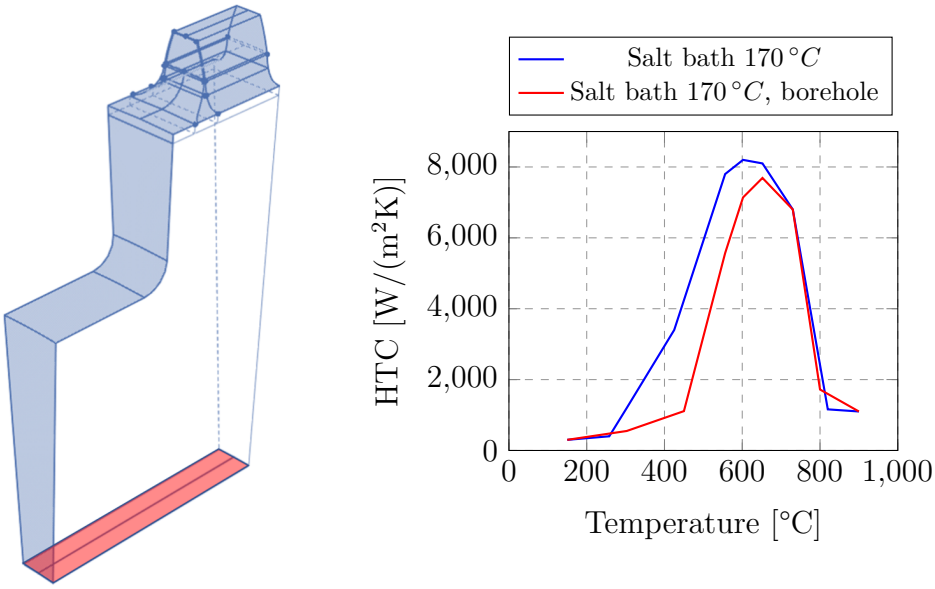


Figure A8.5: Applied heat transfer coefficient and quenched surfaces in heat treatment simulation: salt bath AS135 with temperature 170 °C, inverse fit with initial parameters from [167].

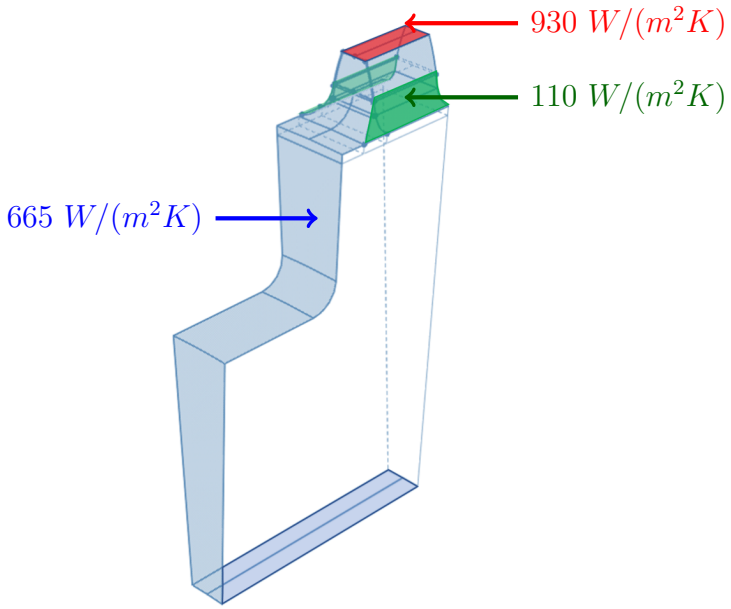


Figure A8.6: Applied heat transfer coefficient and quenched surfaces in heat treatment simulation: high pressure gas with 18 *bar* N_2, values derived from [158].

A9. Residual stress simulation results for cylindrical samples

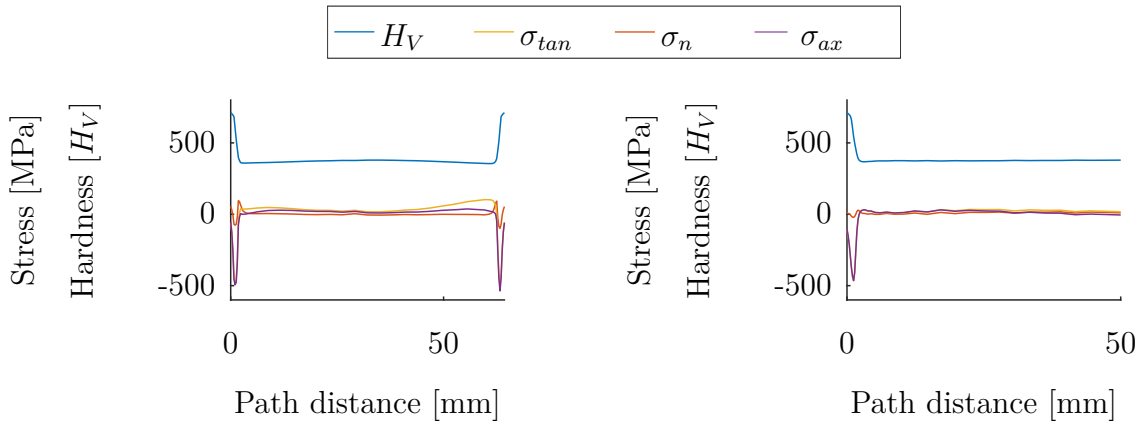


Figure A9.7: Results for heat treatment simulation 1 on cylindrical samples along *path 1* (left) and *path 2* (right).

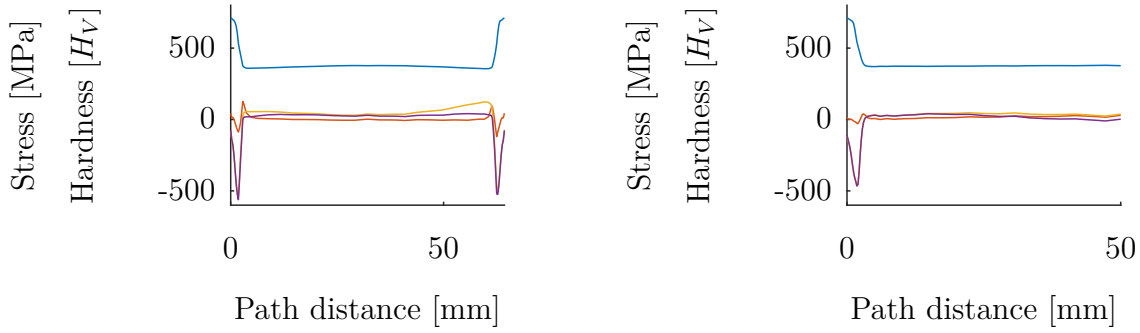


Figure A9.8: Results for heat treatment simulation 2 on cylindrical samples along *path 1* (left) and *path 2* (right).

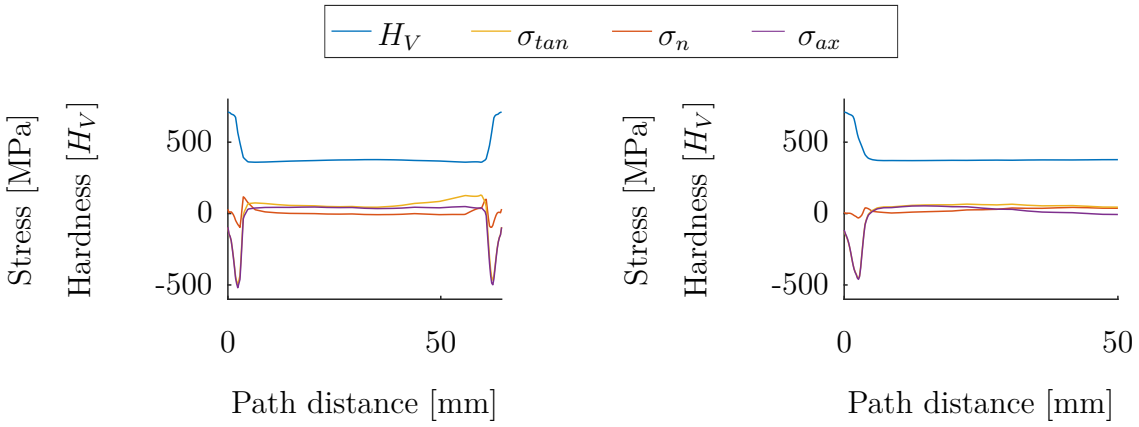


Figure A9.9: Results for heat treatment simulation 3 on cylindrical samples along *path 1* (left) and *path 2* (right).

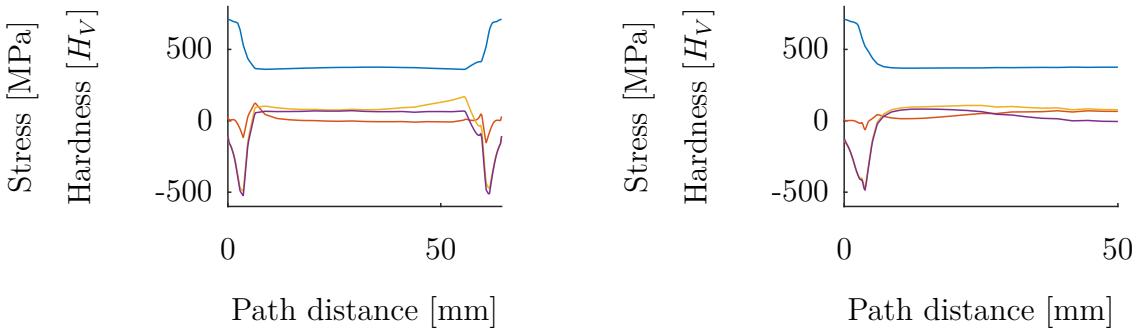


Figure A9.10: Results for heat treatment simulation 4 on cylindrical samples along *path 1* (left) and *path 2* (right).

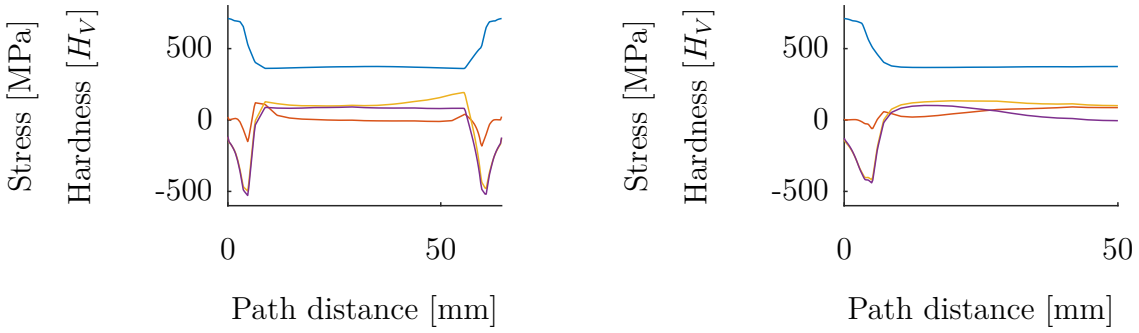


Figure A9.11: Results for heat treatment simulation 5 on cylindrical samples along *path 1* (left) and *path 2* (right).

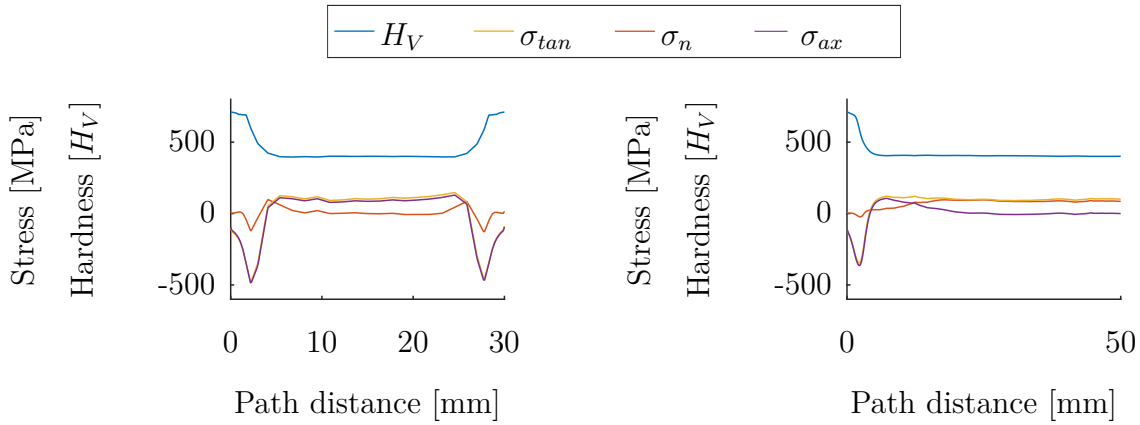


Figure A9.12: Results for heat treatment simulation 6 on cylindrical samples along *path 1* (left) and *path 2* (right).

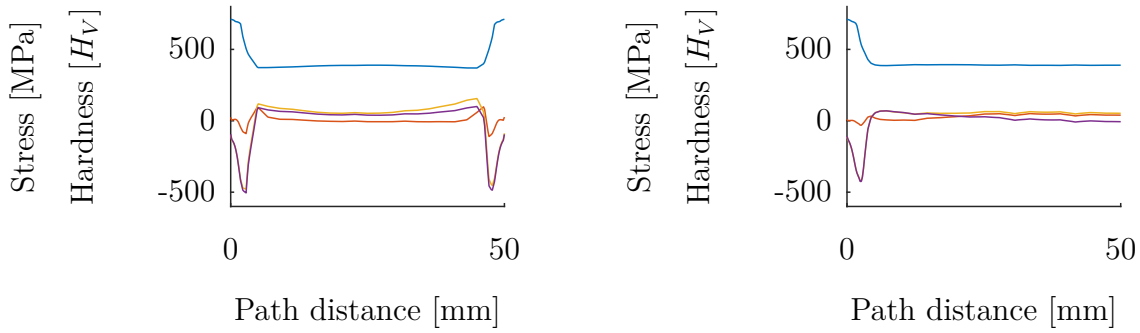


Figure A9.13: Results for heat treatment simulation 7 on cylindrical samples along *path 1* (left) and *path 2* (right).

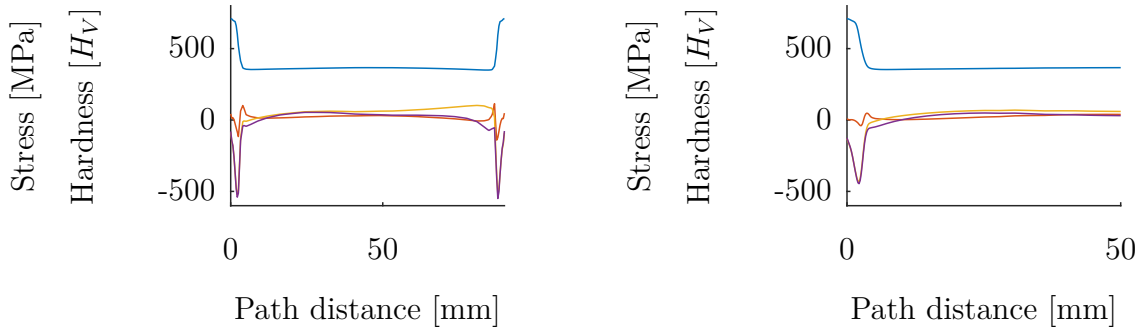


Figure A9.14: Results for heat treatment simulation 8 on cylindrical samples along *path 1* (left) and *path 2* (right).

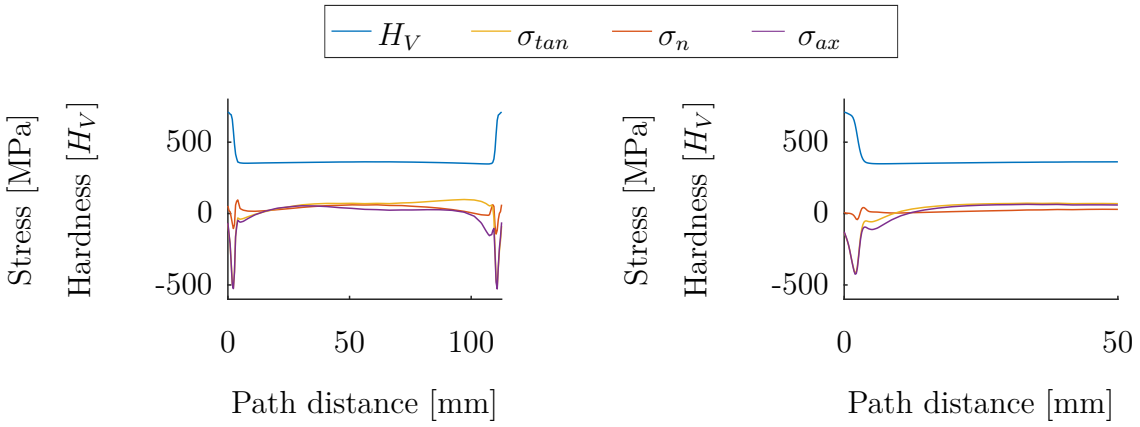


Figure A9.15: Results for heat treatment simulation 9 on cylindrical samples along *path 1* (left) and *path 2* (right).

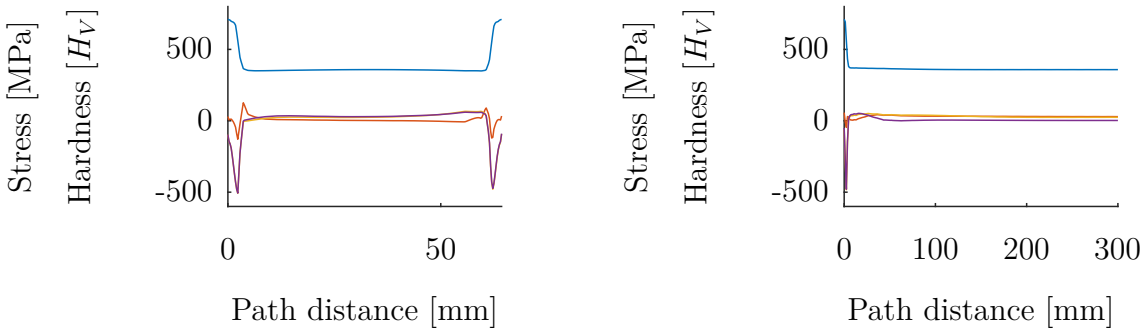


Figure A9.16: Results for heat treatment simulation 10 on cylindrical samples along *path 1* (left) and *path 2* (right).

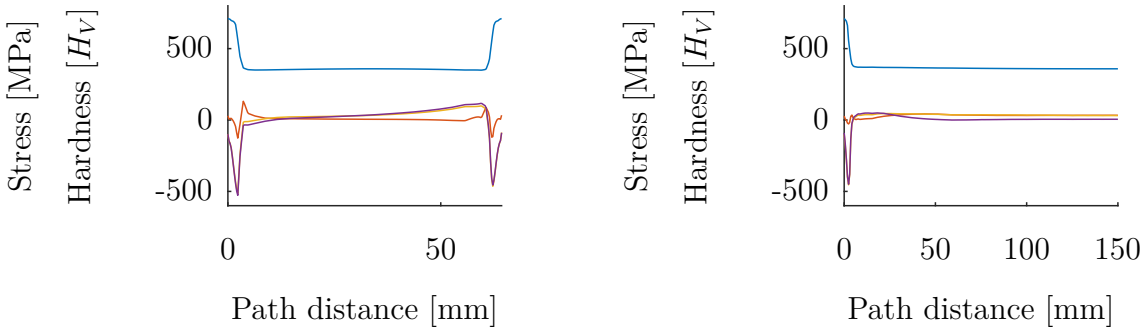


Figure A9.17: Results for heat treatment simulation 11 on cylindrical samples along *path 1* (left) and *path 2* (right).

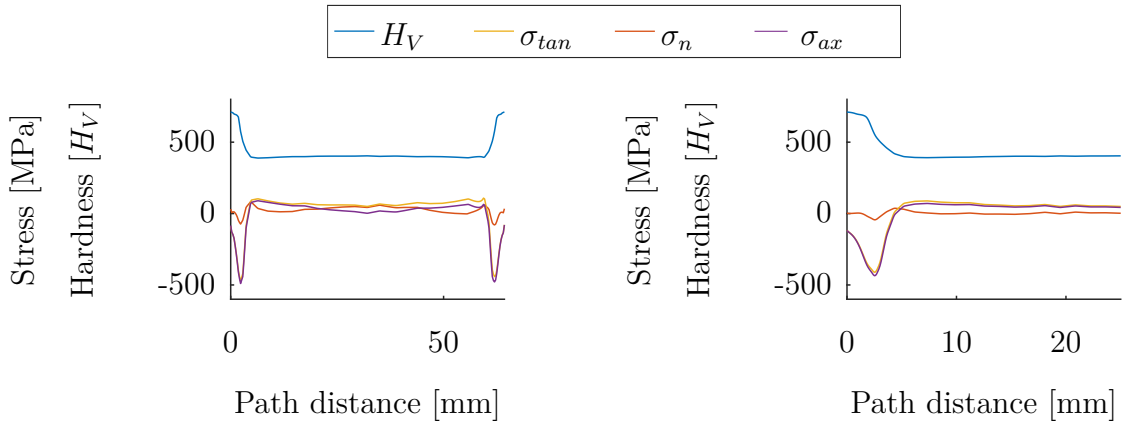


Figure A9.18: Results for heat treatment simulation 12 on cylindrical samples along *path 1* (left) and *path 2* (right).

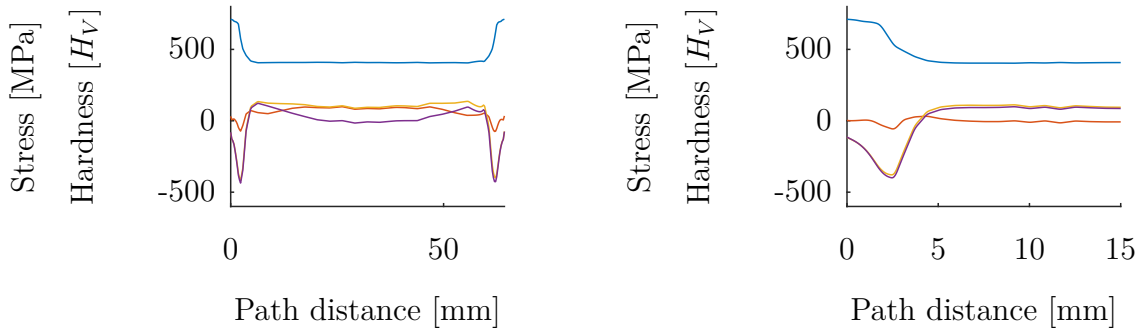


Figure A9.19: Results for heat treatment simulation 13 on cylindrical samples along *path 1* (left) and *path 2* (right).

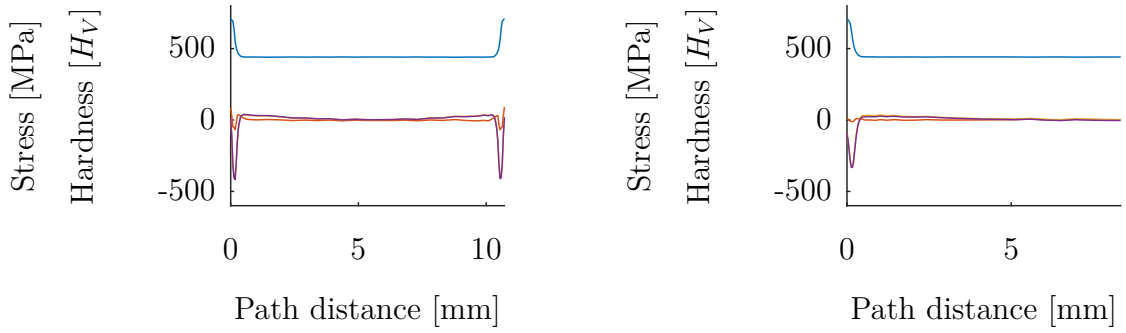


Figure A9.20: Results for heat treatment simulation 14 on cylindrical samples along *path 1* (left) and *path 2* (right).

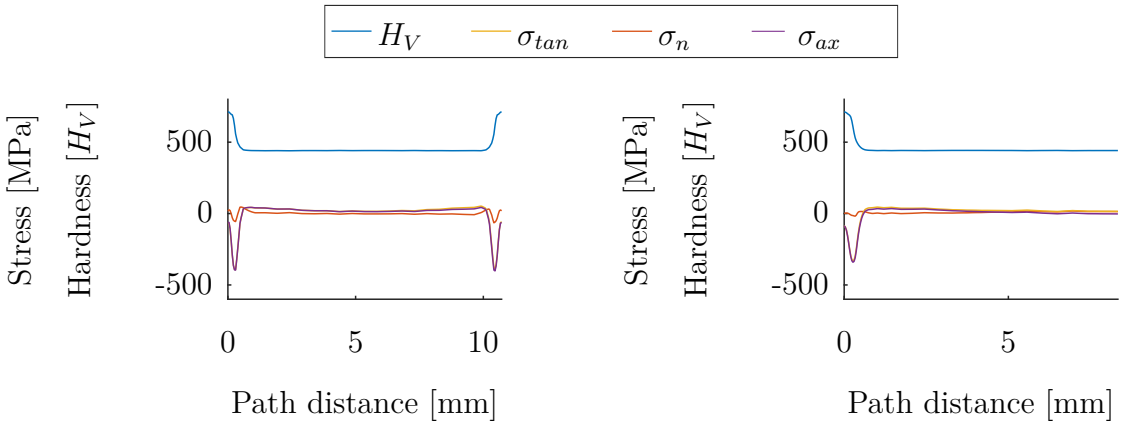


Figure A9.21: Results for heat treatment simulation 15 on cylindrical samples along *path 1* (left) and *path 2* (right).

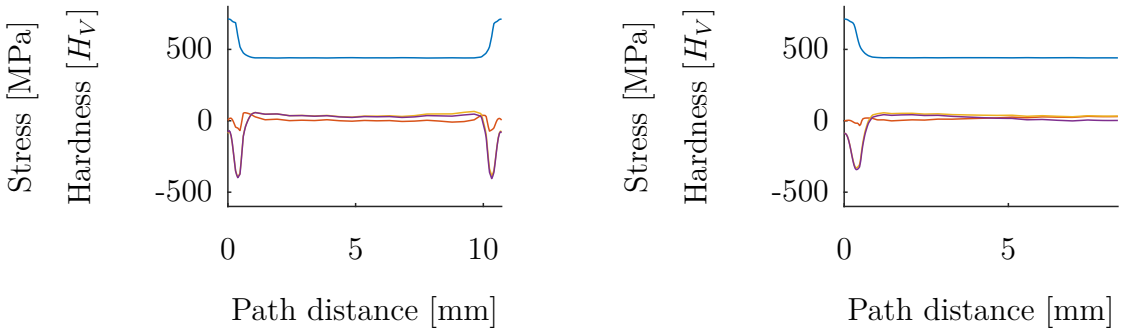


Figure A9.22: Results for heat treatment simulation 16 on cylindrical samples along *path 1* (left) and *path 2* (right).

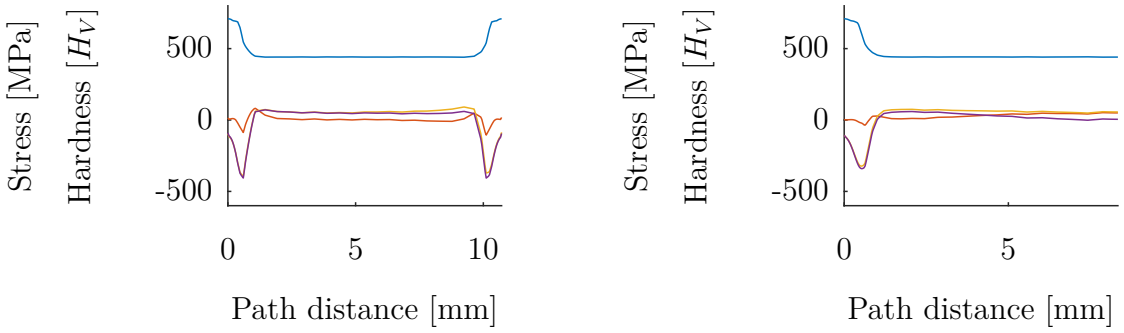


Figure A9.23: Results for heat treatment simulation 17 on cylindrical samples along *path 1* (left) and *path 2* (right).

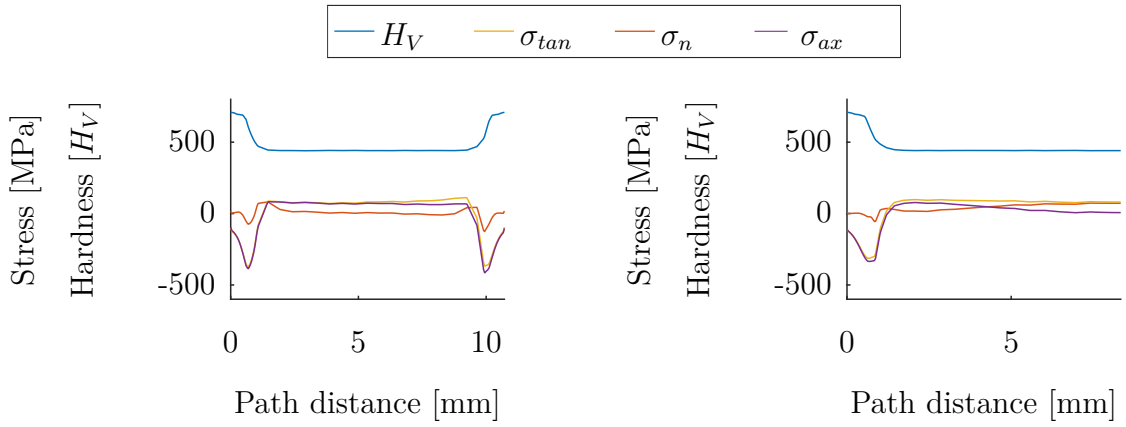


Figure A9.24: Results for heat treatment simulation 18 on cylindrical samples along *path 1* (left) and *path 2* (right).

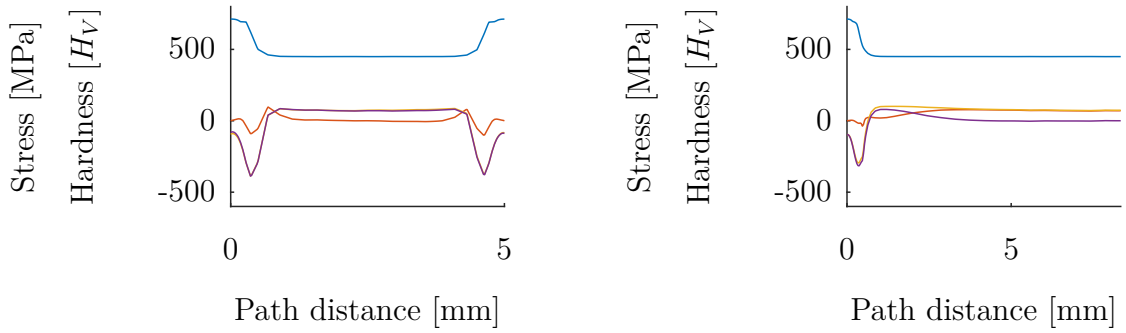


Figure A9.25: Results for heat treatment simulation 19 on cylindrical samples along *path 1* (left) and *path 2* (right).

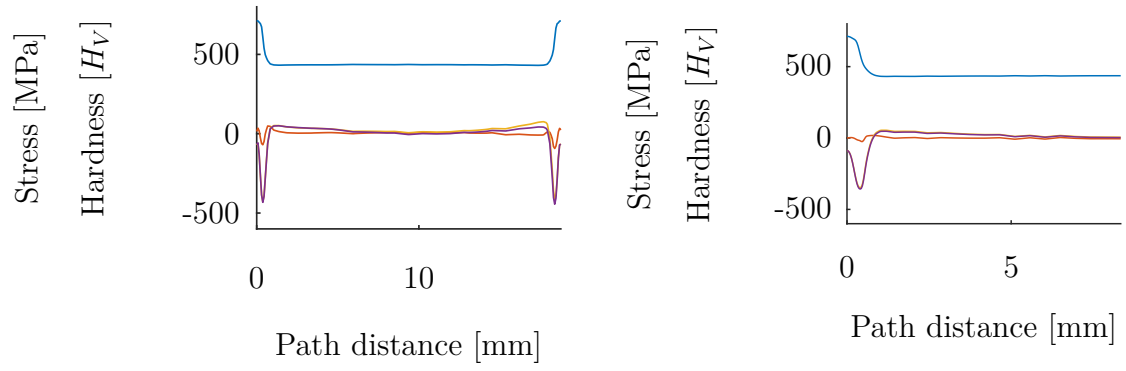


Figure A9.26: Results for heat treatment simulation 20 on cylindrical samples along *path 1* (left) and *path 2* (right).

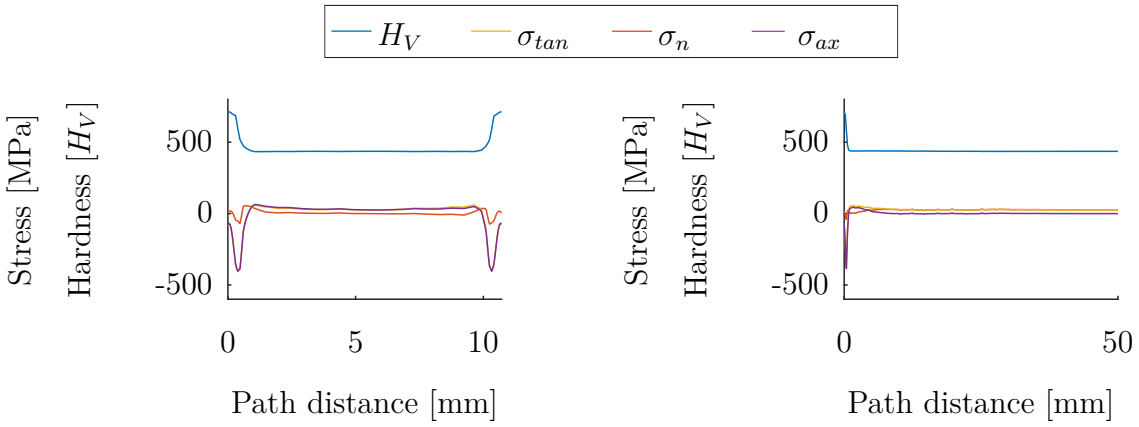


Figure A9.27: Results for heat treatment simulation 21 on cylindrical samples along *path 1* (left) and *path 2* (right).

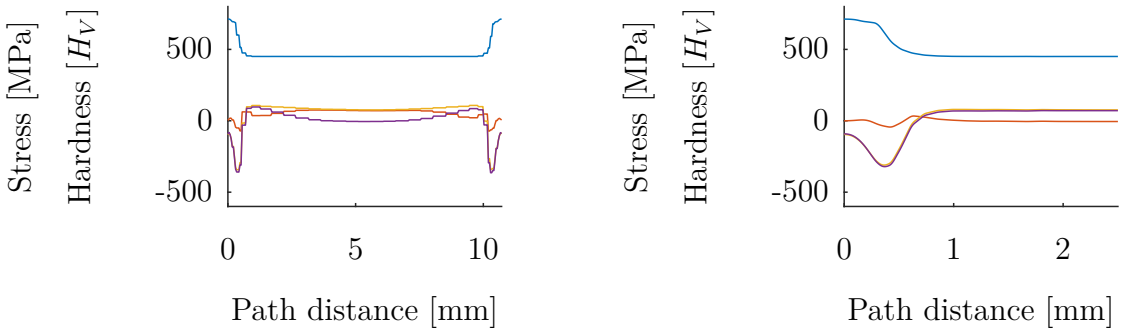


Figure A9.28: Results for heat treatment simulation 22 on cylindrical samples along *path 1* (left) and *path 2* (right).

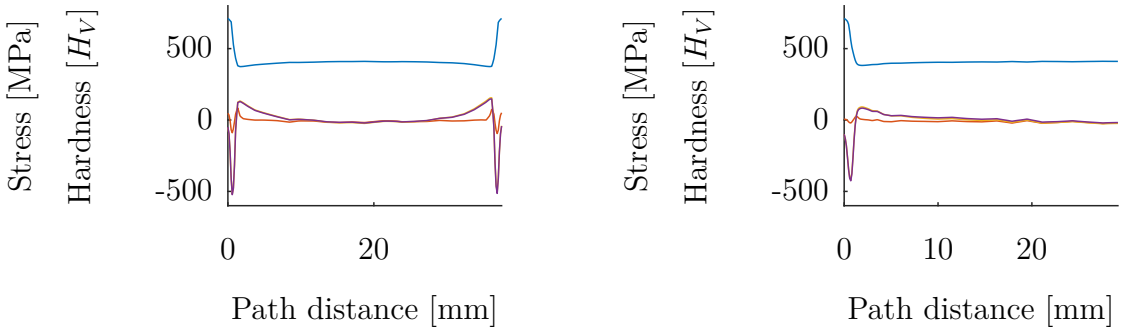


Figure A9.29: Results for heat treatment simulation 23 on cylindrical samples along *path 1* (left) and *path 2* (right).

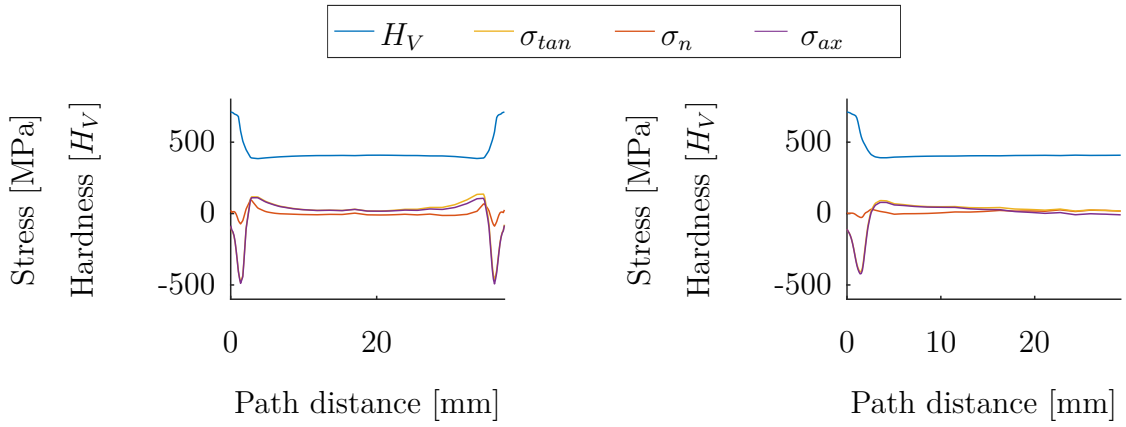


Figure A9.30: Results for heat treatment simulation 24 on cylindrical samples along *path 1* (left) and *path 2* (right).

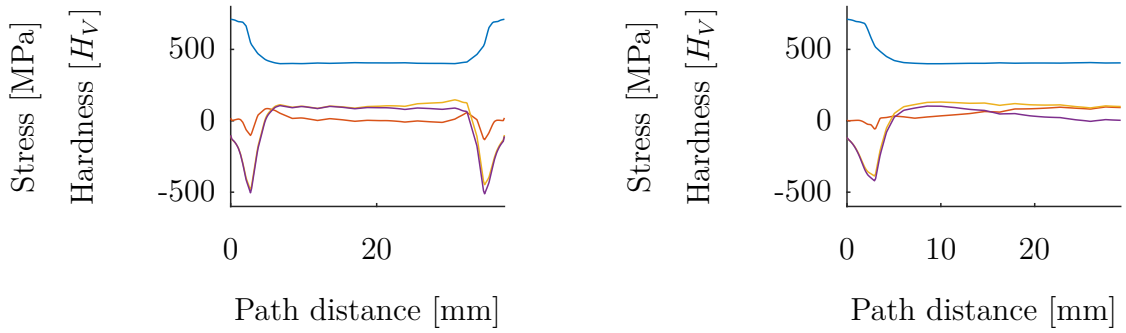


Figure A9.31: Results for heat treatment simulation 25 on cylindrical samples along *path 1* (left) and *path 2* (right).

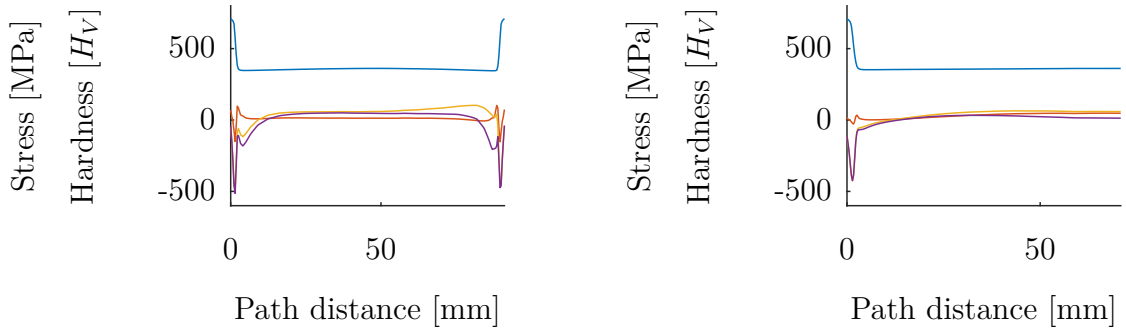


Figure A9.32: Results for heat treatment simulation 26 on cylindrical samples along *path 1* (left) and *path 2* (right).

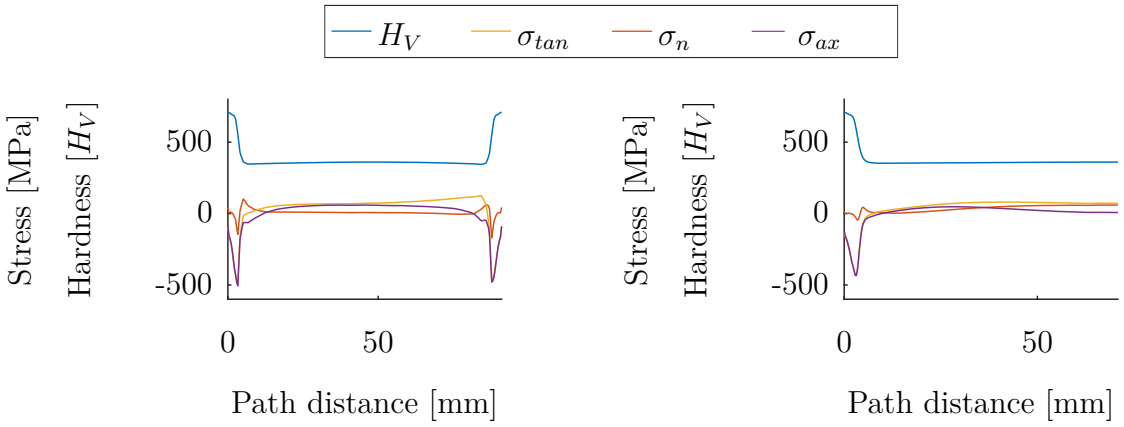


Figure A9.33: Results for heat treatment simulation 27 on cylindrical samples along *path 1* (left) and *path 2* (right).

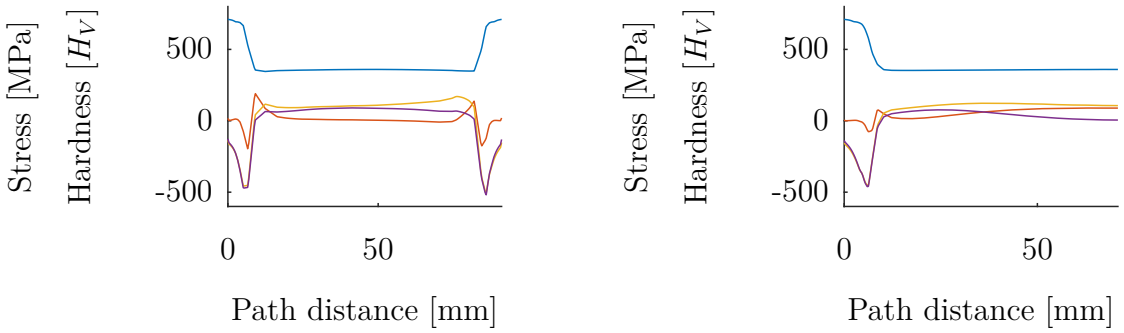


Figure A9.34: Results for heat treatment simulation 28 on cylindrical samples along *path 1* (left) and *path 2* (right).

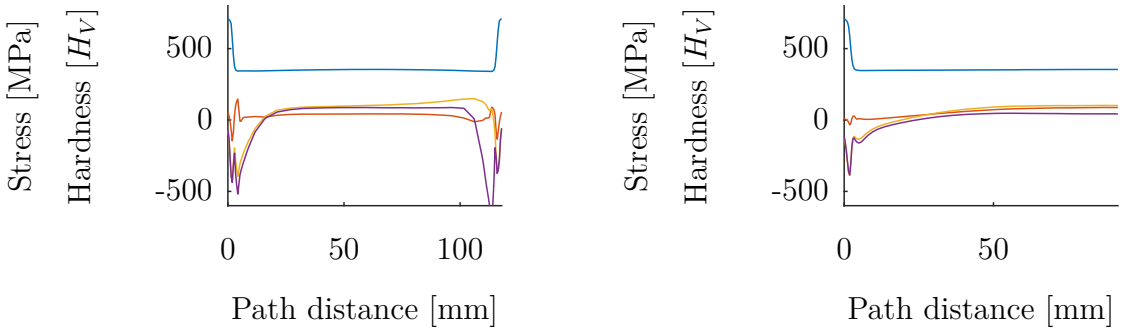


Figure A9.35: Results for heat treatment simulation 29 on cylindrical samples along *path 1* (left) and *path 2* (right).

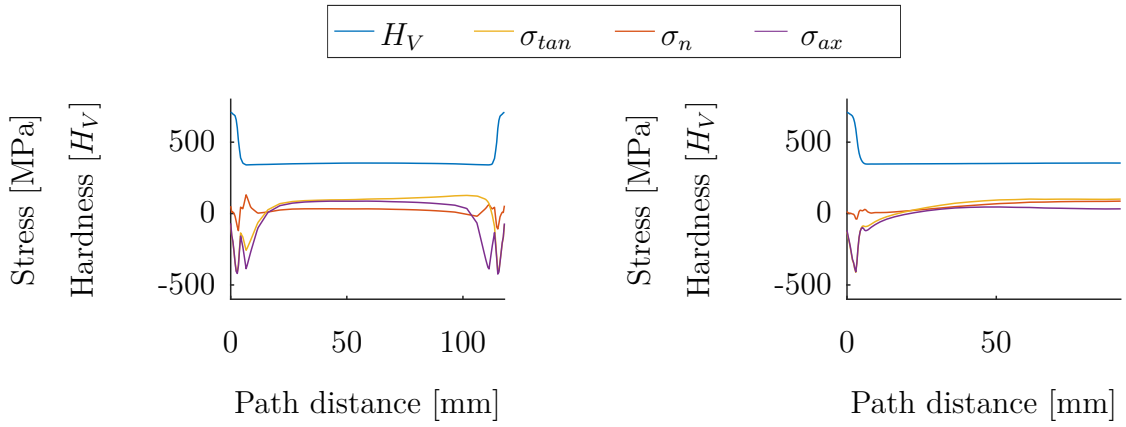


Figure A9.36: Results for heat treatment simulation 30 on cylindrical samples along *path 1* (left) and *path 2* (right).

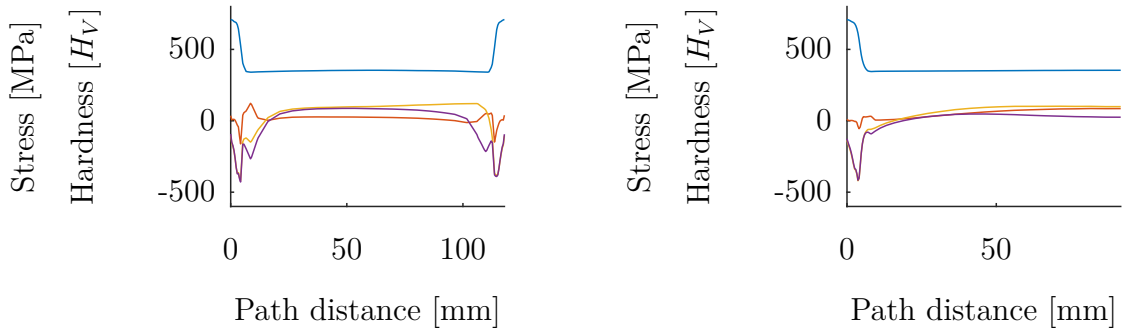


Figure A9.37: Results for heat treatment simulation 31 on cylindrical samples along *path 1* (left) and *path 2* (right).

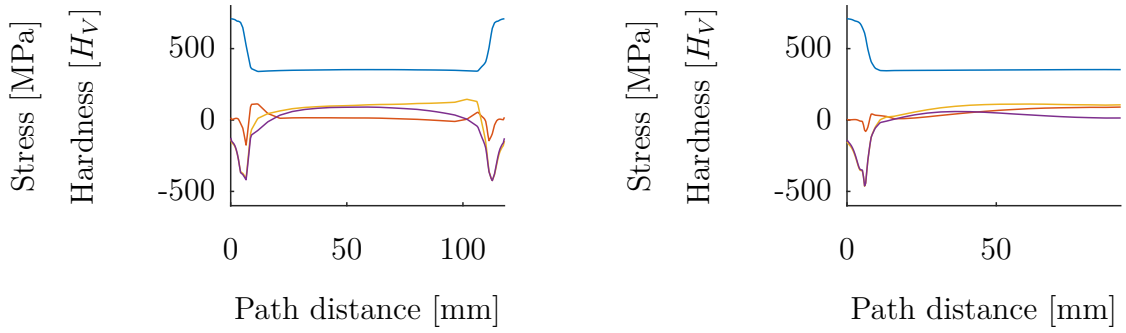


Figure A9.38: Results for heat treatment simulation 32 on cylindrical samples along *path 1* (left) and *path 2* (right).

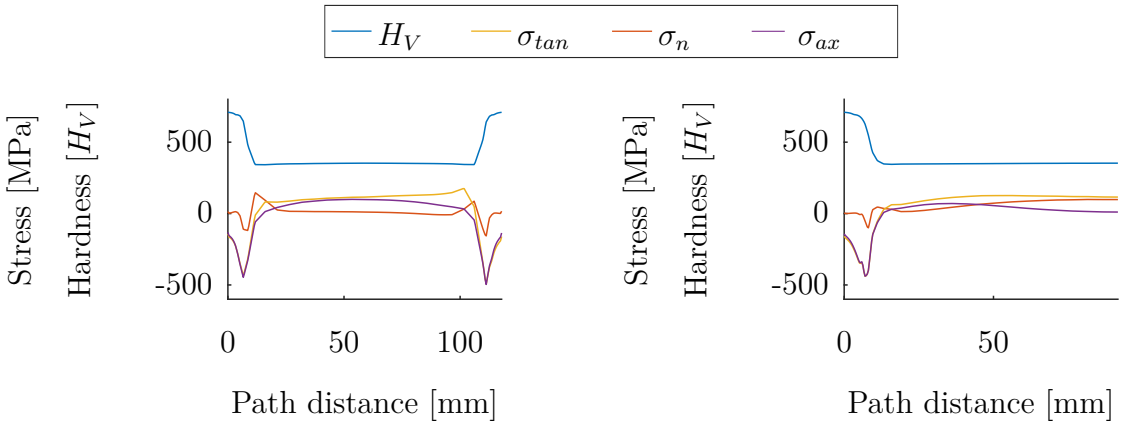


Figure A9.39: Results for heat treatment simulation 33 on cylindrical samples along *path 1* (left) and *path 2* (right).

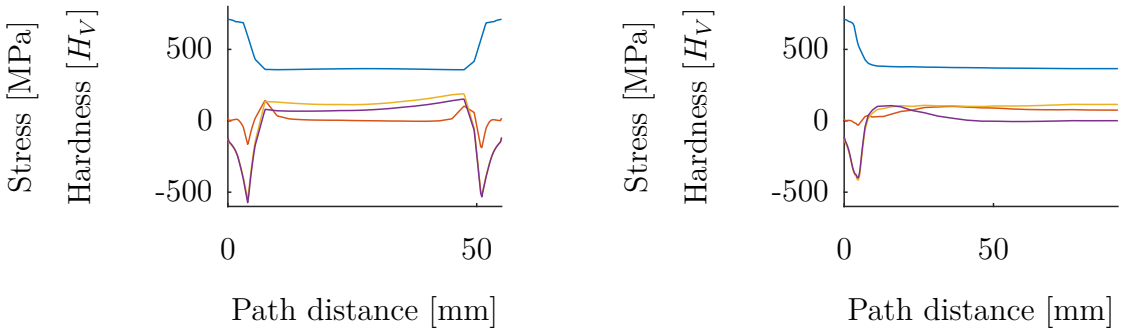


Figure A9.40: Results for heat treatment simulation 34 on cylindrical samples along *path 1* (left) and *path 2* (right).

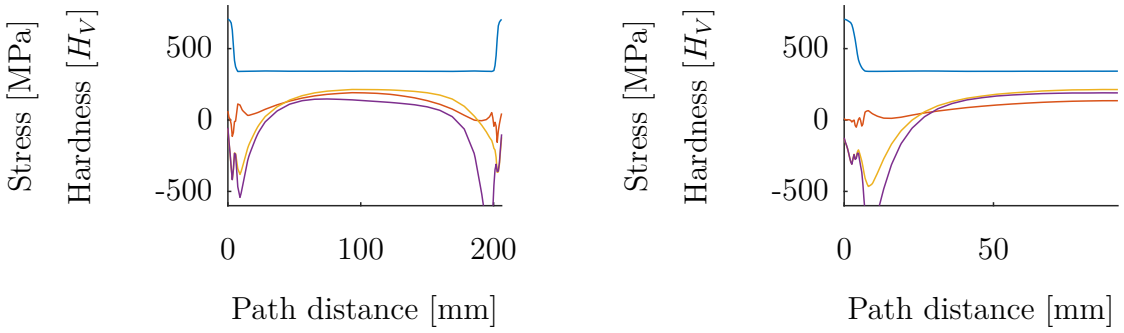


Figure A9.41: Results for heat treatment simulation 35 on cylindrical samples along *path 1* (left) and *path 2* (right).

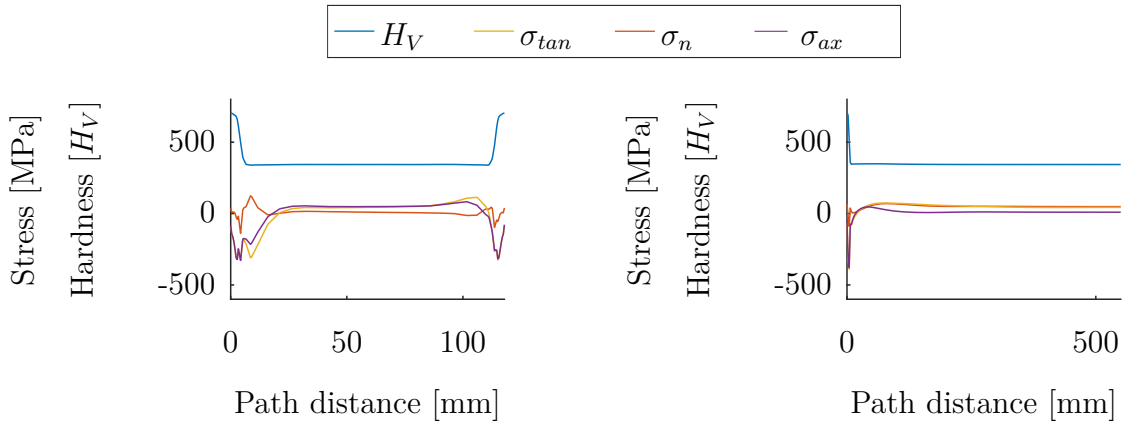


Figure A9.42: Results for heat treatment simulation 36 on cylindrical samples along *path 1* (left) and *path 2* (right).

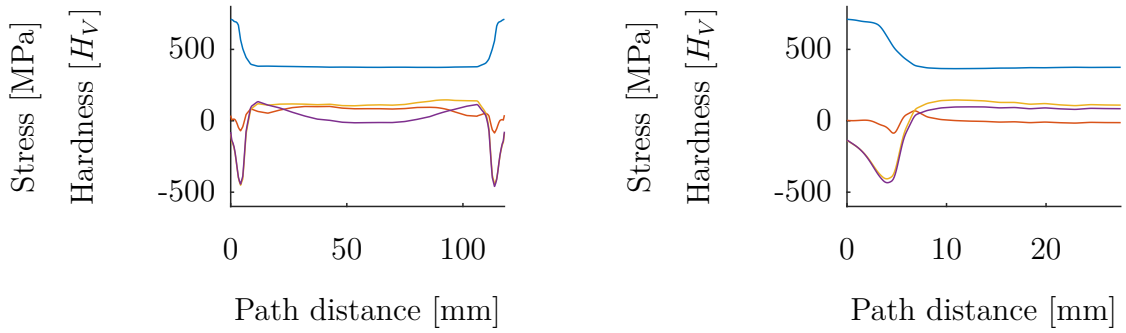


Figure A9.43: Results for heat treatment simulation 37 on cylindrical samples along *path 1* (left) and *path 2* (right).